The University of Nottingham
UNITED KINGDOM · CHINA · MALAYSIA

Development of fluorescent nanosensors for real-time biological assays

Mohamed Mounir Fathallah Elsutohy, Msc

Thesis submitted to the University of Nottingham for the degree of Doctor of Philosophy

September 2016

I. Abstract

The current advances of nanotechnology in medicine and biology open new horizons towards the development of novel tools (nanosensors) for the detection of several biological compounds, disease biomarkers and cellular molecules. Fluorescent nanosensors are utilised as efficient, rapid and sensitive probes in many analytical and biological applications. The small size of nanosensors enables their insertion into live cells, with minimal cellular disturbance, to detect a specific target within the intracellular environment in real-time.

The work described within this thesis outlines the development of fluorescent nanosensors for the detection of cellular and biological markers. Chapter one illustrates a brief introduction for the different types of nanosensors and the methods that are utilised for nanosensor characterisation. Chapter Two describes the development, fabrication and characterisation of size-tuneable ratiometric fluorescent pH nanosensors. The nanosensors were able to detect the pH, one of the most important biological markers, over an extended dynamic range from pH 3.5 to 7.5, encompassing the pH of many biological systems. Chapter Three demonstrates the utilisation of the developed pH nanosensors for the real-time measurement of the intracellular pH of yeast cells, as a model eukaryotic cell, during glucose metabolism. Chapter Four details the study of the process of fluorescence quenching using size controlled core-shell silica nanoparticles. The study showed interesting results for enhanced distance-dependent fluorescence quenching assay using silica nanoparticles. In Chapter Five, aptamer-based fluorescent nanosensors have been developed for the quantitative assay of DNA hybridisation and interferon gamma, a model cytokine.

II. Acknowledgements

First of all, I would like to thank my Lord Allah for providing me the strength, health and wealth to achieve this work.

My deep thanks to my supervisors, Dr Jonathan W. Aylott and Professor Saul J. B. Tendler, for their encouragement, support and helpful scientific discussions throughout my study. I gratefully acknowledge their unlimited advice, valuable recommendations, efforts and guidance.

I wish to thank the people in the Scholarship Division of the Islamic Development Bank (IDB) and the University of Nottingham for funding the project and awarding me the High-Tech Scholarship programme to pursue my PhD.

Special thanks for Dr Veeren Chauhan for his help, assistance and making my life easy in Nottingham.

Many thanks to Dr Mohammad Aref Kyyaly (University of Southampton) and Dr Chris Powell (University of Nottingham) for their sincere co-operation.

To all my friends and colleagues in Boots Science Building, especially, colleagues in D38; Agatha, Shehnaz, Leigh-Ann, Arran and Amjad. I am so grateful for this strong friendship. Thanks for Aziz Aloufi, Abdullah, Safar and Fahd for their support and friendship.

To my exceptional Wife for her continuous sacrifices, love and time she has spent to take care of our family. For my son; Moaaz, and my daughter; Miral, you are the most joyful thing in my life. Big thanks for my sisters, my family, my wife's family and all my friends in Egypt.

And finally….....A very special thanks to my parents for their endless love, patience and praying. I dedicate this thesis to you, with heartfelt gratitude.

III. Contents

I. Abstract I

II. Acknowledgments.....II

III. Contents.....III

IV. List of Figures.....XII

V. List of Tables.....XXI

VI. Abbreviations.....XXII

Chapter One: Introduction 1

1.1. Nanosensors: a new era for biological diagnostic probes.....2

1.1.1. Electrical (electrochemical) nanosensors.....3

1.1.2. Optical nanosensors.....6

1.1.2.1. Fluorescent nanosensors.....6

1.1.2.1.1. Fibre-optic based fluorescent nanosensors.....7

1.1.2.1.2. Nanoparticle-based fluorescent nanosensors.....9

1.1.2.1.3. Quantum dots (QDs) as fluorescent nanosensors.....11

1.1.2.2. Plasmonic (label-free) optical nanosensors.....12

1.1.3. Magnetic nanosensors.....15

1.1.4. Mechanical nanosensors.....17

1.2. Nanosensor characterisation.....19

1.2.1. Dynamic light scattering (DLS).....19

1.2.1.1. Measurement of the hydrodynamic diameters using DLS.....20

1.2.1.2. Measurement of zeta potential by DLS.....21

1.2.2. Electron microscopy for nanoparticle characterisation.....22
1.2.2.1. Scanning electron microscope (SEM).....22
1.2.2.2. Transmission electron microscope (TEM).....23
1.2.3. Fluorescence spectroscopy.....24
1.3. Thesis structure and layout.....28

Chapter Two: Development, fabrication and characterisation of size-tuneable ratiometric fluorescent pH nanosensors for measurement of pH over an extended dynamic range.....29

2.1. Introduction 30
2.1.1. Nanosensor fabrication.....30
2.1.1.1. Polyacrylamide nanosensors.....31
2.1.1.2. Silica nanosensors.....34
2.1.2. Ratiometric fluorescence pH nanosensors 36
2.2. Aim.....40
2.3. Experimental.....41
2.3.1. Materials and chemicals.....41
2.3.2. Fabrication of polyacrylamide nanosensors.....42
2.3.2.1. Covalent conjugation of fluorophores to APMA.....42
2.3.2.2. Preparation of f-PANPs.....42
2.3.2.3. Synthesis of positively-charged polyacrylamide nanoparticles (p-PANPs).....43
2.3.3. Fabrication of silica nanosensors.....44
2.3.3.1. Fluorophore conjugation to APTES.....44
2.3.3.2. Optimised procedure for the production of SNPs.....44

2.3.3.3. Synthesis of amino silica nanoparticles (amino-SNPs) 45
2.3.4. Characterisation of the nanosensors.....45
2.3.4.1. Physical properties characterisation of polyacrylamide nanosensors....45
2.3.4.2. Physical properties characterisation of silica nanosensors.....46
2.3.4.3. Fluorescence detection and establishment of calibration curves.....47
2.3.5. Dye leaching and stability studies using the optimised silica pH nanosensor.....48
2.4. Results and discussion.....49
2.4.1. Polyacrylamide pH nanosensors.....49
2.4.1.1. Production of polyacrylamide pH nanosensors.....49
2.4.1.2. Characterisation of polyacrylamide pH nanosensors.....50
2.4.1.2.1. Size characterisation of PANPs.....51
2.4.1.2.2. Zeta potential measurement of PANPs.....52
2.4.1.2.3. Measurements of the fluorescence signals of the synthesised polyacrylamide pH nanosensors.....53
2.4.2. Silica pH nanosensors.....56
2.4.2.1. Preliminary protocols for the synthesis of silica nanoparticles (SNPs).....56
2.4.2.2. Production of size-tuneable SNPs 59
2.4.2.2.1. Effect of varying amounts of TEOS.....59
2.4.2.2.2. Effect of varying amounts of NH_4OH.....61
2.4.2.2.3. Effect of ethanol quantity and alcohol type.....63
2.4.2.2.4. Effect of different volumes of fluorophore-APTES and fluorophore type.....65
2.4.2.3. Optimum protocol for the preparation of SNPs.....67

2.4.2.4. Synthesis of amino-SNPs.....68
2.4.2.5. Characterisation of the physical properties of the optimised SNPs.....69
2.4.2.5.1. Size and shape characterisation.....69
2.4.2.5.2. Zeta potential measurements.....71
2.4.2.6. Fabrication and optical characterisation of the ratiometric fluorescent silica pH nanosensors.....73
2.4.2.7. Dye leaching and stability studies using the optimum silica pH nanosensor.....77
2.5. Conclusion.....79

Chapter Three: Real-time measurement of the intracellular pH of yeast cells during glucose metabolism using ratiometric fluorescent pH nanosensors.....81

3.1. Introduction.....82
3.1.1. The world of yeast (structure, growth and physiology).....82
3.1.2. Importance of the intracellular pH of yeast cells.....85
3.1.3. Current methods for the measurement of the intracellular pH of yeast cells.....87
3.2. Aim.....89
3.3. Experimental.....90
3.3.1. Materials and chemicals.....90
3.3.2. Yeast strain and growth conditions.....90
3.3.3. Cellular uptake study.....91

3.3.4. Toxicity study 91
3.3.5. Incubation time.....92
3.3.6. Nanosensors calibration 92
3.3.7. Measurement of the intracellular pH of yeast cells 93
3.3.8. Image acquisition and data analysis.....94
3.4. Results and discussion.....95
3.4.1. Silica pH nanosensors.....95
3.4.1.1. Unmodified silica pH nanosensors.....95
3.4.1.2. Positively-charged silica pH nanosensors.....97
3.4.1.3. Separation of silica pH nanosensors from yeast cells.....99
3.4.2. Optimum nanosensors for the measurement of the intracellular pH of yeast.....101
3.4.3. Positively-charged polyacrylamide pH nanosensors (PPA).....102
3.4.3.1. Effect of growth time of yeast on the percentage of cellular internalisation.....103
3.4.3.2. Effect of different stress-based techniques on the cellular internalisation.....106
3.4.3.3. Cellular uptake study.....109
3.4.3.4. Toxicity study of PPA.....111
3.4.3.5. Incubation time.....112
3.4.3. Measurement of the intercellular pH of yeast cells.....114
3.4.4.1. Calibration curve.....114
3.4.4.2. Real-time measurement of the intracellular pH of yeast cells during glucose metabolism.....116
3.5. Conclusion.....123

Chapter Four: Distance-dependent fluorescence quenching study using size controlled core-shell fluorescent silica nanoparticles.....126

4.1. Introduction.....127

4.1.1. Fluorescence quenching,.....127

4.1.1.1. Förster (fluorescence) resonance energy transfer (FRET).....129

4.1.1.2. Dexter energy transfer.....133

4.1.1.3. Nanometal surface energy transfer (NSET).....134

4.1.2. Functionalised silica nanoparticle as a versatile nanosensors platforms.....137

4.1.2.1. Surface functionalisation of SNPs.....137

4.2. Aim.....142

4.3. Experimental 143

4.3.1. Materials and chemicals.....143

4.3.2. Preparation of SNPs 143

4.3.3. Synthesis of core-shell TAMRA-SNPs 144

4.3.4. Surface functionalisation of SNPs with a carboxylic acid moiety.....144

4.3.5. Activation of carboxy-SNPs with EDC/NHS.....145

4.3.6. Conjugation of the activated SNPs to amino-FAM or amino-BHQ2.....145

4.3.7. Characterisation of SNPs models.....145

4.3.8. Calibration of the optimised TAMRA-SNPs with amino-BHQ2.....146

4.4. Results and discussion.....147

4.4.1. Optimisation of the binding reaction between p-SNPs and amino-molecule.....147

4.4.1.1. Production of carboxy-SNPs 147

4.4.1.2. Binding of carboxy-p-SNPs to amino-FAM without EDC/NHS activation.....149
4.4.1.3. Binding of carboxy-p-SNPs to amino-FAM after EDC/NHS activation.....151
4.4.2. Study of fluorescence quenching process using TAMRA-SNPs models.....153
4.4.2.1. Production and characterisation of SNPs models.....153
4.4.2.2. Study of the fluorescence quenching process using Model 1.....156
4.4.2.2.1. Effect of BHQ2 diffusion on the fluorescence quenching of Model 1.....159
4.4.2.2.2. Effect of quencher type on the fluorescence quenching process.....160
4.4.2.3. Study of fluorescence quenching process using core-shell-TAMRA-SNPs.....162
4.4.2.4. Explanation of the fluorescence quenching process using silica models.....165
4.5. Conclusion.....168

Chapter Five: Aptamer-based fluorescent nanosensors for the quantitative assay of DNA hybridisation and interferon gamma.....170

5.1. Introduction.....171
5.1.1. Aptamers 171
5.1.2. Aptamers; the future sensing probes (aptasensors).....173

5.1.3. Cytokines; the signalling biomarkers.....176
5.1.4. The current methods for cytokine detection.....178
5.1.4.1. Classical immunoassays for cytokines detection.....178
5.1.4.2. Flow cytometric methods for cytokines detection.....180
5.1.4.3. Biosensors for cytokine detection.....181
5.1.4.4. Nanosensors for cytokine detection.....183
5.1.4.5. Other methods for cytokine detection.....184
5.2. Aim.....185
5.3. Experimental.....186
5.3.1. Materials and chemicals.....186
5.3.2. Production of the nanosensors.....187
5.3.2.1. Immobilisation of the sensing aptamers onto SNPs.....187
5.3.2.2. Hybridisation of aptamer-SNPs with the quenching segment.....187
5.3.3. Detection of DNA hybridisation.....188
5.3.4. Incubation time for IFN-γ.....188
5.3.5. Detection of IFN-γ.....189
5.3.6. Selectivity studies.....189
5.4. Results and discussion.....190
5.4.1. Selection of the sensing aptamer sequence.....190
5.4.2. The FRET-based nanosensors.....191
5.4.2.1. Sensing strategy.....191
5.4.2.2. Immobilisation of the aptamer onto nanoparticle surface.....193
5.4.2.3. Optimisation of the sensing aptamer concentration.....195
5.4.2.4. Optimisation of the quenching segment concentration (DNA3'Q).....197

5.4.2.5. Quantitative detection of DNA hybridisation using the FRET-based nanosensors.....199
5.4.2.6. The use of the FRET-based nanosensors for IFN-γ detection.....202
5.4.2.7. Selectivity of the nanosensor.....205
5.4.3. The extended-distance quenching nanosensor.....207
5.4.3.1. Optimisation of the initial concentration of TAMRA.....208
5.4.3.2. Selection of the quencher position.....210
5.4.3.3. Quantitative detection of C-DNA hybridisation and IFN-γ using the extended-distance quenching nanosensor.....213
5.5. Conclusion.....216

Chapter Six: Conclusions and Future Work.....218

6.1. Production of ratiometric fluorescent pH nanosensors.....219
6.2. Real-time measurement of the intracellular pH.....222
6.3. Distance-dependent fluorescence quenching study using SNPs.....224
6.4. Aptamer-based nanosensors for the detection of DNA and cytokine.....226

Chapter Seven: References.....228

IV. List of Figures

Chapter One

Figure 1.1: The microscopical images of cells, grown onto conductive surfaces, modified with vertical silicon nanowires.....5

Figure 1.2: A schematic diagram for a fibre-optic fluorescent biosensor that utilises changes in the fluorescence signals due to FRET for analyte quantification.....9

Figure 1.3: Illustrative diagram shows the possible functional groups or sensing elements that can be grafted onto or entrapped inside the PEBBLEs.....10

Figure 1.4: (A) The emission of five batches of QDs, prepared with different size range and excited under a UV lamp. (B) The multicolour image of human epithelial cells that were labelled with these QDs to visualise the sub-cellular organelles 12

Figure 1.5: Localised surface plasmon resonance (LSPR) occurs in noble metal nanoparticles due to light excitation of the outer electrons of the nanoparticle atoms.....13

Figure 1.6: Illustrative diagram shows the shift in the relaxation time (*T2*) of the water protons surrounding super-paramagnetic nanoparticles in different states.....16

Figure 1.7: *In-vitro* detection of target biomolecules using functionalised mechanical nanosensor.....18

Figure 1.8: The Jablonski energy diagram shows the process of light absorption and the possible pathways for the excited molecule.....25

Chapter Two

Figure 2.1: Illustrative diagram shows the synthesis of polyacrylamide nanoparticles (PANPs) *via* free-radical polymerisation reaction. The reaction takes place inside nanometre water droplets, stabilised by surfactants, within an inverse microemulsion.....32

Figure 2.2: The conjugation reaction between amino-acrylamide monomer (APMA) and N-hydroxyl succinimide ester derivative of a fluorophore to produce APMA-fluorophore conjugate that can be used for the production of f-PANPs.....33

Figure 2.3: Synthesis of silica nanoparticles (SNPs) by the Stöber method.....35

Figure 2.4: A schematic diagram for a ratiometric fluorescent pH nanosensor, composed of an inert nanoparticle matrix, encapsulating a pH-sensitive fluorophore and a reference fluorophore within the same matrix.....38

Figure 2.5: Chemical structure of Oregon Green® 488 (OG), 5-(and-6)-carboxyfluorescein (FAM) and 5-(and-6)- carboxytetramethylrhodamine (TAMRA).....38

Figure 2.6: The chemical structure of 3-acrylamidopropyl trimethylammonium hydrochloride (ACTA), which polymerises with acrylamide monomers and bisacrylamide to produce positively charged fluorescent polyacrylamide nanoparticles (p-PANPs).....50

Figure 2.7: (A) and (B) The hydrodynamic diameters of the unmodified fluorescent polyacrylamide nanoparticles (f-PANPs) and positively-charged polyacrylamide nanoparticles (p-PANPs) respectively, measured by a DLS instrument.....51

Figure 2.8: The zeta potential values of the unmodified fluorescent polyacrylamide nanoparticles (f-PANPs) and positively-charged polyacrylamide nanoparticles (p-PANPs), measured by a DLS instrument.....52

Figure 2.9: The fluorescence spectra of the synthesised ratiometric fluorescent polyacrylamide pH nanosensors, suspended in McIlvaine buffer with different pH from pH 3.01 to 8.48.....54

Figure 2.10: The normalised calibration curve of the synthesised polyacrylamide ratiometric fluorescent pH nanosensors, suspended in McIlvaine buffer with pH values from pH 3.01 to 8.5.....55

Figure 2.11: Illustrative diagram shows the covalent binding of amino-silane precursor (APTES) to succinimidyl ester of a fluorophore molecule.....58

Figure 2.12: The Effect of varying amounts of TEOS on the hydrodynamic diameters of p-SNPs and FAM-SNPs.....60

Figure 2.13: The effect of different amounts of NH_4OH, ranging from 2.3 mmol to 38.5 mmol, on the hydrodynamic diameters of p-SNPs and FAM-SNPs.....62

Figure 2.14: The effect of varying amounts of ethanol (0.17 mol to 0.85 mol) on the hydrodynamic diameters of p-SNPs and FAM-SNP.....63

Figure 2.15: The effect of different volumes of the conjugated FAM-APTES, prepared using 1mg/ml of FAM, on the hydrodynamic diameters of the produced FAM-SNPs.....65

Figure 2.16: (A) and (B) The measured hydrodynamic diameters of p-SNPs and f-SNPs, respectively, synthesised using the optimised protocol. (C) and (D) The eSEM and TEM images of p-SNPs while (E) and (F) are the eSEM and TEM images of f-SNPs.....70

Figure 2.17: (A) Zeta potential values of p-SNPs, f-SNPs and amino-SNPs, suspended in PBS, pH 7.4 and measured in water by Malveren Zetasizer DLS instrument. (B) Zeta potential values of p-SNPs and FAM-SNPs measured in different pH values.....72

Figure 2.18: The normalised ratiometric calibration curves for the developed pH silica nanosensors, covalently linked to different ratios of OG: FAM (100%:0%, 75%: 25%, 50%: 50%, 25%: 75% and 0%: 100%).....75

Figure 2.19: (A) The fluorescence spectra of the optimised silica pH nanosensor, covalently linked to OG and FAM (50%: 50%), and a reference fluorophore (TAMRA), suspended in McIlvaine buffer with pH from 2.5 to 8.5. (B) The normalised ratiometric calibration curves for the optimum nanosensor.....76

Figure 2.20: (A) The mean of fluorescence signals of the optimised silica pH nanosensors, covalently linked to OG, FAM and TAMRA over different time period from 5 minutes to 48 hours. The fluorescence intensities were recorded at 520 nm and 577 nm over different time intervals. (B) The normalised ratiometric fluorescence (I_{520}/I577) of the optimised silica pH nanosensor over the same time period, suspended in PBS buffer, pH 7.4.....78

Chapter Three

Figure 3.1: Illustrative diagram represents the shape, structure and cellular organelles of the yeast cell *(Saccharomyces cerevisiae)*.....83

Figure 3.2: Typical growth curve of yeast cells established by measurement of the optical density (OD_{600}) at successive time periods after the beginning of growth.....84

Figure 3.3: (A) Fluorescence image of yeast cells incubated with the unmodified (negatively) silica pH nanosensors (10 mg/mL) for 24 hours, recorded in the red channel and brightfield mode while (B) is the inverted false colour image of A, created by ImageJ® software, used for visualisation of cells-containing nanosensors.....96

Figure 3.4: The image of yeast cells incubated with 10 mg/ml of positively-charged silica pH nanosensors, suspended in growth medium, for 24 hours.....98

Figure 3.5: The fluorescent image of yeast cells incubated with PPA (10 mg/ml) for 24 hours.....102

Figure 3.6: The effect of growth time of yeast on the percentage of cellular internalisation with PPA (10 mg/ml).....105

Figure 3.7: The effect of stress-based techniques/methods on the percentage of the internalised yeast cells with PPA (10 mg/ml) using the specified conditions for each method.....107

Figure 3.8: The fluorescent image, taken in the red channel, for the internalised yeast cells with PPA (10 mg/ml) in NaCl hyper-osmotic solution (154 mM).....108

Figure 3.9: Figure 3.9: (A) The fluorescence microscopy image of yeast cells, incubated with 15 mg/mL PPA, and taken in the red channel. (B) The cellular uptake study of yeast cells incubated with different concentrations of PPA (20 µg/mL- 30 mg/mL) for 4 hours in phosphate buffer. RFUs of TAMRA was recorded on a plate reader (λ_{ex} = 545nm and λ_{em} = 575 nm) as an indicator for the cellular uptake.....110

Figure 3.10: The toxicity study of different concentrations of PPA incubated with a constant number of yeast cells and detected by colony forming unit test (CFU).....112

Figure 3.11: The effect of incubation time on cellular internalisation of yeast cells, incubated with PPA (15 mg/ml), for different times (1hour to 24 hours).....113

Figure 3.12: Normalised calibration curve of positively charged polyacrylamide pH nanosensors (PPA) suspended in the McIlvaine buffer with different pH values which ranged from pH 2.94 to 8.52.....116

Figure 3.13: The colour map images of glucose-starved cells (0 min), incubated with PPA for 4 hours in phosphate buffer and the produced colour map images for the cells after different times of glucose addition from 1 minute and up to 45 minutes.....119-120

Figure 3.14: The response of the intracellular pH of yeast cells during glucose metabolism in real-time.....121

Chapter Four

Figure 4.1: Illustrative diagram shows the FRET process.....131

Figure 4.2: Illustrative diagram shows the mechanism of the Dexter electron exchange/transfer.....133

Figure 4.3: Illustrative diagram shows the process of nanometal surface energy transfer (NSET) from an excited fluorophore to a noble metal nanoparticles surface.....135

Figure 4.4: The classical reaction between carboxylic acid group and amino-molecule.....139

Figure 4.5: A schematic diagram for the chemical reaction between carboxylic acid containing molecule with amino-molecule using the EDC/sulfo-NHS coupling chemistry for the activation of the carboxylic acid group.....140

Figure 4.6: The average of zeta potential values of unmodified p-SNPs and carboxy-SNPs that were prepared using CS.....148

Figure 4.7: The effect of varying concentrations of CS on the zeta potential value of the produced carboxy-SNPs, prepared using different CS concentrations.....149

Figure 4.8: The fluorescence spectra of amino-FAM in solution, measured before binding to SNPs (blank, blue line), after binding to carboxy-p-SNPs without the EDC/NHS activation (red line) and after binding to the EDC/NHS activated carboxy-p-SNPs (green line).....151

Figure 4.9: Illustrative diagrams represent the studied models (1, 2 and 3) and characterisation of these models by DLS and eSEM.....154

Figure 4.10: The fluorescence spectra of Model 1, prepared without binding to BHQ2 (top line, blank) and after binding to different concentrations of BHQ2 (0.02 µmol – 0.52 µmol).....157

Figure 4.11: The relationship between the percentage of fluorescence quenching of Model 1 and different concentrations of BHQ2 which ranged from 0.02 to 0.52 µmol.....159

Figure 4.12: The fluorescence spectra of Model 1, prepared without surface modification or activation, before the addition of amino-BHQ2 (blue line) and after BHQ2 addition (red line).The nanoparticles were stirred for 24 hours with the added BHQ2.....160

Figure 4.13: The fluorescence intensity of amino-FAM molecules after binding to BHQ1-SNPs and p-SNPs.....161

Figure 4.14: The fluorescence intensities of different models of TAMRA-SNPs and TAMRA-core-shell-SNPs after binding to BHQ2.....163

Chapter Five

Figure 5.1: A schematic diagram shows the aptamer folding upon binding to a specific biomarker on a cell surface.....171

Figure 5.2: A schematic diagram for a FRET-based aptasensor (molecular beacon).....173

Figure 5.3: Illustrative diagram for an electrochemical aptasensor for the detection of a target protein.....175

Figure 5.4: A schematic diagram illustrates the use of a FRET-based aptasensor for thrombin detection, as a model protein, based on the displacement of the quenching DNA segment upon thrombin binding.....175

Figure 5.5: The activation, release and major functions of several cytokines....177

Figure 5.6: A schematic diagram shows the process of enzyme-linked immunoassay for the detection of a specific target protein.....179

Figure 5.7: A schematic diagram illustrates the proposed strategy for the development of FRET-based nanosensors for the detection of a complementary DNA sequence.....192

Figure 5.8: A picture shows p-SNPs before (white) and after (pink) the immobilisation of APT-1-TAM.....194

Figure 5.9: The effect of the aptamer concentrations (APT-1-TAM) on the efficiency of the immobilisation reaction of this aptamer onto the surface of p-SNPs.....196

Figure 5.10: The effect of the quenching DNA segment concentrations (DNA3'Q) on the fluorescence signals of TAMRA, attached to the 5' end of APT-1-TAM, after the hybridisation with DNA3'Q.....197

Figure 5.11: (A) The response of the FRET-based nanosensor after the hybridisation with C-DNA with concentrations ranged from 0.1 nmol to 100 nmol and (B) is the linear part of the calibration curve for detection of C-DNA within concretions from 3.75 nmol to 50 nmol.....200

Figure 5.12: The effect of incubation time on the response of the FRET-based nanosensor for the detection of IFN-γ (100 nmol) 203

Figure 5.13: (A) The response of the FRET-based nanosensor after incubation with different concentrations of IFN-γ (3.75 nmol to 1000 nmol) and (B) is the linear calibration curve of the nanosensor after incubation with IFN-γ, concentrations ranged from 15 nmol to 250 nmol.....204

Figure 5.14: The selectivity study of the FRET-based nanosensor for the detection of IFN-γ.....206

Figure 5.15: The proposed analytical design for the extended-distance quenching nanosensor.....207

Figure 5.16: The effect of different volumes of TAMRA-APTES on the percentage of fluorescence quenching after hybridisation of TAMRA-SNPs-APT-1 system to DNA5'Q.....209

Figure 5.17: The percentage of the resultant fluorescence quenching of TAMRA-SNPs after hybridisation/conjugation to different quenching DNA segments, carrying BHQ2 at different positions.....211

Figure 5.18: (A) and (B) The linear calibration curves for the detection of C-DNA hybridisation and IFN-γ, respectively, using the developed extended-distance quenching nanosensor.....214

V. List of Tables

Table 2.1 A summary for previously reported protocols that were repeated in this study for the synthesis of SNPs in the size range ~65 nm.....56

Table 2.2: The optimised amount of NH_4OH (28-30% w/v) that was required used to prepare size-tuneable SNPs, using the optimised protocol, with using constant amounts of other reactants.....67

Table 2.3: The hydrodynamic diameters of the optimised SNPs batches, measured by DLS, and the corresponding size of the same SNPs batches, imaged by eSEM and TEM.....70

Table 4.1: Fluorescent dyes that have been used in biological assays and their corresponding black hole quenchers (BHQ) that have been utilised to establish FRET pairing systems.....132

Table 4.2: Some commercially available organosilanes that have been used for surface functionalisation of SNPs.....138

Table 4.3: A summary for the fluorescence quenching study using different models of TAMRA-SNPs and TAMRA-core-shell-SNPs.....164

Table 5.1: A Summary for the aptamers sequences that were used in this study.....186

Table 5.2: A summary for the limit of detection (LOD) of previously reported methods for the detection of DNA hybridisation, compared with the LOD of the developed FRET-based nanosensor for the detection of C-DNA.....201

VI. Abbreviations

Å	Angstrom
ACTA	3-acrylamidopropyl trimethylammonium-hydrochloride
AFM	Atomic force microscope
Amino-FAM	Fluorescein cadaverine; 5-(5-aminopentyl)thioureidylfluorescein dihydrobromide salt
AOT	Dioctyl sodium sulfosuccinate
APMA	N-(3-aminopropyl)methacrylamide-hydrochloride
APS	Ammonium persulphate
APT-1	ssDNA sequence-5'GGGGTTGGTTGTGTTGGGTGTTGTGT 3' (C6-NH_2))
APT-1-TAM	ssDNA sequence-5' TAMRA-GGGGTTGGTTGTGTTGGGTGTTGTGT 3' (C6 NH_2)
APT-2	ssDNA sequence-5' BHQ2 GGGGTTGGTTGTGTTGGGTGTTGTGTACAACCAACCCC 3' (C6-NH_2)
APTES	(3-aminopropyl)triethoxysilane
ATP	Adenosine triphosphate
BHQs	Black hole quenchers
Bisacrylamide	N, N' methylenebis(acrylamide)
Brij	polyoxyethylene(4) lauryl ether
CCD	charge coupled detector
C-DNA	ssDNA sequence-5' ACACAACACCCAACACAACCAACCCC 3'

CFU	Colony forming unit
CS	Carboxyethylsilanetriol sodium salt, 25 % g/g
DLS	Dynamic light scattering
DNA	Deoxyribonucleic acid
DNA-3'Q	ssDNA sequence-5' ACAACCAACCCC BHQ2 3'
DNA-5'Q	ssDNA sequence-5' BHQ2 ACAACCAACCCC 3'
EDC	1-Ethyl-3-(3-dimethylaminopropyl)-N'-carbodiimide hydrochloride
ELISA	Enzyme linked immunosorbent assay
ELISpot	enzyme-linked immunospot
eSEM	Environmental scanning electron microscope
EtOH	Ethanol
FAM	5-(and-6)-carboxyfluorescein-succinimidylester
FDA	Food and Drug Administration
f-PANPs	Fluorescent polyacrylamide nanoparticles
FRET	Fluorescence (Förster) resonance energy transfer
f-SNPs	Fluorescent silica nanoparticles
GFP	Green fluorescent protein
HPLC	High performance liquid chromatography
IFNs	Interferons
IFN-γ	Interferon gamma
IL	Interleukin
KDa	Kilo Dalton
K_d	Dissociation constant
LOD	Limit f detection

LSPR	Localised surface plasmon resonance
MeOH	Methanol
MES	2-(n-morpholino)ethanesulfonic acid
MRI	Magnetic resonance imaging
NaOH	Sodium hydroxide
NH_4OH	Ammonium hydroxide
NHS	N-hydroxysuccinimide
nm	Nanometre
NSET	Nanometal surface energy transfer
OD_{600}	Optical density at 600 nm
OG	Oregon Green® 488 carboxylic acid succinimidylester-5-isomer
PANPs	Polyacrylamide nanoparticles
P-ATPase	plasma membrane ATPase
PBS	Phosphate-buffered saline
PDGF	Platelet derived growth factor
PDI	Polydispersity index
PEBBLEs	Probes Encapsulated By Biologically Localized Embedding
PEG	Polyethylene glycol
pKa	Acidity constant
PPA	Positively charged polyacrylamide nanosensors
p-PANPs	Positively charged polyacrylamide nanoparticles
p-SNPs	Positively charged silica nanoparticles
QDs	Quantum dots
RFU	Relative fluorescent unit
RNA	Ribonucleic acid

SELEX	Systematic evolution of ligands by exponential enrichment
SEM	Scanning electron microscope
SERS	Surface enhanced Raman spectroscopy
SI	Sandwich immunoassay
SNPs	Silica nanoparticles
SPR	Surface plasmon resonance
ssDNA	Single stranded deoxyribuneculic acid
TAMRA	5-(and-6)-carboxytetramethyl-rhodamine-succinimidylester
TEMED	N,N,N,N-tetramethylethylenediamine
TEOS	Tetraethyl-orthosilicate
TGF- β	Transforming growth factor-β
TNF-α	Tumour necrosis factor alpha
UV	Ultraviolet
V-ATPase	Vacuolar ATPase

Chapter One

Introduction

1.1. Nanosensors: a new era for biological diagnostic probes

There is no doubt that the early identification of disease biomarkers is one of the key factors for disease prevention and effective treatment [1]. During the early stages of disease progression, biomarkers are produced at very low concentrations, making them difficult to be detected. Therefore, the main challenge for the early disease diagnosis is to develop a method that is capable of detecting disease biomarker with high sensitivity and specificity [2]. Traditional screening methods such as blood tests, X-ray investigations and biopsy may not be useful for the early disease diagnosis [2, 3]. Additionally, high throughput bioanalytical techniques/tools, including high-performance liquid chromatography (HPLC), enzyme-linked immunosorbent assay (ELISA), sandwich immunoassay (SI) and flow cytometric methods, provide rapid, sensitive and accurate methods for biomarkers detection. These techniques, however, are time-consuming, expensive, require multiple manipulations and cannot be used for the real-time measurements. As a result, application of such techniques for the early disease diagnosis and biomarker detection is limited [4, 5].

Marked integration between nanotechnology and medicine has contributed in fabrication of smart nanomaterials for multiple medical and biological purposes [6, 7]. Nanosensors are amongst such materials which can be used as low-cost, rapid and sensitive tools for the real-time detection of disease biomarkers, biological compounds and cellular molecules [8-10]. The use of nanosensors in biological assays has established a new era for disease diagnosis and biological measurements, which may be helpful to identify cellular behaviour and disease progression in more detail [11].

Nanosensors are tiny devices (probes) with a size of ~100 nm that could be inserted into live cells to permit intracellular measurements and detect target analyte in the real-time. The utilisation of nanosensors in biological assays provides simple analytical operation and short time of analysis [12-14].

Generally, the materials used for nanosensor fabrication should have the capability of converting the biological/cellular signals, occurring upon analyte interaction, into measurable signals that can be recorded by a suitable device. According to the recorded signal and measurement mode, nanosensors are classified into four major types; *electrical (electrochemical), optical, magnetic* and *mechanical nanosensors* [15].

1.1.1. Electrical (electrochemical) nanosensors

Electrical (electrochemical) nanosensors are fabricated from electro-active nanomaterials that exhibit changes in their electrical properties upon interaction with target analyte. The sensing mechanism is based on detection of the resultant changes in the electrical signal, such as conductance or resistance, of the corresponding nanosensor and can be used for analyte quantification. To facilitate target molecule binding, functionalisation of nanosensors with suitable binding molecules, such as receptors or antibodies, is required [16-18]. Such functionalised electrochemical nanosensors have been reported for the detection of proteins and DNA molecules at concentrations down to fM level [16, 17, 19].

Nanowires, nanorods, nanoribbons or nanotubes, synthesised from conducting or semiconducting materials, have been used for the production of wide varieties of electrochemical nanosensors for biological measurements [17, 20, 21]. Nanowires are tiny needle-like structures that are fabricated with diameters ranging from 1 nm to 100 nm, smaller than the mammalian cell diameter (~10-20 μm), permitting penetration of nanowires into cells [20]. Silicon nanowires and zinc oxide nanowires/nanorods have been utilised for the electrochemical detection of several biomarkers such as pH, calcium, glucose, nucleic acids and proteins [18, 22-24]. In 2001, Lieber and co-workers were the first who reported the use of silicon nanowires for the real-time detection of biomolecules [22]. Further, silicon nanowires have been utilised for the intracellular delivery of biomolecules and measurement of the action potential between live neuronal cells [25, 26]. Nanowires are often grafted onto electroconductive surfaces, such as modified well plates or suitable chips, *e.g.* silicon wafer, to permit the passage of electrical signals. Cells are then grown onto nanowires-modified surfaces to facilitate penetration of the grafted nanowires into cells [17, 20, 25]. Previous studies have shown that cells grow onto nanowires-modified surfaces for many weeks without inhibition of the normal functions of cells [25, 27]. **Figure 1.1** illustrates the penetration of vertical silicon nanowires into cells to detect a specific analyte inside cells [20].

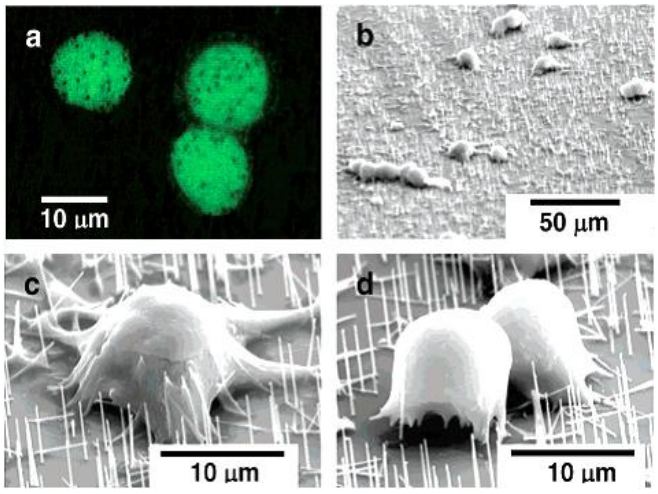


Figure 1.1: The microscopical images of cells, grown onto conductive surfaces, modified with vertical silicon nanowires. The images show that the silicon nanowires penetrate into live cells to detect a specific analyte [20].

Whilst silicon nanowires have been reported for the fabrication of electrochemical nanosensors, electroconductive nanoparticles are other class of nanomaterials that have been developed for the same purpose. Electroconductive nanoparticles are synthesised *via* the incorporation of an electro-active material inside an inert nanoparticle matrix. Changes in the recorded electrical conductance, resulting upon analyte interaction, are utilised to detect the analyte of interest [28, 29]. Despite the conductive nanoparticles have been reported for biomolecular detection in the extracellular environments, their utilisation for the intracellular assays is still challenging due to signal interference with biological fluids [30, 31].

Recently, carbon nanotubes have been reported as efficient tools for drug delivery applications and biomarker detection [32-34]. Carbon nanotubes are fabricated from cylinders of graphene sheets, with diameters ranging from 1 to 10 nm and varying lengths from 50 nm to 1 cm; exhibit interesting mechanical, electrical and conductive properties [32, 35-37]. Based on their electrical properties, carbon

nanotubes have been reported for the development of multiple electrochemical nanosensors for *in-vivo* measurements [38-40].

Despite many electrochemical nanosensors have shown very promising applications for the intracellular assays, some electrochemical nanosensors were unable to detect molecules in high salt concentrations of physiological solutions due to signal interference [18, 41].

1.1.2. Optical nanosensors

Optical nanosensors are other type of nanosensors that utilise the unique properties of light for the quantitative measurements and biological imaging [42]. In general, light properties such as fluorescence, surface plasmon resonance (SPR) and surface enhanced Raman scattering (SERS) all have been used as sensing principles for the fabrication of optical nanosensors [43-45]. Based on the type of the recorded signal, optical nanosensors can be subdivided into two major subtypes mainly, *fluorescent nanosensors* and *plasmonic* (*label-free) nanosensors*.

1.1.2.1. Fluorescent nanosensors

Fluorescence-based detection is one of the most common techniques that have been used in biosensor fabrication and biological imaging. Fluorescence signal detection is based on recording the intensity of light emitted by a fluorescent material, after excitation of such material, which is usually detected at longer wavelength than that used for the excitation. Consequently, any interference from the incident light or excitation source will not influence the detection of the emission. Additionally, the intensity of the emitted light is greatly dependent on

the intensity of the excitation light, which could be increased by using a powerful excitation source such as light-emitting diode (LED). For these reasons, fluorescence-based measurements are more sensitive and specific than other optical techniques such as UV-absorbance or colorimetric-based measurements [46, 47]. The mechanism of fluorescence process is discussed later in this chapter.

Due to high sensitivity, rapid response and ease of use, fluorescent nanosensors have been reported as rapid, ultra-sensitive and accurate tools for the intracellular/biological assays, biomarker detection and cellular imaging [48, 49]. The signal detection in is based on recording changes in the emission signal of the corresponding nanosensor, due to analyte binding, and can be used for quantification. According to the nature of the material used for their fabrication, fluorescent nanosensors can be divided into three major types including *fiber-optic based nanosensors, nanoparticle-based nanosensors* and *quantum dot-based nanosensors*.

1.1.2.1.1. Fibre-optic based fluorescent nanosensors

The first approaches to develop a fluorescent nanosensor for the intracellular measurements were performed by Kopelman and co-workers using optical fibres [50-52]. The nanosensor was designed for the measurement of the intracellular pH and developed *via* entrapment of a pH-sensitive fluorophore inside a polymeric protective matrix, with tip diameters of approximately 20 nm to 100 nm to facilitate cellular insertion. The matrix of the nanosensor was designed to allow protons diffusion and prevent releasing of the entrapped fluorophore to the cellular environment, protecting cells from any unfavoured fluorophore effects. The resultant changes in the recorded fluorescence signals of the entrapped pH-

sensitive fluorophore, corresponding to the hydrogen ions concentration, were utilised for the accurate measurement of the corresponding pH [50, 52].

In fibre-optic fluorescent nanosensors light is transmitted from the fibre end to the corresponding tip *via* evanescent waves to deliver the excitation energy to the fluorescent species located at the fibre tip. Because of the protective fibre matrix and small tip diameter, which is significantly smaller than the wavelength of light that used to excite the fluorescent tag, photons cannot escape from the fibre tip to the external environment. The resultant fluorescence changes, occurring upon analyte interaction with the fibre tips, are detected and used for quantification [53, 54]. Several fibre-optic fluorescent nanoprobes have been developed for the detection of multiple target analytes [55-57]. **Figure 1.2** is a representative example for a fibre-optic fluorescent biosensor that has been reported for detection of a target analyte [58]. In this example, changes in the fluorescence signal are observed as a result of the Förster resonance energy transfer (FRET) process. Upon analyte conjugation with the corresponding fluorescent-labelled antibodies, immobilised onto the fibre tip; the distance required for a detectable FRET changed which then influence the intensity of fluorescence and can be used for quantification. Details of the FRET phenomenon are discussed in Chapter 4.

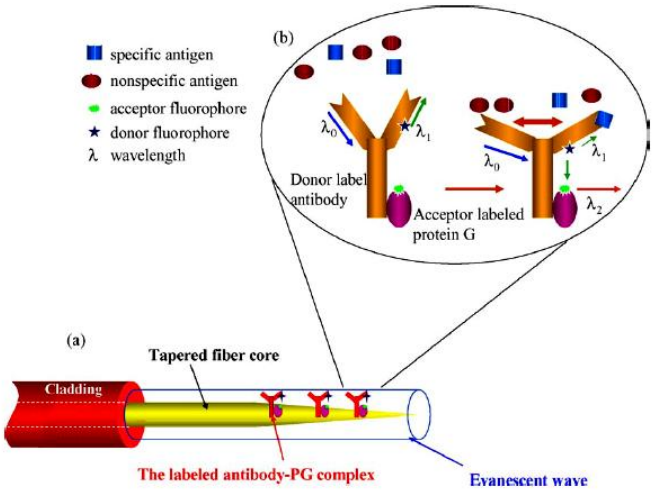


Figure 1.2: A schematic diagram for a fibre-optic fluorescent biosensor that utilises changes in the fluorescence signals due to FRET for analyte quantification. Fluorescent-labelled antibodies were immobilised onto the fibre tip and used as binding ligands [58].

1.1.2.1.2. Nanoparticle-based fluorescent nanosensors

Whilst fibre-optic fluorescent nanosensors protect cells from unfavoured fluorophore effects such as toxicity and photobleaching, some instances of substantial cellular damage have been reported [12, 48, 59]. These physical perturbation and cellular damage occurred during the fibre insertion into cells due to the initial puncture of cellular membranes [60]. In addition, the ability of fibre-optic nanosensors to detect the analyte of interest in different cellular regions is severely limited by the number of fibres that can be inserted inside the cell without destroying it [48]. Such drawbacks encouraged researchers to develop a new generation of fluorescent nanosensors for the intracellular measurements.

In 1998, Kopelman and co-workers introduced the *Probes Encapsulated By Biologically Localized Embedding (PEBBLEs)* as nanoparticle-based fluorescent nanosensors for biological applications [48, 55, 61]. PEBBLEs are spherical fluorescent nanoparticles that typically encapsulate an indicator fluorophore and a reference fluorophore within a biologically inert matrix, developed within the size range of 50 nm to 200 nm. Theses spherical sensing probes can be differentiated from cells, protect them from undesired fluorophore effects, and avoid chemical interferences [12, 62, 63]. In addition, a large number of nanoparticles can be inserted inside cells, with minimal cellular disturbance, allowing the simultaneous target detection within different cellular regions at the same time [62]. Furthermore, PEBBLEs are versatile and can be tailored to accommodate many different sensing elements or modified with several functional groups to facilitate further molecular conjugation [60, 64-66]. **Figure 1.3** is an illustrative diagram which shows some possible elements that can be entrapped inside the nanoparticle matrix or grafted onto the nanoparticle surface to create functionalised nanoparticle [60]. More details on this type of nanosensors are illustrated in Chapter 2.

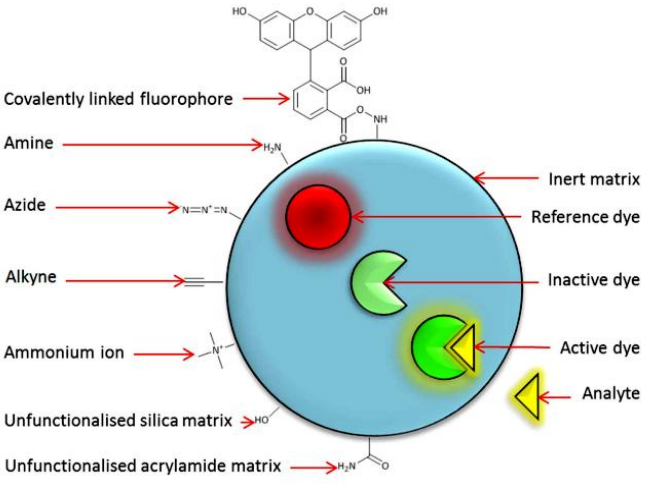


Figure 1.3: Illustrative diagram shows the possible functional groups or sensing elements that can be grafted onto or entrapped inside the PEBBLEs [60].

1.1.2.1.3. Quantum dots (QDs) as fluorescent nanosensors

Quantum dots (QDs) are highly bright, fluorescent materials, fabricated from semiconductors of size below 20 nm. QDs are often synthesised from cadmium-selenide core which is coated with zinc sulphide outer shell to mask their toxicity, enhance water solubility and reduce blinking [67, 68]. QDs absorb photons across a wide range of wavelengths and emit light at specific wavelengths corresponding to their size. Furthermore, QDs have been reported for the production of fluorescent nanosensors and utilised in biological imaging applications [69-71]. The sensing platform is produced *via* attachment of target-specific binding molecules, such as antibodies, oligonucleotides or enzymes, to QD surface. Changes in the emission intensity of QDs, resulting upon target interaction, are used to quantify the corresponding analyte [72-74].

There are many advantages for using QDs in the development of fluorescent nanosensors including size control, large Stokes shift and high brightness. There are, however, some limitations for the application of QDs in biological systems, such as poor water solubility, potent toxicity and blinking [75-77]. Recently, many studies have been published to overcome some of such disadvantages and thus, the utilisation of QDs for the intracellular application is still promising [78-80]. QDs have been successfully utilised for the detection of cellular biomarkers, biological compounds and visualisation of sub-cellular organelles as in **Figure 1.4** [7]. Furthermore, QDs have been used as efficient fluorescent donors in a number of FRET-based applications due to their small size [81-83].

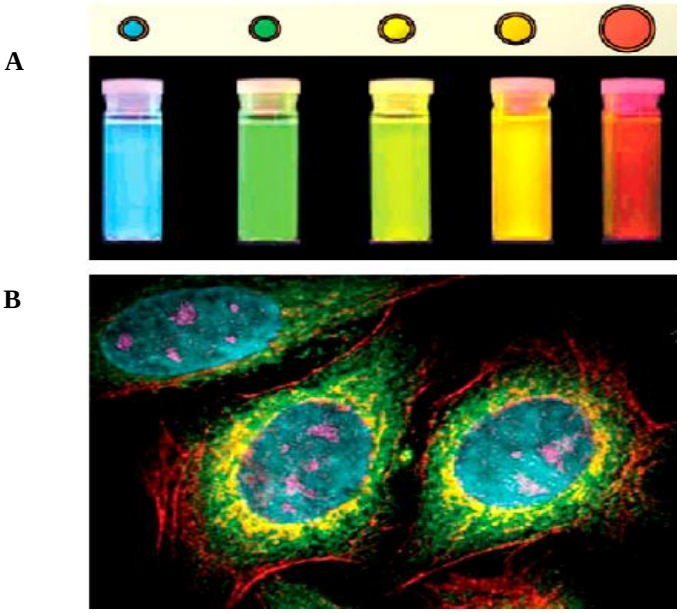


Figure 1.4: (A) The emission of five batches of QDs, prepared with different size range and excited under a UV lamp. (B) The multicolour image of human epithelial cells that were labelled with these QDs to visualise the sub-cellular organelles. The images were taken from [7].

1.1.2.2. Plasmonic (label-free) optical nanosensors

The unique properties of noble metals, occurring upon their interaction with light, have been extensively studied in the last few years [84, 85]. Nowadays, noble metal nanoparticles, especially gold nanoparticles, have been distinguished as distinct nanomaterials in many research fields including biosensors, drug delivery systems, disease diagnosis and treatment [86-88].

At the nanoscale level, most materials exhibit interesting properties/phenomena that cannot be observed in the bulk or individual atoms [89-91]. One of these phenomena, associated with the noble metal nanoparticles, is localised surface plasmon resonance (LSPR) [87, 89, 92]. LSPR occurs spontaneously when a light beam, with a wavelength larger than the nanoparticle diameter, interacts with a noble metal nanoparticle surface. Consequently, the photons are confined within the nanoparticle atoms and become in resonance with the outer free conductive

electrons of the nanoparticle atoms, causing these free electrons to oscillate and induce a SPR close to the nanoparticle surface [89, 93]. Such oscillating electrons generate strong surface electromagnetic fields which propagate around the nanoparticle surface as demonstrated in **Figure 1.5** [94]. As a result, all radiative and non-radiative light properties, such as light absorption, fluorescence, energy transfer, Rayleigh scattering and Raman scattering, are improved [89, 93, 95]. The resultant phenomena are strongly dependent on the nanoparticle composition, size, geometry, dielectric environment, particle–particle separation distance and the refractive index of the medium around the nanoparticle [89, 93, 95].

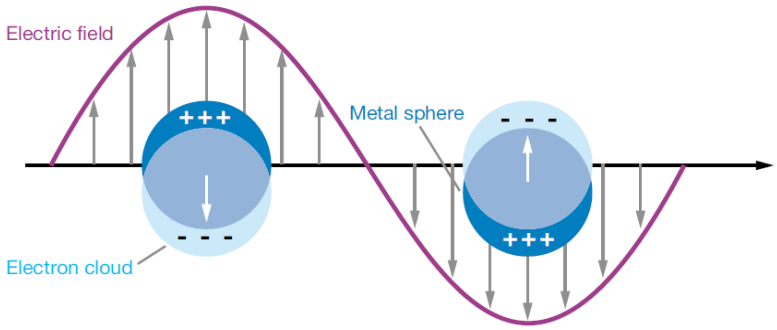


Figure 1.5: Localised surface plasmon resonance (LSPR) occurs in noble metal nanoparticles due to light excitation of the outer electrons of the nanoparticle atoms. This process generates electromagnetic fields that propagate around the nanoparticle surface which further improves other light functions [94].

LSPR, SERS and nanometal surface energy transfer (NSET) all have been reported for the development of label-free optical nanosensors [96-99]. In LSPR-based nanosensors, the intensity of the reflected light by the nanoparticle surface is recorded using a suitable detector, such as two-dimensional arrays of photodiodes or a charge coupled detector (CCD). The recorded signal fluctuations, observed upon target interaction with the nanoparticle, are used to detect the target analyte [94, 100].

El-Sayed and co-workers have developed an approach for the incorporation of gold nanoparticles into cancerous cells by endocytosis. Based on the plasmonic properties of gold nanoparticles, cancerous cells were imaged and differentiated from noncancerous cells [86]. In addition, based on the LSPR properties of gold nanoparticles; cell surface biomarkers, which have critical roles in cancer metastasis, have been detected using antibodies-modified gold nanoparticles [101]. Meanwhile, optical fibres with tip diameters below 100 nm were attached to gold nanorods and then functionalised with specific antibodies to detect the intracellular p53 protein inside the HeLa cells [102]. The light scattering was recorded using a CCD camera connected to an inverted microscope that was used for cellular imaging. Based on LSPR, functionalised gold or silver nanoparticles have been reported in many *in-vivo* measurements and as contrast agents for cellular imaging [103-106].

Meanwhile, SERS-based nanosensors have been developed for multiple biological applications. The signal changes in Raman scattering spectrum were used for the analysis of the corresponding analyte [107, 108]. Gold/silver core shell nanoparticles have been used for the development of SERS-based nanosensors for biomarker detection, single molecule studies and targeting of cancer cells [109-112]. Recently, the combination of SERS with atomic force microscopy (AFM), using gold or gold-coated AFM cantilevers, has produced a new technique called tip-enhanced Raman spectroscopy (TERS). This technique was successfully utilised for studying different cellular regions, cell topography and ultimately for single molecules detection [113, 114].

In addition to LSPR and SERS; NSET is another phenomenon that was observed in noble metal nanoparticles and has been reported in many distance-dependent energy transfer studies. NSET is based on using a plasmonic nanoparticle as a fluorescence quencher for a certain fluorophore, separated by a specific distance from the nanoparticle surface. The signal changes are recorded as the percentage of fluorescence quenching of the fluorophore and utilised for the assay process [99]. More details and applications of this phenomenon are discussed in Chapter 4.

1.1.3. Magnetic nanosensors

Magnetic nanosensors are composed from functionalised core/shell nanoparticles, with a size less than 100 nm, incorporating a super-paramagnetic material such as iron oxide within their core while the outer shell is an inert polymeric material or silica shell, to provide a surface for molecular conjugation and improve water solubility. The key feature of super-paramagnetic nanoparticles is their ability to exhibit magnetization under the influence of an external applied magnetic field. Therefore, the spins of the iron atoms that compose the crystal lattice of nanoparticles core produce a single large localised magnetic dipole which affects the spins of the surrounding water protons. Consequently, these protons dephase their spins and shorten their transverse (T_2) relaxation time, which can be detected by a nuclear magnetic resonance (NMR) or magnetic resonance imaging (MRI) instrument and can be used for quantification [115-117].

Magnetic nanoparticles can bind to proteins, enzymes, antibodies or oligonucleotides to target specific analyte or be delivered for imaging cells, organ or tissue [118, 119]. Previous studies have shown that functionalised super-paramagnetic nanoparticles can form aggregates upon binding to their corresponding target. Compared to individual nanoparticles that contain the same iron oxide concentration, such nanoparticle aggregates can greatly shorten *T2* relaxation time of the surrounding water protons as shown in **Figure 1.6** [116]. Such controlled aggregation or clustering have been utilised to develop magnetic nanosensors for the sensitive and accurate biomarker and viral detection [120].

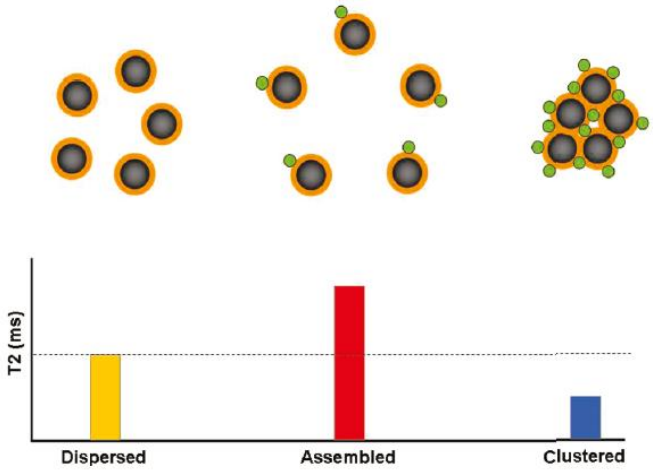


Figure 1.6: Illustrative diagram shows the shift in the relaxation time (*T2*) of the water protons surrounding super-paramagnetic nanoparticles in different states. Aggregation of such nanoparticles, occurring upon analyte binding, shortens *T2* relaxation time of the surrounding water protons, which can be detected and utilised for target molecule quantification [116].

In addition, super-paramagnetic nanoparticles have been reported as contrast agents in MRI. The fundamental principle in MRI is that the unpaired nuclear spins of hydrogen atoms in water and organic compounds align themselves when placed in a magnetic field. A contrast agent which is able to shorten either the longitudinal or transverse relaxation time of such water protons can provide an image with high contrast. Due to the effect of super-paramagnetic iron oxide

nanoparticles on the spins of water protons; such nanoparticles have been used to provide high contrast images in MRI scan, permitting deep tissues imaging in turbid and heterogeneous samples [14, 121].

During the last few years, various magnetic nanosensors have been reported for several *in-vivo* applications including drug delivery, cellular imaging and biomarker detection [116, 119, 122, 123]. However, while magnetic nanosensors provide exceptional anatomic information and deep tissue imaging, they suffer from limited spatial resolution which influences the assay sensitivity. To increase nanosensor sensitivity, combination of fluorescent dyes; especially those emit in near-IR, with the super-paramagnetic material inside the nanoparticle core yields excellent spatial resolution and provides sensitive assays [14, 124].

1.1.4. Mechanical nanosensors

Mechanical nanosensors are fabricated from functionalised nano-cantilevers that are synthesised from piezoelectric materials such as quartz or silicon oxide. The functionalised nano-cantilevers act as tiny balances and used for the sensitive detection of target molecules at concentrations down to pM to fM level [14, 125, 126]. To develop the nanosensor, the surfaces of the nano-cantilevers are functionalised with specific ligands to bind the analyte of interest. When the analyte binds to the immobilised ligands, a marked mass loading occurs, corresponding to the number of the bound molecules, leading to changes in the resonance frequency of the nano-cantilevers [126]. In addition, nano-cantilevers bend due to the surface stress that caused by the target molecules binding. Changes in the resonance frequency and bending of nano-cantilevers are detected

using established techniques, such as optical beam deflection, piezoresistivity, piezoelectricity or capacitance [14, 125, 127, 128]. **Figure 1.7** illustrates the use of a mechanical nanosensor for the detection of biomolecules release [129].

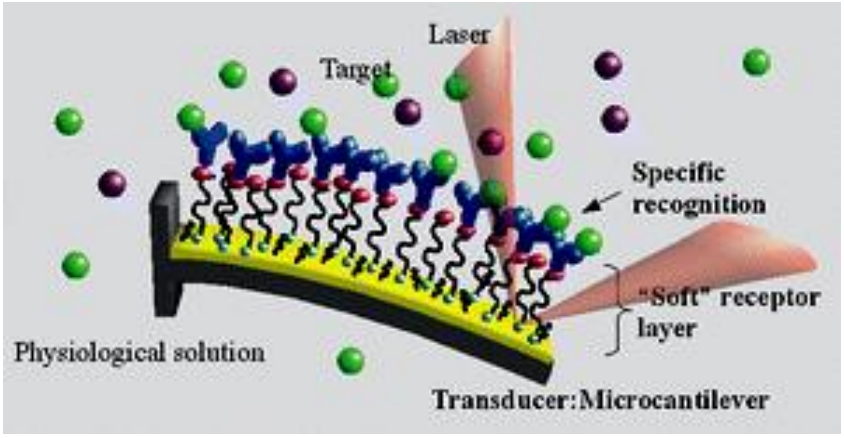


Figure 1.7: *In-vitro* detection of target biomolecules using functionalised mechanical nanosensor. The method can be used for the real-time detection of biomolecules release [129].

However while mechanical nanosensors have been reported for the real-time detection of biomolecules, their application in *in-vivo* clinical studies is limited [127, 130-132]. This because of the sensitivity of detection in fluid; the ideal condition for biological detection, is greatly affected by fluid viscosity and thus, most of mechanical nanosensors have been used to detect biomolecules in vacuum [14]. Recently, the Manalis research group has developed a mechanical nanosensor for the detection of the activated leukocyte cell adhesion molecule, a model cancer biomarker, using nano-cantilevers that were suspended in microfluidic chamber [133]. A similar approach for the ultrasensitive detection of other tumour markers in the serum of breast cancer patients has been reported [134].

1.2. Nanosensor characterisation

Generally, an ideal nanosensor should have sufficient physicochemical properties and sufficient measurable signals. The physical properties of nanosensor are determined by the nature of the material used to fabricate the nanosensor and can be described in the terms of size, shape, electrical surface charge and dispersion.

The work described within this thesis focuses on fabrication of nanoparticle-based fluorescent nanosensors for biological applications; therefore the basics of some techniques that are used for characterisation of such nanosensors are illustrated in the following sections. Characterisation of the physicochemical properties of the nanoparticles that are utilised to fabricate the nanosensors can be used to describe the properties of the corresponding nanosensor [60, 135]. In addition, detection of the optical properties (fluorescence signals) is used to determine the assay procedure.

Tools such as dynamic light scattering (DLS) and electron microscopy are used to identify the physical/morphological properties of nanosensors while fluorescence spectroscopic measurement tools are used to detect their optical (fluorescence) signal to establish the assay process.

1.2.1. Dynamic light scattering (DLS)

DLS is a reliable and rapid characterisation technique for the measurement of hydrodynamic diameter, size distribution and detect dispersity of nanoparticles. Additionally, the same instrumentation can be used for the measurement of electrical charge (zeta potential) on the nanoparticle/nanosensor surface, as illustrated in the following text.

1.2.1.1. Measurement of the hydrodynamic diameters using DLS

When a particle, with a definite size, is suspended in a suitable medium, this particle behaves like an inert sphere that moves with a surrounding solvent layer. The total particle diameter, comprised of the actual particle size and the surrounding solvent layer, is called the hydrodynamic diameter and can be measured by a DLS instrument. Accordingly, due to the solvent layer around the particle, a slightly larger size than the actual size is detected by DLS [136].

A typical DLS instrument uses a light beam, usually laser, to irradiate the surface of moving particles to induce particle polarisation (dipoles). The polarised particles scatter light at the same wavelength of the incident light and propagate in all directions (Rayleigh or Mie light scattering) with intensity proportional to the particle diameter. As the suspended nanoparticles are not stationary, they undergo random Brownian motion within the suspending medium. The velocity of this Brownian motion is dependent on the particle shape, hydrodynamic diameter, concentration of the solution, viscosity of the solvent and temperature [136, 137]. DLS instrumentation detects the intensity of the scattered light and the rate at which the intensity of the scattered light fluctuates due to the Brownian motion and correlate the detected signals overtime. Analysis of these signals is performed by the instrument software and utilised to compute the hydrodynamic diameter of the suspended particle using the Stokes-Einstein's velocity law where:

$$d_H = KT/3\,\pi\eta D \qquad \textbf{Equation 1.1}\ [138]$$

Where d_H is the hydrodynamic diameter of the particle, K is Boltzmann's constant, T is the absolute temperature, η is the viscosity and D is the diffusion coefficient.

1.2.1.2. Measurement of zeta potential by DLS

Zeta potential value is used to assess the electrical charges on the nanosensor or nanoparticle surface and to confirm surface functionalisation or modification with a certain chemical group that can alter surface charges. Furthermore, zeta potential measurement is used to determine the colloidal stability properties of nanoparticle suspension and the tendency of suspended nanoparticles to aggregate [139]. The higher the zeta potential value (either in negative or positive), the more stable nanoparticle in suspension due to the electrostatic repulsion between nanoparticles that have similar surface charges [140].

Theoretically, application of an electric current onto a suspended particle induces this particle to move towards a specific direction with a definite velocity (electrophoretic velocity), rather than undergoing the random Brownian motion [139]. The electrophoretic velocity is dependent on the strength of the applied electric field, dielectric constant of the liquid, viscosity and electrical charge on the particle surface. A DLS instrument, such as Malvern Nanosizer®, applies a constant electrical field to the suspended particles to induce the electrophoretic motion. The rate of this motion is detected and utilised to calculate the zeta potential value of the suspended particles using Henry's equation (**Equation 1.2**) [139, 141].

$$U_E = 2\,\varepsilon\,\zeta\,f(k)/3\,\eta \qquad \textbf{Equation 1.2}\ [139]$$

Where U_E is the electrophoretic mobility, ε is the dielectric constant, ζ is the zeta potential, η is the liquid viscosity and $f(k)$ is Henry's function [139, 141].

1.2.2. Electron microscopy for nanoparticle characterisation

Whilst DLS technique is used to measure the hydrodynamic diameters or size range of nanoparticles/nanosensors, electron microscopy is used to directly detect their ultimate size and shape. Scanning electron microscope (SEM) and transmission electron microscope (TEM) are commonly used for nanoparticle imaging to detect the corresponding morphological properties [138]. Both microscopes focus electron beams onto a sample to produce signals that can be detected and utilised to generate an image for the captured sample. The resulting image is then used to calculate the size and determine the shape and nanoparticle distribution.

1.2.2.1. Scanning electron microscope (SEM)

Scanning electron microscope (SEM) applies beams of accelerated electrons, usually emitted from a heated tungsten filament, with energy from 1 KeV to 30 KeV, to hit the surface of a bulk specimen placed onto a specific holder within a vacuum. Once these electron beams reach the surface of nanoparticle sample, they interact with the sample atoms and most of these electrons are scattered, back-scattered and produce other signals, such as secondary low energy electrons and X-rays, depending on the sample topography and composition. All the resultant signals across the specimen surface are collected and recorded by a suitable detector and then transferred to a scanner which converts such signals into pixels to establish an image for the captured specimen [138].

In the conventional SEM microscope, the sample is placed within a low pressure vacuum and thus, any solvent or water molecules must be removed during sample preparation and before the imaging process. In addition, the conventional SEM requires the samples to be conductive or coated with a layer of a conductive material, such as gold or platinum.

It has been reported that, utilising the conventional SEM for imaging polymeric hydrogel samples is not appropriate due to destruction of such materials by the low pressure vacuum [142]. A great advance in the electron microscopy is the environmental SEM (eSEM) which can be used for imaging degradable polymeric materials and environmental samples. This is because the eSEM permits sample imaging in low-vacuum, humid conditions, providing milder conditions than that required for the conventional SEM. In addition, eSEM does not require the samples to be conductive [138, 143, 144].

1.2.2.2. Transmission electron microscope (TEM)

Transmission electron microscope (TEM) focuses accelerated electrons beams on a thin sample film, placed onto a conductive mesh. In contrast to SEM, TEM has extremely high resolution due to the focused electrons have high energy from 100 KeV to 300 KeV. Due to this high energy, electrons can penetrate throughout the sample and interact with the specimen as it passes through it to provide information about the internal structure of the samples. The transmitted electrons resulting after sample penetration are collected, converted into measurable signals, magnified and focused onto a suitable imaging device, such as fluorescent screen, to produce an image for the captured sample. TEM has been utilised for imaging objects with a size down to 0.2 nm [138, 145].

1.2.3. Fluorescence spectroscopy

The main principle for the development of a fluorescent nanosensor is based on recording the fluorescence signal changes, resulting upon target analyte interaction. The fluorescence process is defined as light emission by a substance that has absorbed light photons during its ground state. The fluorescent substance is named a fluorophore while the excitation and emission maxima are the typical terms that are used to define fluorophore properties. The distance between these two maxima is known as the Stokes shift [146, 147]. The fluorescence process is highly dependent on the chemical structure of the substance and occurs significantly in substances with delocalised electrons, as in systems containing conjugated double bonds [146, 148].

The fluorescence can be easily demonstrated by the Jablonski energy diagram that shows the possible consequences of a particular molecule after interaction with photons, as represented in **Figure 1.8** [146]. When photons with a specific energy are applied to a certain molecule in the ground state, the molecule absorbs photons energy and utilises the absorbed energy to excite an electron; this molecule is then described as ‘an excited molecule’. The excited electron transfers from a lower energy level (ground state) to a higher energy level (excited state) due to absorption of the applied photons energy, as represented by the green lines between the electronic ground energy levels and the excited singlet energy levels on **Figure 1.8**. Once an electron is excited, several consecutive processes may occur depending on the pathway of this excited electron [146, 148, 149].

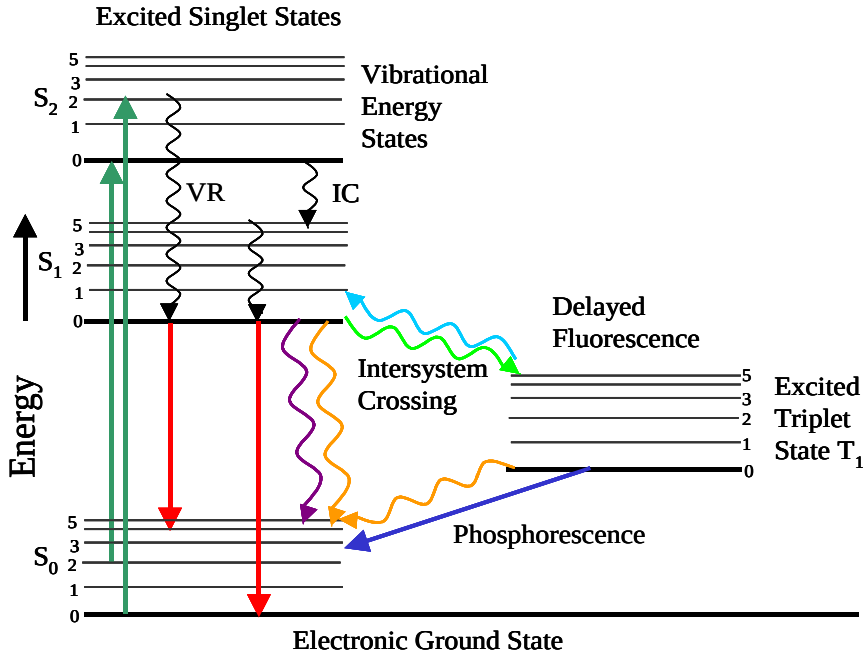


Figure 1.8: The Jablonski energy diagram shows the process of light absorption and the possible pathways for the excited molecule. Image was taken and modified from [146].

As illustrated in **Figure 1.8**, the first pathway for the excited electron is through vibrational relaxation (VR), which is assembled by the curved black arrows within the vibrational energy levels. The absorbed energy may stay within the same molecule or transferred to another nearby molecule, close to the excited one, depending on the nature of surrounding medium. This process is very fast, extremely likely to occur immediately following to the absorbance within 10^{-14} and 10^{-11} seconds.

The second pathway for the excited electron is referred as internal conversion (IC), as indicated by a curved black arrow in **Figure 1.8**. This process occurs when an excited electron transfers from one vibrational high energy level to another vibration level with a lower electronic state, this process is mechanistically identical to VR process.

The most important pathway for the excited molecule occurs through the emission of the absorbed photons at a longer wavelength. This process is known as fluorescence and assembled by the red arrows on the Jablonski diagram (**Figure 1.8**). Fluorescence takes place due to return of the excited molecule to the ground state and occurs within 10^{-8} seconds. The maximum emission wavelength is constant for each particular substance while changes in the intensity of the emitted light are used for the quantitative assays. Due to high sensitivity, simplicity and ease of detection, fluorescence-based techniques have been utilised in several biological studies including cellular imaging, genome studies and single molecule studies [146-148, 150].

In addition, the process of intersystem crossing, which is indicated by the coloured curved arrows on the diagram (**Figure 1.8**), may occur when the excited electron changes the spin from an excited singlet state to an excited triplet state. Intersystem crossing leads to another interesting route where the excited electron returns to the ground electronic state through emission of photons. This process is called phosphorescence which is very similar to the fluorescence but takes longer time ranging from milliseconds to seconds. Phosphorescence occurs as a result of transition of the excited electron from an excited triplet state to a singlet ground state and accompanied by photons emission, as shown by a blue arrow on **Figure 1.8**. Fluorescence and phosphorescence are parts of a big process of light emission that named ‘luminescence’ which plays crucial roles in several biological processes, analytical techniques and medical diagnosis.

Today, fluorescence detection tools have become indispensible in many biological, analytical and clinical laboratories for various daily applications. Spectrofluorometers, fluorescence microscopes, flow cytometers and fluorescence scanners are the most common instruments for fluorescence detection. Each of these instruments consists of four basic units; light source, monochromator or filter, sample holder and detector. The light source is usually laser, xenon lamp, mercury vapour lamp or LED, which is used to excite the fluorescent molecules. The fluorescent sample is placed in a suitable sample holder. The function of monochromator/filter is to select the optimum excitation/emission wavelengths that cross through the sample to the detector, which in turn, converts the collected signals into measurable signals. The data obtained from fluorescence measurement is represented as fluorescence spectra, peaks or fluorescent images depending on the used detection tool [146, 150, 151].

1.3. Thesis structure and layout

The overall aim of this thesis is to develop fluorescent nanosensors, fabricated from bio-friendly materials (polyacrylamide or silica matrix), for real-time detection and biological assays. The main intention for the production of such nanosensors is to use them for the detection of important biological markers such as the intracellular pH, DNA hybridisation and interferon gamma.

Chapter 2 describes the development, fabrication and characterisation of size-tuneable ratiometric fluorescent nanosensors for the measurement of pH changes over an extended dynamic range.

Chapter 3 discusses the real-time measurement of the intracellular pH of yeast cells during glucose metabolism using the optimised nanosensors that were prepared in Chapter 2.

Chapter 4 deals with the study of fluorescence energy transfer/quenching process over different distances using core-shell fluorescent nanoparticles.

Chapter 5 illustrates the quantitative assay of DNA hybridisation process and interferon gamma using aptamer-based fluorescent nanosensors.

Chapter 6 summarises the conclusions of this thesis and defines the potential future work.

Chapter Two

Development, fabrication and characterisation of size-tuneable ratiometric fluorescent pH nanosensors for measurement of pH over an extended dynamic range

2.1. Introduction

2.1.1. Nanosensor fabrication

Fluorescent organic dyes have been extensively used in many analytical, biological and clinical applications for biomarkers detection, non-invasive cellular tracking and biological imaging [152-154]. Despite this, many fluorescent dyes exhibit short life-times, weak fluorescence signals, toxicity and high susceptibility to photobleaching which limiting their use for the long-term detection [155, 156]. Additionally, free fluorophores have also been found to interact with cellular components which hinder their sensing capabilities and/or initiates cellular toxicity [60]. In comparison, due to their inert matrix, signal stability and comparable size, fluorescent nanosensors provide favoured tools for the real-time and long-term detection of biomolecules, chemical compounds, cellular tracking and accurately characterisation of sub-cellular compartments [157].

PEBBLEs have been introduced as fluorescent nanoparticles that are synthesised from biofriendly inert materials, such as polyacrylamide or silica, encapsulating fluorophores within their inert matrix [48, 55, 61, 158]. Due to low cost of preparation, ease of synthesis and size control, fluorescent nanosensors that fabricated from polyacrylamide or silica matrix have been extensively used in many biological and diagnostic applications [159-161].

2.1.1.1. Polyacrylamide nanosensors

Polyacrylamide nanosensors are biologically inert, porous and hydrophilic nanomaterials, fabricated from polyacrylamide nanoparticles (PANPs) that have been widely applied for the detection of several biological and cellular biomarkers [63, 159, 162-164]. PANPs are synthesised *via* free-radical polymerisation reactions which take place within the aqueous phase of an inverse microemulsion [64, 165]. The inverse microemulsion consists of nanometre size-controlled water droplets dispersed within a non-aqueous continuous hexane phase and stabilised by anionic and non-ionic surfactants, such as dioctyl sodium sulfosuccinate (AOT) and Brij 30®. Polymerisation of acrylamide monomers with acrylamide cross-linker; N,N'- methylenebisacrylamide; both of hydrophilic nature, produces uniform PANPs in the size range from ~50 to 200 nm [12].

Free-radical polymerisation reaction is initiated by addition of ammonium persulfate (APS) and N,N,N',N'-tetramethyl-ethylenediamine (TEMED) which act as a free-radical generating system. TEMED accelerates the rate of APS free-radical formation to convert acrylamide monomers into activated acrylamide free-radicals which in turn, react with other acrylamide monomers to initiate the polymerisation chain reaction. **Figure 2.1** shows a schematic diagram for the synthesis of PANPs using an inverse microemulsion polymerisation process.

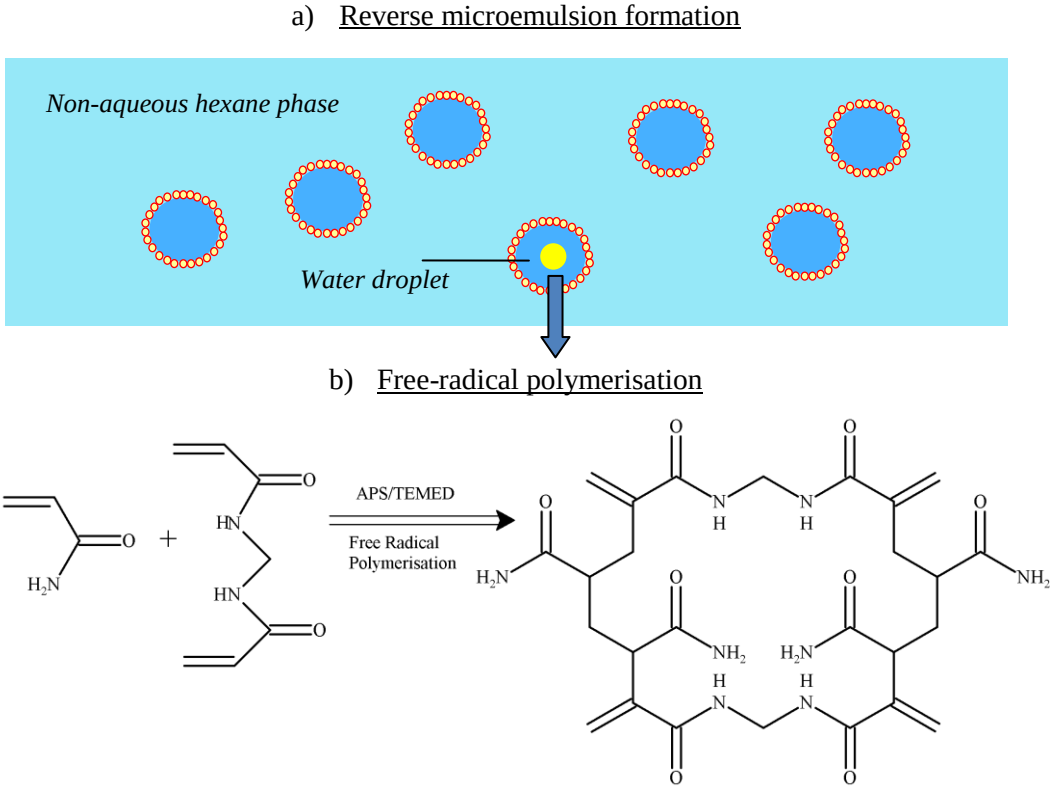


Figure 2.1: Illustrative diagram shows the synthesis of polyacrylamide nanoparticles (PANPs) *via* free-radical polymerisation reaction. The reaction takes place inside nanometre water droplets, stabilised by surfactants, within an inverse microemulsion.

During the polymerisation step, many elements including fluorescent dyes, drugs and oligonucleotide sequence can be attached to or incorporated inside PANPs [64, 65, 164, 166, 167]. The polymerisation process is inhibited by oxygen which can react with APS free radicals; therefore, synthesis of PANPs must be performed in an oxygen-free atmosphere. By the end of the synthesis, PANPs are washed with ethanol to remove the excess surfactants, dried and stored for further use.

Fluorescent polyacrylamide nanosensors are fabricated from fluorescent PANPs (f-PANPs) which can be produced *via* incorporation of fluorophores within the nanoparticle matrix [63, 64, 164]. One of the effective methods for fluorophore incorporation is *via* the physical entrapment (non-covalent trapping) of fluorescent molecules within the pores of the nanoparticle matrix [162]. Because

fluorescent molecules are usually too small to be trapped inside the matrix pores, fluorophore conjugation to another significant molecule (e.g. dextran, 10 KDa) is preferred to give a dye-conjugate that can be retained inside the nanoparticle pores [63]. This entrapment produces fluorescent nanoparticles with sufficient optical properties; however, instances of dye leaching from the nanoparticle matrix have been reported [48, 168, 169]. To overcome this problem, covalent binding of fluorescent molecules to the nanoparticle matrix has been established [137]. This covalent conjugation can be performed through functionalisation of the nanoparticle matrix with a chemical group that can covalently bind to a corresponding reactive moiety on the fluorescent molecule [169]. Alternatively, a chemically active acrylamide monomer, such as N-(3-aminopropyl) methacrylamidehydrochloride (APMA) is conjugated to the fluorophore to produce acrylamide-fluorophore conjugate. Such APMA-fluorophore conjugate can be polymerised with acrylamide monomers during the nanoparticle synthesis to produce f-PANPs that are covalently linked to fluorescent molecules [137]. **Figure 2.2** shows the covalent conjugation of amino-acrylamide monomer (APMA) with N-hydroxyl succinimidyl ester derivative of a certain fluorophore (R) to produce APMA-fluorophore conjugate which is then used for the synthesis of f-PANPs, covalently linked to the fluorophore.

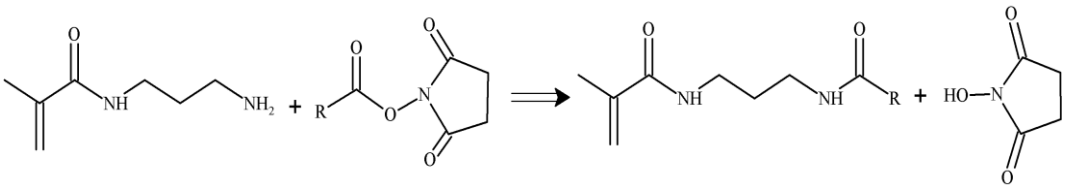


Figure 2.2: The conjugation reaction between amino-acrylamide monomer (APMA) and N-hydroxyl succinimide ester derivative of a fluorophore to produce APMA-fluorophore conjugate that can be used for the production of f-PANPs. R = chemical structure of fluorophore.

2.1.1.2. Silica nanosensors

Whilst many polymeric nanoparticles have a tendency to aggregate and swell in the presence of some solvents which could lead to deformation of nanoparticle shape, loss of nanoparticle structure and cause dye leaching [170, 171]. In contrast, silica nanoparticles (SNPs) are produced from a rigid matrix that can resist solvent swelling and maintain their morphological properties [160, 172]. Additionally, due to the versatile chemistry of silane and improved colloidal properties, SNPs provide a desirable nanosensor matrix [170, 171, 173]. SNPs can be functionalised with several functional groups, such as amine, carboxylic acid, azide, alkyl and PEG, to facilitate further binding of biomaterials/ligands to SNPs surface [174-176].

Synthesis of SNPs was firstly described by Stöber and co-workers in 1968 using a two-step reaction; *hydrolysis and condensation*, using ammonium hydroxide (NH_4OH) as a catalyst [177]. The process of SNPs synthesis takes place *via* fast hydrolysis of a silica alkoxide precursor, usually tetraethyl orthosilicate (TEOS) in alcoholic medium, to form silanol monomers which are then combined (condensed) together to produce a network of uniform and monodispersed SNPs (**Figure 2.3**). According to the Stöber study, the average size of the resultant SNPs can be controlled by varying the initial concentration of each reactant/catalyst [177].

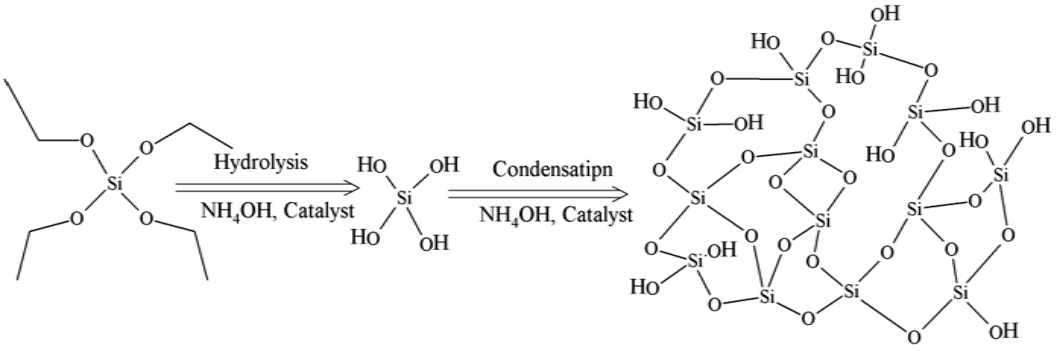


Figure 2.3: Synthesis of silica nanoparticles (SNPs) by the Stöber method. The synthesis is performed *via* hydrolysis and condensation of a silica alkoxide precursor; tetraethylorthosilicate (TEOS), in alcoholic medium using ammonium hydroxide (NH_4OH) as a catalyst.

Fluorescent silica nanoparticles (f-SNPs) are produced through covalent binding of fluorescent molecules to SNPs matrix. This covalent linking is performed *via* conjugation of a chemically active silane compound, such as 3-aminopropyl-triethoxysilane (APTES), with fluorophores to produce APTES-fluorophore conjugates which are then used to form covalent bonds with the nanoparticle matrix [178].

An alternative to the Stöber method, a reverse microemulsion has been reported for the synthesis of SNPs [179, 180]. In this method, synthesis of SNPs takes place inside nanometre water droplets that are formed within a non-aqueous microemulsion. The size range of SNPs, produced by this method, is determined by the nature of the surfactant, hydrolytic reagent, pH, temperature and reaction time. Despite the size of SNPs, produced by the reverse microemulsion method, is comparable to that produced by the Stöber method, the reverse microemulsion process is time consuming, more complicated, produces low nanoparticle yield and requires a number of reagents. In addition, removal of the surfactants from SNPs and controlling the nanoparticle size and morphology are difficult [181].

2.1.2. Ratiometric fluorescence pH nanosensors

To develop a nanoparticle-based fluorescent pH nanosensor, a pH-sensitive fluorophore is encapsulated within the nanoparticle matrix. The main criterion for the selection of such pH-sensitive fluorophore is determined by the pKa value of this fluorophore which limits the capability of the nanosensor to detect pH changes within two pH units, where pH=pKa±1 [182, 183].

Commercially available pH-sensitive fluorophores, such as 5(6)carboxy-fluorescein (FAM), carboxy-SNARF-1 and Oregon Green® (OG), have been used in many analytical and biological applications. FAM and carboxy-SNARF-1 have been used to detect pH in near-neutral or slightly alkaline pH ranges where the pKa of such fluorophores is either ~6.4 or 7.0 for FAM or carboxy-SNARF-1, respectively [184]. Meanwhile, many cell types, such as the centre of tumour, yeast cells, and some cell organelles (*e.g.* lysosomes), exhibit acidic pH values [185, 186]. Accordingly, it is inappropriate to use these fluorophores (FAM or SNARF-1) for the measurement of the pH of such cells/organelles where the pH value of such cell type could be outside the effective fluorophore pH range. Another pH-sensitive fluorophore with a lower pKa, such as OG (pKa ~4.6), may provide an alternative fluorophore to measure the slightly acidic pH range. However, this fluorophore is only effective within pH from 3.5 to 5.5, where pH=pKa±1 [63, 137, 187].

It is obvious that, utilisation of a single fluorophore to measure the pH will not cover the entire biological/physiological pH of many cells or organisms which lies between pH 4.5 and pH 8.1, depending on the cell type or organelle [188-191]. As a result, combination of two pH sensitive fluorophores, such as OG 488 and

FAM, could provide favoured probes for the detection of pH changes over an extended dynamic range due to the merged activity of both fluorophores. Additionally, a great advantage for this combination is that both fluorophores have almost the same excitation (~488 nm) and emission maxima (~520 nm), permitting the pH detection at the same wavelength [63, 137, 187].

However, depending on direct fluorescence measurements for pH detection may give inaccurate and non-robust data. This is due to the inherent drawbacks of direct fluorescence measurements; such as fluctuations of light intensity source, dye-photobleaching, and the effects of concentration and orientation of the indicator fluorophore [192]. To overcome these drawbacks, ratiometric fluorescence measurements have been successfully established to correct the recorded fluorescence signals and to provide reliable and accurate measurements [63, 137].

Ratiometric fluorescence measurements are based on using the ratio of the intensity of two fluorescence peaks instead of the absolute intensity of one peak. Therefore, the resultant ratio would be constant regardless the orientation or concentration of the fluorophores [193, 194]. To develop a ratiometric fluorescent pH nanosensor, a reference pH-insensitive fluorophore is combined with an indicator pH-sensitive fluorescent dye as illustrated in **Figure 2.4**.

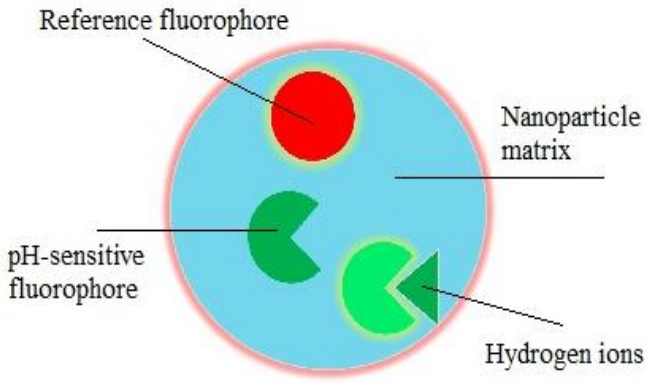


Figure 2.4: A schematic diagram for a ratiometric fluorescent pH nanosensor, composed of an inert nanoparticle matrix, encapsulating a pH-sensitive fluorophore and a reference fluorophore within the same matrix.

Examples for the reference pH-insensitive fluorophores are those derived from rhodamine, such as 5(6)-carboxytetramethylrhodamine (TAMRA). Such pH-insensitive fluorophores exhibit excitation and emission maxima at ~550 nm and 575 nm which can be distinguished from the emission maxima of OG or FAM. Accordingly, to fabricate a ratiometric fluorescent pH nanosensor for the detection of pH over an extended range, two pH-sensitive fluorophores, such as OG and FAM, are combined with a reference pH-insensitive fluorophore such as TAMRA. The combination of two pH-sensitive fluorophores, have different pKa, is utilised to extend the effective dynamic pH range of the nanosensor while the reference fluorophore is used to provide ratiometric fluorescence measurements [63, 137, 187]. **Figure 2.5** shows the chemical structures of OG, FAM and TAMRA.

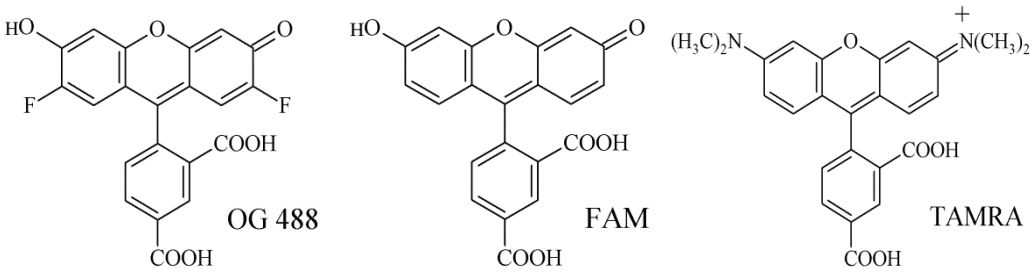


Figure 2.5: Chemical structure of Oregon Green® 488 (OG), 5-(and-6)-carboxyfluorescein (FAM) and 5-(and-6)- carboxytetramethylrhodamine (TAMRA).

Calibration curve for the ratiometric fluorescent pH nanosensor is constructed by calculating the ratio between the fluorescence intensities of the indicator fluorophore/s and reference fluorophore, measured in different pH values. The typical behaviour of this calibration curve is usually sigmoidal in shape while the effective dynamic pH range of the nanosensor is considered as the region between the minimal and maximal response of this sigmoidal curve. The fitting equation of ratiometric calibration curve can be established using **Equation 2.1** [63, 137].

$$pH = -\frac{\log 10\,(\frac{R_{max} - R_{min}}{R_i - R_{min}} - 1)}{\mathrm{b}} + \mathrm{pKa} \qquad \textbf{Equation 2.1 [63, 137]}$$

Where R_i is the ratio between the fluorescence of indicator/reference fluorophores, R_{min} and R_{max} are the minimum and maximum responses of the nanosensors, respectively, pKa is the point corresponding to half of the response of the ratiometric nanosensors and b is the slope of the linear part of the responsive calibration curve.

Using similar approaches for such ratiometric fluorescence measurements, several ratiometric fluorescent nanosensors have been reported for the detection of many analytes including oxygen free radicals, zinc ion and other biomolecules [195-197].

2.2. Aim

Recently, studies have been published on the development of ratiometric fluorescent polyacrylamide nanosensors for the pH detection over an extended dynamic range [63, 137]. Based on this work, the general aim of this chapter is to synthesis such polyacrylamide pH nanosensor to improve the physicochemical properties of such nanosensor. In addition, to fabricate size-tuneable ratiometric fluorescent pH nanosensors, composed from silica matrix, for the detection of pH over a wide dynamic pH range.

The main intention for the production of such nanosensors is to use them for the real-time measurement of the intracellular pH of yeast cells during glucose metabolism as discussed in Chapter 3.

The first aim of Chapter 2 is to synthesise and characterise ratiometric fluorescent polyacrylamide pH nanosensors, using the previously protocol that was reported and optimised [137]. Additionally, enhancement of the physical properties of these nanosensors through functionalisation with a positively-charged group and study this effect on cellular uptake is illustrated in Chapter 3.

The second aim of this chapter is to establish and optimise a reproducible protocol for the synthesis of size-tuneable SNPs, which is then used to produce ratiometric fluorescent silica pH nanosensors for the pH detection over an extended dynamic range. Tuning the size of the developed SNPs and the pH response of the corresponding nanosensor are investigated and optimised. Successful fabrication of such nanosensors may enable their application for measurement of the pH value of many biological systems and cell types.

2.3. Experimental

2.3.1. Materials and chemicals

The succinimidyl ester derivatives of Oregon Green® 488 (OG), 5-(and-6)-carboxyfluorescein (FAM) and 5-(and-6)-carboxytetramethylrhodamine (TAMRA) were obtained from Invitrogen, USA. Acrylamide 99% minimum, N, N' methylenebis(acrylamide) (bisacrylamide), polyoxyethylene(4) lauryl ether (Brij 30®) were purchased from Fluka Analytical, UK. *N*-(3-aminopropyl)methacrylamide hydrochloride (APMA) and 3-acrylamido propyl trimethylammonium hydrochloride (ACTA) were obtained from Polysciences Inc, Germany. Dioctyl sulfosuccinate sodium (AOT), ammonium persulphate (APS), N,N,N,N-tetramethylethylenediamine (TEMED), hexane, sodium borate and ethanol absolute (99.5%) were obtained from Fisher Scientific, UK. Tetraethyl-orthosilicate (TEOS, 99%), (3-aminopropyl) triethoxysilane 98% (APTES), citric acid monohydrate, sodium dihydrogen phosphate and disodium hydrogen phosphate were purchased from Sigma-Aldrich, UK. Ammonium hydroxide solution (28-30%, NH_4OH) was obtained from Acros Organics, USA. Deionised water (18 MΩ.cm) was used throughout the present work. Unless otherwise mentioned, all the chemicals that used throughout this study were of analytical grade.

2.3.2. Fabrication of polyacrylamide nanosensors [137]

2.3.2.1. Covalent conjugation of fluorophore to APMA

Briefly, 5 mg of APMA was dissolved into 2.5 mL of sodium borate buffer (50 mM, pH 9.50) and then 200 µL of this solution was added to 1 mg of the succinimidyl ester derivative of each fluorophore (OG, FAM and TAMRA), prepared into separate vials. The reaction mixtures were stirred for at least 24 hours in the dark at room temperature and then stored at 4° C until further use.

2.3.2.2. Preparation of f-PANPs

Into a 250 mL round bottom flask, 1.590 g of AOT and 3.080 g of Brij 30® were mixed together and purged under argon for 15 minutes followed by addition of 42 mL of deoxygenated hexane that had previously purged with argon for at least 30 minutes. The flask was sealed under inert argon atmosphere using a balloon with continuous stirring. Following this, 540.0 mg of acrylamide and 160.0 mg of bisacrylamide, dissolved into 1.5 mL of deionised water, were added to the sealed flask using a syringe. APMA-fluorophore conjugates, purged with argon, were then added using 15 µL of OG-APMA, 15 µL of FAM-APMA and 60 µL of TAMRA-APMA, by a syringe. Finally, 30 µL of APS (10% w/v) and 15 µL of TEMED were added and the stirring was continued for 2 hours in the dark under sealed argon atmosphere. The reaction was halted by removing the stopper and exposing the flask content to air. To isolate the synthesised f-PANPs, hexane was removed by rotary evaporation at 30° C and then 30 mL of ethanol was added to the flask content. The mixture was transferred into a 50 mL falcon tube and centrifuged for 10 minutes at 6000 rpm. Washing with 30 mL ethanol was performed 5 times and in the last wash, 10 mL of ethanol was added and removed

by rotary evaporation at 30 °C. The dried nanoparticles were stored at -20 °C until further use.

2.3.2.3. Synthesis of positively-charged polyacrylamide nanoparticles (p-PANPs) [142]

The same procedure, described for the preparation of f-PANPs, was followed. Prior to the addition of acrylamide and bisacrylamide to the sealed flask, 5% of acrylamide monomers and bisacrylamide were replaced by ACTA (75% w/v). In this step, 513.0 mg of acrylamide, 152.0 mg of bisacrylamide and 119 µL of ACTA (75% w/v) were dissolved into 1.5 mL water and then added into the sealed flask containing the surfactants and hexane mixture then the procedure was followed as described for the synthesis of f-PANPs.

2.3.3. Fabrication of silica nanosensors

2.3.3.1. Fluorophore conjugation to APTES [198]

Before the synthesis of f-SNPs, accurately weighed 1.0 mg of the succinimidyl ester derivatives of OG, FAM and TAMRA were dissolved separately into 1 mL of absolute ethanol and stirred with excess molar volume of APTES, for 24 hours in the dark. Fluorophore-APTES conjugates were stored in the dark at 4 ºC until further use.

2.3.3.2. Optimised procedure for the production of SNPs

Preparation of plain silica nanoparticles (p-SNPs): Into a scintillation vial, 16.75 mL of absolute ethanol was mixed well with 0.75 mL of NH_4OH (28-30% w/v), for at least 30 minutes. Following this, 500 µL of TEOS was added drop-wise to ethanol-NH_4OH mixture, with continuous stirring for 24 hours at room temperature. The vial content was centrifuged at 6000 rpm for 30 minutes and washed three times with 30 mL of absolute ethanol to collect p-SNPs. After the final washing step, the suspension containing nanoparticles was transferred into a 50 mL rounded bottom flask to evaporate ethanol using a rotary evaporator at 30 °C and then the dried nanoparticles were stored at 4 °C.

Preparation of f-SNPs: The same procedure for the preparation of p-SNPs was followed. Prior to the addition of TEOS, 40 µL of OG-APTES, 40 µL of FAM-APTES and 80 µL of TAMRA-APTES were added to the mixture and stirred for 24 hours in the dark. Following this, 500 µL of TEOS was added drop-wise to the reaction mixture and the protocol was followed as described for the preparation of p-SNPs.

2.3.3.3. Synthesis of amino silica nanoparticles (amino-SNPs) [199]

10 mg of f-SNPs were suspended into 1.0 mL of ethanol followed by addition of 18 µL of APTES. The reaction mixture was stirred for 2-4 hours, in the dark at room temperature, followed by centrifugation and washing, for three times using phosphate buffer.

2.3.4. Characterisation of the nanosensors

The hydrodynamic diameters, size distribution and zeta potential values of the synthesised PANPs and SNPs were measured Malvern Zetasizer Nano II DLS instrument. eSEM (Philips XL30 FEG ESEM) and TEM (JEOL 2000 FX II EM) were utilised for imaging SNPs. Fluorescence intensities of the developed nanosensors were recorded on a Varian Cary Eclipse fluorescence spectrophotometer at the selected excitation and emission maxima of each fluorophore.

2.3.4.1. Physical properties characterisation of polyacrylamide nanosensors

The hydrodynamic diameters of the synthesised PANPs were measured by DLS using suspensions of either f-PANPs or p-PANPs (1.0 mg/mL), prepared in deionised water and sonicated for 15 minutes. The same suspensions were utilised to measure the zeta potential using disposable zeta potential cuvettes.

2.3.4.2. Physical properties characterisation of silica nanosensors

The hydrodynamic diameters of each batch of SNPs were measured by DLS using 20 µL of the original suspensions that contain SNPs, produced after the nanoparticle synthesis. The volumes were made to 3 mL with deionised water followed by measurements of the hydrodynamic diameters of the corresponding SNPs batch.

To measure the zeta potential of p-SNPs, f-SNPs or amino-SNPs, 0.5 mg/mL of the corresponding nanoparticles were suspended in deionised water and sonicated for at least 1 hour followed by measurements of zeta potential using Malvern Zetasizer Nano II DLS instrument.

For eSEM and TEM imaging of the optimised p-SNPs and f-SNPs, 0.1 mg of the optimised SNPs batches were suspended separately into 1 mL of deionised water and sonicated for at least 1 hour. For eSEM imaging, 15 µL of each nanoparticle suspension were deposited onto separate glass cover slips, attached to black eSEM stubs. The samples were dried overnight followed by coating with platinum for 12 seconds and then the samples were imaged by eSEM (Philips XL30 FEG ESEM).

For the TEM imaging, the suspensions of SNPs were deposited onto the TEM copper grids. The images were taken using 200 keV under nitrogen atmosphere by JEOL 2000 FX II EM TEM microscope.

2.3.4.3. Fluorescence detection and establishment of calibration curves

Fluorescence intensities of the pH-sensitive fluorophores (OG and FAM) were measured at maxima 520 nm after excitation at 488 nm while the fluorescence of TAMRA was recorded at emission wavelength of 577 nm after excitation at 545 nm.

Into separate scintillation vials, 1 mg/mL of polyacrylamide nanosensor and 0.5 mg/mL of the optimised silica nanosensor were suspended in McIlvain buffer (0.1 M citric acid and 0.2 M disodium hydrogen phosphate), prepared with pH values from pH 2.5 to 8.5 and measured by a pH meter [200]. The suspended nanosensors were sonicated for at least 30 minutes followed by measurements of the fluorescence signals of each incorporated fluorophore using the corresponding nanosensor in different pH values. The fluorescence intensities of each fluorophore were normalised against blank samples of buffers where no nanosensor was added.

To establish the normalised calibration curves of the corresponding nanosensor, the ratios between the normalised fluorescence intensities of OG or FAM to that of TAMRA, measured in different pH values, were calculated. The normalised calibration curves for the nanosensors were fitted as a function between the mean of the ratiometric fluorescence intensities, measured at 520 nm and 577 nm ($I_{520}/_{577}$), against the corresponding pH value. Microsoft Excel® software was used for the data analysis and to establish the graphs.

2.3.5. Dye leaching and stability studies using the optimised silica pH nanosensor

For the dye leaching studies, the optimised silica pH nanosensor was suspended in phosphate-buffered saline (PBS) and then the fluorescence intensity of each fluorophore was measured. Following this, the suspended nanoparticles were centrifuged and the fluorescence intensity of each fluorophore (OG, FAM and TAMRA) was measured in the supernatant, resulting after the centrifugation, and in the nanoparticles suspension, prepared after resuspending SNPs pellets in PBS.

To investigate the fluorescence signal stability of the optimised silica pH nanosensor, the nanosensor was suspended in PBS buffer, followed by measurements of the fluorescence intensities of OG, FAM and TAMRA over consecutive time intervals from 5 minutes to 48 hours. The suspensions were kept in the dark during the duration of the experiment.

2.4. Results and discussion

2.4.1. Polyacrylamide pH nanosensors

2.4.1.1. Production of polyacrylamide pH nanosensors

In the present study, polyacrylamide pH nanosensors were produced by the process of inverse microemulsion polymerisation as previously reported [137]. This previously reported protocol was established to produce ~50 nm f-PANPs that were covalently linked to two pH-sensitive fluorophores (OG and FAM, with a ratio of 1:1) and a reference fluorophore (TAMRA), permitting ratiometric fluorescence pH measurements. Prior to the nanoparticle synthesis, succinimidyl ester derivatives of OG, FAM and TAMRA were covalently conjugated to APMA as previously shown in **Figure 2.2**. The resultant APMA-fluorophore conjugates were directly added to the reaction mixture to facilitate covalent binding of fluorophores to the polyacrylamide matrix. This covalent binding protocol has been established to overcome leaching problems, associated with optical nanosensors where the fluorophores are physically entrapped within their matrix [137].

Polyacrylamide pH nanosensors were prepared without any modifications using the aforementioned protocol. In addition, positively-charged polyacrylamide nanosensors (PPA), composed from p-PANPs, were synthesised *via* modification of f-PANPs using a positively-charged acrylamide monomer (ACTA) as previously reported [142]. This modification was performed to enhance cellular uptake of polyacrylamide pH nanosensors, as discussed later in Chapter 3. In this reaction, ACTA was utilised to replace 5% of the total acrylamide monomers and bisacrylamide to produce p-PANPs. This acrylamide monomer was selected

amongst several acrylamide modifying monomers to decrease nanoparticles aggregation [201]. During the initial synthesis procedure, ACTA was added and polymerised with acrylamide monomers to incorporate trimethylammonium ions into the nanoparticle matrix. As a result, the net positive charges onto the nanoparticle surface; and hence the corresponding nanosensor, increased and shown later in this chapter [142]. **Figure 2.6** shows the chemical structure of ACTA which can be used to incorporate positively-charged trimethylammnium ions into polyacrylamide matrix.

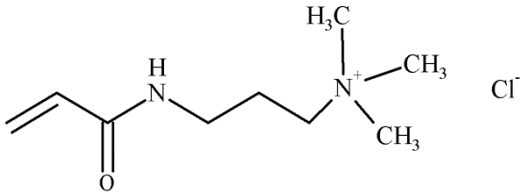


Figure 2.6: The chemical structure of 3-acrylamidopropyl trimethylammonium hydrochloride (ACTA) which polymerises with acrylamide monomers and bisacrylamide to produce positively charged fluorescent polyacrylamide nanoparticles (p-PANPs).

2.4.1.2. Characterisation of polyacrylamide pH nanosensors

Characterisation of the produced PANPs was performed as reported [63, 137]. The hydrodynamic diameters and zeta potential values of f-PANPs and p-PANPs were measured by a DLS instrument. Fluorescence measurements of the nanosensors were performed to detect the response of the nanosensors in various pH values to establish the calibration curves.

2.4.1.2.1. Size characterisation of PANPs

The hydrodynamic diameters of the synthesised f-PANPs and p-PANPs were measured by a DLS instrument. The results revealed that the hydrodynamic diameters of f-PANPs and p-PANPs were centred at ~44 nm and 47 nm, respectively, as shown in **Figure 2.7**. Moreover, the polydispersity index (PDI) of f-PANPs and p-PANPs were 0.137 and 0.152, respectively. These results are congruent with that found in the literature [137, 162, 166, 194, 202].

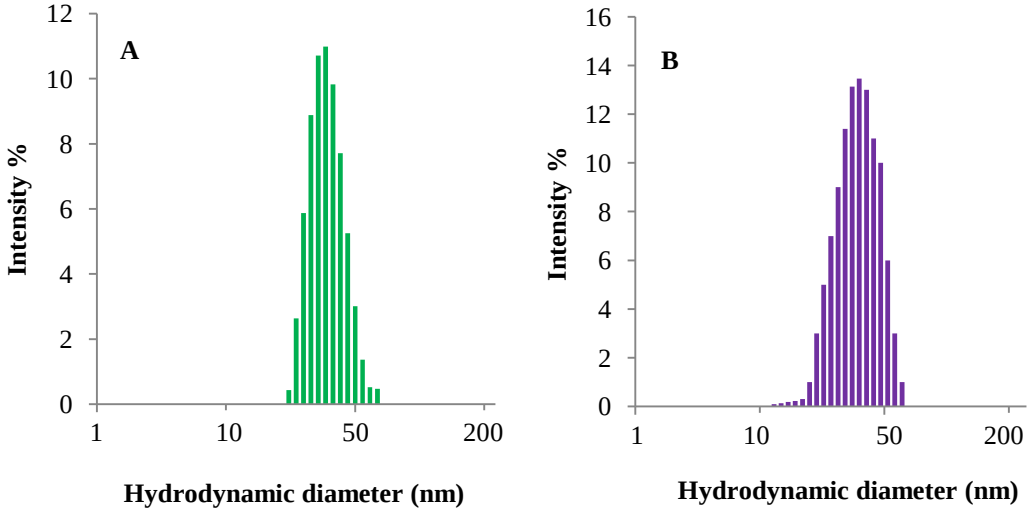


Figure 2.7: (A) and (B) The hydrodynamic diameters of the unmodified fluorescent polyacrylamide nanoparticles (f-PANPs) and positively-charged polyacrylamide nanoparticles (p-PANPs) respectively, measured by a DLS instrument.

The PDI value is used to describe the dispersion and size distribution of nanoparticles. Generally, well dispersed nanoparticles with narrow size distribution should have PDI value ≤ 0.70 [142]. Therefore, the synthesised f-PANPs and p-PANPs are considered to have relatively narrow size distribution and sufficient dispersion properties. In addition, the obtained results illustrate that modification of PANPS with ACTA did not markedly influence the nanoparticle size range.

2.4.1.2.2. Zeta potential measurement of PANPs

Measurement of the zeta potential was used to assess the electrical charge onto the surface of the synthesised polyacrylamide pH nanosensors and as an indicator for modification of the nanoparticle matrix with ACTA. As shown in **Figure 2.8**, the zeta potential values of f-PANPs and p-PANPs were +3.4 ± 4 mV and +19 ± 5 mV, respectively. The value of zeta potential was significantly increased in the positive direction after modification of the nanoparticle matrix with ACTA, which indicates the successful modification of the nanoparticle matrix with the positively-charged trimethylammonium ions. Such positively-charged ions were incorporated within the nanoparticle matrix, increasing the total positive charges onto the nanoparticle surface [142]. As a result, the colloidal stability properties and cellular uptake of polyacrylamide nanosensors were improved as discussed in Chapter 3.

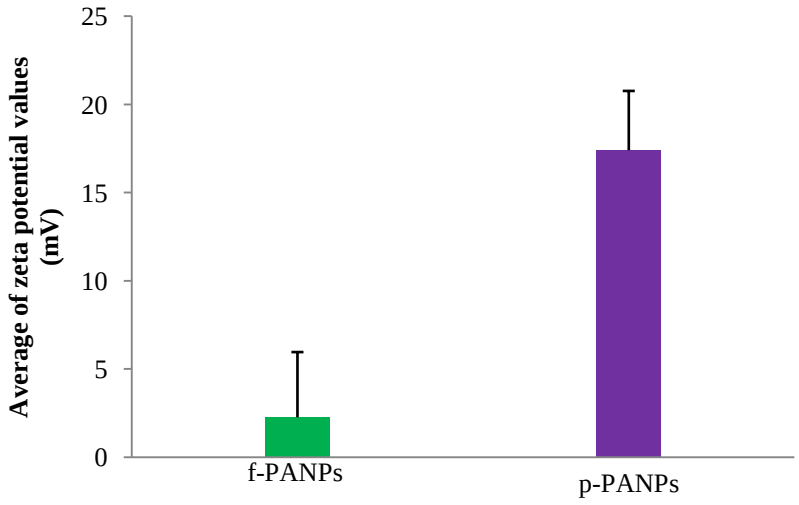


Figure 2.8: The zeta potential values of the unmodified fluorescent polyacrylamide nanoparticles (f-PANPs) and positively-charged polyacrylamide nanoparticles (p-PANPs), measured by a DLS instrument.

2.4.1.2.3. Measurements of the fluorescence signals of the synthesised polyacrylamide pH nanosensors

It has been reported that covalent binding of fluorophores to polyacrylamide matrix did not influence the position of both excitation and emission maxima of the conjugated fluorophores [137]. In this study, OG and FAM exhibited emission maxima at 520±5 nm while the emission maxim of TAMRA was obtained at 577±5 nm, similar to that recorded for the corresponding free fluorophore.

To detect the pH response of the synthesised polyacrylamide pH nanosensors, the fluorescence intensity of each fluorophore, encapsulated within the nanoparticle matrix, was recorded in different pH values ranging from pH 3.0 to 8.5. As shown in **Figure 2.9**, the fluorescence intensities of the pH sensitive fluorophores (OG and FAM) were gradually increased as the pH value increased while the fluorescence signals of TAMRA did not significantly affected. Therefore, the fluorescence intensity of TAMRA was used to establish the ratiometric fluorescence measurements. In addition, McIlvaine buffer was chosen in this study due to the similarity of the components of this buffer to the biological buffers and also could be prepared with an extended buffer capacity range [200].

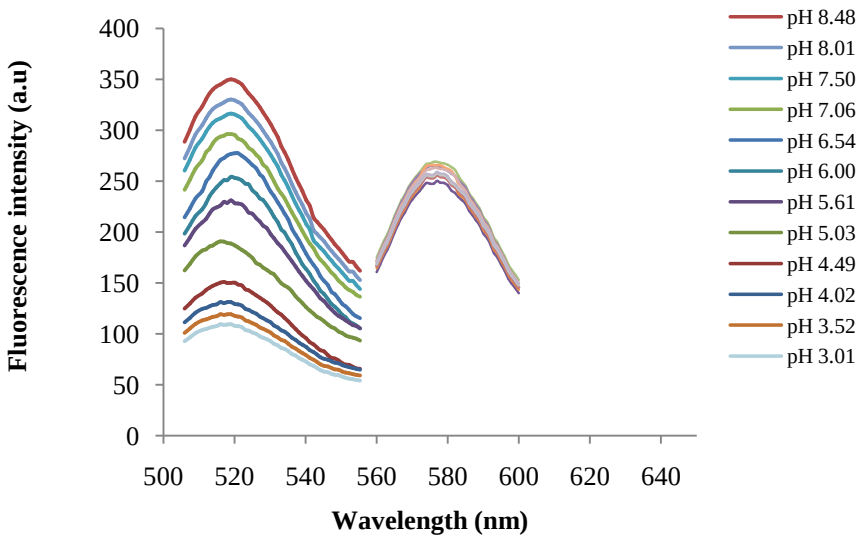


Figure 2.9: The fluorescence spectra of the synthesised ratiometric fluorescent polyacrylamide pH nanosensors, suspended in McIlvaine buffer in different pH from pH 3.01 to 8.48. The mission spectra on the left part are related to the pH sensitive fluorophores (OG and FAM) while fluorescence spectra of TAMRA are shown on the right part of the graph, as recorded on a spectrofluorometer.

The normalised ratiometric calibration curve for the synthesised polyacrylamide pH nanosensors was constructed using the ratio between the fluorescence intensity of the pH sensitive fluorophores and that of the reference fluorophore, recorded in different pH values. As shown in **Figure 2.10**, the response of the nanosensors is sigmoidal in shape, similar to the typical calibration curve of pH-sensitive fluorophores [60, 63, 137]. The effective dynamic pH range of the nanosensors is considered as the area between the minimal and maximal responses of the normalised calibration curve, which can be used for the accurate and reliable detection of pH [63]. Accordingly, the effective response of the synthesised polyacrylamide pH nanosensors is between pH 3.5 to pH 7.5 as could be seen from **Figure 2.10**.

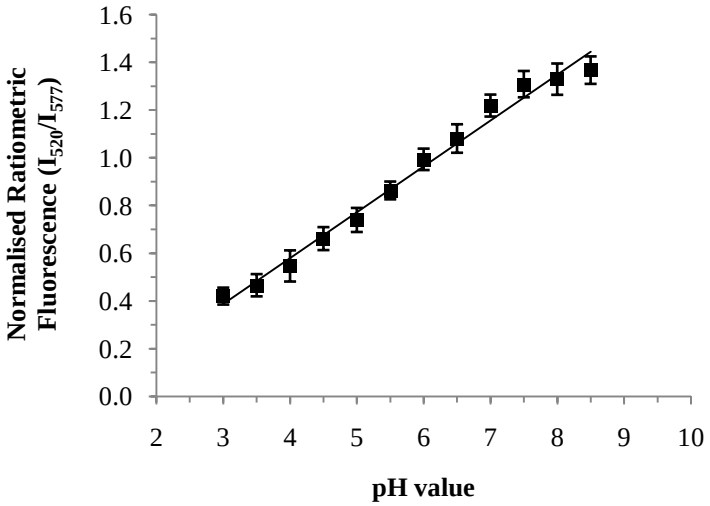


Figure 2.10: The normalised calibration curve of the synthesised polyacrylamide ratiometric fluorescent pH nanosensors, suspended in McIlvaine buffer with pH values from pH 3.01 to 8.5.

The sigmoidal behaviour of the nanosensors is controlled by the pKa values of the pH-sensitive fluorophores (OG and FAM). As in the first part of the normalised calibration curve, below pH 5.5, the activity of the nanosensors is mainly controlled by OG (pKa~4.6) while over pH 5.5, the nanosensors activity is governed by FAM (pKa of ~6.4). Combination of these two pH-sensitive fluorophores has extended the responsive dynamic pH range of the nanosensors to be from pH 3.5 to pH 7.5, which indicates the potential use of these nanosensors for the pH detection of many biological systems that have pH value within the effective pH range of the synthesised nanosensor.

2.4.2. Silica pH nanosensors

2.4.2.1. Preliminary protocols for the synthesis of silica nanoparticles (SNPs)

In this study, the first challenge was to establish robust and reproducible protocol for the synthesis of SNPs with a size range below 100 nm to facilitate their potential intracellular incorporation. In the present work, many previously reported protocols for the synthesis of ~65 nm SNPs were attempted while the obtained size range of each SNPs batch, prepared using the corresponding protocol, was measured by DLS and compared to the reported size as summarised in **Table 2.1** [203-207]. Such protocols produced SNPs with significantly different size range than that reported. Whilst the utilised technique for size measurement varied from one study to another; in this work Malvern Zetasizer® DLS instrument was used as rapid and reliable technique for the measurement of the hydrodynamic diameters of the resultant SNPs, prepared using each protocol.

Table 2.1: A summary for previously reported protocols that were repeated in this study for the synthesis of SNPs in the size range ~65 nm. These protocols were repeated and the hydrodynamic diameters of the resultant SNPs were measured by DLS and compared to the size reported in each study

Reported protocol by	**Volumes of reactants used (mL)***	**Reported size (nm)**	**Measured diameters (nm)****	**Ref**
Rossi et. al.	25 EtOH, 1 H_2O, 1.5 NH_4OH, 2 TEOS	65	185	[203]
Rao et. al.	31.4 EtOH, 5.4 H_2O, 1.9 NH_4OH, 0.26 TEOS	70	320	[204]
Canton et. al.	20 EtOH, 2.5 H_2O, 0.8 NH_4OH, 0.9 TEOS	65	190	[205]
Lim et. al.	50 MeOH, 1 H_2O, 3 NH_4OH, 0.6 TEOS	20	165	[206]
Estévez et. al	16.75 EtOH, 1.25 NH_4OH, 0.71 TEOS	67	140	[207]

* Abbreviation, EtOH and MeOH are for ethanol and methanol respectively. **Mean of the hydrodynamic diameters of three different SNPs batches, prepared using each method.

As shown in **Table 2.1**, Rossi, et. al. have reported a protocol for the synthesis of SNPs with a size range of 65 nm [203]. When this protocol was repeated, the measured hydrodynamic diameters of the resulting SNPs were almost three times larger than the reported size range. Similarly, the hydrodynamic diameters of SNPs, synthesised by previously reported protocols, were ~320 nm and ~190 nm, despite the reported size was 70 or 65 nm for each protocol, respectively [204, 205]. In addition, when another protocol that has reported by Lim and co-workers was repeated; the measured hydrodynamic diameters of the resulting SNPs were ~165 nm instead of the reported 20 nm [206]. As in **Table 2.1**, the protocol that has reported by Estévez and co-workers for the production of ~67 nm SNPs was followed and the measured hydrodynamic diameters of SNPs, produced by this protocol, were about 140 nm [207]. Further, the Wiesner group has reported a method for the synthesis of f-SNPs with a size range of about 20-30 nm. When this protocol was repeated, the resultant hydrodynamic diameters were significantly changed from one batch to another and ranged from ~185 nm to 600 nm instead of the reported 20 nm [208].

According to Stöber, varying the initial concentrations of each reactant/catalyst, involved in SNPs synthesis, may affect the size of the produced SNPs [177]. Meanwhile, amongst all protocols that were attempted in this study, Estévez's protocol produced SNPs with the smallest size range of about 140 nm, as illustrated in **Table 2.1**. As a result, based on the Stöber study conclusion and using Estévez's protocol as a starting point, a reproducible protocol for the synthesis of SNPs with a tuneable size range has been established in the present work. To achieve this, the effect of each reactant/catalyst quantity (TEOS, NH_4OH, ethanol, FAM-APTES) on the hydrodynamic diameters of the resulting

p-SNPs and f-SNPs was investigated and optimised. The hydrodynamic diameters of the resulting SNPs were measured by DLS instrument to provide fast and accurate measurements for the corresponding size range of the resulting SNPs.

FAM was firstly used for the production of FAM-SNPs as an exemplar for f-SNPs. Before the synthesis of FAM-SNPs, succinimidyl ester derivative of FAM was conjugated to amino-silane derivative (APTES), with the molar ratio of 1: 1.2 for FAM: APTES, to ensure complete conjugation. The resulting FAM-APTES conjugate is susceptible for hydrolysis and condensation, similar to the silica precursor (TEOS), therefore, this dye-conjugate was utilised to produce FAM-SNPs, covalently linked to FAM molecules, as represented in **Figure 2.11**.

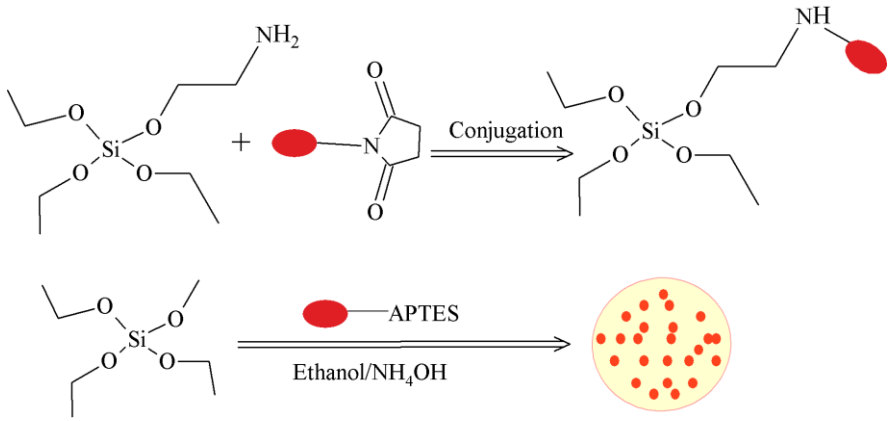


Figure 2.11: Illustrative diagram shows the covalent binding of amino-silane precursor (APTES) to succinimidyl ester derivative of a fluorophore (●) to produce fluorophore-APTES conjugate, which is used for the synthesis of f-SNPs.

2.4.2.2. Production of size-tuneable SNPs

2.4.2.2.1. Effect of varying amounts of TEOS

As previously mentioned, the initial experiments for the synthesis of SNPs were performed using the protocol that has been reported by Estévez and co-workers. This protocol was based on using 3.1 mmol (710 µL) of TEOS, 9.9 mmol (1.28 mL of 28-30% w/v) of NH_4OH and 16.75 mL of absolute ethanol (0.29 mol) [207]. The measured hydrodynamic diameters of the resultant SNPs were about 140 nm, as illustrated earlier in **Table 2.1**. To study the effect of varying TEOS amounts on the size of SNPs, different quantities of TEOS ranging from 0.80 mmol to 8.8 mmol (180 µL – 2000 µL) were utilised while the amounts of NH_4OH and ethanol were kept constant. To synthesise FAM-SNPs, 50 µL of FAM-APTES conjugate was used.

The results revealed that the hydrodynamic diameters of the produced p-SNPs or FAM-SNPs did not markedly change upon increasing the amount of TEOS from 0.80 mmol to 8.8 mmol. As shown in **Figure 2.12**, the hydrodynamic diameters of p-SNPs and FAM-SNPs were in the range of 145±15 nm and 130±19 nm, respectively, using the studied amounts of TEOS. These results were in agreement with the Stöber study which concluded that increasing the quantity of TEOS did not markedly influence the final size of the resulting SNPs [177]. However, previous studies have shown an increase or a decrease in the nanoparticle size upon increasing the amounts of TEOS [204, 209].

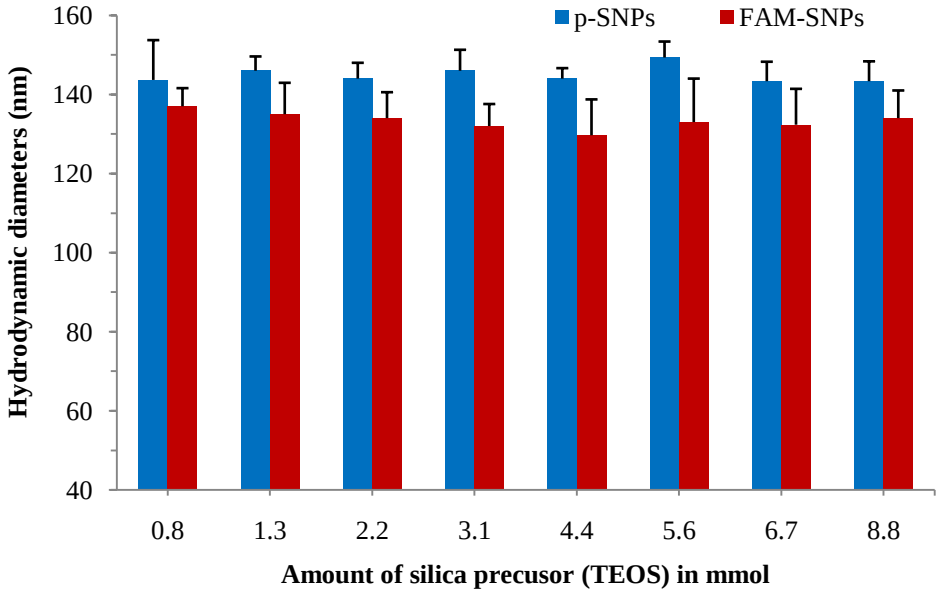


Figure 2.12: The effect of varying amounts of TEOS on the hydrodynamic diameters of p-SNPs (blue bars) and FAM-SNPs (red bars), synthesised using the Estévez's protocol [207]. The mean of PDI for p-SNPs and FAM-SNPs were ≤ 0.1respectively. The number of batches were n=5.

Synthesis of SNPs can be explained by the von Weimarn and Ostwald ripening theories that generally explain how a particle with a definite size is formed [210, 211]. According to the von Weimarn theory, for any particle to be formed, a supersaturated solution of the corresponding ions/molecules is required to produce primary unstable small nuclei (nucleation). Any further increase in the ions/ molecules amounts above the supersaturation point will increase the rate of nucleation and form new primary nuclei. This occurs spontaneously to relieve the increase in the degree of supersaturation until the equilibrium point is achieved. Once these primary nuclei reach equilibrium, they combine together to form secondary, thermodynamically stable larger nuclei which grow to form more thermodynamically stable uniform particles, with the same size (Ostwald ripening theory) [210, 211]. During the synthesis of SNPs, TEOS is firstly hydrolysed into silanol monomers to produce primary nuclei which are then condensed together to form SNPs. The rates of hydrolysis (rate of nucleation) and condensation (rate of

particle growth) are controlled by the catalyst (NH_4OH) [177]. In these experiments, the amount of NH_4OH was constant; therefore, the number of the hydrolysed TEOS molecules and the number of the primary nuclei were constant. This means that further addition of TEOS did not affect the hydrolysis process as the added TEOS molecules remained unhydrolysed.

Further, the measured hydrodynamic diameters of p-SNPs were slightly larger than that of FAM-SNPs which could be attributed to the potential increased solubility/supersaturation of FAM-APTES conjugates in ethanol. Overall, the hydrodynamic diameters of the developed p-SNPs or FAM-SNPs did not markedly affected by varying amounts of TEOS from 0.80 mmol to 8.8 mmol (180 µL – 2000 µL). As a result, 2.2 mmol (500 µL) was selected as the optimum TEOS amount that was used throughout this study.

2.4.2.2.2. Effect of varying amounts of NH_4OH

According to Stöber, increasing NH_4OH quantity during the nanoparticle synthesis will increase the size of SNPs. However, other studies have shown the reverse effect [177, 204]. In this study, the effect of different amounts of NH_4OH, from 2.3 mmol to 37.2 mmol (0.3 mL to 5.0 mL), on the produced size of SNPs was investigated. As represented in **Figure 2.13**, the hydrodynamic diameters of p-SNPs and FAM-SNPs gradually increased as the amount of NH_4OH was increased. The hydrodynamic diameters of p-SNPs increased from ~65 nm to 900 nm while the hydrodynamic diameters of FAM-SNPs ranged from ~45 nm to 750 nm using the aforementioned NH_4OH amounts. Additionally, all the produced

SNPs batches were monodisperse and uniform in size as the PDI values were ≤0.1 for all the resultant SNPs batches.

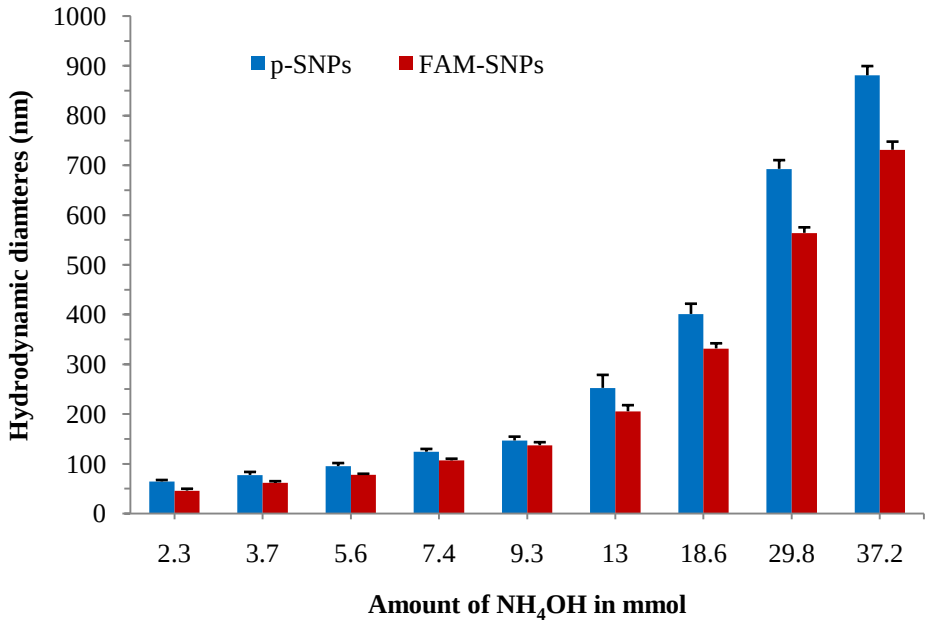


Figure 2.13: The effect of different amounts of NH_4OH, ranging from 2.3 mmol to 38.5 mmol, on the hydrodynamic diameters of p-SNPs and FAM-SNPs.

It was noticed that, elevating NH_4OH quantity increased the final yield of SNPs. This could be explained by the catalytic effect of NH_4OH on the rates of hydrolysis and condensation of TEOS. Increasing the amount of NH_4OH will increase the rate of TEOS hydrolysis which in turn, increases the total number of the primary nuclei (number of nanoparticles), and hence, the final nanoparticle yield. Additionally, increasing NH_4OH quantity increases the rate of condensation, the rate of growth, which increases the total diameter of the produced SNPs. In summary, the above results revealed that the size ranges of SNPs and the obtained yield can be readily tuned through careful control of the amount of NH_4OH. As a way forward, to obtain a considerable nanoparticle yield (~100 mg) and produce SNPs below 100 nm, 5.6 mmol (0.75 mL) of NH_4OH was used throughout the present study as the optimum NH_4OH quantity.

2.4.2.2.3. Effect of ethanol quantity and alcohol type

Previous studies have been published to investigate the effect of alcohol amount and type on the size and dispersity of SNPs; synthesised *via* the Stöber method [212, 213]. To study this effect, varying amounts of ethanol from 0.17 mol to 0.85 mol (10 mL to 50 mL) were utilised while the optimised amounts of TEOS (2.2 mmol, 500 µL) and NH_4OH (5.6 mmol, 0.75 mL) were used throughout these experiments. As illustrated in **Figure 2.14**, while the amount of ethanol increased from 0.17 mol to 0.42 mol (10 mL to 25 mL); the hydrodynamic diameters of p-SNPs were ~92±15 nm (PDI ≤ 0.052) and ~78±11 nm (PDI ≤ 0.070) for FAM-SNPs. The measured hydrodynamic diameters slightly increased above 100 nm; for all batches, when the amount of ethanol was elevated above 0.42 mol to 0.85 mol. As a result, 0.29 mol of ethanol (16.75 mL) was used as the optimum amount of ethanol to produce SNPs with size ranges below 100 nm.

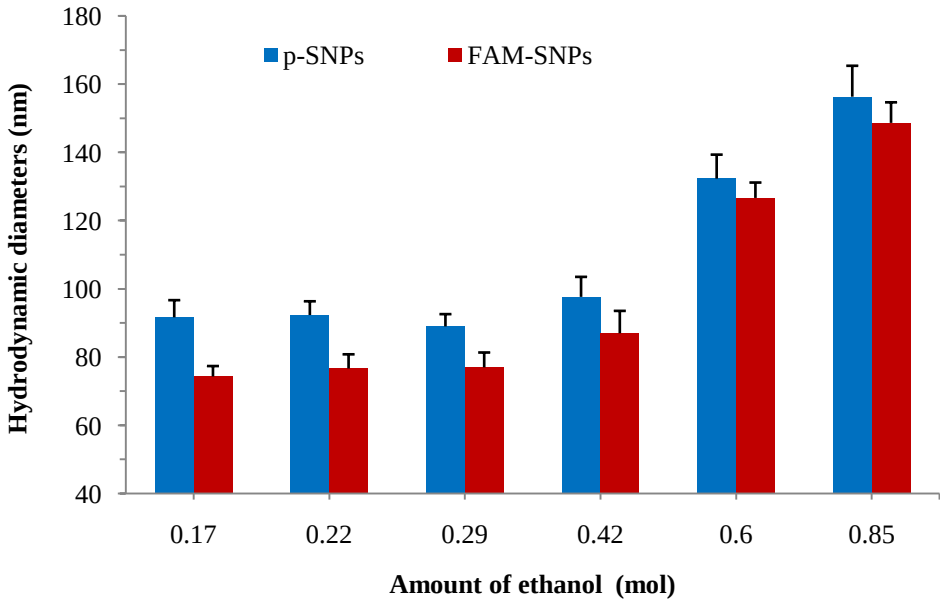


Figure 2.14: The effect of varying amounts of ethanol (0.17 mol to 0.85 mol) on the hydrodynamic diameters of p-SNPs and FAM-SNP.

In addition, the effect of alcohol type on the hydrodynamic diameters of SNPs was investigated. The results showed that using methanol (0.29 mol) for the synthesis of SNPs produced slightly smaller SNPs than that prepared using the optimised amounts of ethanol (0.29 mol). The hydrodynamic diameters of the resultant SNPs, prepared by methanol, were about 63±12 nm (PDI ≤ 0.040) and 55±16 nm (PDI ≤ 0.049) for p-SNPs and FAM-SNPs respectively. This slight nanoparticle size reduction, observed when methanol was used instead of ethanol, may be due to the enhanced solubility/supersaturation of the hydrolysed monomers in methanol than in ethanol [209]. In spite of using methanol produced SNPs with smaller diameter than that prepared using ethanol; methanol was excluded from this study due to the high toxicity and harmful effect [214].

In contrast, when 0.29 mol isopropanol was used for the synthesis of SNPs, several DLS peaks were observed with major DLS peaks at ~220 nm and ~185 nm for p-SNPs and FAM-SNPs, respectively. Additionally, the PDI values of the resultant SNPs were above 1.812, indicating polydisperse SNPs and wide nanoparticle size distribution. These results may indicate the possible effect of alcohol polarity on the size and distribution of SNPs. It has been reported that when the alcohol polarity decreased, the size of SNPs was increased due to increasing the number of the non-polar group onto the nanoparticle surface which may lead to aggregation [215, 216]. Overall, for further experiments, ethanol was selected as the optimum medium for the production of SNPs with the optimised amount of 0.29 mol (16.75 mL).

2.4.2.2.4. Effect of different volumes of fluorophore-APTES and fluorophore type

The effect of different quantities of FAM-APTES conjugates on the size of FAM-SNPs was studied. Different volumes of FAM-APTES ranging from 10 µL to 1000 µL were added to the ethanol-NH_4OH mixture prior to the addition of TEOS to allow the hydrolysis of FAM-APTES conjugates. As illustrated in **Figure 2.15**, the size range of FAM-SNPs did not significantly vary while the volume of FAM-APTES was ≤ 300 µL as the measured hydrodynamic diameters were less than 100 nm for all batches. When the volume of FAM-APTES was elevated above 300 µL, the resultant nanoparticle size slightly increased above 100 nm whilst the largest FAM-SNPs batch, with a size range of 175±13 nm, produced when 1000 µL of FAM-APTES was utilised.

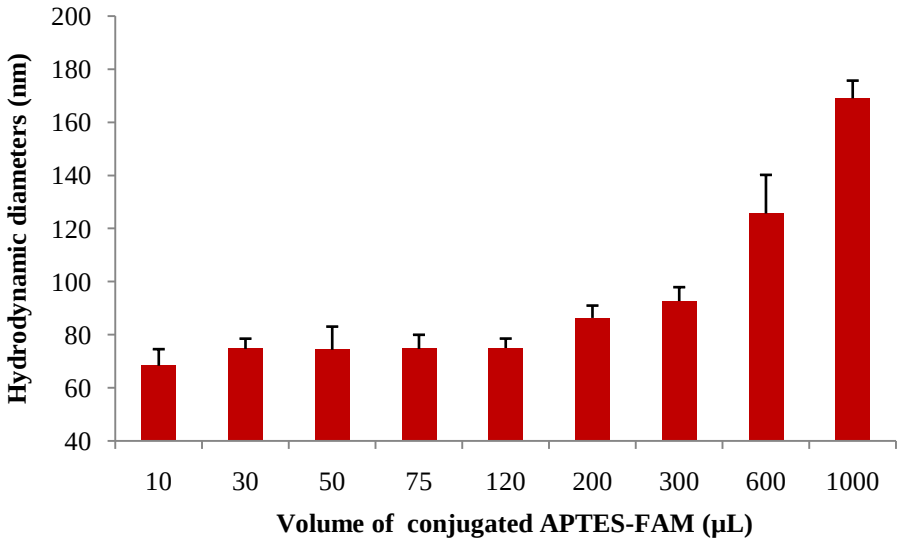


Figure 2.15: The effect of different volumes of the conjugated FAM-APTES, prepared using 1 mg/mL of FAM, on the hydrodynamic diameters of the produced FAM-SNPs.

The slight increase in the size of FAM-SNPs, occurred upon increasing the volume of FAM-APTES over 300 µL, may be attributed to the increased number of FAM-APTES monomers that may grow onto the nanoparticle nuclei, leading to slight increase in the nanoparticle size.

Further, the effect of fluorophore type on the hydrodynamic diameters of f-SNPs was studied using OG-APTES or TAMRA-APTES conjugates instead of FAM-APTES conjugates. The results revealed that the measured size ranges of OG-SNPs or TAMRA-SNPs were similar to that obtained for FAM-SNPs, prepared using the same volume of fluorophore-APTES conjugate. Additionally, there was no marked difference in the measured size ranges of SNPs produced using a single fluorophore or combined fluorophore conjugates, provided that, the total volume of all fluorophores-APTES conjugates kept below 300 µL.

2.4.2.3. Optimum protocol for the preparation of SNPs

To summarise the size tuneability study of SNPs, different size ranges of p-SNPs and f-SNPs can be readily produced by optimising the amount of NH_4OH. The results revealed that the amount of NH_4OH plays an important role in controlling the size of SNPs while changing the amounts of all other reactants have shown minimal effects on the resulting nanoparticle size.

Overall, to obtain considerable yield of SNPs (~100 mg) with a size range below 100 nm, the amounts of TEOS, NH_4OH and ethanol were optimised to 2.2 mmol (500 µL), 5.8 mmol (0.75 mL) and 0.29 mol (16.75 mL), respectively. Additionally, the total volume of fluorophore-APTES was kept below 300 µL to produce f-SNPs with a size range below 100 nm, regardless the used fluorophore/s. **Table 2.2** illustrates the optimum amount of NH_4OH that was required for the production of size-tuneable SNPs, prepared using the optimised protocol.

Table 2.2: The optimised amount of NH_4OH (28-30% w/v) that was required used to prepare size-tuneable SNPs, using the optimised protocol, with using constant amounts of other reactants*

NH_4OH amount (mmol)	**Approximate hydrodynamic diameters (nm)**		**Approximate yield (mg)**
	p-SNPs	f-SNPs	
2.3 (0.3 mL)	65	45	Below 15 mg
3.7 (0.5 mL)	75	60	Below 40 mg
5.6 (0.75 mL)	95	75	50-150
7.4 (1.0 mL)	125	100	150
9.3 (1.25 mL)	145	137	200
13 (1.75 mL)	250	200	200-250
18.6 (2.5 mL)	400	330	150-350
29.8 (4.0 mL)	690	550	500
37.2 (5.0 mL)	900	750	Over 400

* The optimised amounts of TEOS and ethanol were 2.2 mmol (500 µL) and 0.29 mol (16.75mL) respectively. The volume of FAM-APTES conjugate was 50 µL.

2.4.2.4. Synthesis of amino-SNPs

In general, to increase cellular uptake of a nanosensor, the size of nanoparticles, utilised for fabrication of such nanosensor, should be less than 100 nm. In addition, the nanosensor surface should contain a positively-charged group which is favoured to overcome the negatively-charged nature of the phospholipid bilayer of the cellular membrane [217, 218]. To confer positive charges onto the surface of the developed silica nanosensors, APTES was used to add a positively-charged amino group to the nanoparticle surface using a previously reported procedure [199]. In this reaction, APTES is hydrolysed into amino-silane monomers which then form a covalent link with the silica matrix to produce amino-SNPs, grafted with a positively-charged amine group onto their surfaces. The results revealed that the size range of the unmodified SNPs was about 75 nm while the size range of amino-SNPs was 78±8 nm, with PDI of 0.083, indicating the negligible effect of this modification on the nanoparticle size range. Characterisation of the unmodified SNPs and amino-modified SNPs is discussed in the following sections.

2.4.2.5. Characterisation of the physical properties of the optimised SNPs

2.4.2.5.1. Size and shape characterisation

In this work, the optimised protocol for the synthesis of SNPs was utilised to produce p-SNPs and f-SNPs, with hydrodynamic diameters of about 92 nm and 75 nm, respectively, as measured by the DLS instrument and shown in **Figure 2.16 A and B**. The mean of the PDI values of p-SNPs and FAM-SNPs were 0.067 and 0.083, respectively, indicating the narrow size distribution of the developed SNPs.

In addition, eSEM and TEM were used to investigate the size, shape and size distribution of the optimised p-SNPs and FAM-SNPs. As shown in **Figure 2.16 C and E**, the eSEM results showed that the optimised p-SNPs and FAM-SNPs are spherical in shape with size ranges of 89±4 nm and 75±6 nm, respectively. These results agreed to that obtained from the TEM images for p-SNPs and f-SNPs as the size of p-SNPs and f-SNPs were 86±7 nm and 69±5 respectively (**Figure 2.16 D and F**). The measured hydrodynamic diameters of the optimised SNPs batches, measured by DLS, and the corresponding size, obtained by the eSEM and TEM, are summarised in **Table 2.3**.

However, the sizes of p-SNPs and f-SNPs, measured by eSEM and TEM, were slightly smaller than the hydrodynamic diameters, detected by DLS. This is expected due to that the measured size range by the DLS is expressed as hydrodynamic diameter, which consists of the actual nanoparticle size and the diameter of a thin solvent layer, surrounding the suspended nanoparticle as discussed earlier in Chapter 1.

Table 2.3: The hydrodynamic diameters of the optimised SNPs batches, measured by DLS, and the corresponding size of the same SNPs batches, imaged by eSEM and TEM.

Technique used	p-SNPs	f-SNPs
DLS	92±9 nm	79±11nm
eSEM	89±4 nm	72±8 nm
TEM	86±7 nm	69±5 nm

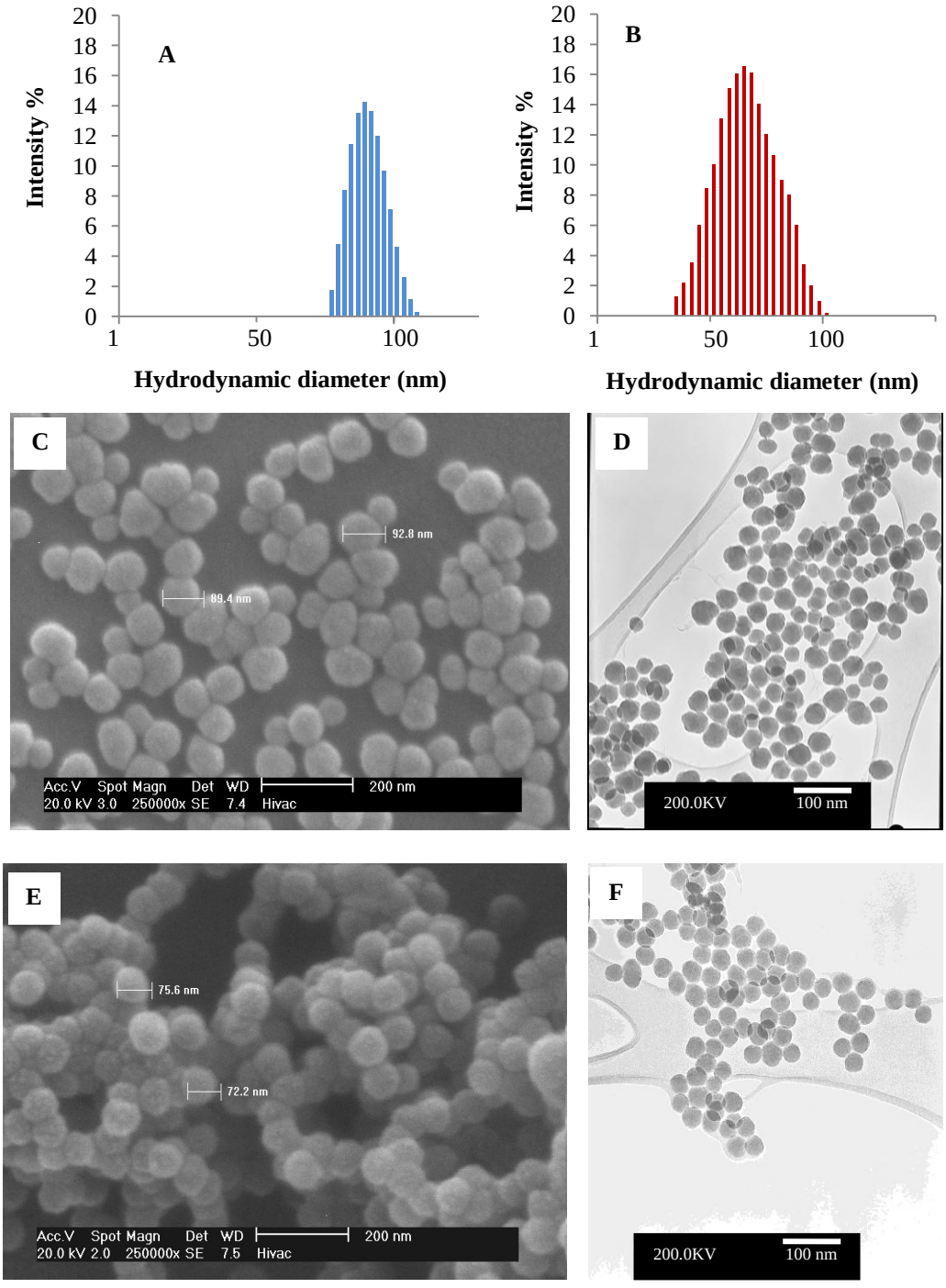


Figure 2.16: (A) and (B) The measured hydrodynamic diameters of p-SNPs and f-SNPs, respectively, synthesised using the optimised protocol. (C) and (D) The eSEM and TEM images of p-SNPs while (E) and (F) are the eSEM and TEM images of f-SNPs.

2.4.2.5.2. Zeta potential measurements

The colloidal stability properties and surface modification of the developed SNPs were determined by measuring zeta potential value. As represented in **Figure 2.17 A**, the measured zeta potential of p-SNPs and FAM-SNPs, synthesised without any surface modifications, were -31±12 mV and -26±7 mV respectively. This indicates that SNPS, prepared by the optimised protocol, have sufficient colloidal stability properties. Additionally, surface modification of the nanoparticles with APTES (amino-SNPs) was assessed by detecting the value of zeta potential. The results revealed that the zeta potential of amino-SNPs was +18±5 mV. This marked increase in the measured zeta potential after modification with APTES indicates the successful surface modification of the nanoparticle with the positively-charged amino group. Further, the effect of pH on zeta potential value was studied to investigate the nanoparticle stability in suspension. p-SNPs and FAM-SNPs were suspended separately in different pH values ranged from pH 3.0 to 8.0. The results are shown in **Figure 2.17 B** indicate that the zeta potential value decreases as the pH increased which could be attributed to the ionisation of the free OH group on silanol molecule of silica network whilst the most stable SNPs suspensions were observed when the pH was above pH 5.0.

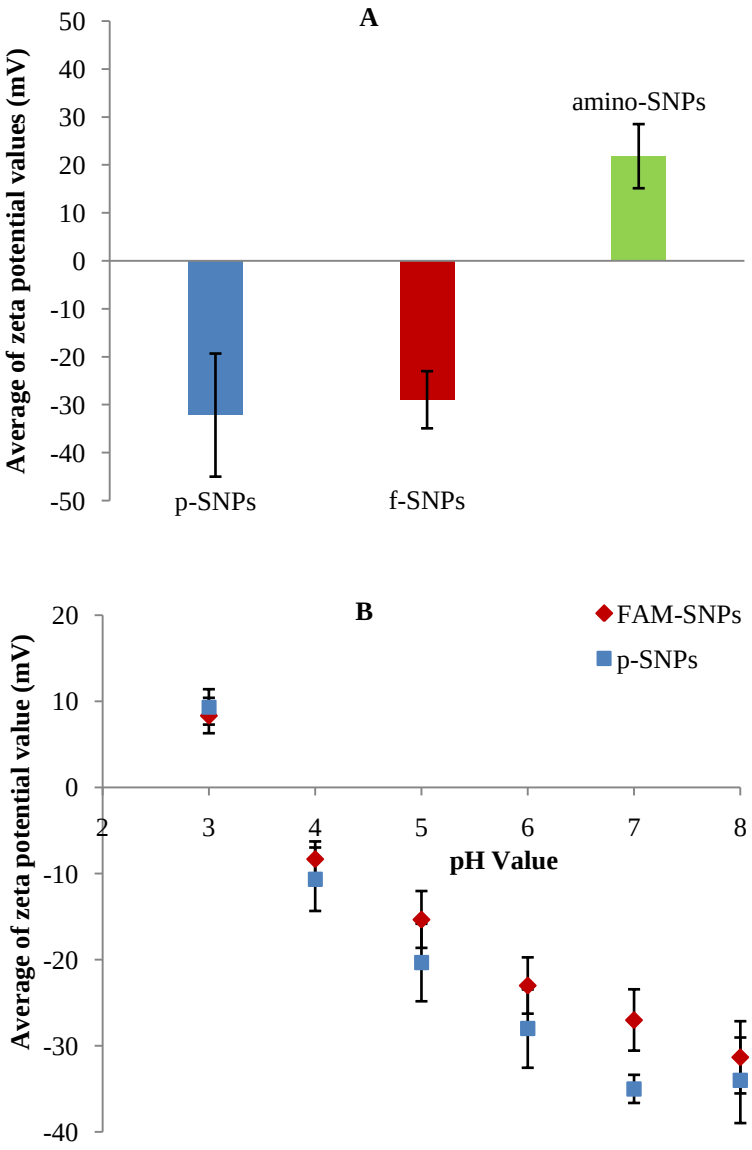


Figure 2.17: (A) Zeta potential values of p-SNPs, f-SNPs and amino-SNPs, measured in water by Malvern Zetasizer DLS instrument. (B) Zeta potential values of p-SNPs and FAM-SNPs measured in different pH values.

2.4.2.6. Fabrication and optical characterisation of the ratiometric fluorescent silica pH nanosensors

To fabricate the ratiometric fluorescent silica pH nanosensors, OG, FAM and TAMRA were covalently linked to the silica matrix. To facilitate this covalent binding, APTES was conjugated to the succinimidyl ester group of each fluorophore, prior to the nanoparticle synthesis, as previously illustrated in **Figure 2.11**. The produced fluorophore-APTES conjugates were added to the reaction mixture to form covalent bonds between fluorophores and silica matrix. In addition, this conjugation did not influence the position of the fluorescence maxima of the corresponding fluorophores, as the recorded fluorescence signal of each fluorophore was similar to that recorded for the corresponding free fluorophore.

To produce optimum silica pH nanosensors with tuneable effective pH ranges; different ratios of OG-APTES: FAM-APTES were used during the initial nanoparticle synthesis while the volume of TAMRA-APTES was kept constant in all cases. The ratios of OG-APTES: FAM-APTES were 100%: 0%, 75%: 25%, 50%: 50%, 25%: 75% and 0%:100%, respectively. The optimised protocol for the preparation of f-SNPs was followed to produce different batches of silica pH nanosensors containing different ratios of the pH-sensitive fluorophores. Further, the measured hydrodynamic diameters of all the resulting SNPs batches were in the range of ~75 nm for all the resultant batches.

Investigations were made to study the fluorescent response of each corresponding pH nanosensor, fabricated from SNPs and encapsulating a certain ratio of OG: FAM. The nanosensors were suspended separately in McIlvaine buffer, prepared with different pH values from pH 2.5 to 8.5, and the fluorescence intensities of each fluorophore were recorded against blank buffer samples.

The results showed that fluorescence intensities of OG/FAM significantly increased as the pH value of the McIlvaine buffer elevated while the fluorescence intensity of TAMRA remained nearly constant. Further, the responsive pH ranges of the developed nanosensors significantly varied corresponding to the ratio of OG/FAM that was utilised to prepare the nanosensors. To detect the effective pH range of the developed nanosensors, the normalised ratiometric calibration curves (I_{520}/I_{577}) were established using the ratio between the fluorescence intensity of OG/FAM and TAMRA versus pH. As shown in **Figure 2.18**, the effective dynamic pH range of each nanosensor is dependent on the ratio of the incorporated pH-sensitive fluorophores which controls the activity of the nanosensor due to the pKa effect of the pH-sensitive fluorophores.

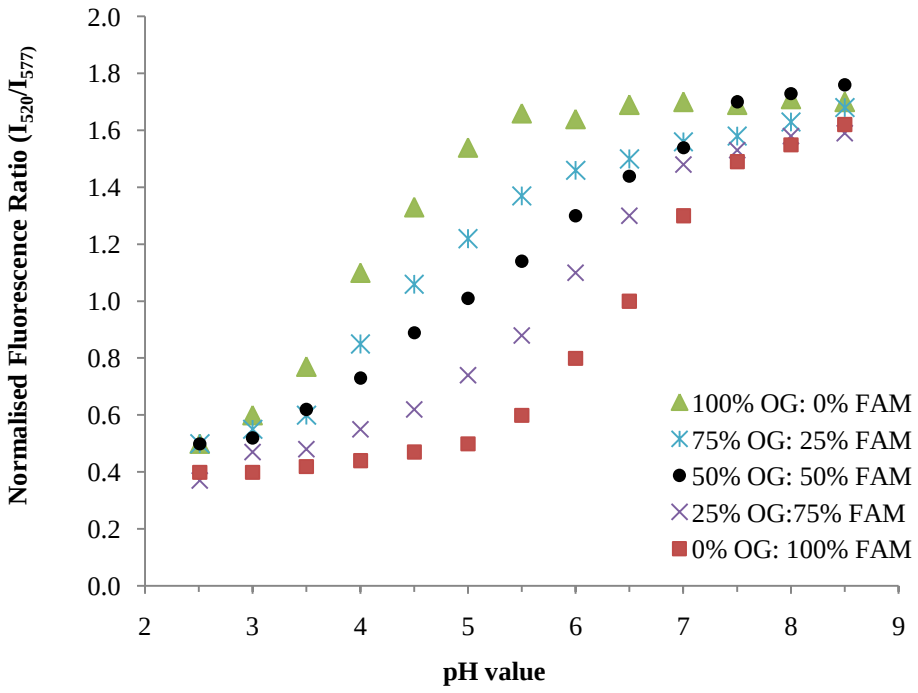


Figure 2.18: The normalised ratiometric calibration curves for the developed pH silica nanosensors, covalently linked to different ratios of OG: FAM (100%:0%, 75%: 25%, 50%: 50%, 25%: 75% and 0%: 100%).

For the nanosensor that incorporated OG only (100% OG: 0% FAM), the effective dynamic pH range of the nanosensor (pKa±1) was controlled by the activity of OG (pKa ~4.6) with an effective response from pH 3.5 to 5.5 where pH = pKa±1 and indicated by the green curve on **Figure 2.18**. Similarly, the responsive pH range of the nanosensor encapsulating only FAM was from pH 5.5 to 7.5 as the activity of this nanosensor was controlled by the pKa of FAM (~6.4), as represented by the red curve on the normalised calibration curve. Furthermore, tuning the ratio of OG: FAM produced nanosensors with tuneable effective pH responses while the maximum extended response was observed for the nanosensor incorporating a ratio of 50%: 50% of OG: FAM, as indicated by the black curve on **Figure 2.18**. The effective dynamic pH range of this optimised nanosensor was from pH 3.5 to 7.5 as shown in **Figure 2.19**. Therefore, such nanosensor

encapsulating OG: FAM with the ratio of 50%: 50% was selected as the optimum silica pH nanosensor that can detect pH changes over an extended, wide dynamic pH range from pH 3.5 to 7.5.

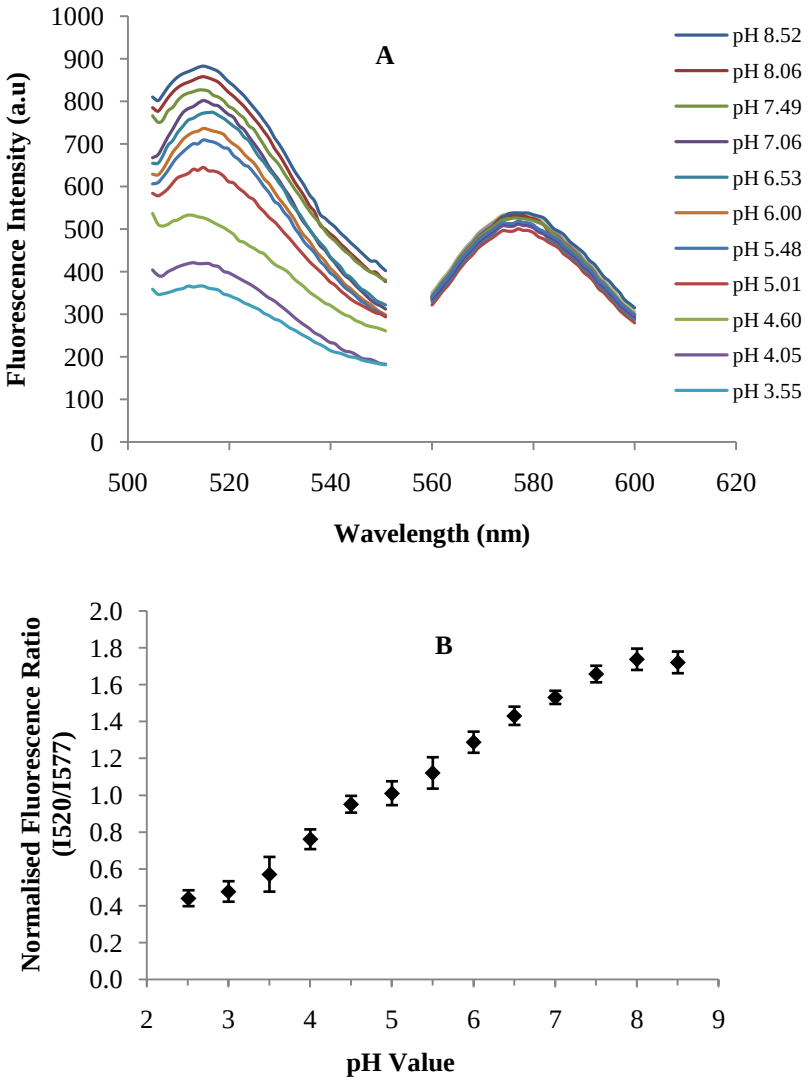


Figure 2.19: (A) The fluorescence spectra of the optimised silica pH nanosensor, covalently linked to OG and FAM (50%: 50%) and a reference fluorophore (TAMRA), suspended in McIlvaine buffer with pH from 2.5 to 8.5. (B) The normalised ratiometric calibration curves for the optimum nanosensor.

2.4.2.7. Dye leaching and stability studies using the optimum silica pH nanosensor

In this study, the optimised silica pH nanosensor was synthesised *via* covalent binding of fluorophores to silica matrix. In addition, ratiometric fluorescence measurements were utilised to provide robust and reproducible pH measurements, independent of the nanosensor concentration or fluorescence signal fluctuations. Despite these advantages, dye leaching and fluorescence stability studies of the optimum silica pH nanosensor were performed in PBS buffer, pH 7.4.

Dye leaching is a common problem that is associated with optical nanosensors in which fluorescent molecules are physically entrapped within the nanoparticle matrix rather than being covalently linked to the nanoparticle matrix [219, 220]. Using the optimised silica pH nanosensor, dye leaching study was performed in PBS buffer, pH 7.4. The results showed a negligible dye leaching from the silica matrix as the fluorescence signals, recorded in the supernatant after centrifugation of f-SNPs, did not exceed 2% of the original fluorescence intensity of the nanosensor. Additionally, almost all the recorded fluorescence signal of each fluorophore was obtained in the nanoparticle suspension, prepared after resuspending the nanoparticle pellets in the buffer.

Meanwhile, the stability of fluorescence signals from the optimum fluorescent silica pH nanosensor was investigated over successive periods from 5 minutes to 48 hours. As shown in **Figure 2.20 A**, there is a slight decrease in the recorded fluorescence intensity of the incorporated fluorophores, measured over the studied time periods. However, the ratios of the recorded fluorescence (I_{520}/I_{577}) remained

constant over the duration of the experiment as in **Figure 2.20 B**. These results also indicate the advantageous use of the ratiometric fluorescence measurements compared to using the direct fluorescence measurements which may produce inaccurate data due to fluorescence signal fluctuations over time.

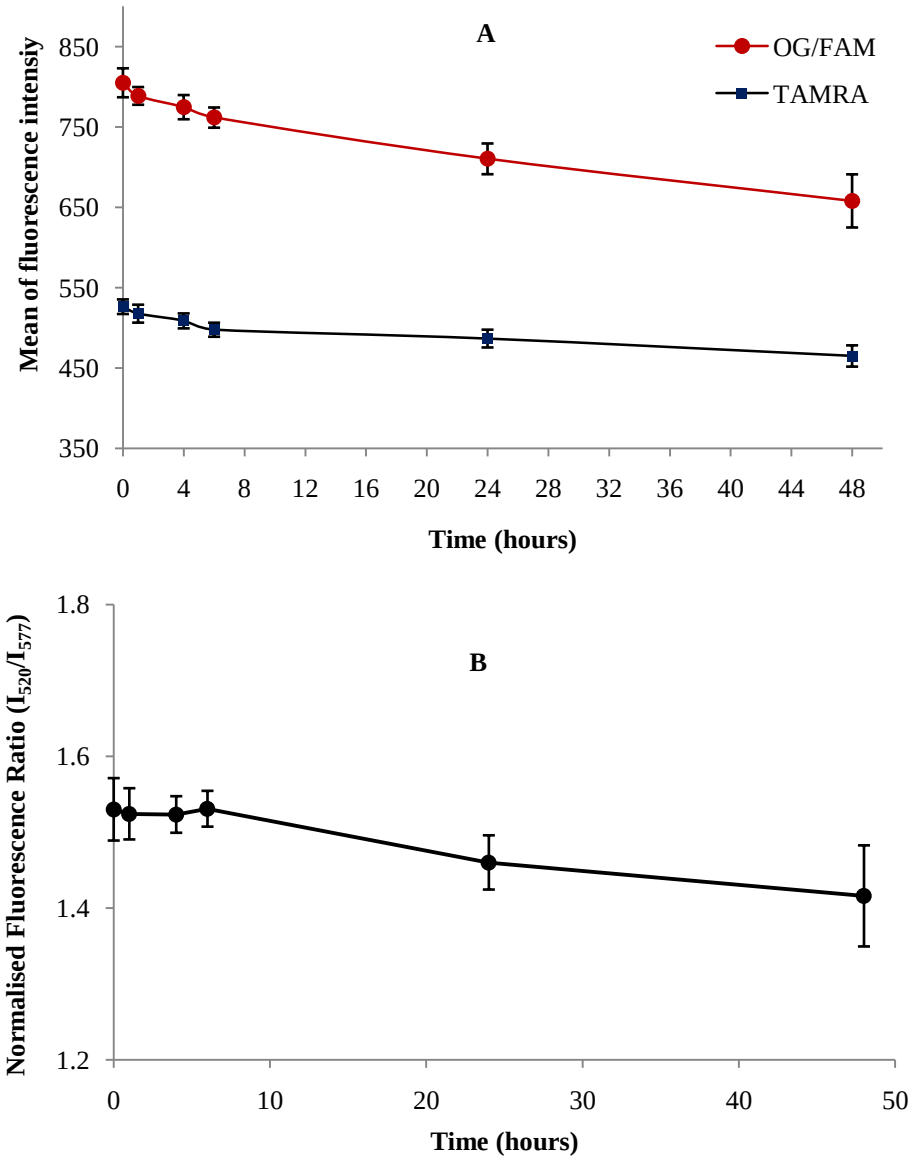


Figure 2.20: (A) The mean of fluorescence signals of the optimised silica pH nanosensors, covalently linked to OG, FAM and TAMRA over different time period from 5 minutes to 48 hours. The fluorescence intensities were recorded at 520 nm and 577 nm over different time intervals. (B) The normalised ratiometric fluorescence (I_{520}/I577) of the optimised silica pH nanosensor over the same time period, suspended in PBS buffer, pH 7.4.

2.5. Conclusion

In the present study, two types of ratiometric fluorescent pH nanosensors have been presented. The nanosensors were synthesised from two different matrices, polyacrylamide or silica, and covalently linked to two pH sensitive fluorophores (OG and FAM) and a reference fluorophore (TAMRA) to provide ratiometric fluorescence pH measurements. These two matrices were selected to produce two types of pH nanosensors with different physical and colloidal properties. In addition, combination of such two pH sensitive fluorophores that have different pKa values extended the effective dynamic pH range of the nanosensors from pH 3.5 to 7.5.

Polyacrylamide nanosensors, with a size of ~50 nm, were synthesised and characterised using a previously reported protocol that has been optimised [137]. Despite there are many previously reported protocols for the synthesis of SNPs, when such protocols were attempted in this study, the obtained size ranges of the resulting SNPs were different from that reported. In the present work, a reproducible protocol for the synthesis of size-tuneable and monodisperse SNPs was successfully established. The study was achieved by optimising the amount of each reactant/catalyst (TEOS, NH_4OH, ethanol and dye-APTES conjugate) that are involved in the synthesis of SNPs. The results showed that, the amount of NH_4OH plays an important role in controlling the size of the resultant SNPs while the quantities of the other reactants have shown minimal effects on the size of SNPs.

Under the specified conditions, different sized SNPs ranging from 45 nm to 900 nm can be readily produced. Additionally, fluorescent SNPs (f-SNPs) that incorporating different ratios of fluorophores within their matrix were prepared.

The surfaces of nanosensors were successfully modified with positively-charged groups to study the effect of this modification on the cellular uptake of the nanosensors as discussed in Chapter 3. ACTA was utilised to incorporate positively-charged groups within the polyacrylamide matrix while APTES was used for functionalisation of SNPs with amino group to confer positive charges on the nanosensor surface. In addition, colloidal stability of SNPs was investigated in different pH values from pH 3.0 to 8.0 while sufficient stability was obtained when SNPs were suspended in a buffer with a pH value above 5.0.

The responsive pH range of the optimised ratiometric fluorescent silica pH nanosensors can be easily tuned by varying the initial ratios of the pH-sensitive fluorophores. The maximum dynamic nanosensor response was obtained when the ratio of OG: FAM was 50%: 50%. The optimum nanosensor can successfully detect pH changes over an extended dynamic range from pH 3.5 to 7.5, covering the physiological pH range of many cell types and organelles located within the effective range of the nanosensor. In addition, the optimised silica nanosensor exhibited a stable fluorescence response for 48 hours and showed a negligible dye leaching when suspended in PBS buffer, pH 7.4.

Chapter Three

Real-time measurement of the intracellular pH of yeast cells during glucose metabolism using ratiometric fluorescent pH nanosensors

3.1. Introduction

3.1.1. The world of yeast (structure, growth and physiology)

Yeast cells (*Saccharomyces cerevisiae)* are unicellular microorganisms representing a model to study the developed eukaryotic cell [221, 222]. Yeast is extensively used in many research and industrial applications for the production of enzymes and antibodies, drug delivery, gene therapy, health care industry and food production [223]. The yeast cell is non-motile; with a diameter of about 5-10 µm, requires glucose for maintaining normal growth and reproduces mainly *via* the budding process [221, 222]. As shown in **Figure 3.1**, a yeast cell is round to ovoid in shape, composed of a large vacuole containing water droplets, enzymes, amino acids and other molecules [222]. The vacuole is the most acidic organelle of the yeast cell, functionally similar to the lysosomes of mammalian cells [224]. The yeast vacuole is surrounded by a single membrane containing vacuolar-ATPase (V-ATPase) complex. This membrane plays an important role in regulation and stabilisation of the intracellular pH. Accumulation of protons inside the vacuoles makes them mostly acidic [224, 225]. In addition, the yeast cell has a distinct nucleus that carries the chromosomes inside and divides during cell reproduction. Aerobic respiration of cells occurs inside the mitochondria through the glycolysis cycle to generate the energy (ATP molecules) required for cell growth and division. Additionally, the term fermentation is used to describe the anaerobic respiration pathway where the cell oxidises glucose to produce ethanol and ATP in the absence of oxygen [226, 227].

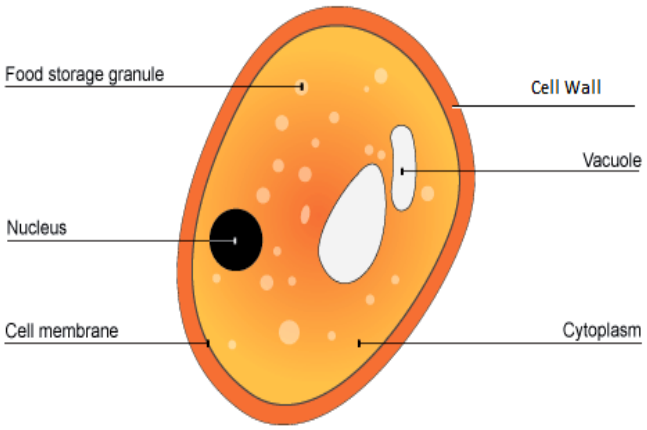


Figure 3.1: Illustrative diagram represents the shape, structure and cellular organelles of the yeast cell *(Saccharomyces cerevisiae).*

As shown in **Figure 3.1**, the yeast cell is surrounded by a cell wall to protect the cell from environmental changes, such as the extracellular pH or osmotic pressure. The cell wall is considered as the first line of defence, plays an important role in cellular permeability and is responsible for cell rigidity and structure [228]. The inner part of the cell wall has a high content of β-glucans polysaccharide complex whilst the outer wall contains polysaccharide-mannoprotein and chitin to form a rigid layer around the cell. Cellular permeability is highly dependent on the degree of cell wall thickness, which is determined by the growth phase. Whilst the cell wall affects the general permeation of many materials into the cell, selective cellular uptake and molecular permeation are regulated by the cell membrane, which is composed principally of a phospholipid bilayer [221, 229-231].

Generally, yeast cells pass through four definite phases during their life; lag-phase, exponential (log) phase, stationary phase and death phase [232, 233]. As represented in **Figure 3.2**, the first growth phase is known as lag-phase that occurs within the first few hours from starting the growth. During this phase, the cells uptake massive amounts of nutrients, such as amino acids, glucose, minerals and vitamins, from the growth medium to start the synthesis of proteins, DNA and other cellular components that are required for cell division [234]. Once the cells come out of their lag-phase, they enter directly into the exponential phase, which is characterised by a marked increase in the cell number due to the reproduction process. During the exponential phase, which can last for up to 3 days, cells consume glucose and other nutrients to maintain normal growth and cellular proliferation [221, 234]. While nutrients are consumed from the growth medium, the cellular division slows and cells enter into their stationary phase where the cells adapt themselves to survive in less favoured conditions [235]. During the stationary phase, the rate of cell division is similar to the death rate; therefore, the number of cells does not markedly change. Eventually, cells enter the death phase if the growth conditions are not improved [233, 235].

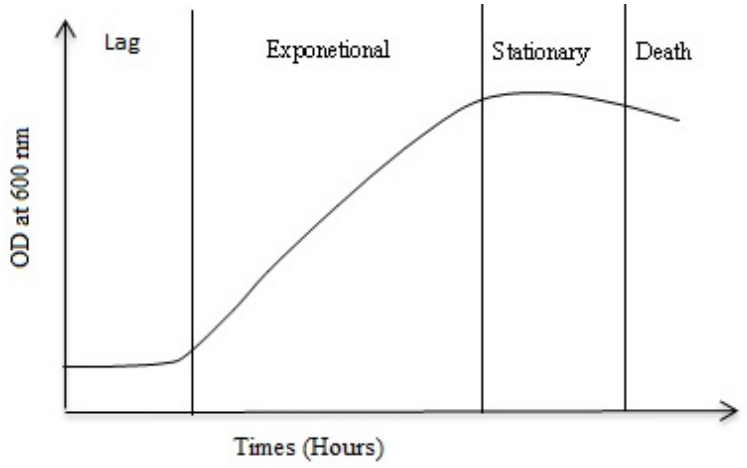


Figure 3.2: Typical growth curve for the yeast cells which can be established by measurement of the optical density (OD_{600}) at successive time periods after the beginning of growth.

The growth of yeast cells can be assessed by measurement of the absorbance intensity of cell suspensions using a spectrophotometer at 600 nm (optical density at 600 nm) [236, 237]. Optical density (OD_{600}) measurement is a simple method for detecting the number of yeast cells in 1 mL sample suspension which can be further used to indicate the growth phase. Theoretically, depending on the cell strain, growth medium and conditions, each OD_{600} with a value of 1.0 contains roughly $1\text{-}3\times10^{7}$ cells/mL [232, 237, 238]. **Figure 3.2** illustrates the typical growth curve for the yeast cells which can be determined by measurements of OD_{600} over successive time periods.

3.1.2. Importance of the intracellular pH of yeast cells

The intracellular pH of yeast cells is an important factor that affects cell survival and several biochemical processes including enzyme production and activation, endocytosis, ion transportation and cellular apoptosis [186, 239, 240]. The intracellular pH of a yeast cell is accurately regulated by two types of proton pump systems namely, V-ATPase and plasma membrane ATPase (P-ATPase). The pH homeostasis is controlled by these two ATPase systems, creating a small pH gradient between the cytoplasm and vacuoles. As a result, two pH values, *cytoplasmic and vacuolar*, can be observed within the yeast cell [241, 242]. Furthermore, other cell organelles such as mitochondria and Golgi apparatus exhibit their own pH values to maintain the normal processes, associated with such organelles [190].

Maintenance of the cytoplasmic pH is highly important for the yeast to maintain normal survival whilst regulation of the vacuolar pH is important for a number of other cellular functions [225, 241, 243]. Vacuolar pH is regulated by V-ATPase whereas the cytoplasmic pH is controlled by the dual action of both ATPase systems (V-ATPase and P-ATPase). To regulate the intracellular pH, V-ATPase transfers the cytosol protons into the vacuoles while P-ATPase pumps the cytosol protons out of the cytoplasm, to the medium, to maintain the cytoplasmic pH [224, 242]. Activation of both proton-pump systems (V-ATPase and P-ATPase) is highly dependent on glucose concentration and the amount of energy (ATP molecules), produced upon glucose metabolism [242, 244]. Depletion of glucose inside the cell reduces the activity of both ATPase systems which results in accumulation of protons in the vacuoles and cytoplasm and lowers the total value of the intracellular pH. This may explain why glucose-starved yeast cells exhibit lower pH values than those grown on glucose as previously reported [242, 245]. The low pH value of glucose-starved yeast cell is reversibly elevated upon addition of glucose to the medium. However, the mechanism of the intracellular pH changes of yeast cell during glucose metabolism is not fully understood and further investigations are required [246, 247].

Beside this complicated process of the intracellular pH homeostasis in yeast, many studies have shown that the yeast can resist changes in the external pH of the growth medium up to pH 7.5 while an optimal growth conditions takes place at pH from 5.0 to 6.5 [248]. Above pH of 7.5, the cell looses its tolerance while yeast cannot survive in an acidic pH <2.5 or alkaline pH medium >8.5 [186, 239, 240, 249].

3.1.3. Current methods for the measurement of the intracellular pH of yeast cells

Currently, several approaches for the measurement of the intracellular pH of yeast cells have been reported. These methods include ^{31}P nuclear magnetic resonance spectroscopy [250, 251], pH-sensitive fluorophores [186, 246, 247, 252], green fluorescent protein [253, 254] and investigation of the distribution of radio-labelled weak acids [255, 256]. However, marked variations in the measured intracellular pH of yeast cells were observed from one study to another depending on the measurement technique, strain used and growth conditions [186, 190, 249]. In addition, due to the close convergence of the pH of yeast organelles, most of the previously reported studies dealt with the intracellular pH of yeast cells as an absolute value. However, some reports distinguished between the vacuolar, cytoplasmic and mitochondrial pH [240, 245, 249].

Based on the growth conditions and the technique used for pH measurement, the vacuolar pH of yeast cell exhibited a value of ≥ 4.5 while the cytoplasmic pH was about $\geq$ pH 5 [190, 225, 241]. Most of the previously reported methods for the detection of the intracellular pH of yeast require sophisticated, expensive instruments and invasive manipulation of cells. In addition, such methods cannot be applied for the long-term or real-time measurement of the intracellular pH of the yeast. Furthermore, many methods were not able to spatially resolve the pH differences amongst cells, where it is supposed that each cell has its own specific pH value [240].

Due to high sensitivity and ease of use, fluorescence detection is still the common technique that is used for the measurement of the intracellular pH of yeast. Fluorescent probes such as pHluorin (pKa of ~7.2), SNARF-1 with a pKa ~7, FAM (pKa ~6.4), SNARF-4 (pKa ~6.4) and other fluorophores have been utilised for the measurement of the intracellular pH of yeast [186, 245, 249, 252, 257, 258]. Although these methods provide convenient experimental setup, the inherent drawbacks of direct use of fluorophores; *e.g.* toxicity and signal fluctuation, still influence the accuracy of the measurements. In addition, the pKa restriction of the used fluorophore limits the effective pH range of the measurement to two pH units, where pH=pKa±1. This narrow effective pH range may be outside the range of the intracellular pH of many cell types including yeast [187, 240]. The inability of these reported methods to measure the pH of individual cells and the pKa limitations of the used fluorophores make such methods inappropriate for the accurate real-time measurement of the intracellular pH of yeast. Accordingly, utilisation of a probe that is capable of detecting the pH changes over an extended wide dynamic pH range may provide an accurate tool to monitor the intracellular pH changes of yeast cells in the real-time.

3.2. Aim

The general aim of Chapter 3 is to utilise the ratiometric fluorescent pH nanosensors that were fabricated and optimised in Chapter 2 for the real-time measurement of the intracellular pH of yeast cells during glucose metabolism.

Yeast was selected as a model cell due to the biological, industrial and pharmaceutical importance, additionally, their unique cellular structure and properties. The success of using the developed nanosensors to detect the real-time pH changes of yeast cells will evaluate the application of such nanosensors as potential probes for real-time pH detection of other cell type.

To achieve this study, many factors that influence the accuracy of the measurement must be considered. Generally, using nanosensors for the biological assays requires optimisation of factors such as incubation time, maximum cellular uptake and minimum toxicity. In addition, a big challenge when dealing with yeast cells is to overcome the cell wall rigidity to permit the nanosensors insertion [259].

Accordingly, the aim of the present study is to optimise all factors that may affect the measurements. Once these factors are optimised, the real-time measurement of the intracellular pH of yeast cells upon glucose metabolism can be achieved.

3.3. Experimental

3.3.1. Materials and chemicals

Ratiometric fluorescent pH nanosensors, fabricated from silica and polyacrylamide, were prepared and optimised as described in Chapter 2. Yeast cells strains, growth cultures and media were kindly donated by the Bioenergy and Brewing Science Centre, University of Nottingham, UK. Phosphate buffer with a pH of 5.5 was prepared using disodium hydrogen phosphate and potassium dihydrogen phosphate, obtained from Sigma-Aldrich, UK. Glucose was purchased from Fischer-Scientific, UK.

Tecan Spark M10 plate reader and Varian Cary Eclipse fluorescence spectrophotometer were used to record the fluorescence signals while a Nikon inverted fluorescence microscope was used for the nanosensors calibration, counting, visualising and imaging the cells.

3.3.2. Yeast strain and growth conditions

The yeast strain used in this study was *Saccharomyces cerevisiae* NCYC2592. The cells were incubated, with shaking at 28 °C and 150 rpm, in a 250 mL Erlenmeyer flask containing 50 mL of minimal (YNBD) medium with 6.7 g/L yeast nitrogen base without amino acids (Difco®) and 20 g/L of glucose. The medium was inoculated by a single colony, taken from yeast culture that had previously cultivated on YNBD-agar. The cells were harvested after 16-18 hours where $OD_{600} = 1.0 \pm 0.2$.

3.3.3. Cellular uptake study

Yeast cells were grown in 50 mL of YNBD medium for 16-18 hours and the optical density (OD_{600}) of 1 mL of cell suspension was measured by a spectrophotometer at 600 nm followed by centrifugation at 5000 rpm for 10 minutes at 4 °C. The cell pellets were resuspended in 1 mL of phosphate buffer, pH 5.5 using a vortex mixer and then centrifuged at 5000 rpm for further 10 minutes at 4 °C. This washing step was repeated three times with phosphate buffer followed by the incubation of 100 µL of cell suspensions with varied concentrations (20 µg/mL-30 mg/mL) of PPA, prepared by serial dilution using phosphate buffer of a pH 5.5. The cells were then incubated with PPA for 4 hours followed by centrifugation and washing for at least five times using 1 mL of phosphate buffer. Following this, 100 µL of the cells, that were incubated with PPA, were transferred into 96-black well plate block (Costar 96 well plate, from Bio-Rad, UK) and the relative fluorescence units (RFUs) of TAMRA were recorded using Tecan plate reader at 575 nm after excitation at 545 nm against a blank yeast sample that were not incubated with the nanosensors.

3.3.4. Toxicity study

The same procedure that was described for the cellular uptake study was followed. After the cellular incubation with PPA (20 µg/mL-30 mg/mL) and performing the washing steps; 10^5 times serial dilution of the cell suspensions were made using phosphate buffer for each corresponding PPA concentration. Following this, 100 µL of the diluted cell suspensions were spread on YNBD-agar in Petri dishes. The Petri dishes, containing the cells, were incubated for 48 hours at 28 °C. The number of the produced colonies, corresponding to each yeast

sample incubated previously with PPA (20 µg/mL-30 mg/mL), was counted and compared to the number of the colonies of the control sample, where no nanosensors were incubated and treated similarly.

3.3.5. Incubation time

100 µL of yeas cell suspensions, prepared in phosphate buffer as in the cellular uptake study, were incubated with 15 mg/mL of PPA for different time intervals ranging from 1 to 24 hours followed by centrifugation and several washing with phosphate buffer. The fluorescence intensity of TAMRA was measured by a spectrofluorometer at 575 nm using excitation maxima at 545 nm.

3.3.6. Nanosensors calibration

PPA (1 mg/mL) was suspended in the McIlvaine buffer, prepared with different pH values from pH 2.94 to 8.50. Following this, 25 µL of PPA, suspended in each pH value, were transferred into glass dishes and calibration images were taken using the fluorescence microscope in the merged channels (green, red channels and brightfield mode). The microscope was focused using a scratch inside the glass bottom of each dish and subsequently moved away from the scratch to acquire the images. Images were taken from three different areas around the centre of the scratch, Background-corrected ratiometric images were established by using MATLAB® software and were used to construct the calibration curve as reported [137].

3.3.7. Measurement of the intracellular pH of yeast cells

After growing cells for 16-18 hours, cells were collected as previously described and suspended in phosphate buffer. The glucose starvation process was initiated by incubation of 100 µL of cell suspension, with PPA (15 mg/mL) for 4 hours in phosphate buffer without any glucose or nutrients. The incubated cell suspensions were centrifuged and washed, several times. Following this, 5 µL of glucose-starved cell suspensions was transferred to standard glass coverslips and cell imaging was started.

Images were immediately taken of yeast cells using the fluorescence microscope in the merged channels (green, red and brightfield) at the same time as PPA calibration under the same parameters. Once the images of glucose-starved cells were acquired, 10 mM D(+) glucose was added to the cell suspensions and images were continuously taken at successive time intervals which ranged from 1 minute to to 45 minutes. The time lapse between each image was set to 1 minute within the first 10 minutes and then every 5 minutes during the remaining experiment duration.

All the taken images for the cells (both glucose-starved and after addition of glucose) and PPA calibration were collected for the analysis using MATLAB® software and were used to calculate the intracellular pH using ImageJ® software.

3.3.8. Image acquisition and data analysis [137].

Automated images acquisition and data analysis of PPA and cells were performed according to a previously reported protocol, established by the Aylott research group [137]. Ratiometric fluorescent images and background images (buffer without nanosensors) were acquired in all channels (red, green and brightfield) for each corresponding pH value. Images were taken using a 40x objective lens (Olympus) in the green channels for OG and FAM (excitation at 490 nm, fluorescence at 520 nm), red channels for TAMRA (excitation at 550 nm, fluorescence at 575 nm) and brightfield mode. The size of all images was set to 1024×1024 pixels.

Background-corrected ratiometric images were generated automatically using MATLAB® software after subtraction of the background images (blank samples containing buffers with no nanosensors) from the corresponding ratiometric fluorescent images. The calibration curve of PPA was constructed as a function between the mean of the pixel ratios of three background-corrected ratiometric images (green/red) of PPA versus the corresponding pH value. A similar procedure was followed to generate the background-corrected ratiometric images for the yeast cells. Calculations of the intracellular pH of the cells were performed using ImageJ® software by selection of a pixel-wise area of the background-corrected ratiometric images of the cells-containing PPA. The results were matched with the calibration curve data. Additionally, the same approach was followed for measurements of the intracellular pH of cells after glucose addition to establish the real-time measurements. ImageJ® software was used to construct the coloured map pH images.

3.4. Results and discussion

3.4.1. Silica pH nanosensors

3.4.1.1.Unmodified silica pH nanosensors

Initial experiments were performed using the optimised ratiometric fluorescent silica pH nanosensors that were developed in Chapter 2. The zeta potential value of such silica pH nanosensors was about -26±4 mV, as the nanosensors were suspended in the growth medium of yeast. Different concentrations of such nanosensors that ranged from 1 mg/mL to 20 mg/mL were incubated with the cells for 24 hours from the beginning of the growth followed by centrifugation and several washing using phosphate buffer with a pH 5.5. This pH value was selected as an optimal working pH similar to the pH of the growth medium, to minimise any physical perturbations to the yeast cells [186, 239, 240, 249].

After nanosensors incubation, all the incubated cells were separated by centrifugation and then visualised and counted using fluorescence microscopy (≥100 cells per image) in the brightfield mode whilst the fluorescence signal of TAMRA, recorded in the red channel, was performed to visualise the cells-containing nanosensors. Despite the exact localisation of the nanosensors was not known, the term cellular internalisation is used throughout this study to describe the cells-containing nanosensors. The percentage of cellular internalisation was calculated by comparing the number of the fluorescent cells (cells-containing nanosensors), observed in the red channel, with the number of total cells (fluorescent and non-fluorescent) that were counted in the brightfield mode.

The results showed that after incubation of negatively-charged silica pH nanosensors with the yeast cells for 24 hours from the beginning of growth, the percentage of cellular internalisation (fluorescent cells in the red channels) was approximately nil as illustrated in **Figure 3.3 A. Figure 3.3 B** is a false colour image, generated by processing the fluorescent image using ImageJ® and used for visualisation of cells-containing nanosensors. Additionally, increasing the concentration of nanosensors did not influence the percentage of internalisation. Further, the same results were obtained when these experiments were repeated in several days using different batches of unmodified (negatively-charged) silica pH nanosensors and imaging multiple areas.

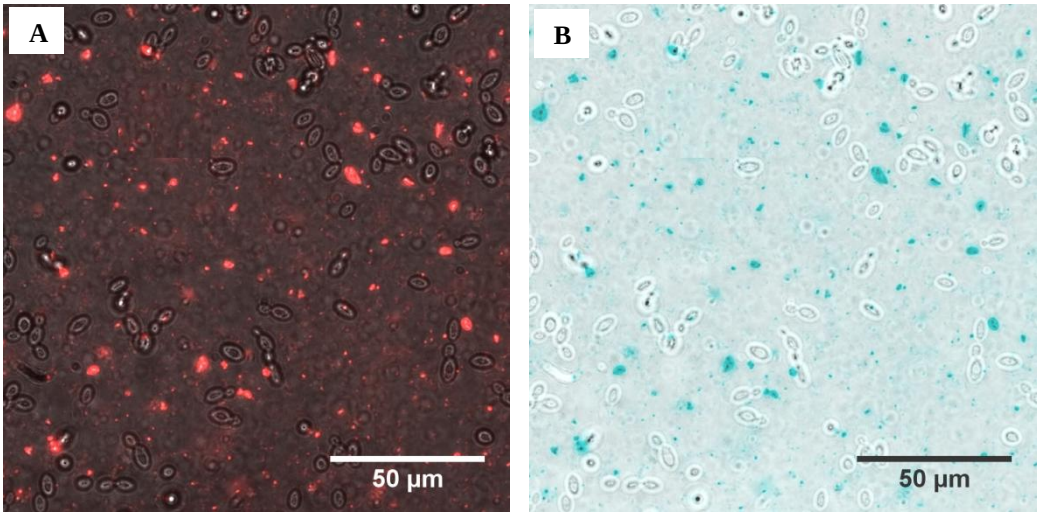


Figure 3.3: (A) Fluorescence image of yeast cells incubated with the unmodified (negatively) silica pH nanosensors (10 mg/mL) for 24 hours, recorded in the red channel and brightfield mode while (B) is the inverted false colour image of A, created by ImageJ® software, used for visualisation of cells-containing nanosensors.

As shown in **Figure 3.3**, high noise in the image background was observed when the yeast cells were separated from the negatively-charged silica pH nanosensors by centrifugation. This background noise was observed even when a low concentration of nanosensors (1 mg/mL) was used and several washing were performed. This noise may be attributed to precipitation of SNPs with the yeast

cells during the centrifugation process, making the accurate measurement of the intracellular pH impossible. As a result, before performing any measurements or analysis, removal of this background noise is necessary. To try to solve this problem, other alternatives for centrifugation were studied and discussed later in this chapter.

The reason for the lack of cellular internalisation with the negatively-charged silica pH nanosensors may be attributed to the electrostatic repulsions between the negatively-charged nanosensors and yeast cells where the zeta potential of yeast cells was -4.2±2 mV as detected by DLS. This probably prevents approaching of the nanosensors to the cells. These results are in agreement to previously reported studies that have explored the effect of nanoparticle surface charge on cellular internalisation of yeast cells and others cell types [217, 218, 260-266]. These studies have shown that the percentage of cellular internalisation markedly increased when positively-charged nanoparticles were used instead of the negatively-charged nanoparticles, both fabricated from the same matrix within the same size [217, 218, 260-266]. Based on these studies and the observations obtained in this work, positively-charged silica pH nanosensors with a size range similar to the unmodified silica pH nanosensors were used instead.

3.4.1.2. Positively-charged silica pH nanosensors

To confer positive charges onto the surface of silica pH nanosensors, amino-SNPs, were synthesised and characterised as in Chapter 2 (page 68). The size of amino-SNPs was about 78 nm while the zeta potential value was +16±8 mV, measured in the growth medium. Positively-charged silica pH nanosensors (10 mg/mL) were incubated with yeast cells from the beginning of growth, for 24

hours. As could be seen from **Figure 3.4**, a number of yeast cells was successfully internalised with the positively-charged silica pH nanosensors.

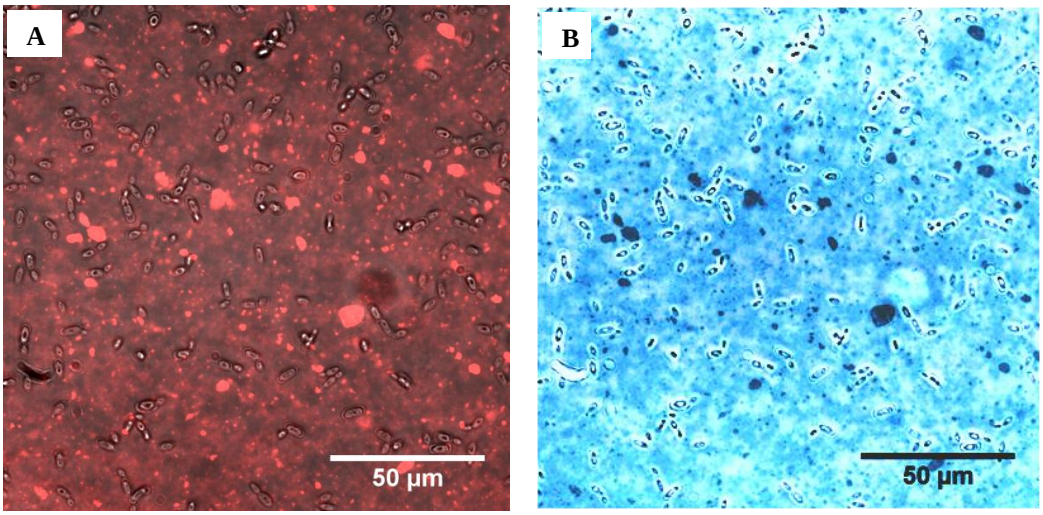


Figure 3.4: (A) The fluorescent image of yeast cells incubated with 10 mg/mL of positively-charged silica pH nanosensors, suspended in growth medium for 24 hours, and taken in the red channel and brightfield mode of the fluorescence microscope. (B) The inverted false colour image of A created by ImageJ® and used for visualisation of the internalised cells which appear as blue dots.

Despite this successful cellular internalisation, it was difficult to calculate the accurate percentage (number) of the internalised cells due to the observed high background noise, which probably resulted from precipitation of amino-SNPs with the yeast cells upon using centrifugation. Roughly about 15-20% of cells were internalised with amino-SNPs. However, separation of the non-internalised amino-SNPs from the cells by centrifugation was inappropriate as most of amino-SNPs were precipitated. Regardless of the observed high background noise, these experiments illustrate that to increase the number of the internalised yeast cells with nanosensors, positively-charged nanosensors are required; otherwise the lack of cellular internalisation will be the inevitable result. These results are similar to that found in the literature for studying the effect of nanoparticle surface charges on cellular internalisation [217, 218, 260-266].

3.4.1.3.Separation of silica pH nanosensors from yeast cells

Unlike for mammalian cells, there are no available surfaces, such as well plates, for attaching the yeast cells onto their surfaces to separate them from the excess non-incorporated materials. Centrifugation is still the most efficient tool that has been reported for the separation of yeast cells from excess non-incorporated materials, including nanoparticles [65, 259]. However, the use of centrifugation for the separation of the non-internalised silica pH nanosensors (unmodified and positively-charged) from the yeast created high background noise due to precipitation of SNPs with the cells. This noise made cellular imaging and hence the accurate fluorescence measurements extremely difficult. Precipitation of SNPs with yeast cells, which occurred upon centrifugation, may be attributed to the high density of SNPs (1.96 g/mL) [171]. To solve this problem, many trials have been made to find an alternative tool to centrifugation to separate yeast cells from the excess non-internalised silica pH nanosensors.

It has been reported that commercially available poly-l-lysine well plates; prepared by modification of the plate surface with poly-l-lysine polymer to create positive charges onto plate surface, can be used for the adherence of several cell types through electrostatic attraction of their cellular membrane to the plate surface [267, 268]. However, when such plates were utilised in this work to separate yeast cells from silica nanosensors, the majority of cells were lost as the cells did not stick adequately to the plate surface.

Another alternative tool to centrifugation is vacuum filtration, which is considered as a useful tool for separation of multiple compounds/proteins, based on their size differences [269]. The average size of yeast cell is about 5-10 μm, whilst the size

of SNPs is about 75 nm. Therefore, 2 µm Milipore filter membranes were utilised to separate the yeast cells from the excess SNPs. Despite this technique removed a part of the non-internalised SNPs, the efficiency of separation was too low and the majority of cells were lost by the consecutive process. Additionally, the resultant background noise was not completely removed.

Further, centrifuge tube filters with a membrane pore size 0.45 µm were used; again, the resultant background noise remained due to precipitation of SNPs in the separation tube. Meanwhile, dialysis technique, which is used to separate molecules based on the size differences, cannot be applied in the present study as it takes too long; affecting the viability of the internalised cells. However, in the present study, phosphate buffer with pH 5.5 was used as the optimal for nanosensor incubation and cell separation. This pH value did not affect greatly on the colloidal stability of SNPs as the zeta potential value of was ~ -20 mV or +19 mV for the negatively-charged or positively-charged silica nanosensors in pH 5.5 respectively.

Overall, centrifugation is still the most efficient method for the separation of nanoparticles from yeast cells and maintains the number of cells without significant change. Despite the successful cellular internalisation of yeast cells with the positively-charged silica pH nanosensors, separation of the excess non-internalised silica pH nanosensors from the yeast cells has not yet achieved and created high background noise. Therefore, the resulting images using silica pH nanosensors were excluded. At this stage, pH nanosensors that are fabricated from silica matrix may not be the optimum nanosensors for the accurate measurement of the intracellular pH of yeast cells; alternative pH nanosensors, fabricated from

different matrix with a lower density than SNPs, may provide a solution for the precipitation problem of SNPs.

3.4.2. Optimum nanosensors for the measurement of the intracellular pH of yeast

Taking into consideration the investigations that were performed using silica pH nanosensors, many criteria are required to design an optimum nanosensor which is capable of detecting the intracellular pH of yeast cells. These criteria include a requirement for a positive charge on the nanosensor surface to overcome the negative nature of the plasma membrane and facilitate cellular insertion of nanosensors. In addition, the matrix used to fabricate nanosensors should have lower density than that of silica to overcome the precipitation problem and removes the noisy background. Meanwhile, the surface of PANPs can be readily prepared with positive charges as shown in Chapter 2 and polyacrylamide has a low density of 1.11 g/mL compared to that of silica (1.96 g/mL). Therefore, investigations were conducted using polyacrylamide nanosensors instead of SNPs [171, 201].

However, previously reported studies showed that ≤ 50% of yeast cells have been internalised with unmodified polyacrylamide nanosensors that have almost the same size range to those prepared in Chapter 2 [259, 270]. Based on these studies and the findings of improved cellular internalisation using the positively-charged silica pH nanosensors that were shown previously in this work, PPA was utilised to investigate the pH measurement of yeast cells.

3.4.3. Positively-charged polyacrylamide pH nanosensors (PPA)

PPA composed of ~45 nm p-PANPs that were covalently linked to OG, FAM and TAMRA, synthesised and characterised in Chapter 2. The nanosensors were used for the ratiometric fluorescence detection of pH changes over an extended dynamic range from pH 3.5 to 7.5, as discussed in Chapter 2. PANPs were modified with ACTA to incorporate positively-charged trimethylammonium ions into the nanoparticle matrix which increased the net positive charges on the nanosensor surface as characterised by measuring the zeta potential of PPA of about +19 mV as illustrated earlier in Chapter 2.

Yeast cells were incubated with PPA (10 mg/mL) for 24 hours followed by centrifugation and washing, for several times, using phosphate buffer. The number of yeast cells internalised with PPA (≥100 cells per measurement/image) was counted using the fluorescence microscopy in the red channel, for TAMRA, and compared to the total number of cells (internalised and non-internalised), counted in brightfield mode. The results showed that almost 50% of the imaged yeast cells were successfully internalised with PPA as represented in **Figure 3.5**.

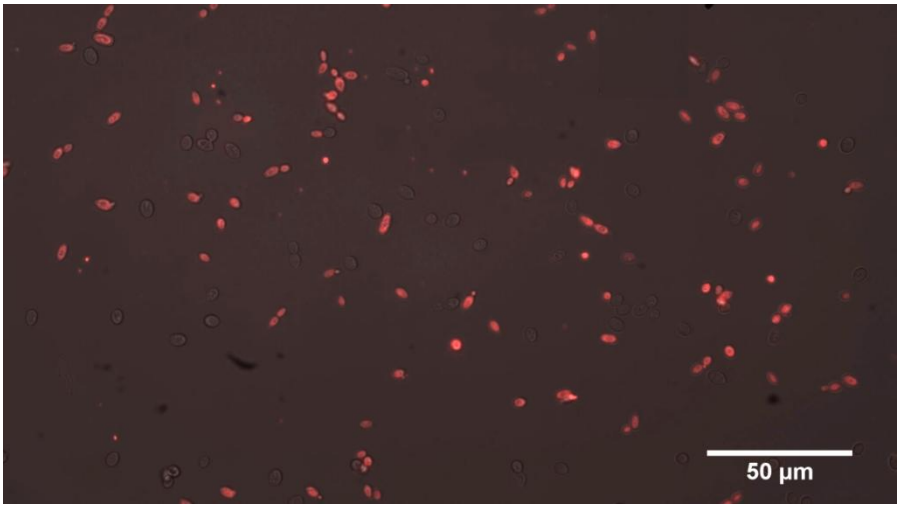


Figure 3.5: The fluorescent image of yeast cells incubated with PPA (10 mg/mL) for 24 hours. Image was taken in the red channel for TAMRA and illustrates that ~50% of cells were internalised with PPA, with a clear background.

This 50% is acceptable when dealing with the yeast as the cell is surrounded by a cell wall that may affect cellular permeation. Additionally, previously reported studies have shown that the percentage of cellular internalisation of yeast cells with polyacrylamide nanosensors, prepared without any surface modification, did not exceed 50%. However, in all of these studies, a stress-based technique such as electroporation was applied to enforce the cells to uptake the nanosensors [259, 270].

In addition to the improved percentage of cellular internalisation with PPA, the noisy background, resulted when silica pH nanosensors were used, did not occur when PPA was utilised and a clear background was observed as in **Figure 3.5**. This indicates that high signal to noise ratio can be established and hence, the accurate measurement of the intracellular pH of yeast using PPA can be achieved.

3.4.3.1.Effect of growth time of yeast on the percentage of cellular internalisation

Investigations were performed to study and optimise the maximum cellular internalisation with PPA. As previously mentioned, a yeast cell is surrounded by a cell wall that plays a major role in permeation of materials into the cell. The degree of cellular permeation is highly dependent on the cell wall thickness, which in turn depends on the growth phase (time) of the cell [228]. Therefore, the effect of growth time of yeast on the percentage of cellular internalisation with PPA was studied and optimised. This study was performed to select the optimum time/point where PPA should be incubated with the cells to obtain the maximum cellular internalisation. In these experiments, cells were grown for 12-36 hours (OD_{660} = 0.40 to 2.2) in the absence of PPA followed by collection of cells using

phosphate buffer. Following this, cells were incubated with PPA (10 mg/mL), in phosphate buffer with a pH 5.5, for at least 4 hours. The results represented in **Figure 3.6** illustrate that the percentage of cellular internalisation with PPA (10 mg/mL) markedly changed when the growth time of yeast changed. When yeast cells were grown for 12 hours, followed by incubation with PPA for further 4 hours in phosphate buffer, ~45% of cells were successfully incorporated with PPA. This percentage slightly increased as the growth time of yeast increased until 20 hours while the maximum cellular internalisation with a percentage of about 65% was obtained when the growth time ranged from 16 to18 hours, before incubation yeast cells with PPA.

Upon increasing the growth time over 20 hours, a marked decline in the number of fluorescent cells (cells-containing PPA) was observed. Approximately 35% and 20% of cells were incorporated with PPA when the growth time was elevated to 24 hours and 30 hours, respectively. In addition, the percentage of cellular internalisation markedly decreased to ~7% when the growth was continued for 36 hours before incubation of yeast cells with PPA.

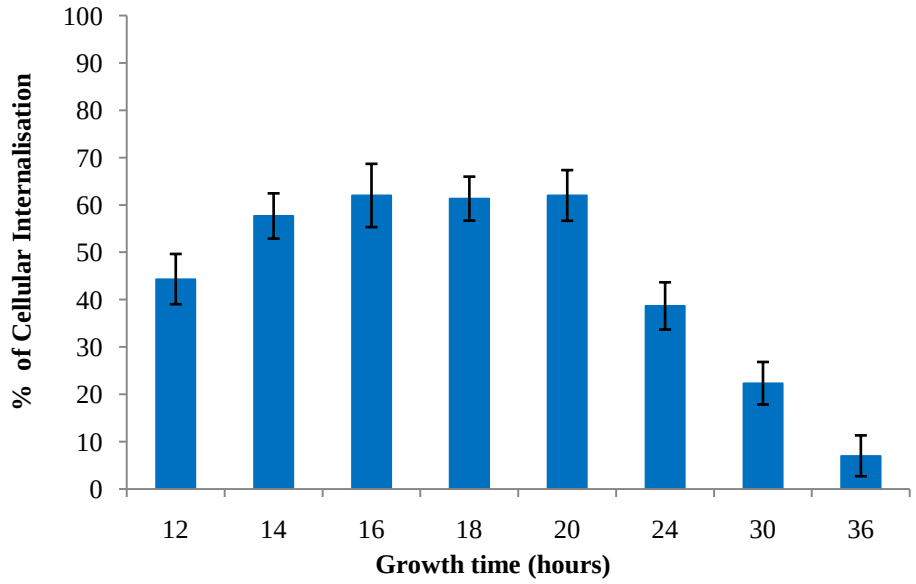


Figure 3.6: The effect of growth time of yeast on the percentage of cellular internalisation with PPA (10 mg/mL). Cells were normally grown for different time periods (12-36 hours) before incubation with PPA and counted by the fluorescence microscope in the brightfield mode and red channel to calculate the percentage of the internalised cells with PPA.

The above results may indicate the effect of the cell wall thickness of yeast on the percentage of cellular internalisation [229, 230]. During the first 12 hours (lag phase or early exponential phase, OD_{600} = 0.4±0.2), new daughter yeast cells, surrounded by thin cell walls, were produced; such yeast cells could be easily traversed by PPA. When the growth continued to the mid-exponential phase (16-24 hours, OD_{600} ~0.81 – 1.40), yeast cells rapidly divided to produce more daughter cells which increased the percentage of cellular internalisation to about 65% of the total cells. As the growth time increased over 24 hours, cells consumed nutrients from the growth medium to maintain their normal growth. Upon consumption of nutrients, yeast cells prepared themselves to enter into their stationary phase and thickened their cell wall. This was accompanied by more difficult permeation of PPA into cells and may explain why the percentage of the

fluorescent cells reduced down to ~7% as the growth time elevated to 36 hours, before incubation with PPA.

As a way forward, for maximum cellular internalisation with PPA (~65%), yeast cells were grown for 16-18 hours (OD_{600}=1.0±0.2) and collected using phosphate buffer followed by incubation with PPA for further 4 hours using the same buffer.

3.4.3.2.Effect of different stress-based techniques on cellular internalisation

Several stress-based techniques for the incorporation of materials into yeast cells have been reported. The technique is named according to the type of stress used. All these techniques aim to induce stress onto the yeast cell to cause a temporarily shock to cells and open gates/holes into their cell wall to permit the insertion of the material of interest into cells. Amongst these techniques, heat shock [271, 272], triton-X-10%/amphotricin-B mixture [186], hyper-osmotic NaCl solution (154 mM) [273] and electroporation [259, 270, 274], all were attempted in this work to study their effect on the incorporation of PPA into yeast cells.

The cells were grown for 16-18 hours (OD_{600}=1.0±0.2) and mixed with a constant concentration of PPA (10 mg/mL) and then the recommended procedure for each method was followed under the specified conditions as reported. As illustrated in **Figure 3.7**, 10±3.5% of yeast cells were internalised with PPA when the heat shock technique was utilised to incorporate PPA into cells. Moreover, 20±4.1% of yeast cells were incorporated with PPA when triton-X (10%)/amphotricin-B mixture was utilised. In addition, almost all cells (100±8.4%) were successfully incorporated with PPA within the first hour of incubation when the hyper-osmotic NaCl solution (154 mM) method was applied as shown in **Figure 3.8**.

Further, electroporation has been previously reported for the incorporation of unmodified polyacrylamide nanosensors with a percentage of ~50%. In the present work, when electroporation was applied, almost the same reported percentage (50±9.3%) of cellular internalisation with PPA was obtained. In contrast, 65±3.1% of yeast cells were internalised with PPA when the optimised protocol for the delivery of PPA into yeast cells was utilised. This optimised protocol was based on incubation of PPA with yeast cells in phosphate buffer (pH 5.5), for 4 hours after cell growth for 16-18 hours (OD_{600}=1.0±0.2)

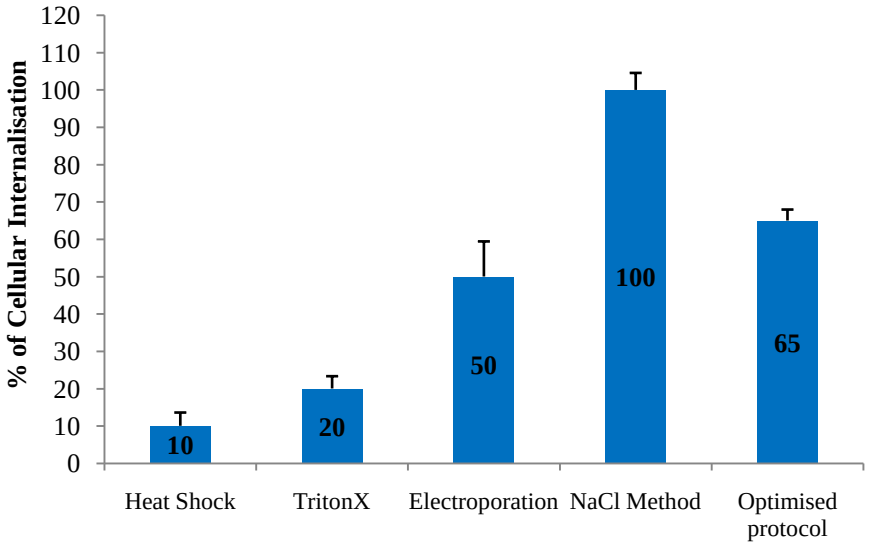


Figure 3.7: The effect of stress-based techniques/methods on the percentage of the internalised yeast cells with PPA (10 mg/mL) using the specified conditions for each method.

Despite all the yeast cells were incorporated with PPA using the NaCl hyper-osmotic solution (154 mM) as in **Figure 3.8**, such yeast cells were inflated, swollen and some cells ruptured during visualisation of cells under the fluorescence microscope. Compared to the protocol that was optimised in this study for the delivery of PPA to yeast cells; however, this protocol gave maximum cellular internalisation of about 65%, the cells were intact and healthy

as visualised without any signs of swelling or rupture. For this reason, the hyper-osmotic NaCl solution method was excluded from this study.

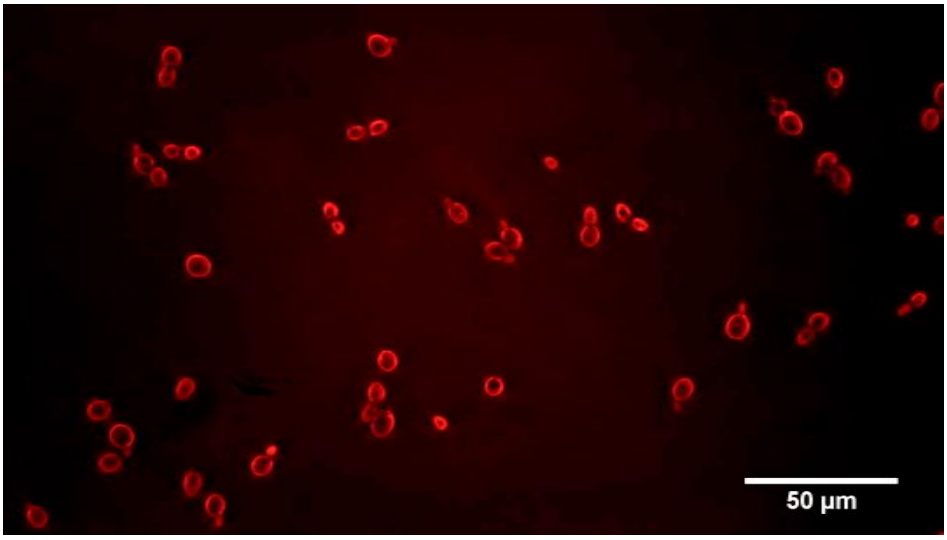


Figure 3.8: The fluorescent image, taken in the red channel, for the internalised yeast cells with PPA (10 mg/mL) in NaCl hyper-osmotic solution (154 mM).

Whilst none of the stress-based techniques improved the percentage of the internalised cells with PPA (except the hyper-osmotic solution method), the use of stress may cause cellular interruption. As a result, all of these stress-based techniques were excluded from the present study. For further experiments described in this chapter, to deliver PPA into yeast cells, the cells were grown to 16-18 hours (OD_{600}=1.0±0.2) followed by collection of the cells and incubation with PPA in phosphate buffer, pH 5.5, for 4 hours at room temperature.

3.4.3.3.Cellular uptake study

In order to select the optimum concentration of PPA, required for maximum cellular uptake (internalisation), a study of cellular uptake of PPA by yeast cells was performed. Yeast cells were grown for 16-18 hours (OD_{600} = 1.0±0.2) followed by incubation with different concentrations of PPA, ranged from 20 µg/mL to 30 mg/mL, in phosphate buffer for 4 hours. After PPA incubation, cells were separated by centrifugation and visualised under the fluorescence microscope to ensure that the recorded fluorescence signals resulting from the cells-containing PPA. As could be seen from **Figure 3.9 A**, cells-containing PPA exhibit sufficient fluorescence signals, recorded in the red channels of the fluorescence microscope, while the non-internalised cells did not produce any fluorescence signal. Additionally, clear background was observed which indicates that the observed fluorescence of TAMRA was resulted from the cells-containing PPA and not from the background (non-internalised nanosensors).

For ease and quick fluorescence detection, a plate reader was used to record the fluorescence signal of the internalised cells with PPA using the fluorescence of the reference fluorophore (TAMRA) as an indicator for the cellular uptake/internalisation. As shown **Figure 3.9 B**, the RFUs of TAMRA, arising from cells-containing PPA, markedly increased when PPA concentration increased from 20 µg/mL to 10 mg/mL and then remained without marked change as PPA concentration increased up to 25 mg. When PPA concentration elevated over 25 mg/mL, a slight decrease in the recorded RFUs was observed. These results indicate that the maximum cellular uptake of PPA was successfully achieved when 10 mg/mL was used and hence any further increase in PPA

concentration did not markedly influence the cellular internalisation percentage as cells reached their maximum capacity. Meanwhile, the slight decline in the measured fluorescence that was observed when PPA concentration increased above 25 mg/mL may indicate cellular death. For further experiments within this study, to obtain maximum cellular uptake of yeast with PPA, 15 mg/mL of PPA was utilised as the best concentration.

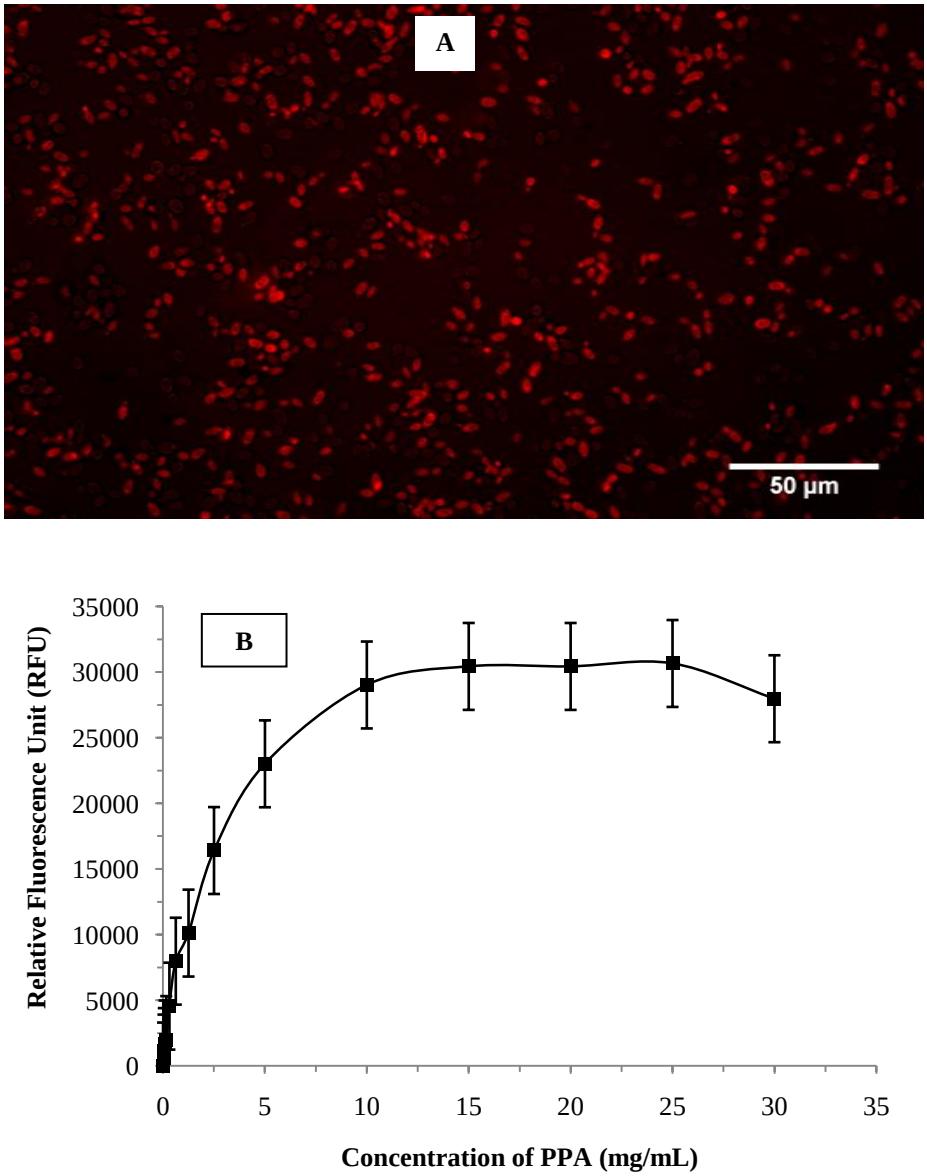


Figure 3.9: (A) The fluorescence microscopy image of yeast cells, incubated with 15 mg/mL PPA, and taken in the red channel. (B) The cellular uptake study of yeast cells incubated with different concentrations of PPA (20 µg/mL- 30 mg/mL) for 4 hours in phosphate buffer. RFUs of TAMRA was recorded on a plate reader (λ_{ex} = 545nm and λ_{em} = 575 nm) as an indicator for the cellular uptake.

3.4.3.4.Toxicity study of PPA

A colony forming unit (CFU) test was used to study the toxic effect of PPA on yeast cells. CFU has been reported as a robust and simple test to estimate the number of live bacterial or fungal cells [265]. Theoretically, each single live cell can continuously divide by the binary fission to form a single colony [275]. In this experiment, yeast cells were incubated with different concentrations of PPA (20 µg/mL-30 mg/mL). Following this, cells were separated and diluted to 10^5 times with phosphate buffer using serial dilution and then spread onto YNBD-agar. The number of the produced yeast colonies after incubation, corresponding to each PPA concentration, was counted and compared to the produced colonies of the control samples, where no PPA was incubated with the cells and treated similarly.

As illustrated in **Figure 3.10**, the produced colonies were detected as small dots on the agar plate. The results showed that below a concentration of 25 mg/mL of PPA, the number of the resulting colonies were almost the same as the control sample, while the number of colonies slightly decreased when the concentrations of PPA was increased above 25 mg/mL. These results suggest that PPA with a concentration above 25 mg/mL may cause cellular toxicity as the number of the produced colonies was declined. As a way forward, 15 mg/mL of PPA was used as the optimum non-toxic concentration of PPA that was also used to give maximum cellular uptake.

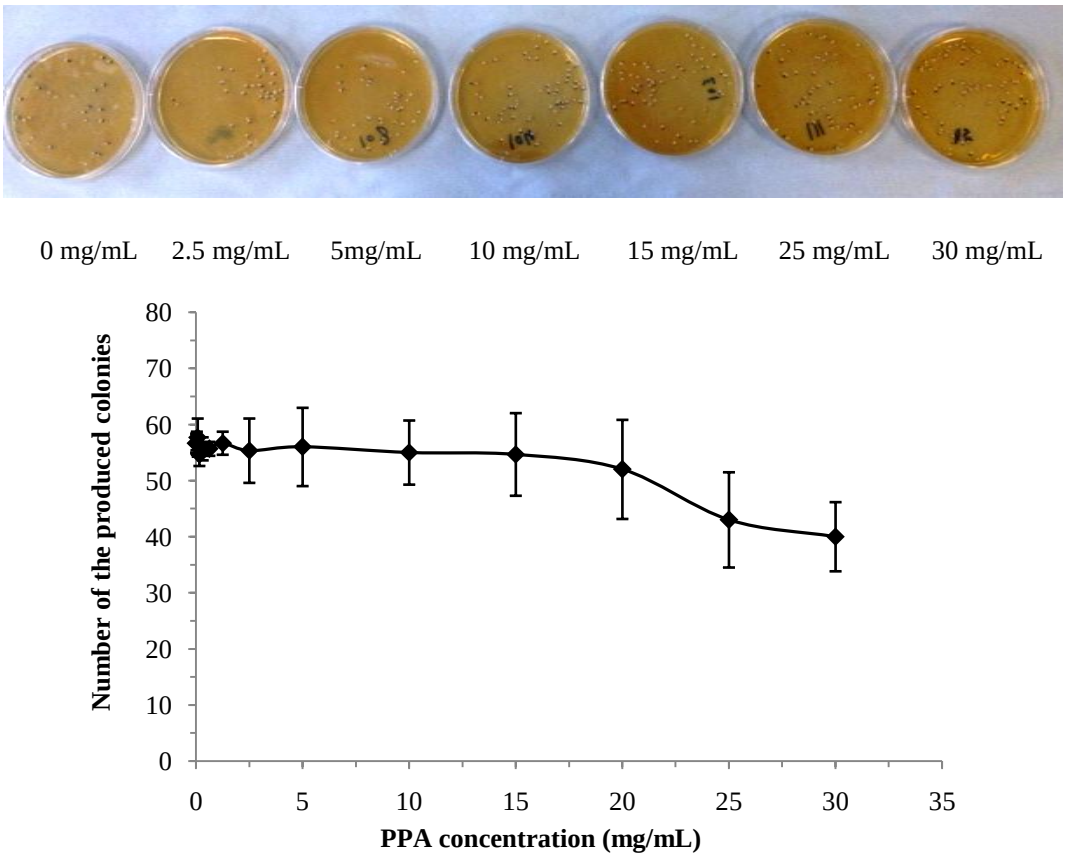


Figure 3.10: The toxicity study of different concentrations of PPA incubated with a constant number of yeast cells and detected by colony forming unit test (CFU). The image shows some selected Petri dishes with the produced colonies after incubation with different PPA concentrations. The graph represents the exact number of the produced colonies using each PPA concentrations and compared to the control, where no nanosensors were incubated.

3.4.3.5.Incubation time

The effect PPA incubation time on the yeast internalisation was investigated. The yeast cells were grown for 16-18 hours (OD_{600} = 1.0±0.2) followed by incubation with PPA (15 mg/mL) for different time intervals which ranged from 1 to 24 hours. After the separation of cells from the non-internalised PPA, cells were counted and visualised under the fluorescence microscope to ensure that all the non-internalised PPA was removed. Measurement of the fluorescence intensity of TAMRA was used to indicate the effect of incubation time on the percentage of cellular internalisation with PPA.

As shown in **Figure 3.11**, the fluorescence intensity of TAMRA, resulting from the cells-containing PPA (15 mg/mL) was markedly increased as the incubation time increased up to 2 hours and remained nearly at the same level as the incubation time elevated to 8 hours. While when the incubation time increased over 8 hours, the fluorescence intensity of TAMRA gradually decreased, due to possible photobleaching of TAMRA or death of some cells. Such photobleaching may be resulted from the consecutive exposure of these fluorescent samples to UV lights during the duration of the measurement. In summary, the results showed that 2 hours of incubation were enough for yeast cells to reach their maximum PPA uptake. Overall, to obtain the maximum percentage of cellular internalisation for the majority of yeast cells (65%), 4 hours of incubation between yeast cells and PPA was selected as the optimum incubation time.

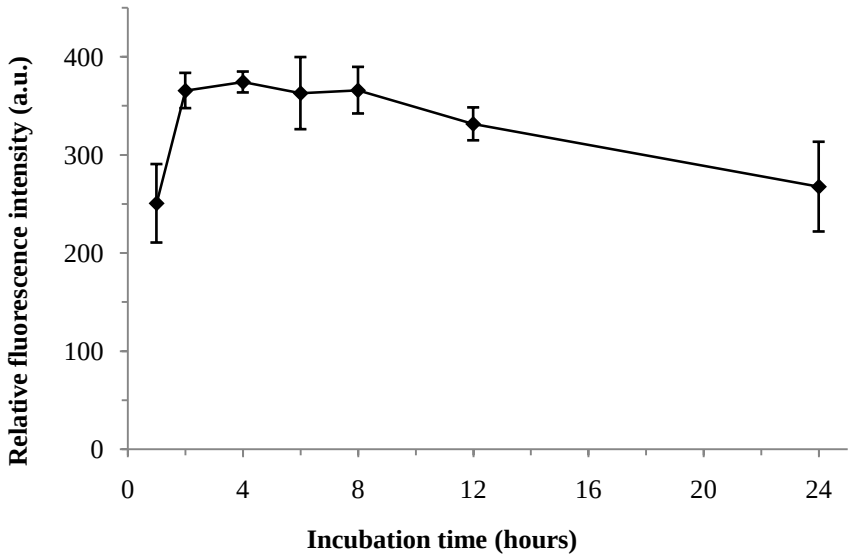


Figure 3.11: The effect of incubation time on cellular internalisation of yeast cells using PPA (15 mg/mL), for different times (1hour to 24 hours). Fluorescence intensity of TAMRA (λ_{ex} = 545 nm, λ_{em} =575 nm) was used as an indicator for the cellular internalisation.

3.4.4. Measurement of the intercellular pH of yeast cells

3.4.4.1.Calibration curve

To measure the pH of a biological system using pH nanosensors, calibration of the nanosensors under similar conditions to cellular uptake is required [142]. The simplest method for pH nanosensor calibration is to suspend this nanosensor into a buffer solution of pre-determined pH values [187, 276, 277]. The nanosensor suspensions are imaged using a fluorescence microscope under the same parameters and at the same time as the cell imaging. The drawback of this approach is that many factors that affect the measurements; such as cellular environment, are not taken into consideration. An alternative to this method is through *in-situ* calibration of the nanosensor using cell lysate or permeablized cells [12, 278].

Previous studies for the calibration of different pH-sensitive fluorophores in yeast cell lysate or permeablized yeast cells have been reported [186, 274]. These studies were based on using electroporation, amphotricin-B or nigricin to increase the cellular diffusion of hydrogen ions into yeast cells. However, these studies showed that there were no marked differences when pH-sensitive fluorophores calibrated either in buffer, cell lysate or inside the permeablized cells. Therefore, based on these studies, PPA were calibrated in the biological McIlvaine buffer, prepared with pH from 3.0 to 8.5, to establish the calibration curve of PPA [200]. The nanosensors were suspended in McIlvaine buffer (with exact pH of 2.94 to pH 8.52) and stirred at room temperature for 4 hours to resemble the same conditions of cellular uptake.

PPA calibration was performed using fluorescence microscopy at the same time of image acquisition of the yeast cells using the same parameters. Fluorescence signals were described as the pixels intensity of the images that were taken in the green channel for the indicator pH fluorophores (OG and FAM) and in the red channel for the reference TAMRA. Ratiometric images were taken in the merged channels of the microscope (green, red and brightfield). Additionally, the background images (buffer without nanosensor) of the corresponding ratiometric image were taken and subtracted from the corresponding ratiometric fluorescent images to generate the background-corrected ratiometric images. Automation of data analysis and construction of the calibration curve were performed using MATLAB® and ImageJ® as previously reported and detailed in the experimental part of this chapter [137].

The normalised calibration curve of PPA was constructed as a function between the mean of the pixel ratio of three background-corrected ratiometric images, taken in the merged channels (green, red and brightfield), versus the corresponding pH value. As shown in **Figure 3.12**, the shape of the calibration curve is sigmoidal, similar to that obtained on the spectrofluorometer in Chapter 2 and the effective dynamic pH range is from pH 3.5 to pH 7.5.

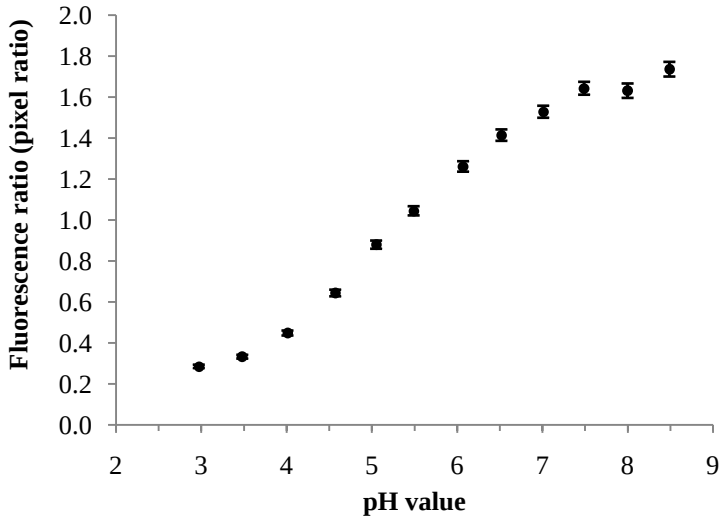


Figure 3.12: Normalised calibration curve of positively charged polyacrylamide pH nanosensors (PPA) suspended in the McIlvaine buffer with different pH values which ranged from pH 2.94 to 8.52. Fluorescence ratio was expressed as the ratio of the pixel intensities of background-corrected ratiometric images, taken in the merged channels of the fluorescence microscope for each corresponding pH value.

3.4.4.2. Real-time measurement of the intracellular pH of yeast cells during glucose metabolism

Once the calibration curve of PPA was constructed, real-time measurement of the intracellular pH of yeast cells during glucose metabolism was conducted. To achieve this, yeast cells were firstly starved of glucose by incubation with PPA for 4 hours in phosphate buffer without any nutrients. After cell separation, glucose-starved cells were imaged using the fluorescence microscope followed by addition of 10 mM D(+) glucose to the starved cells.

To establish the real-time pH measurements, cells were imaged every minute within the first ten minutes after the addition of glucose. Images were further taken every 5 minutes up to 45 minutes after glucose addition. Cells imaging was performed in the merged channels (red, green and brightfield) of the fluorescence microscope under the same conditions of nanosensors calibration.

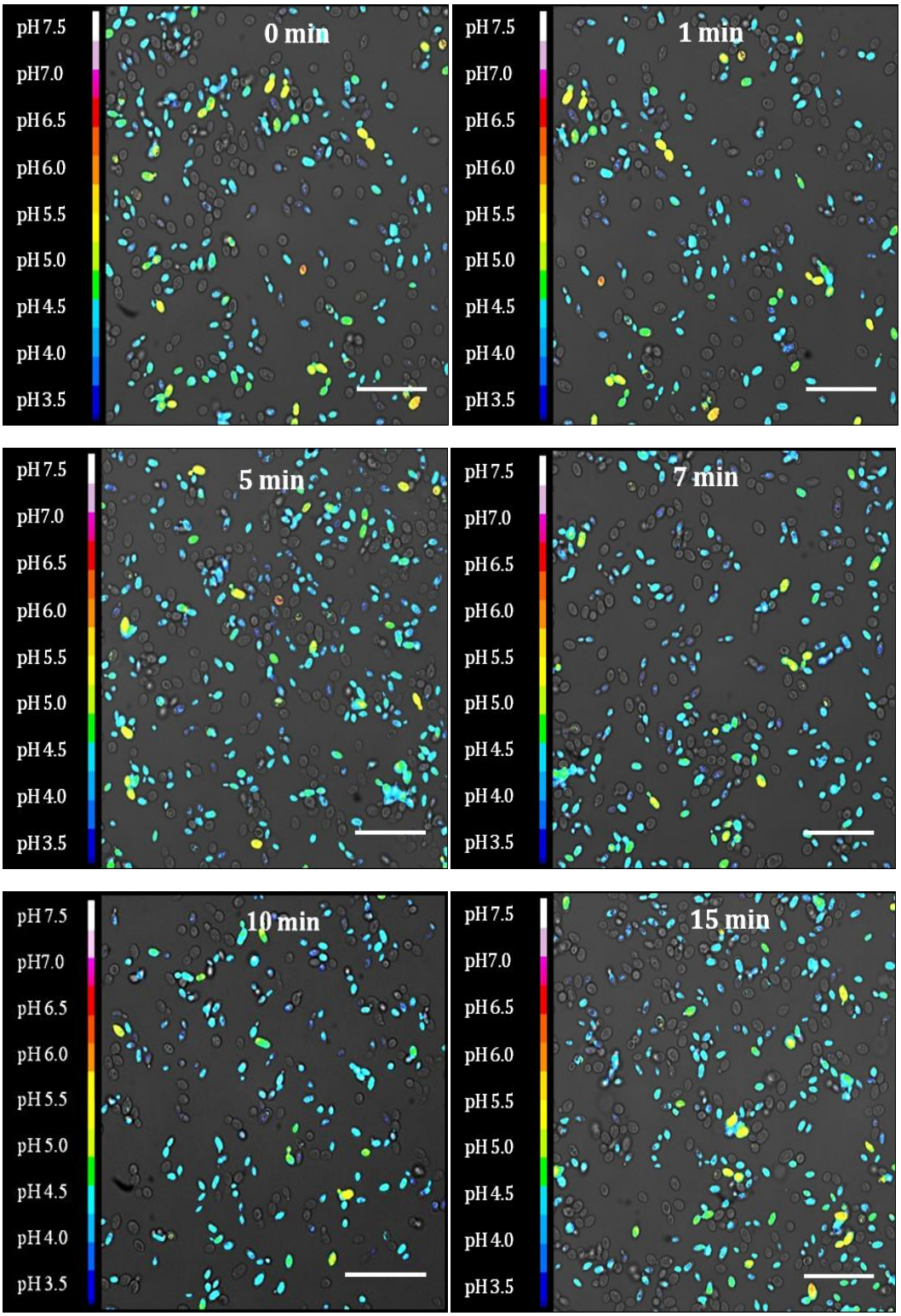
Automated background-corrected ratiometric images of the cells were established by subtraction of the background image from the corresponding ratiometric image using MATLAB®. Additionally, ImageJ® was used to produce the colour map images of the cells (**Figure 3.**13**)** and for data analysis.

To measure the intracellular pH, the areas of the fluorescent cells (cells-containing PPA) in the background-corrected ratiometric images were selected and the pixel intensities of the selected areas were calculated using ImageJ®. The fitting equation of the calibration curve was applied to measure the pH of the imaged cells using MATLAB® and ImageJ® [137, 142]. The results represented in **Figure 3.13** indicate that each glucose-starved cell exhibited its own pH value which may depend on the growth phase and the cell age. Therefore, to establish an accurate procedure for measuring the intracellular pH, the area intensity of each cell-containing PPA in the background-corrected ratiometric images was selected and used to calculate the intracellular pH of the corresponding yeast cell. In addition, to simplify the data presentation, the mean of the pH value of all fluorescent yeast cells, calculated at each time point, was utilised to establish the real-time measurements curve.

The results revealed that the mean of the intracellular pH of glucose-starved yeast cells (0 minute) was 4.67±0.15 as could be seen in **Figure 3.13** at 0 min and represented in **Figure 3.14**. Despite each cell showed its own specific pH value, all cells behaved similarly after glucose addition to the glucose-starved cells as shown in **Figure 3.13** and **Figure 3.14**. After 1 minute of glucose addition, the mean of the intracellular pH of all cells slightly decreased to pH 4.56±0.09, followed by gradual decrease in the intracellular pH within the first 10 minutes

after glucose addition whereas the mean of the intracellular pH reached the minimum level with a pH value of 3.86±0.13.

After 10 minutes of glucose addition, the mean of the intracellular pH of all fluorescent cells gradually increased and reached a maximum level with a pH 5.21±0.26 after 25 minutes of glucose addition. This pH value was remained almost stable for further 15 minutes with a mean pH of 5.19±0.19 before decreasing again to pH of 4.71±0.22 after 45 minutes of glucose addition, starting a new cycle of glucose starvation process. These results are in agreement to previously reported studies that quantitatively measured the intracellular ATP concentration and pH changes of glucose-starved yeast cells during glucose metabolism [279, 280]. These studies have shown that cells consume glucose within 40 to 45 minutes after glucose addition to the glucose-starved yeast cells, which are similar to the results obtained in this study. **Figure 3.13** represents the colour map images of yeast cells, imaged at different times after glucose addition. Different locations were used for cell imaging due to difficulty in fixing yeast cells on the glass slide upon addition of glucose. **Figure 3.14** illustrates the response curve established by calculating the mean of the intracellular pH during glucose metabolism in the real-time.


pH 7.5
pH7.0
pH 6.5
pH 6.0
pH 5.5
pH 5.0
pH 4.5
pH 4.0
pH 3.5
0 min
1 min
5 min
7 min
10 min
15 min

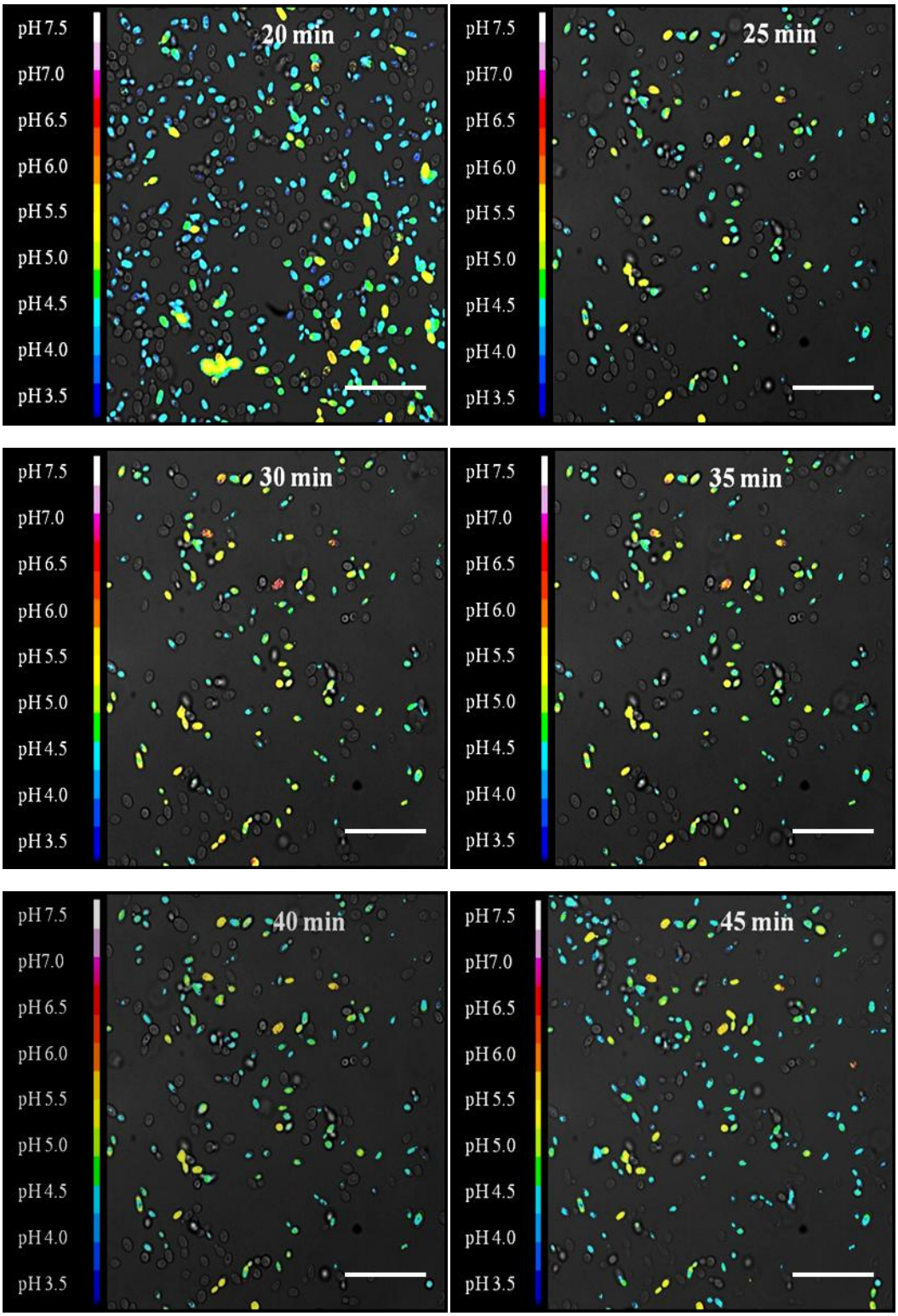


Figure 3.13: The colour map images of glucose-starved cells (0 min), incubated with PPA for 4 hours in phosphate buffer and the produced colour map images for the cells after consecutive time periods of glucose addition from 1 minute and up to 45 minutes. The colour map images were established by ImageJ®. Scale bar = 50 μm.

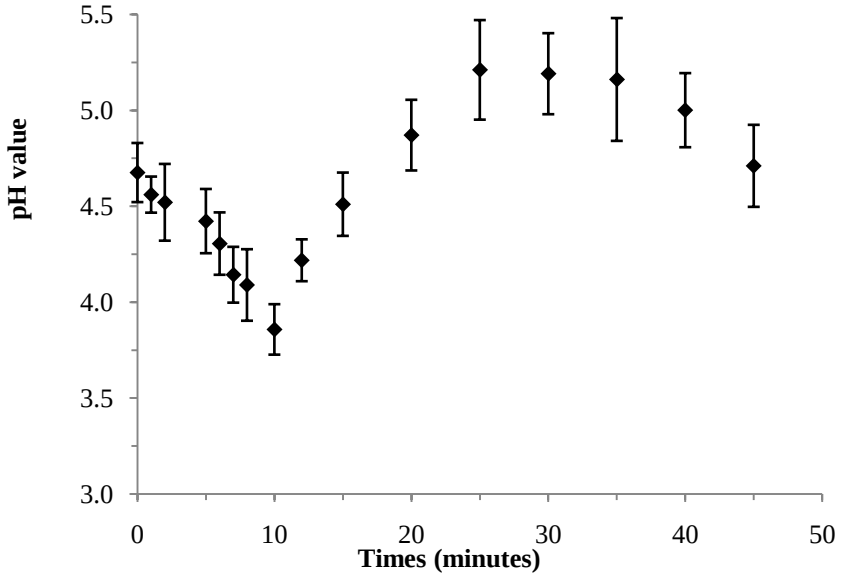


Figure 3.14: The response of the intracellular pH of yeast cells during glucose metabolism in real-time. Glucose was added to glucose-starved cells and the mean of pH was calculated for the corresponding time period after glucose addition.

The hypothesis to explain the decrease in the intracellular pH of yeast cells, observed within the first 10 minutes after glucose addition could be attributed to the activation of V-ATPase system of the vacuoles to stabilise the cytoplasmic pH, which is very important to maintain cellular survival. Activation of V-ATPase system transports protons from the cytoplasm to the vacuoles, leading to proton accumulation inside the vacuoles (the largest cell organelle) which in turn reduces the total pH of the whole cell. Once the cell return its cytoplasmic pH to normal, cell redistribute protons and regulate the pH of other cell organelles to their normal functions. This explains why the intracellular pH was gradually increased after 10 minutes of glucose addition. As the cells consume glucose, they produce more energy (ATP) which activates the P-ATPase system. This energy is consumed by the cells to maintain their pH; this explain why the intracellular pH maintained constant and stable for 15 minutes, after 25 minutes and up to 45 minutes from glucose addition. After 40 minutes of glucose addition, the yeast

cells consumed glucose and thus the cells became glucose-starved. As the generated energy inside the cells reduced, the ATPase systems were deactivated which resulting in accumulation of the protons inside the cells and lowering the intracellular pH.

The real-time changes in the intracellular pH of yeast cells during glucose metabolism was successfully investigated using the ratiometric fluorescent pH nanosensors. However, it was not possible to distinguish between the vacuolar and cytoplasmic pH of the yeast cells due to limitations on imaging capability. Nevertheless, the obtained results suggest that the time required for the yeast cells to restore their normal pH is approximately 25 minutes after glucose addition to glucose-starved cells, while the yeast cells that uptake glucose can keep their normal pH to further 15 minutes before the cells loose their pH homeostasis.

3.5. Conclusion

In this chapter, two types of ratiometric fluorescent pH nanosensors for pH detection over an extended dynamic pH range; from pH 3.5 to 7.5, have been utilised to measure the real-time intracellular pH of yeast cells during glucose metabolism. The nanosensors were fabricated from two different matrices, silica and polyacrylamide, prepared and characterised as discussed in Chapter 2.

The results revealed that surface modification of the nanosensors with positively-charged groups improved the cellular uptake of nanosensors whilst negatively-charged nanosensors were not taken up by yeast cells. Initial experiments were performed using silica pH nanosensors where almost none of cells incorporated with the negatively-charged silica pH nanosensors. In contrast, 15-20% of yeast cells were successfully incorporated with the positively-charged silica nanosensors (amino-SNPs). However, separation of the excess silica nanosensors (non-incorporated) from yeast cells, using centrifugation, was difficult due to precipitation of the high density SNPs (density 1.96 g/mL). This problem created significant noise in the fluorescent images and made accurate measurements impossible. Many alternative tools to centrifugation have been attempted, however, successful separation of SNPs from yeast cells has not yet achieved.

In comparison, when positively-charged polyacrylamide pH nanosensors (PPA) were utilised, almost 65% of yeast cells were traversed by these nanosensors. This percentage of cellular internalisation was improved when compared to that found in the literature using unmodified polyacrylamide nanosensors that have a similar size rage [259, 270]. This indicates that the presence of positive charges on the nanosensors surface may overcome the negative cell membrane and incorporate

PPA into cells. In addition, this protocol eliminates the need to use stress-based techniques, such as electroporation, for the nanosensor incorporation. In addition, due to the low density of polyacrylamide (1.1 g/mL), the precipitation problem that was observed with SNPs, density of 1.96 g/mL, did not occur when PPA was utilised. This removed the noisy background and permitted accurate measurement of the intercellular pH of the internalised cells.

In this study, many factors that influence the accuracy of the measurement were studied and optimised. These include maximum cellular internalisation/uptake with minimum cellular toxicity and the best incubation time. Under the determined optimal conditions, the real-time measurement of the intracellular pH of yeast cells during glucose metabolism was successfully achieved using the synthesised PPA.

Glucose-starved yeast cells exhibited a pH value of 4.67±0.15, which decreased to pH 3.86±0.13 within the first 10 minutes of glucose addition. After that, the intracellular pH of yeast cells gradually increased up to pH 5.21±0.26 after 25 minutes of glucose addition and then remained stable for further 15 minutes before decline again to pH 4.71±0.22 after 45 minutes of glucose addition.

The measurement of the intracellular pH of yeast cells during glucose metabolism has shown that glucose-starved cells exhibited a lower pH than those grown on glucose. Additionally, the intracellular pH of glucose-starved cells elevated upon the addition of glucose to the starved cells, however; the time taken by the cells to restore their normal pH, after the glucose addition, was different from a study to another depending on the yeast strain used, growth medium and growth conditions [190, 246, 247].

In comparison, this study has shown that cells restore their normal intracellular pH after 25 minutes of glucose addition and can maintain this pH value for further 15 minutes.

In conclusion, the ability of the yeast cells to regulate their pH upon glucose metabolism was successfully monitored using the synthesised PPA in real-time. This validates the use of these nanosensors for the real-time measurement of the intracellular pH of other cell types.

Chapter Four

Distance-dependent fluorescence quenching study using size controlled core-shell fluorescent silica nanoparticles

4.1. Introduction

4.1.1. Fluorescence quenching

The term ‘fluorescence quenching’ is used to refer to any process that causes a decrease in the fluorescence intensity/signal of any fluorescent material. This process occurs by different mechanisms, such as collisional and static quenching [146]. *Collisional (dynamic) quenching* is the simplest quenching process which occurs spontaneously whenever the excited fluorophores are in contact with the quencher molecules, dispersed within the same medium. This type of quenching takes place due to random collision of the quencher molecules with the fluorophore while the latter is in the excited state [281]. The mechanism of collisional quenching may be attributed to intersystem crossing or charge transfer between the excited fluorophore and the diffused quencher, facilitating the non-radiative transition of the excited fluorophore to its ground state. Common examples of such quenchers are oxygen and halogens [146, 282]. The degree of fluorescence quenching is controlled by many parameters summarised by the Stern-Volmer equation as represented in **Equation 4.1** [146, 283].

$$\frac{I_0}{I} = 1 + k_q \tau_0 [Q]$$ **Equation 4.1** [283]

Where I_0 and I are the fluorescence intensities of the fluorophore in the absence and presence of the quencher, respectively, k_q is the quencher rate diffusion coefficient, τ_0 is the fluorescence lifetime and Q is the concentration of the quencher [283].

Static quenching is another mechanism for the fluorescence quenching which occurs as a result of complex formation between a fluorescent molecule and a quencher molecule providing a non-fluorescent complex. The reaction takes place at the ground state of the fluorophore before the excitation [284]. Static quenching is highly dependent on the quencher concentration, temperature and the dissociation constant of the formed fluorophore-quencher complex. Generally, both types of fluorescence quenching, *collisional and static*, require molecular contact between the fluorophore and quencher [146, 283, 285].

In 1948, Theodor Förster introduced the theory of FRET, representing the first quantum theory that explains the distance-dependent resonance energy transfer from an excited fluorophore (donor) to a nearby acceptor (quencher) *via* a non-radiative pathway [286]. This process is usually accompanied by fluorescence quenching of the donor molecules and can be detected. The rate of fluorescence quenching is highly dependent on the separation distance between the donor and the corresponding acceptor [286, 287].

However, the term 'FRET' has subsequently been used to describe many processes that are dependent on the distance between the fluorescent/donor molecule and the corresponding quencher/acceptor, this term has been misused in studies where the fluorescence transfer/quenching was observed within distances longer than that described by Förster [288-291]. In spite of the widespread use of the FRET theory, this is not the only explanation for fluorescence energy transfer from a fluorescent donor to an acceptor within a certain distance. Many theories have been established to explain the distance-dependent fluorescence

transfer/quenching. The common factor in all of these theories is that the fluorescence of the donor molecule is quenched by an acceptor.

4.1.1.1. Förster (fluorescence) resonance energy transfer (FRET)

FRET is a distance-dependent physical process that describes the non-radiative transfer of electronic energy from an excited donor to a nearby acceptor, separated by a distance from 1 to 10 nm [150, 286]. The donor molecule is fluorescent whilst the acceptor molecule can be either another fluorophore or a quencher. The process can be monitored by measurement of the fluorescence quenching of the donor fluorophore or the increased fluorescence intensity of the fluorescent acceptor.

The mechanism of FRET is due to dipole-dipole (resonance) coupling between the donor and the acceptor molecules, occurring upon excitation of the donor fluorophore [283, 285]. According to Förster, the efficiency of energy transfer is dependent on many factors including the distance between the donor-acceptor pair, Förster radius, the extent of their spectral overlap, the conformational orientation of both the donor and the acceptor and the refractive index of the medium, as illustrated in **Equation 4.2** and **Equation 4.3** [150, 292].

$$E = \frac{R_0^6}{R_0^6 + r^6}$$ **Equation 4.2** [150, 292]

Where E is the efficiency of energy transfer, r is the distance between the donor and its corresponding acceptor and R_0 is the Förster radius at which the energy transfer is 50 %.

As shown in **Equation 4.2**, the efficiency of energy transfer is inversely proportional to the six power of the separation distance (r) between the donor and the corresponding acceptor whilst the most efficient energy transfer occurs when r becomes close to the value of R_0 for a given donor-acceptor pair. This limits the reliable detection of energy transfer to the range of $r = 0.5R_0$ (E = 98.5%) to $r = 2R_0$ (E = 1.5%), which consequently restricts the use of the FRET to detect molecules within a distance from ~3 to 7 nm (30-70 Å). This permits the application of the FRET as a molecular ruler for the determination of distances within the macromolecules and protein folding processes [293, 294]. In addition to the distance factor, the emission spectrum of the donor fluorophore must overlap with the excitation spectrum of the acceptor to allow the dipole-dipole coupling [146, 150, 295-297]. Further, the Förster radius (R_0), measured in angstroms (Å), depends on the dipole orientation factor of both the donor and acceptor (k^2), spectral overlap integral of the donor-acceptor pair (J(λ)), the refractive index of the medium (η) and fluorescence quantum yield of the donor in the absence of the acceptor (Q_D), as shown in **Equation 4.3** [150, 292]. **Figure 4.1** shows the spectral overlap between the emission spectrum of a donor molecule (D) with the absorption spectrum of a nearby acceptor (A), separated by a distance (r) and dependence of the efficiency of energy transfer on the separation distance [298].

$$R_0\ (\text{Å}) = 2.11 \times 10^{-2}.[k^2\ .J(\lambda).\eta^{-4}.Q_D]^{\frac{1}{6}} \qquad \textbf{Equation 4.3} \text{ [150, 292]}$$

Where R_0 is the Förster radius, k^2 is the dipole orientation factor, J(λ) is the spectral overlap integral, η is the refractive index of the medium and Q_D is the quantum yield of the fluorophore.

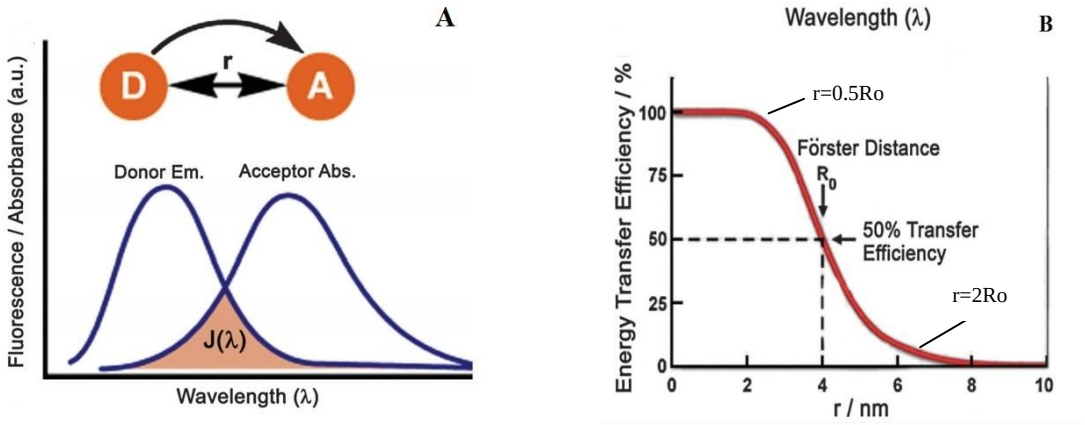


Figure 4.1: (A) Illustrative diagram shows the spectral overlap between the emission spectrum of a fluorescence donor (D) with the excitation spectrum of a nearby acceptor (A), separated by a specific distance (r) to achieve the FRET. (B) Effect of the separation distance between the donor–acceptor pair on the efficiency of energy transfer [298].

Many fluorescent donors and their corresponding acceptors have been extensively used in studies that utilising the FRET phenomenon as the design principle [299-301]. Until the last decade, fluorescent organic dyes were the most common acceptors that have been used in the FRET systems [58, 302, 303]. This increases the background noise and necessitates the use of complex filters to remove this noise [304, 305]. Commercially available non-fluorescent compounds, called black hole quenchers (BHQs), have been specifically designed to be used in the FRET assays instead of fluorescent acceptors [9, 306-308]. BHQs are molecules with a broad absorption profile that can absorb light within the same emission range of the donor molecules without re-emission of the absorbed light. Such molecules, BHQs, are assigned with numbers 1, 2 and 3 to illustrate their absorption range [309]. **Table 4.1** summarises some fluorescent dyes that have been used in biological applications and their corresponding commercially available BHQs that are used to establish a FRET.

Table 4.1: Fluorescent dyes that have been used in biological applications and their corresponding black hole quenchers (BHQs) that have been utilised to establish FRET pairing systems

Fluorescent Dye*	Corresponding BHQ	Absorption maxima of BHQ
OG, FAM, JOE and TET	BHQ1	534 nm
TAMRA, ROX, Cy3, CY3.5 and Red 640	BHQ2	579 nm
Cy5, Cy5.5	BHQ3	672 nm

*The corresponding commercial names (abbreviations) are used for the listed fluorophores.

In addition, luminescent semiconductor-QDs have recently been used as fluorescent donors in many FRET-based biosensors instead of using organic fluorophores [310-313]. Application of QDs in biological assays remains promising; however, there are some undesirable effects as previously discussed in Chapter 1 [78, 80]. Many other fluorescent donors such as green fluorescent protein, lanthanides and f-SNPs have been reported for the development of FRET systems [312, 314, 315].

Despite the extensive history of FRET and its applications, Förster theory is not the only explanation for distance-dependent fluorescence energy transfer. It is valuable to share the opinion of R. Clegg who published a comprehensive article on the full history of energy transfer, he stated: "*there are other modes of energy transfer, and circumstances where Förster transfer is not valid; these require different theoretical foundations. However, reserving "Förster" for the "F" in FRET, whenever we mean Förster transfer, gives credit to the person who made it possible for us to gain valuable, quantitative insight into so many processes at the molecular scale, through relatively easy experiments.*" [316].

4.1.1.2. Dexter energy transfer

Dexter energy transfer is another theory that explains the mechanism of fluorescence quenching between an excited donor fluorophore and a nearby acceptor. Dexter energy transfer differs greatly from the FRET in the distance scale and underlying mechanism. As represented in **Figure 4.2**, this process occurs through a non-radiative pathway due to the exchange of an excited electron of the donor molecule with another electron of the acceptor, accompanied by fluorescence quenching of the donor molecule [317].

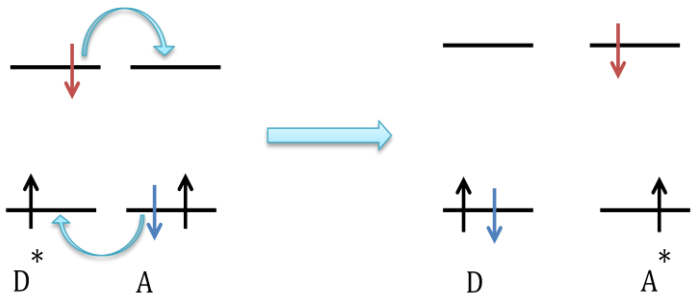


Figure 4.2: Illustrative diagram shows the mechanism of the Dexter electron exchange/transfer from an excited donor (D^*) to a nearby acceptor (A). Image was taken and modified from [318].

Unlike Förster model which is used to describe the resonance energy transfer within a distance from 1 to 10 nm (10-100 Å) *via* dipole-dipole coupling, Dexter energy transfer occurs at the very short distances that typically less than 1 nm (10 Å) [319]. Due to the electronic exchange over this short distance, the wavefunction (electron cloud) of the excited electron must overlap with that of the acceptor to allow the electronic exchange process [320].

4.1.1.3. Nanometal surface energy transfer (NSET)

The advances in nanoscience have contributed in fabrication of nanomaterials which exhibit new, interesting properties/phenomena that cannot be observed in the bulk material or individual atoms [89-91]. It is obvious that, using some of the established theories; such as the FRET, to explain these new properties/ phenomena is difficult and there is a need to revise such theories at this time.

NSET has been recently introduced to explain the energy transfer from a fluorescent organic dye molecule (donor) to a plasmonic noble metal nanoparticle (acceptor), separated by a longer distance than that reported for FRET [321-323]. NSET phenomenon can be observed within a distance up to 20 nm, which is almost twice the maximum distance of the typical FRET systems. Similar to the conventional FRET, the process of NSET can be assessed by recording the fluorescence quenching of the donor molecule [324]. The efficiency of energy transfer (E) of NSET depends on the inverse fourth power of the distance between the donor and acceptor (r) as shown in **Equation 4.4** [322, 325, 326].

$$E = \frac{1}{1 + \left[\frac{r}{r_0}\right]^4}$$ **Equation 4.4** [322, 327]

Where E is the efficiency of energy transfer, r is the separation distance between the donor and its corresponding acceptor and r_0 is the separation distance when the efficiency of energy transfer is 50%.

This enhanced efficiency of energy transfer, compared to that of the FRET, may be attributed to the interaction between the dipole of the excited donor fluorophore with the electromagnetic field of the conducting electrons that resonate around the plasmonic nanoparticle surface due to LSPR [322, 328]. Therefore, a small dipole in the excited fluorophore induces a large dipole in the nanoparticle, leading to an enhancement in the efficiency of energy transfer [322, 329].

Another suggested mechanism for the process of NSET is based on formation of electron-hole pairs near to the nanometal surface which allows the electronic energy transfer from the excited fluorophore to the nearby nanoparticle surface [330-332]. **Figure 4.3** is an illustrative diagram that shows the energy transfer from fluorophores to gold nanoparticles, separated by a specific distance. The process may occur due to the interaction of fluorophore dipole with the enhanced electromagnetic fields of the resonating electrons located close to the nanoparticle surface [329].

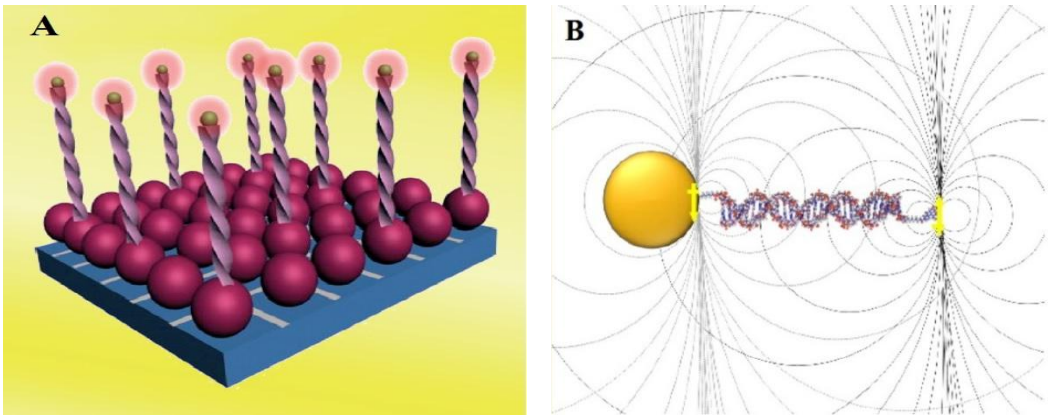


Figure 4.3: (A) Illustrative diagram shows the process of energy transfer from an excited fluorophore to a noble metal nanoparticles surface due to NSET [329]. (B) The dipole coupling of the excited fluorophore with electromagnetic field of gold nanoparticle, occurring due to LSPR [322].

However, previous reports have shown that the efficiency of NSET is dependent on the inverse fourth power of the distance between fluorophore and gold nanoparticle; other instances of enhanced energy transfer have been reported over this distance [332-335]. The Liu research group has discovered that the fluorescence quenching of QDs/DNA-core-shell structure was observed over a separation distance up to 70 nm. In addition, the efficiency of energy transfer was dependent on the 2.7^{th} power of the separation distance between the centre of QDs and the surface of gold nanoparticles [333]. Reineck et. al. have reported that the efficiency of energy transfer between fluorescent molecules and gold nanoparticles was observed within a separation distance up to 38 nm using silica shells as spacer/separator between the donor fluorophore and the nanoparticle surface [336]. Furthermore, the fluorescence quenching of QDs/silica shell was studied over a distance up to 150 nm using 13 nm gold nanoparticles as fluorescence quenchers [337]. In addition, f-SNPs and core-shell f-SNPs have been utilised as fluorescent donors to study the fluorescence quenching over different distances up to 50 nm while the quenchers were plasmonic nanoparticles [288, 289, 336, 338, 339]. Generally, NSET has been reported as a technique to study fluorescence energy transfer over distances up to 100 nm, which is almost 10 times like the distance of the conventional FRET [291, 327, 329, 332, 340, 341].

However while the utilisation of plain silica shells as spacers has improved the energy transfer over longer distances than that reported for typical FRET or NSET [336, 342]. The mechanism of this enhanced energy transfer/quenching is not fully understood and further investigations are required [336, 341, 342].

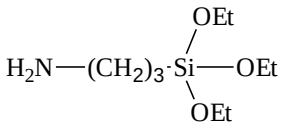
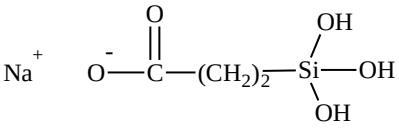
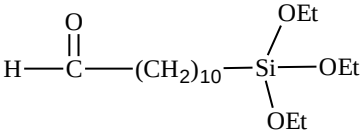
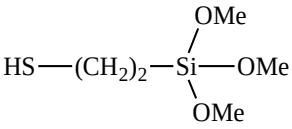
4.1.2. Functionalised silica nanoparticle as a versatile nanosensor platform

In many studies, DNA sequences have been used as spacers between the fluorescent donor and the corresponding acceptor to study the energy transfer over different distances [306, 343-345]. However when using DNA as a molecular spacer, the precise distance control is a challenge and the conductivity effect of DNA is still a matter of debate [336]. In contrast, when silica shells have been utilised as spacers, the distance between the donor and acceptor can be controlled [288, 289, 336-338, 346]. Additionally, using the silica shells as spacers has been established to provide a versatile surface that can be readily functionalised to permit further molecular conjugation.

4.1.2.1. Surface functionalisation of SNPs

The wide use of SNPs and core-shell SNPs as desirable platforms in nanosensor technology is attributed to the favoured surface chemistry of silane, biocompatibility, low toxicity and size control of silica [347-349]. Surface functionalisation of SNPs is performed to develop an active surface that can bind to several biomolecules, such as antibodies or aptamers, producing sensing platforms [180, 350-353]. Additionally, such functionalisation is used to increase the cellular uptake of the silica-based nanosensors, as previously discussed in Chapter 3. The most popular approach for surface modification of SNPs is *via* post-synthesis grafting of the required functional group based on a condensation reaction between the non-functionalised SNPs and another organosilane compound that carries the required functional group [348, 354]. Many commercially available organosilane derivatives have been reported for SNPs functionalisation and summarised in **Table 4.2**.

Table 4.2: Some commercially available organosilanes that have been used for surface functionalisation of SNPs [355]

Silane compound	**Chemical Structure**	**Group Added**	**Reactive towards**
(3-aminopropyl)-triethoxysilane (APTES)		Amine	NHS-ester Carboxylic acids Isothiocyanate
Carboxyethylsilane-triol sodium salt (CS)		Carboxylic acid	Amino groups EDC
11-(triethoxysilyl)-undecanal		Aldehyde	Secondary-amines Cyanide Nitriles
(3-mercaptopropyl) trimethoxysilane		Sulfahydryl	Maleimide

As shown in **Table 4.2**, APTES can be used to modify the surface of SNPs with amine group to facilitate further binding to carboxylic acid-containing molecules or NHS-biomolecules [356]. In addition, amino-SNPs were reacted with the activated ester of biotin (NHS-biotin) to develop biotin-functionalised SNPs capable of binding to streptavidin-biomolecules [171].

Further, carboxylic acid functionalised-SNPs (carboxy-SNPs) can be produced *via* the modification of SNPs with carboxy-silane derivatives, such as carboxyethyl-silanetriol sodium salt (CS). This modification has been extensively reported in many studies and is considered as the most common surface modification for

SNPs that has been reported [179, 351, 357-359]. Carboxy-SNPs are then used for binding the amine moiety of amino-containing biomolecules *via* formation of an amide bond as shown in **Figure 4.4** [180, 360-363].

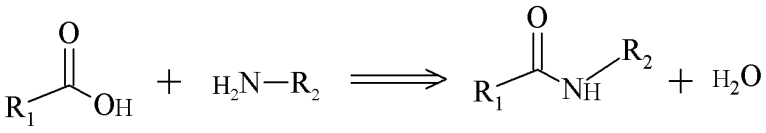


Figure 4.4: The classical reaction between a carboxylic acid group and amino-molecule.

This classical chemical reaction has been widely used for binding a carboxylic acid moiety; such as carboxy-SNPs, to amino-molecules. The efficiency of this reaction is, however, quite low and activation of the carboxylic acid groups prior to the reaction may be required; especially, when the concentration of the amino-molecules is low [363]. Generally, to increase the efficiency of this reaction, more reactive acid derivatives such as acid anhydride or acyl chloride are favoured instead of the carboxylic acid moiety [363-365].

1-Ethyl-3-(3-dimethylaminopropyl)-N'-carbodiimide hydrochloride (EDC) and N-hydroxysuccinimide (NHS) have been extensively used to mediate the formation of an amide bond between carboxylic acids and amines [363]. This activation technique is frequently used in particle and surface conjugation procedures, making this process the most popular activation technique in use today [363]. The EDC/NHS coupling chemistry is based on using the zero-length carbodiimide crosslinker (EDC) to activate the carboxylic acid group and form an amine reactive o-acylisourea intermediate that spontaneously reacts with the primary amine group to form an amide bond. Unfortunately, this reactive intermediate is highly unstable and rapidly hydrolysed in aqueous solutions [363]. To increase the reaction stability, water solubility and improve the efficiency of

conjugation, NHS or sulfo-NHS is coupled with EDC to react with the resultant unstable intermediate. This produces a stable NHS-ester intermediate that can react with an amine group with high efficiency [358, 363, 366]. **Figure 4.5** shows the activation reaction scheme of a carboxylic acid group using the EDC/sulfo-NHS coupling chemistry to form a stable intermediate that reacts with amino-molecule with high efficiency [363].

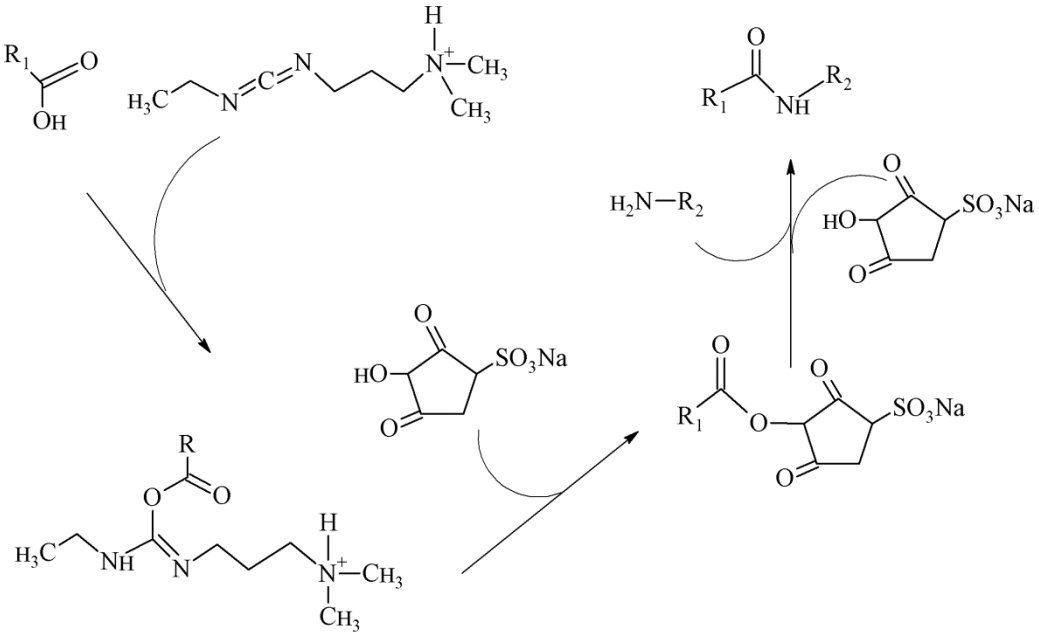


Figure 4.5: A schematic diagram for the chemical reaction between carboxylic acid containing molecule with amino-molecule using the EDC/sulfo-NHS coupling chemistry for the activation of the carboxylic acid group [363].

Further, EDC/NHS activation reaction is highly sensitive to the pH of the medium while the most efficient reaction occurs within pH from 4.7 to 6.0. Additionally, primary amine-free and carboxylate-free buffers, such as 2-(n-morpholino) ethanesulfonic acid (MES) buffer, with a pH from pH 5 to 6, is usually used as the medium for the activation reaction [363].

In addition to APTES and CS, other organosilanes such as triethoxypropyl-undecanal, 3-mercaptopropyl trimethoxysilane and various PEG-silanes are occasionally used for surface functionalisation of SNPs to add aldehyde, sulfahydryl group and PEG linker to SNPs surface, respectively [173, 367-371].

4.2. Aim

It is clear that, at the nanometre scale, some materials behave distinctly from the bulk or individual atoms [89-91]. Additionally, the energy generated during the fluorescence can be transferred over different distances depending on the type and properties of the fluorescent donor and the corresponding acceptor. Different examples of enhanced distance-dependent fluorescence transfer/quenching between f-SNPs/core-shell-SNPs and a nanometal surface have been reported [288, 289, 336-338, 346].

Until now, energy transfer or fluorescence quenching between f-SNPs, as fluorescent donors, and a non-metal molecular acceptor/quencher, such as BHQs, has not yet been studied. Herein, the overall aim of Chapter 4 is to investigate the fluorescence quenching of f-SNPs, over different distances, using BHQs as fluorescence quenchers.

The first aim of this Chapter is to prepare carboxy-SNPs that can bind to amino-containing molecules with high efficiency. The effect of the EDC/NHS activation process on the efficiency of binding is investigated and optimised. To achieve this, p-SNPs are used to optimise the factors that may affect the binding reaction.

The second aim is to utilise the optimised SNPs to prepare different models of TAMRA-SNPs and TAMRA-core-shell-SNPs; modified with carboxylic acid groups, to bind to amino-BHQ2, the selective non-metal quencher for TAMRA. These models are then used to investigate the fluorescence quenching of TAMRA after binding to BHQ2 using silica shells as spacers over different distances.

4.3. Experimental

4.3.1. Materials and chemicals

Fluorescein cadaverine; 5-(5-aminopentyl)thioureidylfluorescein dihydrobromide salt (amino-FAM) was obtained from Life Technologies, USA. Carboxyethyl-silanetriol sodium salt, 25 % g/g (CS) was purchased from abcrGmbH, Germany. 1-Ethyl-3-(3-dimethylaminopropyl)-N'-carbodiimide hydrochloride (EDC) and N-hydroxysuccinimide (NHS) were purchased from Sigma-Aldrich, UK. 2-(n-morpholino)ethanesulfonic acid (MES) was obtained from Fisher Scientific, UK and was used for the preparation of 0.2 M MES buffer at pH of 5.7, pH was adjusted using 0.1 M NaOH. Amino modified black hole quencher 1® (amino-BHQ1), succinimidyl ester derivative of BHQ1 and amino modified black hole quencher 2® (amino-BHQ2) were purchased from Biosearch Technologies, USA. The chemicals that were used for the synthesis of SNPs batches/models were previously described in Chapter 2.

4.3.2. Preparation of SNPs

The production of p-SNPs, TAMRA-SNPs or BHQ1-SNPs was performed using the optimised protocol that was detailed in Chapter 2 (page 44). Firstly, succinimidyl ester derivatives of either TAMRA or BHQ1 (1 mg) were dissolved separately into 1 mL of absolute ethanol and conjugated to certain volumes of APTES. The molar ratio of TAMRA or BHQ1 to APTES was 1:1.2. The reaction mixtures were stirred for 24 hours in the dark and then 100 µL of the conjugated TAMRA-APTES or BHQ1-APTES were used for the synthesis of TAMRA-SNPs or BHQ1-SNPs, respectively. The optimised protocol for the preparation of SNPs was then followed as described in Chapter 2.

4.3.3. Synthesis of core-shell TAMRA-SNPs [372]

Into separate scintillation vials, 10 mg of TAMRA-SNPs, with the size ~75 nm, were accurately weighed, suspended into 1 mL of absolute ethanol and sonicated for at least 30 minutes followed by the addition of either 30 µL or 50 µL of NH_4OH (28-30%). The mixtures were stirred for 30 minutes, followed by consecutive three additions of 17 µL of TEOS with 15 minutes time intervals between each addition. The vials with their contents were gently stirred for 24 hours and then the produced TAMRA-core-shell-SNPs were centrifuged and washed three times with 1 mL of PBS; pH 7.4, and used directly for surface functionalisation.

4.3.4. Surface functionalisation of SNPs with a carboxylic acid moiety [372]

10 mg of p-SNPs, TAMRA-SNPs or BHQ1-SNPs were suspended separately into 1 mL of PBS buffer and sonicated for 30 minutes while the suspensions of TAMRA-core-shell-SNPs, prepared as in the last step, were used directly. To functionalise the surfaces of all SNPs batches/models with a carboxylic acid moiety, 40 µL of CS was added to each scintillation vial containing the specified silica batch/model and the mixtures were gently stirred for 24 hours in the dark. Following this, the resultant carboxy-SNPs, produced using each batch/model, were centrifuged and washed with 1 mL of PBS. The last washing was performed with 1 mL of 0.2 M MES buffer at pH of 5.7 and the resulting nanoparticle suspensions, of all batches, were used for the EDC/NHS activation step.

4.3.5. Activation of carboxy-SNPs with EDC/NHS

30 µL of freshly prepared EDC and NHS solutions (500 mg/mL in 0.2 M MES buffer, pH 5.7) were added to each carboxy-SNPs batch/model, suspended in 0.2 M MES buffer. The reaction mixtures were gently stirred for 30 minutes followed by centrifugation and washing, three times with 1 mL PBS buffer. After the last wash, the suspensions of each sample were used for binding to amino-FAM or amino-BHQ2 in PBS buffer, pH 7.4.

4.3.6. Conjugation of the activated SNPs to amino-FAM or amino-BHQ2

The EDC/NHS activated p-SNPs, or BHQ1-SNPs were reacted with 20 µL of amino-FAM, prepared using 1 mg of amino-FAM, dissolved in 1 mL ethanol, while the suspensions of the activated TAMRA-SNPs and TAMRA-core-shell-SNPs were reacted with 120 µL (0.25 µmol) of amino-BHQ2 (1 mg/mL, prepared in ethanol). The mixtures were gently stirred for 24 hours followed by centrifugation and several washings with 1 mL of PBS. Following this, the produced SNPs, conjugated to amino-molecules, were directly used for the measurements of fluorescence intensity/quenching against blank samples of each batch, treated similarly.

4.3.7. Characterisation of SNPs models

DLS instrument was used to measure the hydrodynamic diameters and zeta potential values of the developed SNPs batches/models while eSEM was utilised to characterise the size and shape of the corresponding SNPs sample. Fluorescence measurements were performed using a Varian Cary Eclipse fluorescence spectrophotometer. The fluorescence intensity/quenching of amino-FAM was

recorded at 520 nm after excitation at 490 nm while the emission intensity/ quenching of TAMRA was measured at 575 nm after excitation at 550 nm.

4.3.8. Calibration of the optimised TAMRA-SNPs with amino-BHQ2

Different amounts of amino-BHQ2 which ranged from 0.02 µmole to 0.52 µmole (10 µL to 250 µL of 1 mg/mL) were reacted with the EDC/NHS activated TAMRA-SNPs (~10 mg/mL) for 24 hours, followed by centrifugation and washing. Following this, the fluorescence signals/quenching of TAMRA-SNPs after binding to amino-BHQ2 were recorded against blank TAMRA-SNPs samples, treated similarly without the reaction with amino-BHQ2.

4.4. Results and discussion

In this study, the surfaces of SNPs were utilised to bind amine-containing molecules. The binding reaction was based on surface functionalisation of SNPs with carboxylic acid groups to prepare carboxy-SNPs, providing a surface that could be conjugated to amino-molecules *via* an amide bond. In order to establish an efficient procedure for this binding, p-SNPs were firstly used and conjugated to amino-FAM to optimise factors that may influence the efficiency of binding. Once this efficient binding is achieved, TAMRA-SNPs and TAMRA-core-shell SNPs were prepared and conjugated to amino-BHQ2, using the optimised protocol, to investigate the process of fluorescence quenching over different distances.

4.4.1. Optimisation of the binding reaction between p-SNPs and amino-molecule

4.4.1.1. Production of carboxy-SNPs [372]

Initial experiments for the surface functionalisation of SNPs were performed using p-SNPs, with the size range of ~85 nm prepared and characterised as previously described in Chapter 2. CS was utilised as a silane derivative which is able to add a carboxylic acid moiety to the surface of p-SNPs, producing carboxy-p-SNPs [372]. Measurements of the zeta potential values were used to evaluate this surface functionalisation. The results revealed that the zeta potential value of unmodified p-SNPs was ~ -31±5 mV. As shown in **Figure 4.6**, this value significantly increased in the negative direction to -55±3 mV after CS modification, indicating the successful surface functionalisation of p-SNPs with

the carboxylic acid groups. In addition, this modification step did not markedly influence the size of SNPs as the measured hydrodynamic diameters of carboxy-SNPs were 91±9 nm which is almost in the same size range of the unmodified p-SNPs.

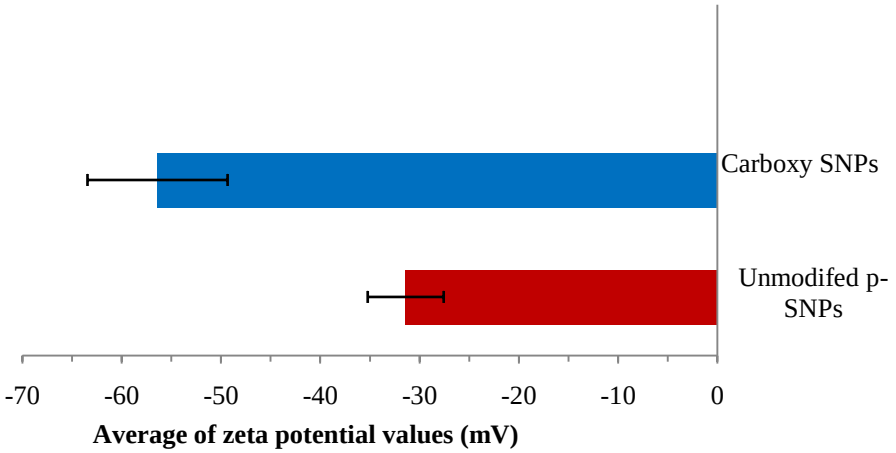


Figure 4.6: The average of zeta potential values of unmodified p-SNPs and carboxy-SNPs, prepared using CS.

To optimise the best amount of CS that is required for maximum surface modification, different amounts of CS (25% w/w), ranging from 0.0336 mmol to 0.336 mmol (20 µL to 200 µL), were utilised for surface functionalisation of p-SNPs. The zeta potential values of the resulting carboxy-p-SNPs were measured before and after functionalisation of p-SNPs with the corresponding CS quantity. The results showed that varying amounts of CS did not significantly affect the zeta potential value of the produced carboxy-SNPs as this value remind at about -55±8 mV for all carobxy-SNPs, produced after functionalisation of p-SNPs using the studied amounts of CS (**Figure 4.7**). The obtained results were in agreement to that found in the literature which concluded that the varying amounts of CS did not markedly influence the functionalisation process [173, 372]. These results suggest that the surface of SNPs could be saturated with the carboxylic acid

moiety using this concentration range of CS. As a result, for surface functionalisation of SNPs with carboxylic acid groups, 0.067 mmol (40 µL) of CS (25% w/w) was used as the optimum amount of CS and was used for all the further experiments.

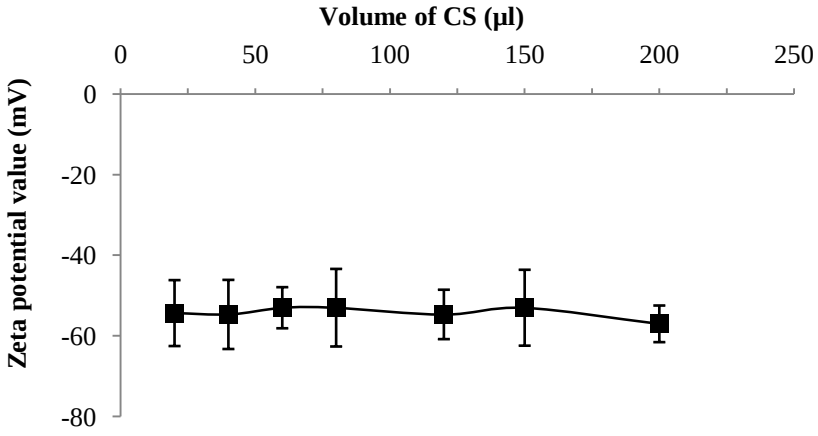


Figure 4.7: The effect of varying amounts of CS on the zeta potential value of the produced carboxy-SNPs using different CS quantities.

4.4.1.2. Binding of carboxy-p-SNPs to amino-FAM without EDC/NHS activation

It has been reported that; prior to the binding of a carboxylic acid moiety to amine-containing molecule, activation of the carboxylic acid group using the EDC/NHS coupling chemistry is favoured to form a highly active intermediate that can bind to amine- containing molecules with high efficiency [180, 373, 374]. In this study, the effect of the EDC/NHS activation on the binding of carboxy-SNPs to amino-molecules has been studied. Firstly, the surface of carboxy-p-SNPs was utilised to bind to amino-FAM without the EDC/NHS activation. The fluorescence intensity of amino-FAM was measured before and after binding to carboxy-p-SNPs. The efficiency of binding was calculated using **Equation 4.5**.

$$\%\ of\ Binding\ = \frac{F_B}{F_T} \times 100$$ **Equation 4.5**

Where F_B is the fluorescence intensity of the bound amino-FAM to carboxy-p-SNPs and F_T is the fluorescence intensity of the total amino-FAM before binding.

After the reaction, the nanoparticles were collected by centrifugation and then the fluorescence intensity of amino-FAM molecules that were linked to carboxy-p-SNPs was measured in the nanoparticle suspension while the fluorescence of the unbound free amino-FAM was recorded in the supernatant, resulted from nanoparticle separation. The results revealed that the majority of amino-FAM molecules did not bind to carboxy-p-SNPs that were prepared without the EDC/NHS activation. As shown in **Figure 4.8**, the fluorescence intensity of amino-FAM molecules that were linked to p-SNPs, measured in the nanoparticle suspension, did not exceed 15% of the total fluorescence intensity of amino-FAM (blank), recorded before the reaction with carboy-p-SNPs. Whilst, the fluorescence intensity of the unbound amino-FAM, detected in the supernatant, was almost 70-80% of the original fluorescence intensity of amino-FAM, measured before the reaction. Additionally, increasing the concentrations of amino-FAM did not improve the percentage of binding as it remained at this level. These results may indicate that the carboxylic acid groups, grafted onto the nanoparticle surface, were not reactive enough to bind amino-FAM with sufficient efficiency. These results reflect that the efficiency of binding of amino-molecule to carboxy-SNPs, prepared without the EDC/NHS, will not exceed 15% and activation of the carboxylic acid groups may be required to improve the reaction efficiency.

4.4.1.3. Binding of carboxy-p-SNPs to amino-FAM after EDC/NHS activation

The binding reaction between amino-FAM and carboy-p-SNPs was studied after activation of carboxy-p-SNPs using the EDC/NHS coupling chemistry. The same concentration of amino-FAM, utilised to investigate the binding of carboxy-p-SNPs without EDC/NHS activation, was used. A similar protocol for the nanoparticle separation and fluorescence measurements were performed as previously described for the reaction without the EDC/NHS activation.

The results showed that a significant increase in the fluorescence intensity of the linked amino-FAM, measured in the nanoparticle suspension, was observed after binding to the EDC/NHS-activated p-SNPs. The fluorescence intensity of amino-FAM, measured after conjugation to the EDC/NHS activated SNPs was ~70% of the fluorescence intensity of the total amino-FAM, recorded in the solution prior to the reaction. This indicates that the percentage of the linked amino-FAM to the EDC/NHS activated carboxy-p-SNPs and hence, the efficiency of binding was ~70% as in **Figure 4.8**.

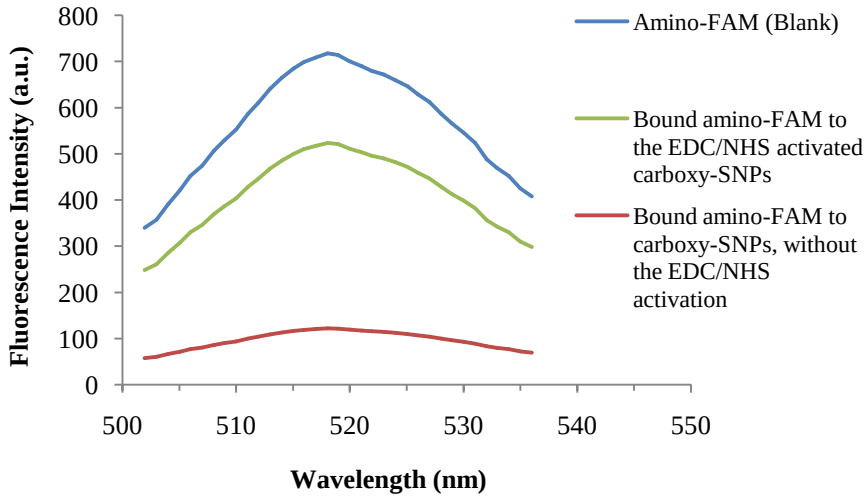


Figure 4.8: The fluorescence spectra of amino-FAM, measured in solution prior to the binding with SNPs (blank, blue line), after binding to carboxy-p-SNPs, prepared without the EDC/NHS activation (red line) and after binding to the EDC/NHS activated carboxy-p-SNPs (green line).

This improved binding efficiency, resulting after the EDC/NHS activation, demonstrates the importance of this activation process for the conjugation of amino-molecules to SNPs surface. As a result, the EDC/NHS activation process was utilised to bind amino-molecules to the surface of carboxy-SNPs.

Further, varying concentrations of either EDC or NHS did not influence the efficiency of this binding which could indicate that the utilised concentrations of EDC and NHS exceeded the required concentration to activate all or most of the carboxylic acid groups, grafted onto the surface of SNPs.

4.4.2. Study of fluorescence quenching process using TAMRA-SNPs models

The optimised procedure for the binding of amino-molecules to the EDC/NHS activated p-SNPs was further utilised for the conjugation of amino-BHQ2 to the surface of the EDC/NHS activated TAMRA-SNP. This was performed to study the fluorescence quenching or fluorescence energy transfer between TAMRA and BHQ2 molecules through silica matrix over different distances. In this study, three models of TAMRA-SNPs and TAMRA-core-shell-SNPs were prepared, characterised and linked to amino-BHQ2, using the optimised EDC/NHS protocol.

4.4.2.1. Production and characterisation of SNPs models

The optimised protocol that was described in Chapter 2 for the production of f-SNPs was followed to prepare TAMRA-SNPs with the size range of ~75 nm (Model 1) or BHQ1-SNPs, with the same size range of Model 1. Additionally, Model 1 was utilised to synthesis two further models of TAMRA-core-shell-SNPs. These core-shell models were produced through formation of plain silica shells with different thicknesses around Model 1 to produce TAMRA-core-shell-SNPs, encapsulating TAMRA molecules within their core and separated from BHQ2 over different distances, using silica shells as spacers. The hydrodynamic diameters and size range of these models were measured by DLS instrument and imaged by eSEM as shown in **Figure 4.9**. Model 2 consisted of ~25 nm plain silica shell@75 nm TAMRA-SNPs core, to produce TAMRA-core-shell-SNPs with a total diameter of ~100 nm, whilst Model 3 composed from ~50 nm plain silica shell@75 nm TAMRA-SNPs, producing TAMRA-core-shell-SNPs with a

total diameter of ~125 nm. **Figure 4.9** illustrates diagrams for the prepared models of TAMRA-SNPs and TAMRA-core-shell-SNPs, their measured hydrodynamic diameters and the corresponding eSEM image for each model.

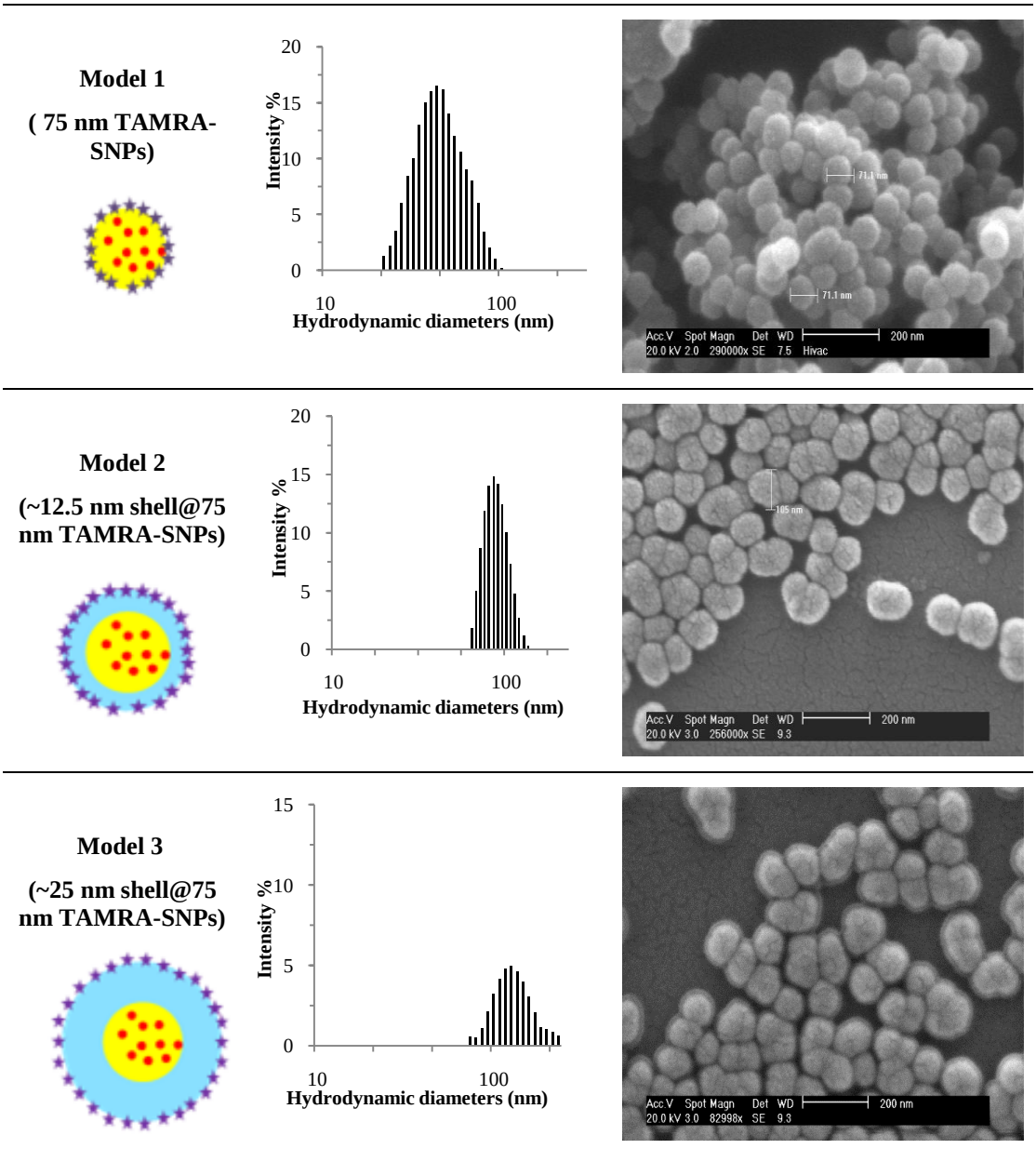


Figure 4.9: Illustrative diagrams represent the studied models (1, 2 and 3) and characterisation of these models by DLS and eSEM. The purple stars in the diagram represent the molecules of BHQ2 while the red dots represent TAMRA molecules. The blue circles around the diagram show the plain silica shells while the yellow circles represent the fluorescent nanoparticle or the fluorescent core.

The process of silica shell formation was based on using silica precursor (TEOS) and the catalyst, NH_4OH, to produce silanol monomers that could be condensed onto the surface of TAMRA-SNPs, producing silica shells around the fluorescent nanoparticles. Similar to the synthesis of SNPs, the shell thickness can be controlled by varying the concentration of NH_4OH, as discussed in Chapter 2. This concentration must be carefully selected to form a silica shell with a specific thickness around the nanoparticle [160, 372, 375, 376].

After the production of the aforementioned models, CS (25% w/w) was used to functionalise their surfaces with carboxylic acid groups, using the optimised procedure described earlier in this chapter for the surface modification of SNPs. The zeta potential value of each model was measured before the functionalisation which was in the range of -30 ±9 mV for all batches. This value was significantly decreased to ~ -50 mV after modification with CS which indicates successful surface functionalisation. Further, all the developed models were utilised to investigate the process of fluorescence quenching of TAMRA after binding to amino-BHQ2 using the EDC/NHS activation process.

However, accurate size-control of the silica shell in Model 2 and Model 3 was difficult and the resultant core-shell models were not perfect spheres as in **Figure 4.9**. These changes in nanoparticle shape and the surface area of Model 2 and Model 3 could influence the fluorescence quenching process due to variations in the number of the linked BHQ2 molecules to the nanoparticle surface. However, plain silica shells with different thickness have been synthesised around the nanoparticles as detected by DLS and confirmed by eSEM. The measured radii of these shells were greater than 10 nm which is beyond the Förster radius of FRET.

Further, the fluorescence quenching in this study was investigated for nanoparticle batches that contain the same amounts of TAMRA and not for individual nanoparticles. Therefore, such surface area and shape change could have minimum effect on the results discussed below.

4.4.2.2. Study of the fluorescence quenching process using Model 1

The fluorescence quenching/transfer process was firstly investigated using Model 1. In this study, TAMRA was utilised as a fluorescent donor while BHQ2 was used as the corresponding quencher/acceptor. TAMRA was selected as an exemplar pH-insensitive fluorophore that can emit light in the visible region at ~575 nm which greatly overlaps with the excitation spectrum of BHQ2, making BHQ2 a convenient quencher/acceptor for the emission of TAMRA.

To study the fluorescence quenching/transfer between TAMRA and BHQ2 throughout the silica matrix, the EDC/NHS activated Model 1 was conjugated to amino-BHQ2 using the optimised procedure, described in this chapter. The fluorescence intensity of Model 1 was recorded after binding to amino-BHQ2, against a blank sample of Model 1, treated similarly and prepared without binding to amino-BHQ2. The percentage of fluorescence quenching was calculated as the mean of the differences between the fluorescence intensity of TAMRA, recorded without BHQ2 binding (blank) and after binding to amino-BHQ2 using **Equation 4.6**.

$$\%\ of\ Q = \frac{F_b - F_q}{F_b} \times 100 \qquad \textbf{Equation 4.6}$$

Where % of Q is the percentage of fluorescence quenching, F_b is the fluorescence intensity of the studied model without binding to amino-BHQ2 and F_q is the fluorescence intensity of the studied model after covalently binding to BHQ2.

The results shown in **Figure 4.10** illustrate that a significant quenching of the fluorescence intensity of Model 1 was observed after binding to amino-BHQ2. The maximum percentage of fluorescence quenching was ~75% of the original fluorescence intensity of the blank sample of Model 1, prepared without binding to amino-BHQ2. In addition, the effect of varying amounts of amino-BHQ2 on the fluorescence quenching was investigated as in **Figure 4.10**. In these experiments, the same batch of Model 1 (10 mg/mL) was used, modified with CS, activated using the EDC/NHS and then linked to varying amounts of amino-BHQ2, ranging from 0.02 µmol to 0.52 µmol (10 µL to 250 µL of 1 mg/mL). The percentage of fluorescence quenching was calculated against blank samples, treated similarly and prepared without binding to BHQ2.

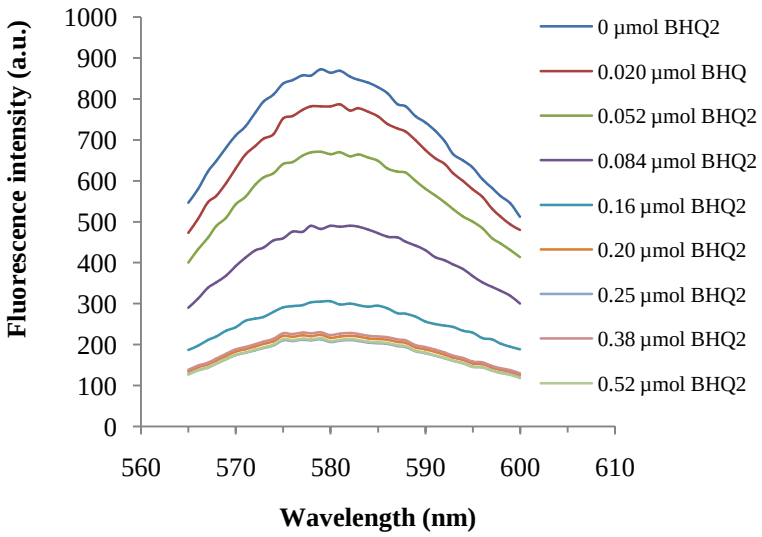


Figure 4.10: The fluorescence spectra of Model 1, prepared without binding to BHQ2 (top spectrum, blank) and after binding to different amounts of BHQ2 from 0.02 µmol to 0.52 µmol (all other spectra).

As shown in **Figure 4.10**, the fluorescence intensity of TAMRA molecules, encapsulated in Model 1, gradually decreased as the amount of BHQ2 was increased. Further increasing the amount of BHQ2 above 0.2 µmol (100 µL of 1 mg/mL) did not influence the percentage of fluorescence quenching as it reached the maximum level of about 75%. Such results indicate the dependence of the fluorescence quenching of TAMRA on the quantity of BHQ2. The relationship between the mean (n=5) of the percentage of quenching, resulting from Model 1, and BHQ2 amount was constructed. As represented in **Figure 4.11**, the percentage of TAMRA quenching gradually increased as the amount of amino-BHQ2 was increased from 0.02 µmol to 0.2 µmol (10 µL to 100 µL, 1 mg/mL) and then remained without significant changes as the amount of BHQ2 increased from 0.2 µmol to 0.52 µmol. The obtained relationship is similar to the typical Beer–Lamabert's calibration curve for the UV-visible measurements [377]. Therefore, 0.25 µmol (120 µL of 1 mg/mL) of amino-BHQ2 was used throughout this study as the optimum amino-BHQ2 amount that could achieve maximum fluorescence quenching (~75%) of the original fluorescence of Model 1.

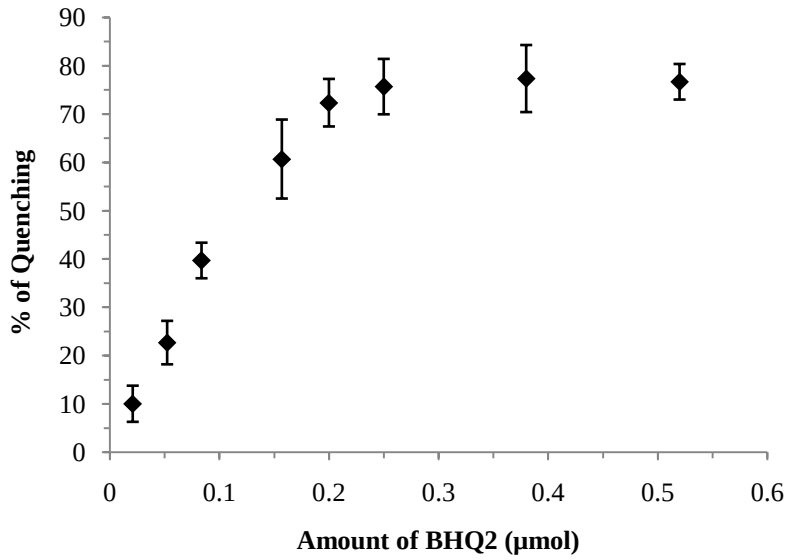


Figure 4.11: The relationship between the percentage of fluorescence quenching of Model 1 and different amounts of BHQ2, ranged from 0.02 to 0.52 µmol.

4.4.2.2.1. Effect of BHQ2 diffusion on the fluorescence quenching of Model 1

Investigations were made to study the effect of BHQ2 diffusion through silica matrix on the fluorescence quenching that was observed in Model 1. In these experiments, Model 1 was prepared without any surface functionalisation and stirred with amino-BHQ2 (0.25 µmol), for 24 hours, followed by centrifugation and washing of the nanoparticle suspension. The fluorescence signal/quenching of TAMRA, encapsulated in Model 1, was measured before and after the addition of amino-BHQ2 to the unmodified Model 1. As represented in **Figure 4.12** the measured fluorescence intensity of TAMRA was almost the same before and after the addition of BHQ2 to the unmodified Model 1, which indicates the negligible diffusion of BHQ2 molecules throughout the silica network. These results reflect that the florescence quenching that was observed in Model and previously demonstrated in **Figure 4.11** is due to the effect of the linked BHQ2 molecules to

the nanoparticle surface, not due to random diffusion of BHQ2 molecules through silica matrix.

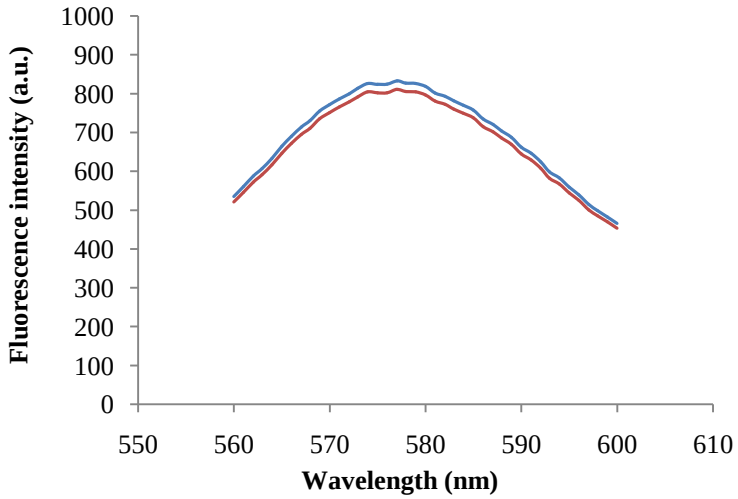


Figure 4.12: The fluorescence spectra of Model 1, prepared without surface modification or activation, measured before the addition of amino-BHQ2 (blue line) and after BHQ2 addition (red line).The nanoparticle suspension was stirred for 24 hours with the added BHQ2.

4.4.2.2.2. Effect of quencher type on the fluorescence quenching process

To study the effect of quencher type on the fluorescence quenching/transfer, BHQ1-SNPs, with a size of ~75 nm, were prepared and activated as described for Model 1 using the EDC/NHS process. BHQ1 is a molecular quencher that can absorb light in the range from 480 nm to 580 nm while the maximum wavelength at 534 nm. This makes BHQ1 an efficient quencher for the emission of FAM due to the spectral overlap of the emission spectrum of FAM with the excitation spectrum of BHQ1 [378]. In this work, amino-FAM was linked to the surface of the EDC/NHS activated BHQ1-SNPs. After nanoparticle separation, the fluorescence intensity/quenching of the linked amino-FAM was recorded in the nanoparticle suspension and compared to the fluorescence of amino-FAM; with the same concentration, conjugated to the surface of p-SNPs as a blank sample.

As shown in **Figure 4.13**, the difference between the fluorescence intensity of amino-FAM that attached to p-SNPs and those linked to BHQ1-SNPs; using the same concentration of amino-FAM, was ~90% which could be attributed to the FRET process. These results reveal that the fluorescence quenching process could be achieved between a fluorescent donor and a corresponding acceptor thorough the silica matrix regardless the type of the donor or the corresponding acceptor molecule.

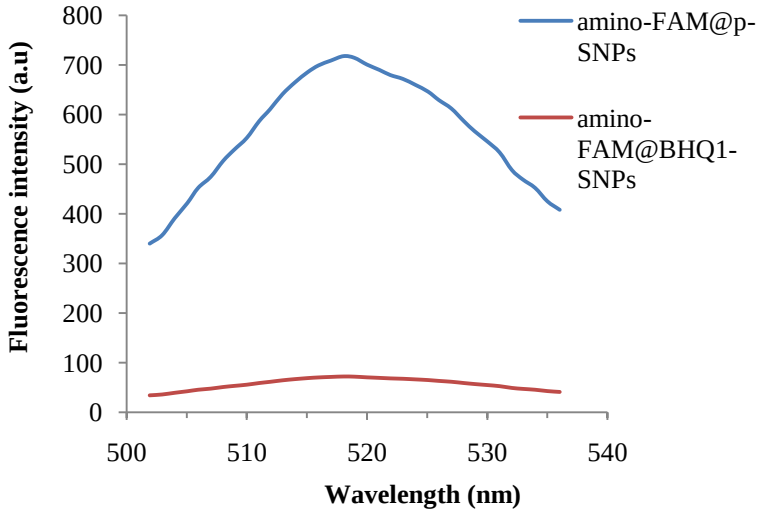


Figure 4.13: The fluorescence intensity of amino-FAM molecules after binding to BHQ1-SNPs (red spectrum) and p-SNPs (blue spectrum).

4.4.2.3. Study of fluorescence quenching process using core-shell-TAMRA-SNPs

Model 2 and Model 3 were prepared and utilised to investigate the fluorescence quenching of TAMRA molecules, encapsulated within the fluorescent core, and BHQ2 over different distances using silica shells as spacers. The production of Model 2 and Model 3 was based on utilising the same batch of Model 1 that was previously used to investigate the fluorescence quenching of TAMRA using Model 1. The same nanoparticle batch was used to minimise any batch to batch variation and prepare TAMRA-core-shell-SNPs, incorporating the same amount of TAMRA molecules as in Model 1. Furthermore, the same number of centrifugation and washing cycles was performed throughout these experiments to minimise any errors that may result due to loss of nanoparticles.

The fluorescence quenching of TAMRA in Model 2 and Model 3 was studies after their binding to amino-BHQ2 (0.25 µmole), using the EDC/NHS chemistry. The percentages of fluorescence quenching of Model 2 and Model 3 were calculated using **Equation 4.6** after their binding to BHQ2, and compared to blank samples of each model. As shown in **Figure 4.14** and summarised in **Table 4.3**, the percentage of fluorescence intensity of TAMRA was significantly reduced using these two models due to the effect of BHQ2. Maximum fluorescence quenching with the percentage of ~45% or 25% was obtained using Model 2 or Model 3, respectively. Additionally, increasing BHQ2 amounts above 0.25 µmol did not influence these percentages of quenching. **Figure 4.14** shows the fluorescence spectra of the developed models, measured after their binding to

BHQ2 and compared to the corresponding blank sample, where no BHQ2 was conjugated.

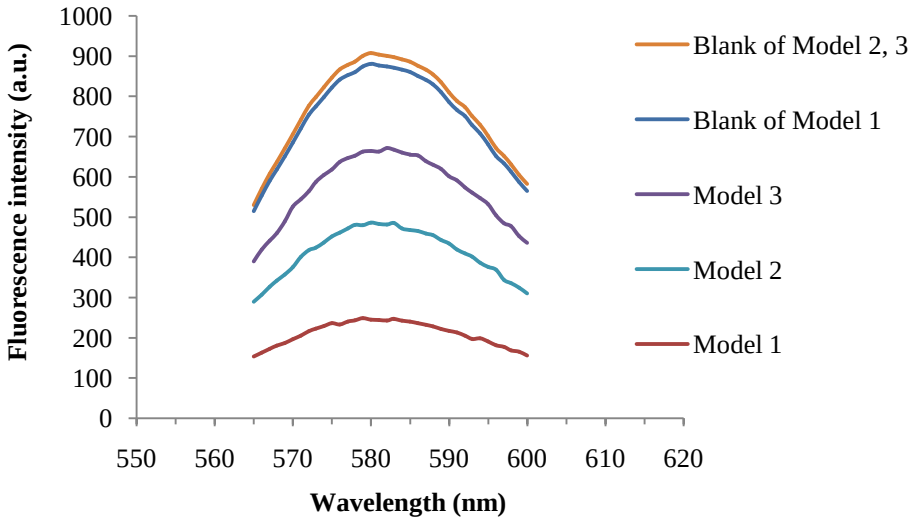
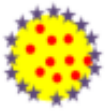
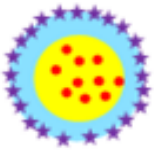
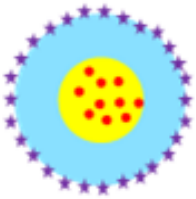


Figure 4.14: The fluorescence intensities of different models of TAMRA-SNPs and TAMRA-core-shell-SNPs after binding to BHQ2 (0.25 µmol), using different separation distances, and compared to the corresponding blank where no BHQ2 was bound.

In comparison to Model 1, the surface areas of Model 2 and Model 3 were different, which means that the number of BHQ2 molecules that could bind to the surface of these models were not be the same as that bound to Model 1. However, the obtained results suggest that the surface of these models probably was saturated with amino-BHQ2 (0.25 µmol) as the percentage of quenching did not significantly change upon increasing the quantity of BHQ2 above the optimised amount (0.25 µmol). **Table 4.3** summarises the fluorescence quenching study using the studied different models of SNPs.

Table 4.3: A summary for the fluorescence quenching study using different models of TAMRA-SNPs and TAMRA-core-shell-SNPs

Model Name	Model 1	Model 2	Model 3
Illustrative diagram			
Approximate diameters	~75 nm	~100 nm	~125 nm
Composition	TAMRA-SNPs	25 nm plain shell@75 nm TAMRA-SNPs	50 nm plain shell@75nm TAMRA-SNPs
Approximate separation distance from the centre of TAMRA and BHQ2	37.5 nm	50 nm (37.5 nm + 12.5 nm)	62.5 nm (37.5 nm+ 25 nm)
Fluorescence quenching (%)	75%	45%	25%

4.4.2.4. Explanation of the fluorescence quenching process using silica models

In the present work, the developed silica models were prepared using the same batch of TAMRA-SNPs to produce different models that incorporating approximately the same amounts of TAMRA molecules. In addition, the same quantity of BHQ2 (0.25 µmol) was utilised to study the fluorescence quenching of TAMRA over different distances using silica shells as spacers. The results revealed that maximum fluorescence quenching with percentages of about 75%, 45% and 25% were obtained for Model 1, Model 2 and Model 3, respectively. Further, increasing the amount of amino-BHQ2 above 0.25 µmol did not markedly affect the percentage of quenching as shown in **Figure 4.10 and Figure 4.11** for Model 1. Additionally, a negligible effect of BHQ2 diffusion through the silica matrix was observed as illustrated in **Figure 4.12**.

At first glance, the percentage of fluorescence quenching (75%) that was observed in Model 1 could be attributed to reabsorption of the emission of TAMRA by BHQ2. However, the fluorescence quenching that resulting from Model 2 and Model 3 caused a rethink of this explanation to take into consideration the improved fluorescence quenching over long distances that was reported when silica was utilised as spacer between fluorophore and noble-metal nanoparticle surface or QDs [288, 289, 336-338, 346].

As the distance (radius) between the centres of Model 1 and BHQ2, attached to the surface, is ~37.5 nm. This distance is approximately four times as the distance that is required for typical FRET. However, the fluorescence quenching that was observed using such model can be explained by FRET as the observed quenching could be resulting from the 10 nm distance closest to the nanoparticle surface.

In Model 2 and Model 3, the scenario is completely different where TAMRA molecules were separated from BHQ2 by silica shells with radii of 12.5 nm and 25 nm (12.5 nm × 2), respectively. The obtained percentage of fluorescence quenching was about 45% and 25% for Model 2 and Model 3, respectively. However, it is supposed that the amount of TAMRA and BHQ2 were almost the same in all models. The only difference between such models was the separation distance between TAMRA and BHQ2. Therefore, changes in the fluorescence quenching of TAMRA using the studied models could be attributed to the difference in the separation distance between TAMRA and BHQ2 using silica as spacer.

Because the separation distances in Model 2 and Model 3 were over the 10 nm barrier of the conventional FRET. Therefore, it is not appropriate to use the Förster theory to explain the fluorescence quenching, occurred in these two models. Meanwhile, previously reported studies have shown some examples of improved fluorescence energy transfer/quenching between a fluorophore and a noble-metal nanoparticle over extended distances up to 40 nm. Such improved quenching was observed only when silica shells were used as spacers between the donor and the corresponding quencher gold nanoparticles; however, all these studied attributed the observed energy transfer/fluorescence quenching to the plasmonic properties of the noble-metal nanoparticles rather than silica [336-339]. However, the role that silica may play to improve the process of fluorescence transfer/quenching is not yet fully understood or proven. According to the obtained results in this study, the fluorescence quenching, resulting from Model 2 and Model 3, can now be identified in more details and could be attributed to the potential role of silica to enhance the fluorescence transfer/quenching over

extended distances. Additionally, the percentage of fluorescence quenching (75%) using Model 1 can be explained by a FRET, which could be produced within the 10 nm near to the nanoparticle surface, plus the other hypothesis that was used to explain the process in Model 2 and Model 3.

Despite the maximum percentage of quenching of Model 1 did not reach 100%, even when high concentration of BHQ2 was used. This may indicate that not all the total distance between the nanoparticle centre and the surface (~37.5 nm) was involved in the process as there were some TAMRA molecules, located close to the centre of Model 1, may not be affected by the BHQ2 molecules.

4.5. Conclusion

In this study, surface modification of SNPs with a carboxylic acid moiety was performed and the resultant carboxy-SNPs were utilised for further conjugation to amino-molecules. The efficiency of binding of carboxy-SNPs to amino-molecules was improved upon activation the surface of carboxy-SNPs with EDC/NHS prior to binding the amino-molecules. The results revealed that the efficiency of binding of carboxy-SNPs to amino-molecules was ~15% when amino-molecules linked to carboxy-SNPs, prepared without the EDC/NHS activation process. Whilst using the EDC/NHS coupling chemistry improved the efficiency of binding to about 70%.

Using the optimised protocol for the binding of amino-molecules to carboxy-SNPs, the study was extended to investigate the process of fluorescence quenching of TAMRA-SNPs after binding to amino-BHQ2. Three different models of TAMRA-SNPs (75 nm, Model 1) and TAMRA-core-shell-SNPs; composed of either 25 nm or 50 nm plain silica shells@75 nm TAMRA-SNPs-core, were prepared. The size control of the silica shells thickness was successfully achieved. In addition, the EDC/NHS activation was utilised to activate the developed models which were then attached to amino-BHQ2 to study the fluorescence quenching/transfer of TAMRA through silica matrix over different distances. The results showed that a distance-dependent fluorescence quenching between TAMRA molecules and BHQ2 could be achieved and a maximum fluorescence quenching was obtained. Furthermore, the relationship

between the percentage of fluorescence quenching and BHQ2 concentration was established.

The effects of BHQ2 diffusion through the silica matrix and type of donor/acceptor pair on the process of fluorescence quenching were studies. The results showed that there was no diffusion of BHQ2 through the silica matrix and hence, the observed fluorescence quenching is attributed to the attached BHQ2 to the surface of TAMRA-SNPs. In addition, the type of the fluorescent donor or the quencher did not influence the process of quenching.

Maximum fluorescence quenching of ~75%, 45% and 25% were obtained after binding of the developed models to 0.25 µmol of amino-BHQ2, using EDC/NHS. Overall, the obtained results may indicate that using silica shells as spacers improved the fluorescence quenching process over extended distances beyond the 10 nm barrier of the typical FRET. However the hypothesis for this enhanced fluorescence quenching over this extended distance is not yet clear. In conclusion, this study showed interesting results of fluorescence quenching/transfer between TAMRA-SNPs and BHQ2 over extended distances for the first time.

Chapter Five

Aptamer-based fluorescent nanosensors for the quantitative assay of DNA hybridisation and interferon gamma

5.1. Introduction

5.1.1. Aptamers

Aptamers are artificial single stranded oligonucleotide sequences (DNA or RNA) that can bind to many targets, including drugs, proteins, nucleic acids, viruses, bacteria or even whole cells, with high affinity and specificity [379]. Aptamers are typically less than 100 mer, selected *in-vitro* from a random library of oligonucleotides that comprised of approximately 10^{12}-10^{14} oligonucleotide sequences by the process of SELEX (systematic evolution of ligands by exponential enrichment). The SELEX process has been patented in 1990 as a method for the identification and production of unique oligonucleotide sequences (aptamers) that have high binding affinity to specific targets [379-383].

However, the full mechanism of aptamer-target binding is not completely known; this could be attributed to the capability of aptamers to fold upon binding to incorporate the small molecules into their nucleic acid structure or integrate into the structure of large molecules. Additionally, aptamers may recognise and bind the corresponding target through structural recognition, a process similar to antigen-antibody recognition as shown in **Figure 5.1** [384].

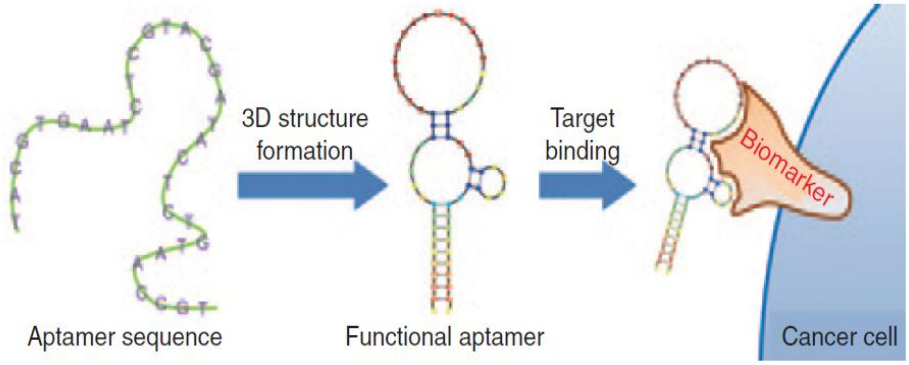


Figure 5.1: A schematic diagram shows the aptamer folding upon binding to a specific biomarker on a cell surface [384].

The affinity of aptamer binding is determined by the dissociation constant (K_d) of aptamer-target complex which is typically in the range of μM to pM. This makes the sensitivity of aptamer binding comparable to that of some monoclonal antibodies and thus, aptamers have also become known as 'chemical antibodies' [384, 385].

Aptamers have several attractive advantages over antibodies which make them very promising ligands to replace the use of antibodies in analytical and diagnostic methods [382, 386, 387]. A significant advantage of aptamers is their *in-vitro* production without the involvement of animals. Therefore a low-cost production, little batch-to-batch variation and production of specific ligands for toxic materials can be achieved. Furthermore, aptamers have considerable resistance to thermal and chemical denaturation, permitting prolonged shelf-life and long-term storage stability. In addition, aptamers elicit little or no immunogenicity to the cellular system [379, 382, 388, 389]. Due to these advantageous characteristics, aptamers have been used in many investigations for therapeutic and biological applications [384, 388, 390-392]. The Food and Drug Administration (FDA) has approved a number of aptamers as therapeutic agents for the treatment of some diseases based on aptamer affinity properties [393]. Furthermore, many aptamers are in the process of clinical trials for the treatment of diseases such as solid tumours, acute myeloid leukaemia, age related diseases and other chronic diseases [384, 393, 394].

5.1.2. Aptamers; the future sensing probes (aptasensors)

The utilisation of aptamers as binding ligands in biological assays has become of high interest in several analytical applications during the last decade. Currently, reports that describe the development of aptamer-based biosensors (aptasensors) for chemical and biological measurements are almost published on a weekly basis [382, 386, 387]. The use of aptamers in biological assays removes the need to use multiple reagents and several washing steps, associated with the antibody-based biosensors. Accordingly, aptasensors may provide rapid and reliable analytical tools that can be applied to detect the target in real-time [395].

Varieties of electrochemical, fluorescent, luminescent or SPR-based aptasensors have been reported for multiple analytical and biological measurements. Particularly, electrochemical and FRET-based aptasensors have been extensively reported for the analytical assays [343, 360, 396-400]. The simplest approach for the development of aptasensors is to detect the DNA hybridisation process, as shown in **Figure 5.2** which represents an example for a FRET-based aptasensor (molecular beacon) for the detection of a DNA hybridisation [324, 401, 402].

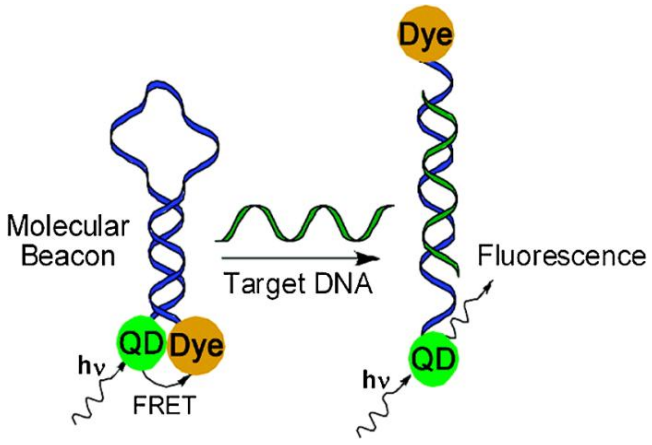


Figure 5.2: A schematic diagram for a FRET-based aptasensor (molecular beacon) that has been reported for the quantitative detection of DNA hybridisation process [401].

In this type of aptasensor, a single stranded DNA (ssDNA) aptamer is labelled with a fluorescent donor at one end while the other end is attached to a corresponding acceptor/quencher. Both ends of this oligonucleotide sequence are complementary to each other and can be hybridised together to form the hairpin or stem-loop DNA structure (molecular beacon) and initiate a FRET process [288, 403]. Upon hybridisation of the target DNA (complementary ssDNA), conformational changes occur which leads to opening of this stem-loop structure, increasing the distance between the donor-acceptor pair. As a result, the fluorescence of the donor, corresponding to the concentration of the hybridised target DNA, is restored and used for quantification [401].

Similar approaches for the development of electrochemical aptasensors for the detection of complementary DNA sequence or target protein have been reported [404-407]. The aptamers are attached to an electroconductive surface, such as gold electrode, at one end while the other complementary end is labelled with a redox tag, such as methylene blue, to allow the passage of electrical current. In the presence of the target molecule (DNA or protein), this hairpin structure is unfolded, pushing the redox tag away from the electro-active surface to alter the electron transfer process (**Figure 5.3**). The recorded changes in the redox current, resulting upon target binding, are used for the quantitative determination of the target analyte [408].

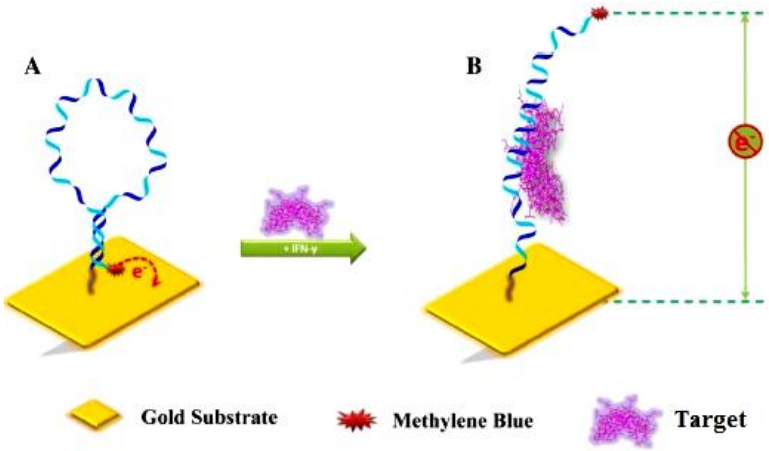


Figure 5.3: Illustrative diagram for an electrochemical aptasensor that has been reported for the detection of a target protein. Image was modified from [408].

In addition to using the aptamer hairpin structural switching as a mechanism for the measurement, other sensing strategies have been reported based on displacement reactions or competitive assays [383, 397, 409, 410]. In these systems, the aptamer is attached to a fluorescent donor or an electro-active surface and then hybridised with a short partial complementary oligonucleotide segment that carrying a corresponding quencher or a redox tag to alter the recorded signal. Upon the target binding, the short oligonucleotide segment, carrying the quencher or the redox tag, is displaced and the recorded signal is changed, corresponding to the target concentration. **Figure 5.4** represents a schematic diagram of a FRET-based aptasensor that has been reported for the detection of thrombin using the displacement mechanism as the principle for the assay [410].

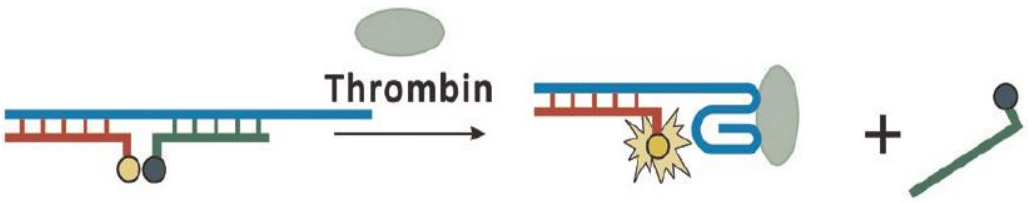


Figure 5.4: A schematic diagram illustrates the use of a FRET-based aptasensor for thrombin detection, as a model protein, based on the displacement of the quenching DNA segment upon thrombin binding [410].

Due to the high affinity of binding and advantageous use of aptamers, aptasensors have been developed for the detection of biological markers and chemical compounds, including DNA sequences, copper, ATP, thrombin, cocaine, bacteria, viruses and cancerous cells [351, 389, 392, 411-418]. Recently cytokines, one of the most important biological and disease biomarkers, have been detected using the corresponding aptamers for molecular recognition. The importance of cytokines and the current analytical methods for their detection are illustrated on the following section.

5.1.3. Cytokines; the signalling biomarkers

Cytokines are cell signalling carriers that affecting nearly every biological process including embryonic development, disease progression, cell differentiation and mediate the immune response of the body. Furthermore, cytokines play vital roles in the progress of the degenerative processes of aging, cancer development and efficiency of vaccines [419].

Cytokines are water soluble endogenous proteins or glycoproteins, with molecular weights of ~10–30 kDa and produced mainly by leukocytes; the cells of the immune system. Most cytokines have a multifunctional biological activity and act primarily as inflammatory mediators, growth promoters for cells including cancerous cells, and defend against pathogens [420, 421]. Because the cytokines are not structural proteins, their biological properties were and are still used for defining the corresponding cytokine. Scientists agreed to use the term ‘interleukins’ to describe the cytokines that are assumed to be primarily targeting the leukocytes. However, it has emerged that interleukins did not target

leukocytes only and hence, the term interleukins is currently used to name and number a new cytokine whenever discovered [422].

Cytokines are released into the blood stream and bind to their corresponding cellular receptors, initiating series of intracellular reactions to stop and fight off the disease [423-425]. **Figure 5.5** illustrates the release and major functions of several cytokines [426].

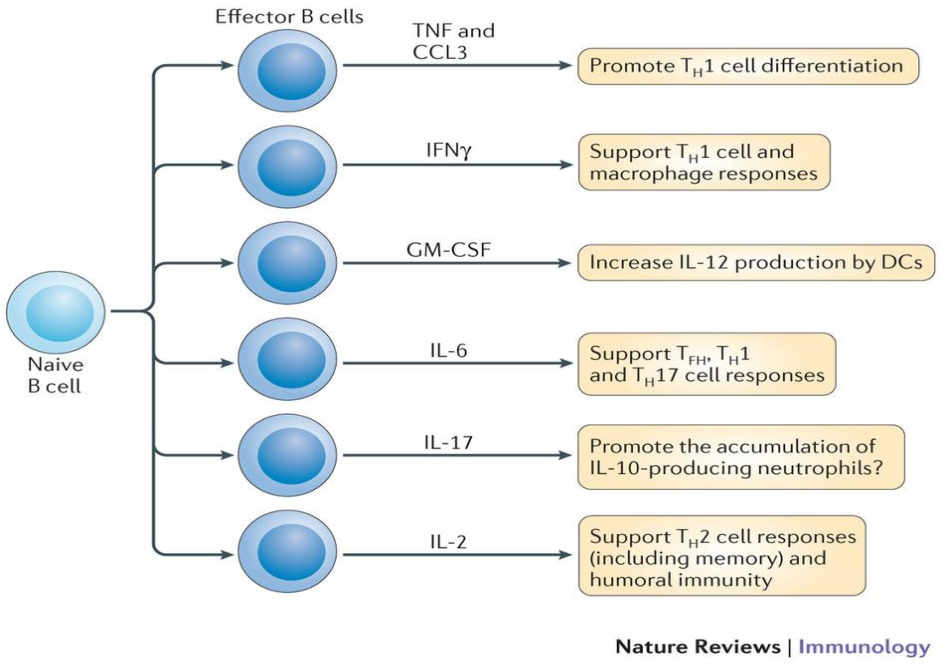


Figure 5.5: The activation, release and major functions of several cytokines [426].

Cytokines are classified into distinct sub-families depending on the type of the secreting-cell, corresponding functions and targets. The interleukins are the biggest family of cytokines with more than 30 subtypes. Each interleukin has a specific, distinct stimulatory, regulatory or inhibitory role, however, there are several interleukins that are involved in all or most of these functions [427]. While the term interleukins is used to describe the major types of cytokines, there are other kinds of cytokines that are not included in the interleukin family. The most prominent of these cytokines are interferons (IFNs), simply classified into IFN-α,

IFN-β, IFN-γ subtypes, secreted mainly by the macrophages and T- lymphocytes to stimulate the entire immune system in response to different pathogens. IFNs play major roles in cellular differentiation and division; one of the most important factors in cancer development [423]. Currently several IFNs, especially IFN-γ, have been approved for the treatment of diseases such as chronic viral hepatitis, genital warts, sclerosis and cancer [428-431].

5.1.4. The current methods for cytokine detection

During the past 25 years, cytokines have become important markers in biology and medicine for the diagnosis, prognosis and treatment of multiple diseases [419, 432]. Due to the vital roles that cytokines play in our life, many analytical methods have been reported for their detection. Generally, these methods can be classified into classical immunoassays, flow cytometry, biosensors, nanosensors and other methods.

5.1.4.1. Classical immunoassays for cytokines detection

ELISA, SI and enzyme-linked immunospot (ELISpot) are the most extensive methods that have been reported for the detection of many cytokines. These methods are based on using the corresponding primary antibodies to capture the cytokine of interest followed by the addition of enzyme-linked secondary antibodies, capable of binding to the target cytokine. Addition of the corresponding substrate for the linked enzyme produces UV/colour absorption or fluorescence signal that can be utilised for the sensitive and quantitative detection of the target cytokine. Several cytokines, including IL-1, IL-5, IL-6, IL-8, IL-33,

IFN-α, IFN-γ, macrophage inflammatory protein 1-beta (MIP-1β and tumour necrosis factor alpha (TNF-α), have been detected using the ELISA, SI or ELISpot methods [433-440]. **Figure 5.6** represents a schematic for enzyme-linked immunoassays for capturing and detection of a target protein using the corresponding antibody [441].

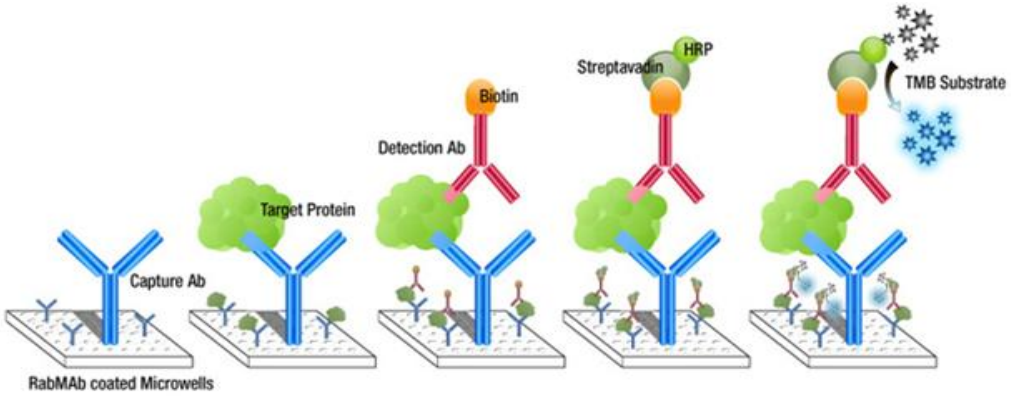


Figure 5.6: A schematic diagram shows the process of enzyme-linked immunoassay for the detection of a specific target protein using the corresponding antibodies for capturing and analysis [441].

Although immunoassays are considered as accurate, sensitive and versatile methods for the detection of wide varieties of biological compounds, including cytokines, they require long operational time and multiple manipulations which limit their application in the real-time assays [442-444].

5.1.4.2. Flow cytometric methods for cytokines detection

Flow cytometry is another technique that has been reported for the multiplexing detection of several cytokines using their corresponding fluorescent-labelled-antibodies [445]. Today, many kits are commercially available for the multiplexing measurements of cytokines using flow cytometry.

Antibodies, labelled with FTIC or Cy5, have been utilised for capturing of IL-2, IL-4, IL-5, IFN-γ and TNF-α, upon their release from stimulated leukocytes. Measurements of the fluorescence signal changes, corresponding to the analyte concentration, were performed using a flow cytometer [446, 447]. Further, ten different cytokines were estimated after binding to their corresponding fluorescent-labelled-monoclonal antibodies. In this method, the antibodies were coupled to the Luminex® microspheres to produce a multiplexing flow cytometric model for the detection of the target cytokines [448]. Similarly, fifteen cytokines, released from activated lymphocytes, have been detected by flow cytometry using their corresponding fluorescent-labelled-antibodies [449].

Despite flow cytometry has been used as accurate and sensitive technique for the detection of several biomarkers, including cytokines; this technique still has some limitations for clinical applications. Because flow cytometric measurements utilise cell suspensions to perform the assay within the suspended cells, therefore, this technique is not applicable in solid tissues or organs. In addition, the data resulting from flow cytometric assays is represented as aggregates, corresponding to the detected species, which is not appropriate to study or monitor individual cell behaviour. Furthermore, common problems, associated with the flow

cytometry, are the slow operation and massive data aggregation which require a skilled person to operate. Also, the flow cytometer is not that cheap to be used in the clinical/biological laboratories for daily use, especially, in the developing countries [450, 451].

5.1.4.3. Biosensors for cytokines detection

Biosensor technology has been reported for the development of several analytical tools for the detection of cytokines [452, 453]. Electrochemical biosensors have been developed for the detection of IL-10, IFN-γ and TNF-α using gold electrodes, modified with antibodies to capture the corresponding cytokine. The resultant changes in the recorded redox signal, occurred upon cytokine binding, have been used for the detection of the cytokine of interest [454, 455].

Further, the Revzin research group has developed many electrochemical biosensors for the detection of different cytokines using the corresponding aptamers as binding ligands. The sensing aptamers were firstly tagged with redox probes and then immobilised onto the surface of gold microelectrodes to develop aptasensors for the electrochemical detection of IFN-γ, TNF-α and transforming growth factor-β (TGF- β), released from the stimulated human leukocytes [408, 456-460].

Optical biosensors have been also described for the assay of several cytokines including IL-1β, IL-4, IL-6, IFN-γ, TNF-α and vascular endothelial growth factor (VEGF), using their corresponding antibodies [461, 462]. Fluorescent fibre-optic biosensors have been reported for the detection of IL-6 and IL-8 using their

corresponding antibodies for capturing of the corresponding cytokine [463-466]. The platelet derived growth factor (PDGF) was quantified using the selective fluorophore-labelled aptamer sequence which was immobilised onto a diamond surface to develop a FRET-based aptasensor for the analysis of PDGF [467]. Further, a FRET-based aptasensor has been reported for the detection of IFN-γ, utilising the aptamer hairpin structure switching as the mechanism for the assay [468, 469].

In addition, label-free biosensors such as SPR, SERS and quartz crystal microbalance (acoustic) biosensors have been developed for the detection of several cytokines [470, 471]. Human IFN-γ, IL-6, IL-8, TNF-α and monocyte chemotactic protein-1 (MCP-1) have been detected after binding to their corresponding antibodies, immobilised onto a suitable surface. Changes in the refractive index of the modified surface, occurring after the target binding, were utilised for the quantitative assay of the corresponding cytokine [472-474]. Commercial Biacore® SPR chips were coated with the antibodies of IL-8 to develop a SPR biosensor capable of detecting pM concentrations of IL-8 in the human saliva [475]. Similarly, the secreted IL-6 from human fibroblasts has been detected after binding to the specific antibody [476]. In addition, SPR aptasensors have been developed for the detection of IFN-γ with a limit of detection (LOD) down to 33 pM [477]. Acoustic (mechanical) biosensors have been developed for the detection of human IFN-β and IFN-γ using antibodies or aptamer sequences for their recognition. The changes in the frequency of the biosensors surfaces were recorded to detect both cytokines [478, 479].

5.1.4.4. Nanosensors for cytokines detection

Electrochemical nanosensors, fabricated from electroconductive nanoparticles, modified with the corresponding antibodies, have been reported for the detection of IL-6 and IL-8 [480-482]. Moreover, carbon nanotubes were coated with gold nanoparticles and attached to the antibodies of IL-6 to develop an electrochemical probe for the detection of this cytokine [483]. Furthermore, electrochemical aptasensors have been developed for the detection of IFN-γ using the selective DNA aptamer as ligands while graphene beads or gold microelectrode were utilised as surfaces for aptamer immobilisation and signal flow [484].

In addition, fluorescent nanosensors have been reported for the detection of IL-6 using f-SNPs as a surface for the assay [485, 486]. Similarly, a FRET-based nanosensor has been reported for the detection of PDGF using QD-labelled DNA aptamer. This QD-labelled-aptamer was hybridised with a complementary DNA segment that bears BHQ molecule to develop a FRET-based assay of PDGF at a concentration down to 0.4 nM [487].

The utilisation of the unique plasmonic properties of gold nanoparticles has contributed in the development of several LSPR and SERS-based nanosensors for the detection of IL-1β, IL-2 and TNF-α after binding to their corresponding antibodies [105, 488-490].

Furthermore, mechanical nanosensors have been utilised for the quantification of IFN-γ using the corresponding antibodies [491].

5.1.4.5. Other methods for cytokines detection

In addition to all the aforementioned methods, classical HPLC technique has been reported for the assay of IFN-α using the monoclonal antibodies for separation and identification [492].

While there are many methods that have been established for the detection of cytokines, there is still a shortage in understanding the full functions, mechanism and performance of cytokines. These because of that many of the current methods for the detection of cytokines are expensive, require long time to perform the assay and utilise sophisticated and expensive instrumentation. Additionally, application of such methods for the real-time measurements is not appropriate [438, 448, 478]. Due to the vital roles that cytokines play in our life; the development of any analytical method for the detection of such biomarkers will contribute greatly in understanding the full roles and functions of cytokines. This could enhance our life quality, help in prophylaxis and treatment of different diseases.

5.2. Aim

The main aim of Chapter 5 is to use the optimised SNPs that have been described in Chapter 2 and Chapter 4, to develop two types of aptamer-based fluorescent nanosensors for the quantitative assays of a DNA hybridisation process and IFN-γ, as a model cytokine. In this study, an aptamer sequence that has been previously reported for the detection of IFN-γ is used as a ligand [408, 457, 460, 468, 469].

The first aim of this chapter is to develop a FRET-based nanosensor for the detection of a DNA hybridisation process and IFN-γ. The nanosensor can be fabricated through the immobilisation of TAMRA-labelled aptamer onto the surface of p-SNPs while the FRET process could be achieved after hybridisation of this TAMRA-labelled aptamer with a partial complementary DNA segment, attached to BHQ2. The proposed fluorescence changes upon hybridisation of this sensing system with a complementary DNA sequence or IFN-γ binding are investigated and utilised for the assay.

The second aim of this chapter is to use Model 1, described in Chapter 4, to develop an extended-distance quenching nanosensor for the detection of DNA and IFN-γ, using the same aptamer that has utilised to in the first aim.

To achieve this goal, many factors that influence the performance and response of the proposed nanosensors are studied and optimised to develop optimum nanosensors that are capable of detecting the DNA hybridisation and IFN-γ. The success of this study could provide sensing platforms that can be applied for the real-time assay of IFN-γ and contribute towards the development of multiplexing model for the assay of cytokines using SNPs as a surface for the assay.

5.3. Experimental

5.3.1. Materials and chemicals

The EDC/NHS activated p-SNPs, with the size of ~85 nm and EDC/NHS activated TAMRA-SNPs with the size of ~75 nm were synthesised and characterised as described in Chapter 2 and Chapter 4. EDC, NHS, PBS (pH 7.4), MES buffer (50 mM, pH 6.0) and Tris-HCl (200 mM, pH 8.6) were prepared in nuclease-free DI water and used throughout this study. Recombinant human IFN-γ (carrier free) was purchased from R&D systems, UK and resuspended in PBS. Human TNF-α, insulin and ATP were obtained from Sigma-Aldrich, UK. The aptamers and DNA sequences were purchased from Biosearch Technologies, USA with the sequences that are shown in **Table 5.1** and were prepared as recommended by the manufacturer. Stock solutions (100 µM) of these aptamers were prepared and further dilutions were performed by serial dilution.

Table 5.1: A Summary for the aptamers sequences that were used in this study

Aptamer	Sequence
Sensing DNA aptamer sequence (APT-1)	5’ GGGGTTGGTTGTGTTGGGTGTTGTGT 3’ (C6-NH_2)
Sensing DNA aptamer, labelled with TAMRA (APT-1-TAM)	5’ TAMRA-GGGGTTGGTTGTGTTGGGTGTTGTGT 3’ (C6 NH_2)
Sensing hairpin DNA aptamer (APT-2)	5’ BHQ2 GGGGTTGGTTGTGTTGGGTGTTGTGTACAACCAACCCC 3’ (C6-NH_2)
BHQ2-3’DNA segment (DNA-3’Q)	5’ ACAACCAACCCC BHQ2 3’
BHQ2-5’DNA segment (DNA-5’Q)	5’ BHQ2 ACAACCAACCCC 3’
Complementary DNA strand (C-DNA)	5’ ACACAACACCCAACACAACCAACCCC 3’

5.3.2. Production of the nanosensors

5.3.2.1. Immobilisation of the sensing aptamers onto SNPs

The EDC/NHS activated p-SNPs or TAMRA-SNPs (Model 1), prepared as described in Chapter 4, were utilised to immobilise the corresponding aptamer sequence onto their surfaces.

To develop the FRET-based nanosensor: the EDC/NHS activated p-SNPs (10 mg), suspended in 1 mL of MES buffer (pH 6.0) were immediately incubated with 1 µM of APT-1-TAM for 4 hours at room temperature, without performing the washing step after the EDC/NHS activation process that was detailed in Chapter 4. After the incubation with APT-1-TAM, the nanoparticle suspensions were centrifuged and washed, at least three times, using Tris-HCl or PBS for the detection of C-DNA or IFN-γ, respectively. The p-SNPs, attached to APT-1-TAM, were stored at 4 °C until further use.

To develop the extended-distance quenching nanosensor: 1 µM of APT-1 was incubated with the EDC/NHS activated TAMRA-SNPs and the same procedure that was described above for the FRET-based nanosensor was followed for the immobilisation process.

5.3.2.2. Hybridisation of aptamer-SNPs with the quenching segment

Production of the FRET-based nanosensor: APT-1-TAM, immobilised onto the surface of p-SNPs as described above, was hybridised with 10 µM of DNA-3'Q in Tris-HCl, pH 8.6. The hybridisation was performed at 37 °C for 2 hours, with gentle shaking, followed by centrifugation and washing. The nanosensor was stored at 4 °C until further use.

Production of the extended-distance quenching nanosensor: the immobilised APT-1 on TAMRA-SNPs surface was hybridised with 10 µM of DNA-5'Q using the same procedure that was described for the production of the FRET-based nanosensor.

5.3.3. Detection of DNA hybridisation

Different concentrations of C-DNA, ranging from 0.1 nM to 100 nM, were incubated separately with 50 µL of the FRET-based nanosensor or the extended-distance quenching nanosensor in 96-Costar® well plates. The volume in each well was made to 150 µL with Tris-HCl and the hybridisation process was performed at 37 °C for 2 hours followed by measurements of the RFUs of TAMRA (emission =580 nm and excitation =545 nm), using a plate reader. The resultant RFUs corresponding to each C-DNA concentration (five determinations) were measured using the corresponding nanosensor, against blank nanosensor samples where no C-DNA was incubated. Excel Microsoft® software was used for the construction of the calibration curves and data analysis.

5.3.4. Incubation time for IFN-γ

The FRET-based nanosensor (50 µL) was incubated with IFN-γ (50 nM, 100 nM and 500 nM) while the total volumes were made to 150 µL, in each well, using PBS buffer. The incubation was performed at 37 °C for different periods ranging from 10 minutes and up to 6 hours followed by measurements of the RFUs of TAMRA, corresponding for each time period using a plate reader.

5.3.5. Detection of IFN-γ

Concentrations of IFN-γ which ranged from 3.75 nM to 1000 nM were incubated separately with 50 µL of the FRET-based nanosensor or the extended-distance quenching nanosensor, in the 96-well plates for 2 hours at 37 °C. The total volume in each well was made to 150 µL using PBS buffer. Measurements of the RFUs of TAMRA were recorded using the corresponding nanosensor against blank samples, treated similarly. The mean of the resultant RFUs, corresponding to each IFN-γ concentration, was used to construct the calibration curve.

5.3.6. Selectivity studies

50 µL of the FRET-based nanosensor was incubated separately with the same concentration of IFN-γ, TNF-α, insulin or ATP (100 nM) for 2 hours at 37 °C. The volumes were made to 150 µL using PBS buffer followed by measurements of the RFUs of TAMRA, against blank nanosensor samples treated similarly.

5.4. Results and discussion

5.4.1. Selection of the sensing aptamer sequence

In this study, the selection of an aptamer sequence which is capable of binding to IFN-γ and also the best position for immobilisation of this aptamer (3' end or 5' end) onto the surface of SNPs were based on previous studies [408, 457, 460, 468, 469]. These studies have shown that the 26-mer DNA aptamer, with the sequence of 5'GGG GTT GGT TGT GTT GGG TGT TGT GT3', has been successfully utilised to bind IFN-γ with high affinity and selectivity. The location of the nucleotides that are responsible for IFN-γ recognition is not entirely clear, however, better binding affinity to IFN-γ has been reported when the 3' end of this DNA sequence was used to immobilise this aptamer onto the surface of analysis, *e.g.* glass or gold electrode, rather than using the 5' end. The aptamer affinity was assessed by the measurement of the K_d of the aptamer binding which was ~3.4 nM or 28.1 nM when the 3' end or the 5' end were used for aptamer immobilisation, respectively, as reported [408, 469]. In the present work, based on such previous studies, the aforementioned DNA aptamer sequence was used as the selective sensing aptamer sequence for the detection of a DNA hybridisation and IFN-γ. In addition, the 3' end of this aptamer sequence was used for the immobilisation of this aptamer onto the surface of SNPs to develop the corresponding nanosensor.

Initial experiments were performed using p-SNPs to develop the FRET-based nanosensor. However p-SNPs did not contribute in the assay signal, they were used to provide a surface of analysis and to optimise factors that may influence the performance of the assay using the second nanosensor type, in which TAMRA-SNPs were used instead of p-SNPs, to provide fluorescence signals that were used for the quantification. Additionally, these nanosensors were fabricated to provide diagnostic tools that could be used for the intracellular detection of INF-γ.

5.4.2. The FRET-based nanosensor

5.4.2.1. Sensing strategy

Development of the FRET-based nanosensor was based on using the optimised p-SNPs, with the size of ~85 nm, prepared as described in Chapter 2, as a surface for the immobilisation of APT-1-TAM. The surface of nanoparticles was modified with a carboxylic acid moiety and activated using the EDC/NHS process as detailed in Chapter 4. APT-1-TAM was purchased with a chemical modification at the 3' end with a primary amine group to bind this amino moiety to the EDC/NHS activated p-SNPs. Additionally, the 5' end of this DNA sequence was labelled with TAMRA to produce fluorescence signal that can be utilised for the measurement. **Figure 5.7** is a schematic shows the proposed FRET-based nanosensor.

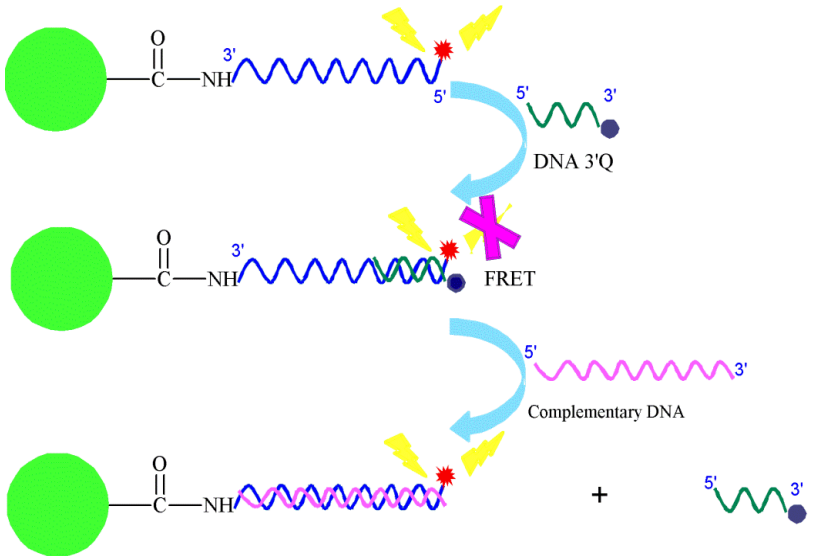


Figure 5.7: A schematic diagram illustrates the proposed strategy for the development of FRET-based nanosensor for the detection of a complementary DNA sequence.

As in **Figure 5.7**, the proposed sensing strategy is based on development of a FRET process between the TAMRA molecules and BHQ2 molecules; the selective quencher for TAMRA. This could be achieved through hybridisation of APT-1-TAM, attached to p-SNPs, with a partial complementary DNA segment that carries BHQ2 at 3' end (DNA-3'Q). This 12-mer quenching DNA segment with the sequence of 5'ACAACCAACCCC-BHQ2 3' was selected to initiate a partial hybridisation with the corresponding complementary 12 base-pairs of APT-1-TAM, located close to the 5' end that labelled with TAMRA.

In the absence of the target analyte (either C-DNA or IFN-γ), the fluorescence of TAMRA is reduced due to the proposed FRET from the TAMRA molecules (at 5' of APT-1-TAM) to BHQ2, attached to the 3' end of DNA-3'Q. After incubation of the target analyte with this sensing system, the quenching DNA segment (DNA3'Q) may be displaced and pushed away from the system, increasing the distance TAMRA and BHQ2. The process can be monitored by measurement of

the restoration in the fluorescence signal of TAMRA, which in turn, can be used for the quantitative determination of the bound target, either C-DNA or IFN-γ. In the present work, before performing the assay, many factors were studied and optimised as discussed in the following text.

5.4.2.2. Immobilisation of the aptamer onto nanoparticle surface

As previously mentioned, the 3' end of APT-1-TAM was modified with an amine group to attach this aptamer end to the surface of the EDC/NHS activated p-SNPs. In this reaction, APT-1-TAM was incubated immediately with the nanoparticles, suspended in MES buffer, pH 6.0 after the EDC/NHS activation process, without the separation or washing of the activated nanoparticles. The fluorescence of TAMRA was detected to indicate the success of aptamer conjugation. The results showed that a successful conjugation was achieved when APT-1-TAM was directly reacted with the EDC/NHS activated p-SNPs (suspended in MES buffer, pH 6.0), without performing the centrifugation and the washing steps of nanoparticles, prior to the reaction with APT-1-TAM. This was monitored by measurement of the fluorescence of TAMRA in the nanoparticle suspension after conjugation to APT-1-TAM. Moreover, aptamer conjugation could be noticed by the pink colour of TAMRA as shown in **Figure 5.8**. This pink colour could not be observed when APT-1-TAM was conjugated to the EDC/NHS activated p-SNPs that had been washed after the EDC/NHS activation and prior to aptamer conjugation.



Figure 5.8: A picture shows p-SNPs before (white) and after (pink) the conjugation of APT-1-TAM.

This protocol for aptamer conjugation was similar to that reported for the conjugation of amino-aptamers to the surface of SNPs using EDC/NHS where the aptamer conjugation was achieved without washing or separation of the EDC/NHS activated nanoparticles [180, 351, 493, 494]. However some general protocols for the EDC/NHS activation recommend elimination of the excess EDC and NHS from the medium before performing the conjugation to amino-containing molecules. This step is mandatory when the coupled molecules have both amine and carboxylic acid moieties within the same molecule, such as proteins. Otherwise, protein polymerisation will occur, resulting in a low efficiency binding. Additionally, the washing step is performed to change the buffer type and the pH value of the medium to select the optimum pH for protein coupling, which should be slightly alkaline (pH 7.4) to prevent protonation of the amino groups of protein [363, 374]. Herein the situation is different where the oligonucleotides do not polymerise together, permitting the immobilisation reaction to be performed in a single step. Furthermore, it is favoured for the aptamers to find the activated carboxylic acid group quickly, especially, when the concentration of amino-oligonucleotides is low [363, 495]. According to the

previous reports and the obtained results, APT-1-TAM were reacted with the nanoparticles immediately after the EDC/NHS activation process without performing the washing or separation of the activated SNPs. This conjugation protocol was established to achieve sufficient aptamer binding and was utilised for all further experiments for aptamer immobilisation.

5.4.2.3. Optimisation of the sensing aptamer concentration

To obtain the maximum response of the FRET-based nanosensor, the optimum concentration of APT-1-TAM was investigated. This was achieved by using different concentrations of APT-1-TAM from 0.02 µM to 2 µM. After aptamer conjugation, the resultant fluorescence signal of TAMRA molecules, attached to the 5' end of the aptamer, was recorded as an indicator for the assembled aptamer molecules onto the nanoparticle surface. As could be seen from **Figure 5.9**, the RFUs of TAMRA gradually increased as the concentration of APT-1-TAM was increased from 0.02 µM up to 0.5 µM and then remained without significant changes when APT-1-TAM concentration elevated above 0.5 µM.

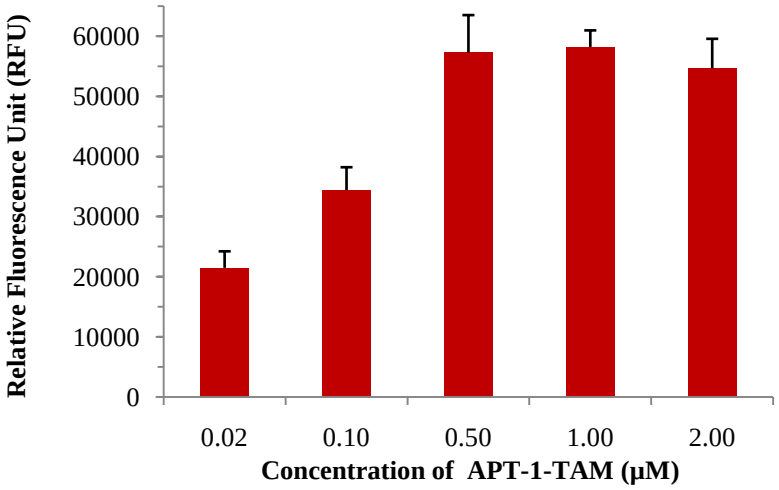


Figure 5.9: The effect of the aptamer concentration (APT-1-TAM) on the efficiency of the immobilisation reaction of this aptamer onto the surface of p-SNPs.

These results indicate that APT-1-TAM with a concentration ≥0.5 µM may be enough to saturate all the carboxylic acid groups on the nanoparticle surface, or may suggest that potential steric hindrance or electrostatic repulsion between the negatively-charged DNA molecules which could prevent more aptamers to be assembled onto the nanoparticle surface [408]. This probably explains why the increase in APT-1-TAM concentrations above 0.5 µM did not significantly increase the number of the immobilised aptamers as the RFUs of TAMRA remained without significant changes. As a result, to ensure maximum aptamer immobilisation and optimum nanosensor sensitivity, 1 µM of the sensing aptamer was selected as the optimum aptamer concentration.

5.4.2.4. Optimisation of the quenching segment concentration (DNA3'Q)

Once the concentration of APT-1-TAM, conjugated to the surface of p-SNPs, was optimised, the best concentration of the quenching DNA segment (DNA3'Q), required o achieve maximum fluorescence quenching, was investigated. To study this, concentrations of DNA3'Q, ranging from 1 µM to 15 µM, were hybridised separately with APT-1-TAM (1 µM), attached to p-SNPs. As shown in **Figure 5.10**, the percentage of fluorescence quenching of TAMRA gradually increased upon increasing the concentration of DNA-3'Q. Above 7.5 µM of DNA3'Q, the percentage of fluorescence quenching of TAMRA did not markedly change and reached the maximum level of quenching at about 90% of the original fluorescence of TAMRA, measured for blank sample. This high percentage of fluorescence quenching indicates that a FRET process between TAMRA and BHQ2 was successfully achieved after the hybridisation of DNA3'Q with the immobilised APT-1-TAM.

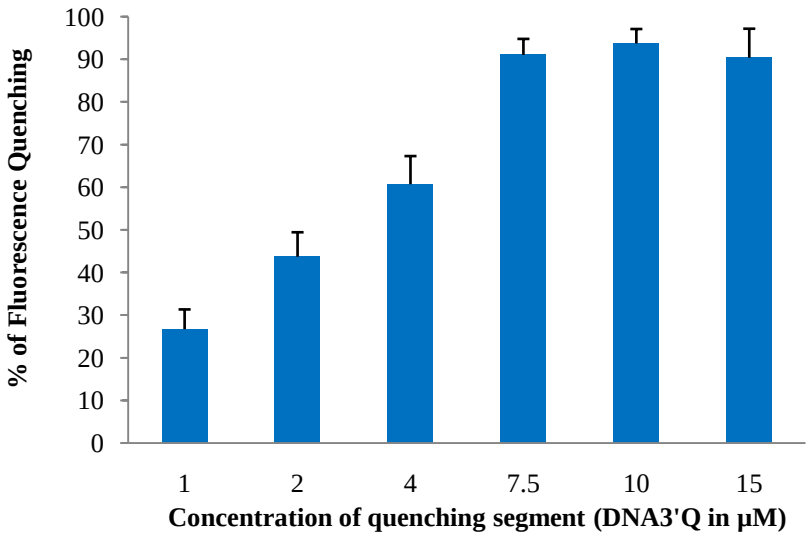


Figure 5.10: The effect of the quenching DNA segment concentrations (DNA3'Q) on the fluorescence signals of TAMRA, attached to the 5' end of APT-1-TAM, after the hybridisation with DNA3'Q.

However, the DNA3'Q concentration required to achieve the maximum fluorescence quenching was higher than that used for APT-1-TAM immobilisation; not an equimolar concentration. This may be attributed to the fact that the quenching DNA sequence is a partial complementary to APT-1-TAM and thus, the hybridisation process and FRET could be only achieved using high concentrations of this partial complementary strand (DNA3'Q). Overall, to obtain maximum fluorescence quenching, 10 µM of DNA3'Q was selected as the optimum concentration of the quenching DNA segment. Additionally, the molar ratio of the aptamer: quenching segment was kept at 1:10 µM throughout this study.

5.4.2.5. Quantitative detection of DNA hybridisation using the FRET-based nanosensor

The capability of the developed FRET-based nanosensor to quantitatively detect a DNA hybridisation was investigated using ssDNA (C-DNA) with the sequence of 5'ACA CAA CAC CCA ACA CAA CCA ACC CC3'. This DNA sequence was used as a target DNA which is a completely complementary oligonucleotide sequence for the corresponding 26-mer of the aptamer sequence (5**'**GGG GTT GGT TGT GTT GGG TGT TGT GT3'). This complete complementary DNA could displace the partial complementary quenching segment (DNA3'Q) from this sensing system, leading to restoration in the fluorescence of TAMRA, which can be used for the quantitative assay of C-DNA.

To establish the assay, different concentrations of C-DNA which ranged from 0.1 nM to 100 nM were hybridised with the complementary oligonucleotide sequence (APT-1-TAM) using the FRET-based nanosensor, at 37 °C for 2 hours. A similar protocol to that reported for a DNA hybridisation was followed [288, 324, 358, 496, 497]. After the hybridisation, the RFUs of TAMRA were recorded for each C-DNA concentration, against blank nanosensor samples, to construct the calibration curve. As shown in **Figure 5.11**, the results revealed that C-DNA was able to displace DNA3'Q from the sensing system as the fluorescence of TAMRA was successfully restored after C-DNA hybridisation. In addition, a linear relationship between the restored fluorescence of TAMRA and C-DNA concentrations was obtained within the range from 3.75 nM to 50 nM of C-DNA as represents in **Figure 5.11**. Furthermore, ~80% of the original fluorescence signal of TAMRA was restored after the hybridisation.

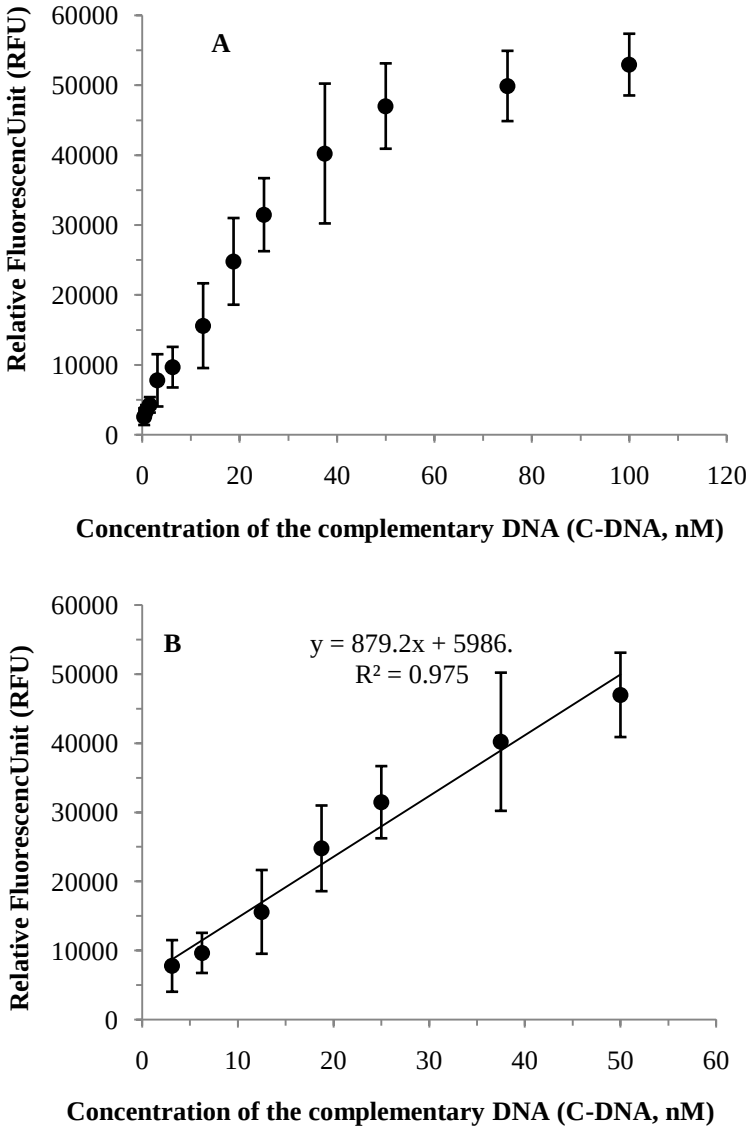


Figure 5.11: (A) The response of the FRET-based nanosensor after hybridisation with C-DNA with concentrations from 0.1 nM to 100 nM and (B) is the linear part of the calibration curve for the detection of C-DNA within concretions from 3.75 nM to 50 nM.

In addition, the sensitivity of the developed FRET-based nanosensor for the quantitative detection of DNA hybridisation was detected by calculating the LOD value using the **Equation 5.1** [498, 499].

$$LOD = \frac{3.3\ SD_a}{b} \qquad \textbf{Equation 5.1}$$

Where SDa is the standard deviation of the intercept and b is the slope [498, 499].

Generally, the value of LOD is used to determine the sensitivity of the analytical method to detect the lowest analyte concentration with high reliability (95% confidence limit) [498-500]. Using the developed FRET-based nanosensor for the detection of C-DNA, the calculated LOD value was ~4 nM. Compared to previously reported methods for the detection of DNA hybridisation, summarised in **Table 5.2**, the developed FRET-based nanosensor has a comparable sensitivity to most of these methods [288, 358].

Table 5.2: A summary for the limit of detection (LOD) of previously reported methods for the detection of DNA hybridisation, compared with the LOD of the developed FRET-based nanosensor for the detection of C-DNA.

Method reported by:	LOD	Ref
Peng et. al.	6.7 nM	[501]
Rao, et. al.	1.2 nM	[358]
Liu, et. al.	67 fM	[502]
Cai, et. al.	0.1 nM	[503]
Wang, et. al.	4 nM	[504]
Wu, et. al.	2 nM	[505]

5.4.2.6. The use of the FRET-based nanosensor for IFN-γ detection

The aptamer sequence, utilised in this study, was selected to bind IFN-γ and to develop nanosensors that can be used for the analysis of this cytokine as a model. Firstly, to investigate the response of the FRET-based nanosensor for the detection of IFN-γ, different concentrations of IFN-γ (50 nM, 100 nM and 500 nM) were incubated with the nanosensor for different time intervals ranging from 10 minutes to 6 hours at 37 °C, followed by measurements of the RFUs of TAMRA after each time interval. As shown in **Figure 5.12** the developed FRET-based nanosensor was able to bind IFN-γ which displaced DNA3'Q from the system as the florescence signals of TAMRA was successfully restored after challenging with IFN-γ. The maximum nanosensor response was achieved after about 1 hour of incubation while the fluorescence of TAMRA remained stable for additional 4 hours followed by a slight decline in the RFUs of TAMRA. This observed decline in TAMRA fluorescence may be attributed to dissociation of IFN-γ-aptamer complex. Therefore, to obtain the maximum response of this nanosensor with a stable fluorescence signal, 2 hours was selected as the optimum incubation time for the assay of IFN-γ at 37 °C. **Figure 5.12** illustrates the incubation time study for the assay of IFN-γ (100 nM) using the FRET-based nanosensor, at 37 °C.

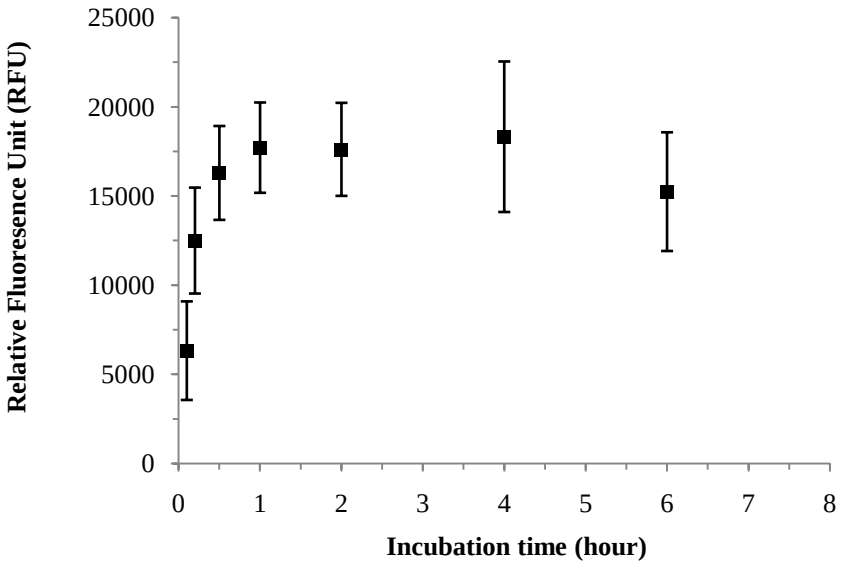


Figure 5.12: The effect of incubation time on the response of the FRET-based nanosensor for the detection of IFN-γ (100 nM).

The calibration curve for the detection of IFN-γ was established using the developed FRET-based nanosensor. Different concentrations of IFN-γ which ranged from 3.75 nM to 1000 nM were incubated separately with constant concentrations of the nanosensor, for 2 hours at 37°C, followed by measurement of the RFUs of TAMRA. The mean of the resultant RFUs was calculated for each corresponding IFN-γ concentration and was utilised to construct the calibration curve. As represented in **Figure 5.13**, the developed FRET-based nanosensor was able to detect IFN-γ within a linear range from 15 nM to 250 nM. Furthermore, ~60% of TAMRA signals were restored after IFN-γ binding to the nanosensor.

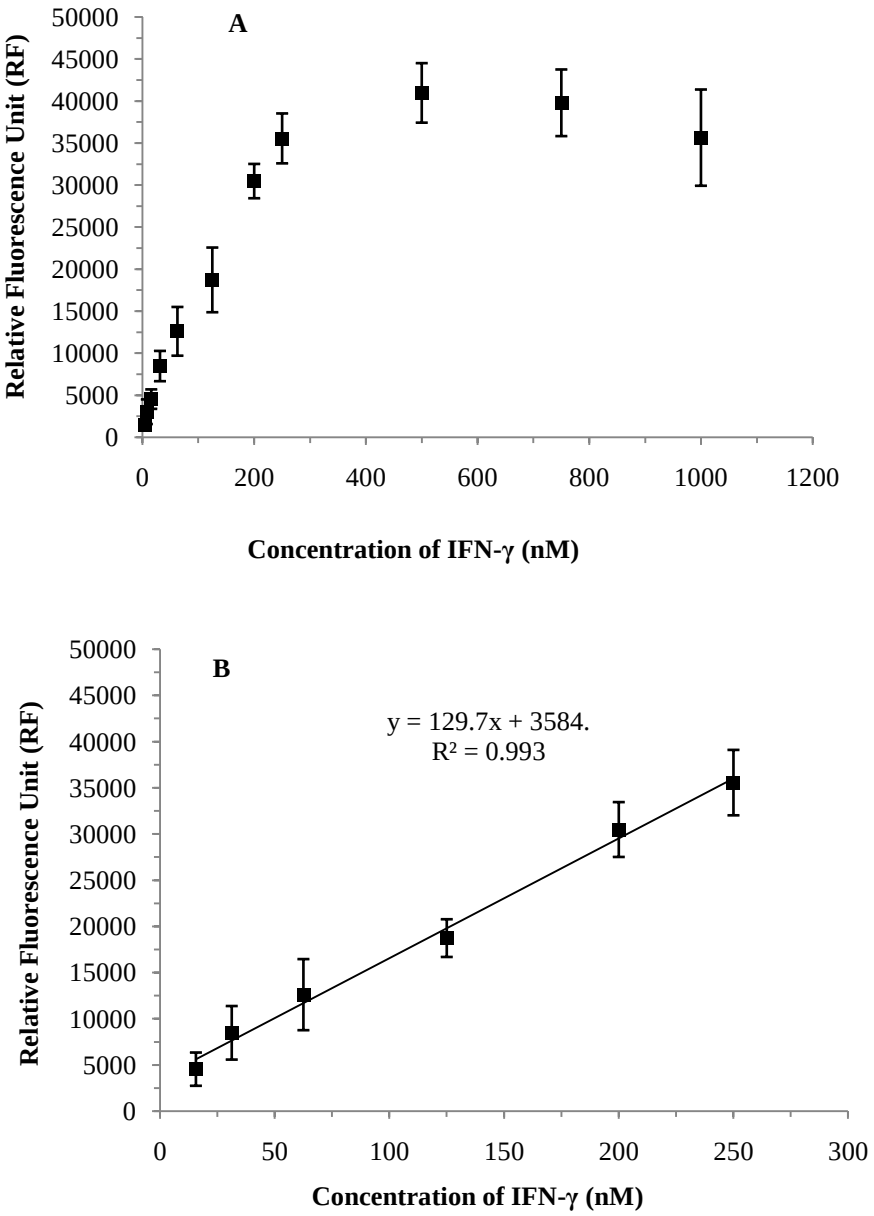


Figure 5.13: (A) The response of the FRET-based nanosensor after incubation with different concentrations of IFN-γ (3.75 nM to 1000 nM) and (B) is the linear calibration curve of the nanosensor after incubation with IFN-γ, with concentrations from 15 nM to 250 nM.

It was noticed that when the concentration of IFN-γ increased above 500 nM, a slight decrease in the RFUs of TAMRA was observed. This may be due to the size of IFN-γ which could be sufficient to hinder the escape of the quenching DNA segment from the nanosensor surface to the surrounding medium and hence, this quenching segment is trapped within the system and the quenching effect still predominant.

In addition, the calculated LOD of the nanosensor to detect INF-γ was 24 nM which indicates that the developed aptasensor have considerable binding affinity to IFN-γ and could be used for the detection of this cytokines within the linear concentration that was shown in **Figure 5.13**. However, the developed FRET-based nanosensor is more sensitive for the detection of DNA hybridisation than IFN-γ detection. This is expected as the sensing aptamer that was utilised to develop the nanosensor is a DNA in nature and hence, it can bind (hybridised) simultaneously with the complementary DNA with high sensitivity.

5.4.2.7. Selectivity of the nanosensor

Despite the sensing aptamer utilised in this study has been reported for the detection of IFN-γ with sufficient affinity and sensitivity, studies were performed to identify the nanosensor selectivity [408, 457, 458, 460, 468, 469]. This was performed to evaluate the application of the developed nanosensor to detect IFN-γ in different environments where other proteins may interfere. The nanosensor was incubated separately, for 2 hours at 37 °C, with 100 nM of IFN-γ, insulin, TNF-α and ATP. After the incubation, the RFUs of TAMRA were detected for each protein and compared to blank nanosensor samples. The results showed that, the

response of the nanosensor to detect IFN-γ was the highest amongst all the other incubated proteins which indicates the significant selectivity of the developed nanosensors for the detection of INF-γ, as shown in **Figure 5.14**.

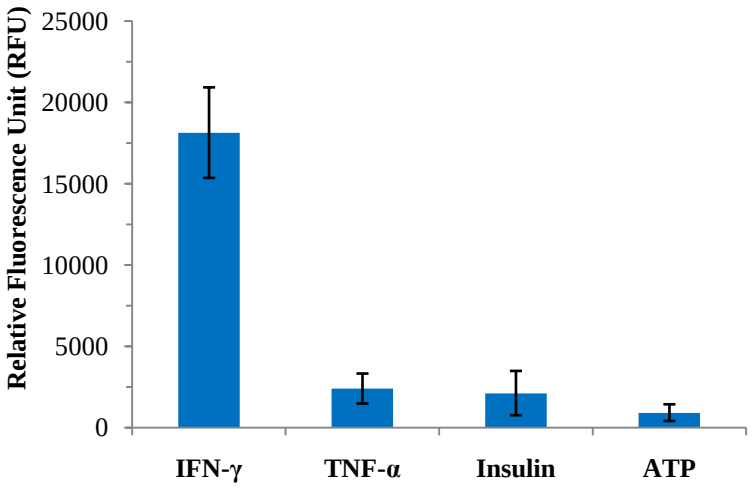


Figure 5.14: The selectivity study of the FRET-based nanosensor for the detection of IFN-γ.

5.4.3. The extended-distance quenching nanosensor

The second nanosensor that was developed in this study for the detection of the DNA hybridisation and IFN-γ was based on using Model 1 (TAMRA-SNPs) that was described previously in Chapter 4. The nanosensor was developed by attachment of the sensing aptamer (APT-1) to the surface of Model 1. APT-1 was then hybridised with a quenching DNA segment that carrying BHQ2 which could reduce the fluorescence of TAMRA molecules, encapsulated inside the silica matrix. As shown in **Figure 5.15**, the proposed sensing mechanism is based on utilising the process of fluorescence quenching; that was observed using Model 1 and discussed in Chapter 4, as the principle of the assay process. Upon the analyte binding, the quenching segment may be displaced, leading to the restoration of TAMRA fluorescence which can be used for quantification.

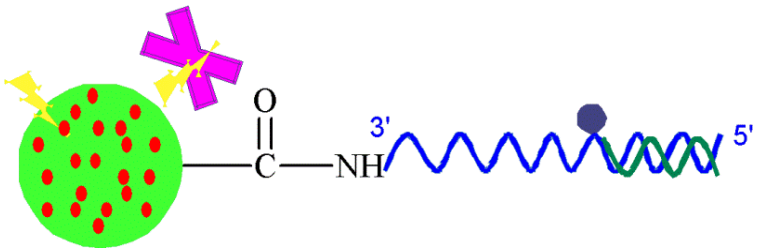


Figure 5.15: The proposed analytical design for the extended-distance quenching nanosensor.

Despite the proposed mechanism of fluorescence quenching of this nanosensor type is not yet clear as detailed earlier in Chapter 4, the term extended-distance quenching nanosensor was used in this study to distinguish this nanosensor, developed using Model 1, from the FRET-based nanosensor, produced using p-SNPs.

Taking into consideration the factors that were discussed under the FRET-based nanosensor; APT-1 was conjugated from the 3' end to the surface of the EDC/NHS activated TAMRA-SNPs, using a similar protocol to that described earlier for the aptamer conjugation in the FRET-based nanosensor. In addition, the molar ratio of APT-1: quenching segment was kept at 1: 10 µM.

To initiate the fluorescence quenching of TAMRA, APT-1 (1 µM) was conjugated to the EDC/NHS activated TAMRA-SNPs and then hybridised with the quenching DNA segment (DNA-5'Q, 10 µM), labelled with BHQ2. Additionally, the incubation time of the nanosensor with C-DNA or IFN-γ was 2 hours at 37 °C. In this study, many factors were studied and optimised before performing the assay as discussed in the following sections.

5.4.3.1. Optimisation of the initial concentration of TAMRA

While the concentrations of the aptamer and quenching segment were kept at 1 µmol and 10 µM respectively, the fluorescence signal of the proposed nanosensor could be controlled *via* optimising the initial concentration of TAMRA, used during the initial nanoparticle synthesis.

Different volumes, ranged from 10 µL to 100 µL, of TAMRA-APTES conjugate were added to the reaction mixture during the initial synthesis of TAMRA-SNPs to produce different batches of TAMRA-SNPs, incorporating different amounts of TAMRA. TAMRA-APTES conjugate was prepared using 0.5 mg/mL of TAMRA and conjugated to APTES under the determined conditions for the nanoparticle synthesis, detailed in Chapter 2. The produced TAMRA-SNPs batches were then

used to investigate the fluorescence signal and optimise the fluorescence quenching of the sensing system after hybridisation of APT-1 (1µM) with the quenching DNA segment (10 µM), linked to BHQ2.

The results revealed that the fluorescence signal of TAMRA, resulting from each TAMRA-SNPs batch, was reduced after hybridisation of APT-1, immobilised onto the nanoparticle surface, with DNA5'Q due to the effect of BHQ2. Maximum fluorescence quenching (~55%) was obtained when the volume TAMRA-APTES, utilised for the nanoparticle synthesis, was below 30 µL. This maximum percentage of fluorescence quenching did not significantly change as the volume of TAMRA-APTES was maintained below 30 µL as illustrated in **Figure 5.16**.

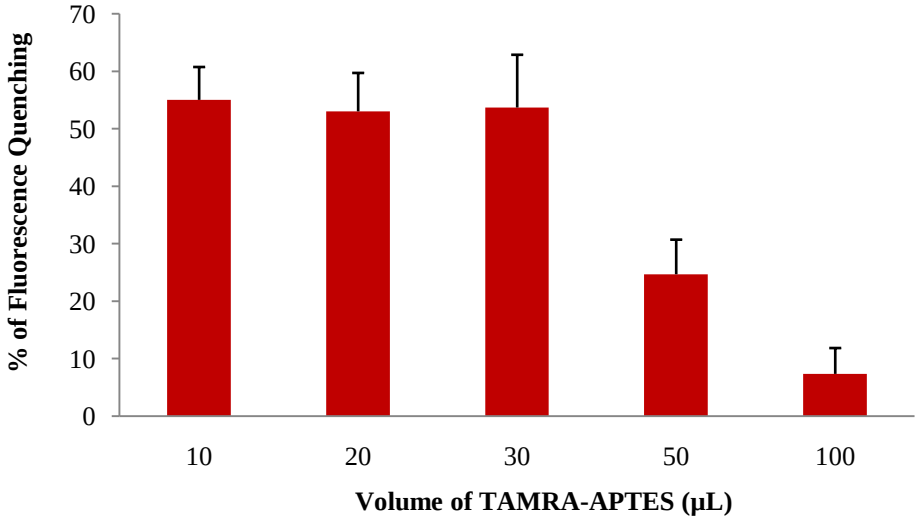


Figure 5.16: The effect of different volumes of TAMRA-APTES on the percentage of fluorescence quenching after hybridisation of TAMRA-SNPs-APT-1 system to DNA5'Q.

As a result, to achieve the maximum fluorescence quenching (55%) of this nanosensor, 20 µL of TAMRA-APTES; prepared using 0.5 mg/mL of TAMRA, was utilised for the synthesis of TAMRA-SNPs which were then used to fabricate the extended-distance quenching nanosensor. In addition, the concentration of APT-1 was 1 µM and the concentration of the quenching DNA segment was 10 µM to achieve maximum fluorescence reduction.

5.4.3.2. Selection of the quencher position

Whilst the proposed mechanism for the fluorescence reduction of the extended-distance quenching nanosensor could be influenced by the separation distance between the fluorophore and quencher, therefore, the effect of the quencher position on the resultant quenching was investigated. DNA3'Q and DNA5'Q, with BHQ2 molecule located on either the 3' end or 5' end, were hybridised separately with APT-1, attached to TAMRA-SNPs. As illustrated in **Figure 5.17**, there was no marked difference in the percentage of fluorescence quenching when either DNA3'Q or DNA5'Q hybridised with APT-1. The maximum percentages of TAMRA quenching were about 50-60% for both systems. However, DNA5'Q showed slightly higher quenching which may be due to the more proximity of BHQ2 of this DNA sequence to the nanoparticle surface.

In addition, APT-2 was used to study the process of fluorescence quenching after conjugation of this DNA sequence to the TAMRA-SNPs surface. This aptamer was purchased with the sequence of 5'BHQ2 GGG GTT GGT TGT GTT GGG TGT TGT GTA CAA CCA ACC CC 3'NH_2. Both ends of APT-2 are complementary to each other and can be hybridised together to form the hairpin

structure. The attached BHQ2 molecules to the 5' end of this aptamer may reduce the fluorescence of TAMRA, encapsulated inside the nanoparticle matrix. Prior to the aptamer conjugation, APT-2 was heated at 95°C for 5 minutes and then cooled to room temperature to form the hairpin structure, as reported [458, 469, 506]. As shown in **Figure 5.17**, nearly 40% of the original fluorescence of TAMRA-SNPs was quenched after conjugation of the EDC/NHS nanoparticles to APT-2.

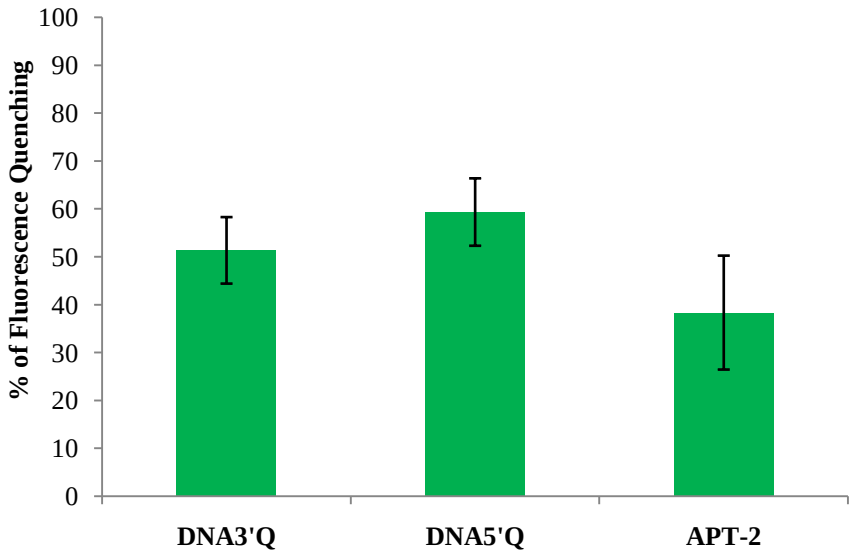


Figure 5.17: The percentage of the resultant fluorescence quenching of TAMRA-SNPs after hybridisation/conjugation to different quenching DNA segments, carrying BHQ2 at different positions.

However all of these systems showed considerable reduction in the fluorescence of TAMRA-SNPs, their response after incubation with C-DNA (100 nM) or IFN-γ (250 nM) was different. The responses of such sensing systems were recorded as the restoration in the fluorescence signal of TAMRA. The fluorescence of TAMRA in the first two systems that were based on displacement of the quenching segments (DNA3'Q or DNA5'Q) was successfully restored after hybridisation with C-DNA or incubation with IFN-γ, as shown in the calibration

curve. In contrast, the sensing system that based on using the hairpin structural switching of APT-2 did not respond at all as the recorded fluorescence signal of TAMRA did not significantly change before or after C-DNA hybridisation or INF-γ incubation.

It has been reported that, the approximate length of each individual base-pair of the DNA molecule is approximately 0.34 nm (3.4 Å) [507]. Therefore, the total length of APT-2, composed of 38 base-pairs, is approximately 13 nm. This means that upon biding of APT-2 system to the target species, the quencher molecule may be located within a maximum distance of ~13 nm far from the nanoparticle surface. Taking into account that the DNA molecules are not present as linear structures around the nanoparticle surface, so, this distance may not be enough to eliminate the quenching effect of BHQ2 as it is still predominant. This hypothesis may explain why the fluorescence signal of TAMRA-SNPs, attached to APT-2, did not markedly change after incubating the nanosensor with C-DNA or IFN-γ. Furthermore, C-DNA is not a complete complementary sequence to APT-2 and the full hybridisation could be only achieved using high concentrations of C-DNA. In comparison, using the first two systems that were developed using APT-1, the quenching segment is completely displaced after analyte binding which makes this quenching segment to move free from the nanoparticle surface to the surrounding medium, leading to restoration in TAMRA fluorescence.

5.4.3.3. Quantitative detection of C-DNA hybridisation and IFN-γ using the extended-distance quenching nanosensor

In order to validate the extended-distance quenching nanosensor for the biological application, the optimised nanosensor was used for the detection of C-DNA and IFN-γ. Similar to the FRET-based nanosensor, the calibration curves were constructed using different concentrations of C-DNA from 0.1 nM to 100 nM while the concentrations of IFN-γ were ranged from 3.75 nM to 1000 nM. After the incubation of this nanosensor with C-DNA or IFN-γ for 2 hours at 37 °C, the restored RFUs of TAMRA was recorded for each concentration of the corresponding analyte against blank. The recorded RFUs were used to indicate the capability of the nanosensor to detect DNA hybridisation or IFN-γ and to establish the calibration curve for the corresponding analyte.

The results revealed that the optimised extended-distance quenching nanosensor was able to detect C-DNA within the linear range from 12.25 nM to 75 nM. In addition, the linear range of the nanosensor to detect IFN-γ was observed over concentrations from 62.5 nM to 300 nM, as shown in **Figure 5.18**.

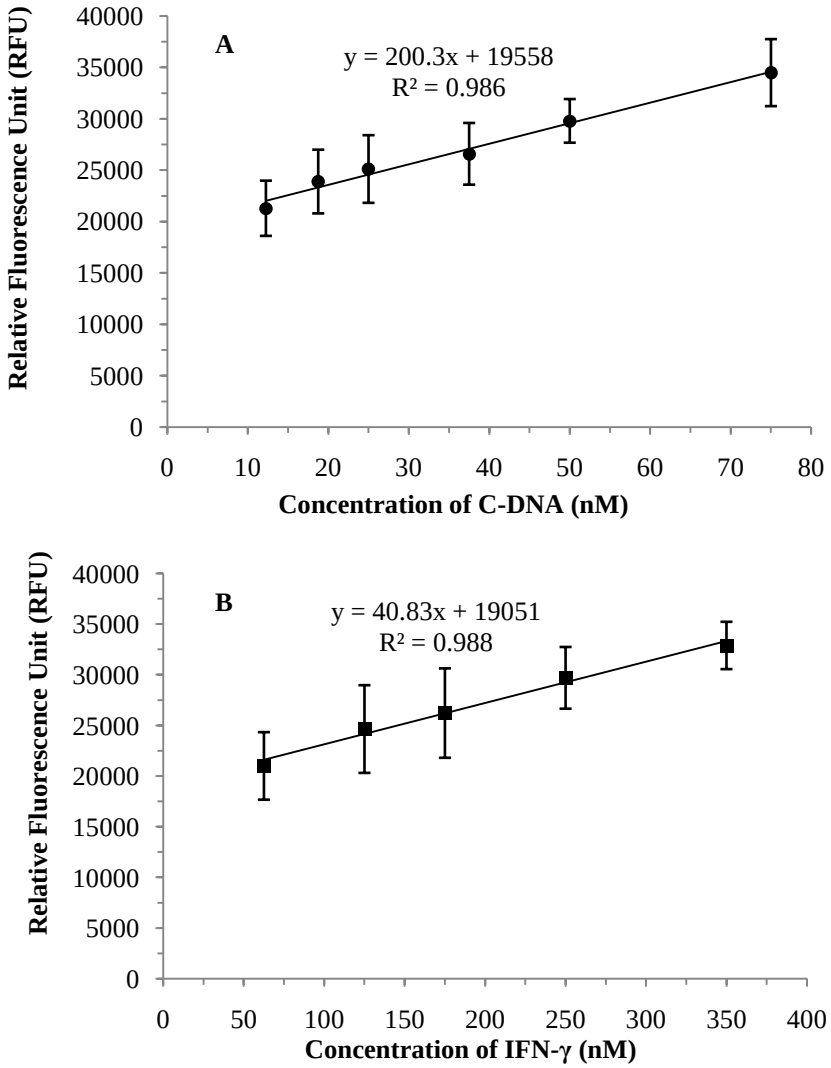


Figure 5.18: (A) and (B) The linear calibration curves for the detection of C-DNA hybridisation and IFN-γ, respectively, using the developed extended-distance quenching nanosensor.

The LOD values of this nanosensor for the detection of C-DNA and IFN-γ were ~12 nM and 40 nM, respectively, which indicate the ability of the optimised extended-distance quenching nanosensor to detect C-DNA hybridisation and IFN-γ with sufficient sensitivity within the indicated linear ranges. However, the sensitivity of the extended-distance quenching nanosensor was lower than that obtained using the FRET-based nanosensor. This may be due to the difference in the percentage of the fluorescence quenching in both nanosensors (FRET and extended-distance quenching) which influences the nanosensor response. The

maximum quenching percentage of the FRET-based nanosensor was ~95% whilst the maximum quenching of the extended-distance quenching nanosensor was ~55%. Therefore, this difference in the fluorescence reduction makes the extended-distance quenching nanosensor less sensitive to detect C-DNA and IFN-γ than using the FRER-based nanosensor.

5.5. Conclusion

Aptamer-based fluorescent nanosensors for the detection of DNA hybridisation and IFN-γ as a model cytokine have been successfully developed. The nanosensors were based on utilising the surface of SNPs to immobilise a sensing aptamer sequence that has the capability to bind IFN-γ. The conjugation process was based on using the EDC/NHS protocol that was detailed in Chapter 4. In addition, the selection of aptamer sequence and the position of the selected aptamer (3' end) for conjugation to the nanoparticle surface were based on previously reported studies [408, 457, 460, 468, 469].

In this study, two different sensing strategies have been utilised to develop the nanosensors. The first nanosensor was developed using the typical FRET process as the principle for the assay while the second nanosensor was based on using the extended-distance quenching that previously shown in Chapter 4. Many factors, including the optimal aptamer concentration, optimum fluorescence quenching and the selection of the optimum quencher position, have been investigated and optimised.

The FRET-based nanosensor was successfully able to detect DNA hybridisation and IFN-γ within the linear ranges from 3.75 nM to 50 nM for DNA and from 15 nM to 250 nM for IFN-γ. In comparison, the extended-distance quenching nanosensor detected the DNA hybridisation and IFN-γ over the linear ranges from 12 nM to 75 nM and from 62.5 nM to 350 nM for C-DNA and IFN-γ, respectively.

While traditional or commercially-available methods for the detection of IFN-γ; such as ELISA or flow cytometry, have shown improved sensitivity than that obtained using the developed nanosensors [508-510]. The developed nanosensors offer many advantages over these methods. The main advantage of the developed nanosensors is that using the aptamers for the nanosensor fabrication eliminates the need of several labelling and washing steps and also improves nanosensors stability. This makes the developed nanosensors suitable tools to detect IFN-γ in different environments where traditional antibody-based immunoassays cannot be used. In addition, due to the biocompatibility and small size of SNPs, the presented nanosensors can be used for the non-invasive incorporation into cellular systems to detect IFN-γ release from live cells in real-time without the need to homogenise the cells.

Despite the sensitivity of the developed nanosensors to detect IFN-γ was less than that previously reported using other aptasesnors [408, 468], the use of the developed nanosensors is still promising due to the aforementioned advantages. Additionally, the surface of SNPs was used for the first time to develop fluorescent nanosensors for the detection of IFN-γ using the corresponding aptamer. This could contribute towards development of multiplexing assay of multiple cytokines using the same sensing mechanism using the aptamer sequences to detect the analytes of interest.

Chapter Six

Conclusions and Future Work

The overall aim of this work to develop fluorescent nanosensors for the real-time biological assays has been successfully achieved. The nanosensors, fabricated from bio-friendly materials; polyacrylamide nanoparticles (PANPs) or silica nanoparticles (SNPs), have been produced and successfully validated for the real-time ratiometric fluorescence measurement of the intracellular pH, one of the most important cellular markers. Furthermore, an improved distance-dependent fluorescence quenching has been reported for the first time using SNPs. Additionally, aptamer-based fluorescent nanosensors have been developed for the detection of DNA hybridisation and INF-γ as a model cytokine. The key conclusions and future perspectives for these investigations are summarised into the following sections.

6.1. Production of ratiometric fluorescent pH nanosensors

The work described in Chapter 2 discussed the synthesis of two types of ratiometric fluorescent nanosensors for the measurement of pH over a wide dynamic pH range. This dynamic pH range was from pH 3.5 to pH 7.5, covering the pH of biological systems and cell types. To obtain this wide dynamic pH range, two pH sensitive fluorophores (OG and FAM) were covalently linked to the corresponding nanosensor matrix while another reference fluorophore (TAMRA) was utilised to provide the ratiometric fluorescence measurements.

Nanosensors that were fabricated from a polyacrylamide nanoparticle matrix, with a size of about 50 nm, were produced using a previously reported protocol that has been published by the Aylott research group *via* reverse microemulsion polymerisation reaction [137].

A second type of nanosensor was fabricated from silica matrix and synthesised using a modified Stöber method for the synthesis of SNPs. Many protocols have been previously reported for the synthesis of SNPs with a size range below 100 nm to facilitate potential cellular insertion [203-207]. However, when such protocols were attempted during this work, the measured size range of the resulting SNPs differed greatly from that reported. Accordingly, the first challenge in this study was to establish a reproducible protocol for the production of size-tuneable SNPs. To achieve this aim, research was conducted to study the effect of varying the amounts of each reactant/catalyst involved in the process of SNPs synthesis. Factors such as the amounts of TEOS, NH_4OH, ethanol and dye-APTES conjugate were investigated and optimised. The results showed that, the quantity of NH_4OH plays an important role in controlling the size of the resultant SNPs while the amounts of other reactants have shown minimal effects on the size of SNPs. Overall, using the conditions reported in Chapter 2 and summarised in **Table 2.2**, size-tuneable SNPs within the range from 45 nm to 900 nm can be readily produced.

In addition, SNPs, synthesised from the hydrolysed TEOS, exhibited a surface with a zeta potential of about -30 mV indicating a negative surface charge on the nanosensors surface which is attributed to the hydroxyl groups of silanol. In contrast, the surface charge of polyacrylamide nanosensor was nearly neutral or slightly positive. In order to enhance cellular uptake, nanosensors were surface-modified with positively-charged groups. This was achieved by incorporation of trimethylammonium ions inside the polyacrylamide matrix using a modifying acrylamide monomer (ACTA). Further, APTES was used for functionalisation of

SNPs with amino group to confer positive charges on the corresponding nanosensor surface.

A limitation to using SNPs with diameters <75 nm was a reduced nanoparticle yield and the inability to collect the nanoparticles efficiently from the solution. A considerable yield of about 100 mg was obtained when SNPs were prepared in the size range of ~75 nm. Therefore, further investigation to separate SNPs with a small size range below 75 nm is required. This could be achieved by using another technique for nanoparticle separation other than centrifugation. Additionally, enhancement of the resulting nanoparticle yield is necessary to collect the nanoparticles. An approach to solve such problems is to use dialysis and freeze-drying for nanoparticle separation which could improve the efficiency of separation and increase the final nanoparticle yield. Further, the size of SNPs could be reduced by using smaller amounts of NH4OH than that reported in this thesis. Following the success of these investigations, production of small SNPs with a size range below 20 nm could be achieved by using the optimised protocol. This could contribute in synthesis of small f-SNPs which could then provide silica-based fluorescent donors in distance-dependent fluorescence energy transfer/quenching processes which could be used as alternatives for QDs which are extensively utilised as FRET donors. In addition, this small nanoparticle size may improve the cellular uptake of silica nanosensors. Furthermore, the versatile chemistry of silica provides a favoured surface to accommodate many ligands which contribute towards the development of multiplexing assay model using SNPs.

6.2. Real-time measurement of the intracellular pH

Validation of the developed ratiometric pH nanosensors for the real-time intracellular assays was successfully achieved using yeast cells. Yeast cells were selected as a unicellular microorganism that represents a model of the developed eukaryotic cells. The investigations detailed in Chapter 3 revealed that positively-charged pH nanosensors were taken up by the cells whilst negatively-charged nanosensors were not taken up. Furthermore, the polyacrylamide pH nanosensors exhibited better cellular uptake and higher signal to noise ratio compared to the silica pH nanosensors. This was rationalised as being due to polyacrylamide nanosensor composed of a low density matrix which can be readily separated from the cells by centrifugation, after nanosensor incubation. Additionally, this improved cellular uptake may be due to smaller size of PANPs (50 nm) than SNPs (75 nm). Further, the optimised protocol for the nanosensor delivery into yeast cells removed the need to use the stress-based techniques that have been previously reported for incorporation of polyacrylamide nanosensors into yeast cells.

The polyacrylamide fluorescent pH nanosensors were successfully applied for monitoring the intracellular pH changes of yeast cells during glucose metabolism in the real-time. Reliable intracellular pH measurements were performed using fluorescence microscopy while MATLAB® and ImageJ® were utilised for the data analysis. The optimised protocol for the nanosensors delivery and performing the assay enabled the application of the nanosensor to measure the intracellular pH of each individual cell. Based on the growth phase and age, each individual yeast cell exhibited its own pH value. However during glucose metabolism, the

response of a population of yeast cells was similar. To establish a simple, reliable relationship between the intracellular pH changes and time, the mean of the intracellular pH of the studied cells was used to establish such relationship.

The results revealed that the cells take about 25 minutes after glucose addition to restore their pH which then remained stable for further 15 minutes. This study discussed the importance of the energy produced during glucose metabolism and the ability of yeast to maintain their normal intracellular pH, enabling cells to keep their pH homeostasis. This phenomenon has been studied for the first time using ratiometric fluorescent pH nanosensors, validating the biological application of the developed nanosensors for the pH measurements.

The optimised protocol for the nanosensors delivery to the yeast cells was successfully used for incorporation of the nanosensors into ~65% of the yeast cells. This percentage of internalisation is acceptable when dealing with yeast and better than the reported percentage [270]. However, further studies are required to improve this percentage with keeping the normal cellular functions. Another limitation that was found in this study was that silica nanosensors were difficult to be used in the assay process due to problems occurred when trying to remove the non-incorporated SNPs from yeast cells. Further solution to this problem is required to incorporate the silica nanosensors into yeast cells. This could be achieved by fabrication positively-charged silica-based pH nanosensors with smaller size than that prepared in this thesis and incubate such nanosensors with the yeast cells for more than 24 hours. Additionally, higher concentrations than 20 mg/mL of nanosensors may be required to achieve maximum cellular uptake.

While real-time measurement of the intracellular pH of yeast cells during glucose metabolism was successfully achieved, we could not differentiate between the pH values of each cell organelles, such as vacuoles, cytoplasm or mitochondria. To achieve this, the future direction for this study is to utilise super-resolution fluorescence microscopy and fluorescence microscopy with higher magnification objectives to provide higher resolution images of the yeast cells. From these images further information about the pH changes of the intracellular organelles will be ascertained. The trade-off in obtaining high resolution images is that less population data is obtained.

6.3. Distance-dependent fluorescence quenching study using SNPs

SNPs and core-shell SNPs have been developed in many studies; the main purpose for using silica in most of these investigations was to utilise the chemistry of silane to provide a platform that can be used for further bimolecular/chemical conjugation. The research detailed in Chapter 4 discussed using the surface chemistry of silica to establish a protocol for the efficient binding amino-molecules to SNPs using the EDC/NHS coupling chemistry. The results revealed that using the EDC/NHS activated SNPs can bind to amino-molecules with efficiency ~70%.

Further, previous studies have been reported some instances of improved fluorescence quenching/energy transfer between fluorescent donor and plamonic nanoparticle, using silica as a spacer, beyond the expected Förster distance [336,

338, 339, 341]. However, these studies attributed this improved process to the plasmonic properties of the noble metal nanoparticle and not to the effect of silica. Until now, fluorescence quenching/transfer between a fluorophore and a molecular quencher, such as BHQs, over different distances using silica as a spacer, has not yet been studied. Therefore, in Chapter 4, investigations were conducted using different models of size controlled TAMRA-SNPs and core-shell TAMRA-SNPs, prepared with different thicknesses of silica shells around the fluorescent core. An optimised protocol for conjugating an amino-functionalised quencher (BHQ2) to the surface of SNPs and core-shell models was developed to study the fluorescence quenching of TAMRA over different distances, using silica shells as spacers. A process of distance-dependent fluorescence quenching of TAMRA was observed over a distance up to 25 nm. Maximum quenching of about 75% was achieved using the optimised TAMRA-SNPs.

The results obtained in Chapter 4 demonstrate that fluorescence quenching occurs over greater distances than that expected, when considering the conventional FRET requirements. However, the mechanism behind this is not clear. The research conducted in this study opens an interesting debate about the role that silica may play in the process of the improved fluorescence quenching. The successful production of small SNPs, with a size below 20 nm, may help to investigate this phenomenon in more detail as it could not be determined if the observed quenching process was due to the FRET process or another mechanism. Therefore, production of small size SNPs, suitable as FRET donors, could help in understanding the phenomenon in more details. In addition, further investigations using gold nanoparticles as fluorescence quenchers instead of BHQ2 and

comparing results to those obtained in this work could provide an additional evidence to gain a complete understanding of this phenomenon.

6.4. Aptamer-based nanosensors for the detection of DNA and cytokine

Cytokines are important biomarkers, whose role are not fully understood and are difficult to measure. There are commercially available kits and previously reported methods for the detection of cytokines using the antibodies for capturing and detection of the cytokine of interest. Despite this, using such methods for the real-time detection of cytokine release is limited. Therefore, nanosensors capable of real-time detection are required. Further, the utilisation of aptamers instead of the antibodies in nanosensor fabrication has contributed in improving the assay process and produced probes that can be used for the real-time assays within the cellular environment.

The work described in Chapter 5 details two types of aptamer-based fluorescent nanosensors for the assay of a model cytokine (IFN-γ). The first nanosensor was based on utilising the conventional FRET phenomenon for the assay procedure while the second nanosensor type was based on the fluorescence quenching of SNPs that was detailed in Chapter 4. DNA aptamer sequence that can bind IFN-γ, with high affinity and selectivity, was used as a ligand while the surface of SNPs was used as a surface for the aptamer immobilisation. The produced nanosensors were successfully hybridised with a target complementary ssDNA to provide a tool for the quantitative assay of DNA hybridisation to optimise the response of the nanosensors. Additionally, based on the aptamer affinity to IFN-γ molecule,

the developed nanosensors were successfully used for the detection of this important cytokine.

The future prospective for this study is to improve the sensitivity of the developed nanosensors for the assay of IFN-γ. A solution for this problem depends on development of SNPs with a reduced size than that prepared in this work, which could further increase the number of the assembled aptamers (ligand) on nanoparticle surface and improve the sensitivity. Once this work is achieved, the potential application for these nanosensors is to detect the release of IFN-γ from stimulated leukocytes in real-time. The successful achievement of this could provide optimum tools for the non-invasive, real-time detection of IFN-γ and contribute in development of versatile nanosensors for detection of other cytokines could be achieved. This could be the core for development of multiplex nanosensor for the detection of several cytokines using the same nanosensor.

Chapter Seven

References

1. Etzioni, R., et al., *The case for early detection.* Nat Rev Cancer, 2003. **3**(4): p. 243-52.
2. Ludwig, J.A. and Weinstein, J.N., *Biomarkers in cancer staging, prognosis and treatment selection.* Nat Rev Cancer, 2005. **5**(11): p. 845-56.
3. Urdea, M., et al., *Requirements for high impact diagnostics in the developing world.* Nature, 2006. **444 Suppl 1**: p. 73-9.
4. Crowther, J.R., *The ELISA Guidebook.* 2001, New Jersey, USA: Humana Press.
5. Sadana, A., *Biosensors: Kinetics of Binding and Dissociation Using Fractals*. First ed. 2003, The Netherlands: Elsevier.
6. Yi, D.K. and Papaefthymiou, G.C., *Nanobiomaterials : development and applications.* Advances in materials science and engineering. 2014, Florida, USA: CRC Press; Taylor & Francis Group. xvii.
7. Jinhao, G. and Xu, B., *Applications of nanomaterials inside cells.* Nano Today, 2009. **4**: p. 37-51.
8. Kosaka, P.M. et al., *Detection of cancer biomarkers in serum using a hybrid mechanical and optoplasmonic nanosensor.* Nat Nanotechnol, 2014. **9**: p. 1047-1053.
9. Zhang, C.Y., et al., *Single-quantum-dot-based DNA nanosensor.* Nat Mater, 2005. **4**(11): p. 826-31.
10. Cash, K.J., et al., *Optical drug monitoring: photoacoustic imaging of nanosensors to monitor therapeutic lithium in vivo.* ACS Nano, 2015. **9**(2): p. 1692-8.

11. Vo-Dinh, T., *Nanotechnology in Biology and Medicine: Methods, Devices and Applications*. Vol. 1. 2007, New york, USA: Taylor and Francis Group, CRC Press. 1-8.

12. Aylott, J.W., *Optical nanosensors--an enabling technology for intracellular measurements.* Analyst, 2003. **128**(4): p. 309-12.

13. Webster, A., et al., *The delivery of PEBBLE nanosensors to measure the intracellular environment.* Biochem Soc Trans, 2007. **35**(Pt 3): p. 538-43.

14. Swierczewska, M., et al., *High-sensitivity nanosensors for biomarker detection.* Chem Soc Rev, 2012. **41**(7): p. 2641-55.

15. Kumar, S.R., *Nanotechnologies for the life science*. Vol. 10. 2007, Weinheim, Germany: Wiley-VCH.

16. Park, I., et al., *Selective surface functionalization of silicon nanowires via nanoscale joule heating.* Nano Lett, 2007. **7**(10): p. 3106-11.

17. Elnathan, R., et al., *Biorecognition layer engineering: overcoming screening limitations of nanowire-based FET devices.* Nano Lett, 2012. **12**(10): p. 5245-54.

18. Zheng, G., et al., *Multiplexed electrical detection of cancer markers with nanowire sensor arrays.* Nat Biotechnol, 2005. **23**(10): p. 1294-301.

19. Zimmerman, J.F., et al., *Free-Standing Kinked Silicon Nanowires for Probing Inter- and Intracellular Force Dynamics.* Nano Letters, 2015. **15**(8): p. 5492-5498.

20. Kim, W., et al., *Interfacing silicon nanowires with mammalian cells.* J Am Chem Soc, 2007. **129**(23): p. 7228-9.

21. Martin, P., et al., *Electrochemical nanobiosensors*. Sensors and Actuators B, 2007. **123**: p. 1195-1205.

22. Cui, Y., et al., *Nanowire nanosensors for highly sensitive and selective detection of biological and chemical species.* Science, 2001. **293**(5533): p. 1289-92.

23. Gao, A., et al., *Silicon-nanowire-based CMOS-compatible field-effect transistor nanosensors for ultrasensitive electrical detection of nucleic acids.* Nano Lett, 2011. **11**(9): p. 3974-8.

24. Fulati, A., et al., *An intracellular glucose biosensor based on nanoflake ZnO.* Sensors and Actuators B, 2010. **150**: p. 673-680.

25. Shalek, A.K., et al., *Vertical silicon nanowires as a universal platform for delivering biomolecules into living cells.* Proc Natl Acad Sci U S A, 2010. **107**(5): p. 1870-5.

26. Patolsky, F., et al., *Detection, stimulation, and inhibition of neuronal signals with high-density nanowire transistor arrays.* Science, 2006. **313**(5790): p. 1100-4.

27. Qi, S., et al., *Effects of silicon nanowires on HepG2 cell adhesion and spreading.* ChemBioChem, 2007. **8**(10): p. 1115-8.

28. Plumere, N. and B. Speiser, *Redox-active silica nanoparticles - Part 2. Photochemical hydrosilylation on a hydride modified silica particle surface for the covalent immobilization of ferrocene.* Electrochimica Acta, 2007. **53**(3): p. 1244-1251.

29. Rahman, M.A., et al., *Gold Nanoparticles Doped Conducting Polymer Nanorod Electrodes: Ferrocene Catalyzed Aptamer-Based Thrombin Immunosensor.* Anal Chem, 2009. **81**(16): p. 6604-6611.

30. Korotcenkov, G., Han, S.D., and Stetter, J.R., *Review of electrochemical hydrogen sensors.* Chem Rev, 2009. **109**(3): p. 1402-33.

31. Zhang, F., et al., *Amperometric sensor based on ferrocene-doped silica nanoparticles as an electron transfer mediator for the determination of glucose in rat brain coupled to in vivo microdialysis.* J Electroanal Chem, 2004. **571**: p. 133-138.

32. Liu, Z., et al., *Carbon Nanotubes in Biology and Medicine: In vitro and in vivo Detection, Imaging and Drug Delivery.* Nano Res, 2009. **2**(2): p. 85-120.

33. Meng L, et al., *Single walled carbon nanotubes as drug delivery vehicles: targeting doxorubicin to tumors.* Biomaterials, 2012. **33**(6): p. 1689-1698.

34. Di Crescenzo, A., et al., *Biocompatible dispersions of carbon nanotubes: a potential tool for intracellular transport of anticancer drugs.* Nanoscale, 2011. **3**(3): p. 925-8.

35. Harrison, B.S. and Atala, A., *Carbon nanotube applications for tissue engineering.* Biomaterials, 2007. **28**(2): p. 344-53.

36. Ebbesen, T.W., et al., *Electrical conductivity of individual carbon nanotubes.* Nature, 1996. **382**: p. 54-56.

37. Kam, N.W. and Dai, H., *Carbon nanotubes as intracellular protein transporters: generality and biological functionality.* J Am Chem Soc, 2005. **127**(16): p. 6021-6.

38. Yoon, I., et al., *Intracellular Neural Recording with Pure Carbon Nanotube Probes.* PLoS One, 2013. **8**(6): p. e65715.

39. Guo, X., et al., *Conductivity of a single DNA duplex bridging a carbon nanotube gap.* Nat Nanotechnol, 2008. **3**(3): p. 163-7.

40. Fakhri, N., et al., *High-resolution mapping of intracellular fluctuations using carbon nanotubes.* Science, 2014. **344**(6187): p. 1031-5.

41. Stern, E., et al., *Label-free immunodetection with CMOS-compatible semiconducting nanowires.* Nature, 2007. **445**(7127): p. 519-22.

42. Chinen, A.B., et al., *Nanoparticle Probes for the Detection of Cancer Biomarkers, Cells, and Tissues by Fluorescence.* Chem Rev, 2015.

43. Jiang, J., et al., *Quantitative measurement of redox potential in hypoxic cells using SERS nanosensors.* Nanoscale, 2014. **6**(20): p. 12104-12110.

44. Anker, J.N., et al., *Biosensing with plasmonic nanosensors.* Nature Mater, 2008. **7**(6): p. 442-453.

45. Kumar, S., et al., *Plasmonic nanosensors for imaging intracellular biomarkers in live cells.* Nano Letters, 2007. **7**(5): p. 1338-1343.

46. Haven, M.C., Tetrault, G.A., and Schenken, J.R., *Laboratory Instrumentation*. Fourth ed. 1995, Toronto, Canada: John Wiley & Sons Inc.

47. Sheehan, D., *Physical Biochemistry: Principles and Applications*. 2009, Oxford, UK: Wiley-Blackwell.

48. Clark, H.A., et al., *Optical nanosensors for chemical analysis inside single living cells. 2. Sensors for pH and calcium and the intracellular application of PEBBLE sensors.* Anal Chem, 1999. **71**(21): p. 4837-43.

49. Yang, L.M., et al., *Real-Time Imaging of Mitochondrial Hydrogen Peroxide and pH Fluctuations in Living Cells Using a Fluorescent Nanosensor.* Anal Chem, 2015. **87**(7): p. 3678-3684.

50. Tan, W., et al., *Submicrometer intracellular chemical optical fiber sensors.* Science, 1992. **258**(5083): p. 778-81.

51. Tan, W., Shi, Z., and Kopelman, R., *Development of Submicron Chemical Fiber Optic Sensors.* Anal Chem, 1992. **1002**(64): p. 2985-2990.

52. Song, A., Parus, S., and Kopelman, R., *High-performance fiber-optic pH microsensors for practical physiological measurements using a dual-emission sensitive dye.* Anal Chem, 1997. **69**(5): p. 863-7.

53. Schwarz, J.A., Contescu, C.I., and Putyer, K., *Dekker Encyclopedia of Nanoscience and Nanotechnology*. Vol. 4. 2004, New York, USA: Marcel Dekker Inc.

54. Vo-Dinh, T., *Biomedical Photonics Handbook.* 2003, Florida, USA: CRC Press.

55. Clark, H.A., et al., *Optical nanosensors for chemical analysis inside single living cells. 1. Fabrication, characterization, and methods for intracellular delivery of PEBBLE sensors.* Anal Chem, 1999. **71**(21): p. 4831-6.

56. Vo-Dinh, T. and Kasili, P., *Fiber-optic nanosensors for single-cell monitoring.* Anal Bioanal Chem, 2005. **382**(4): p. 918-25.

57. Vo-Dinh, T., *Nanosensing at the single cell level.* Spectrochim Acta Part B At Spectrosc, 2008. **63**(2): p. 95-103.

58. Ko, S., and Grant, S.A., *A novel FRET-based optical fiber biosensor for rapid detection of Salmonella typhimurium.* Biosens Bioelectron, 2006. **21**(7): p. 1283-90.

59. Brasuel, M., et al., *Fluorescent nanosensors for intracellular chemical analysis: decyl methacrylate liquid polymer matrix and ion-exchange-based potassium PEBBLE sensors with real-time application to viable rat C6 glioma cells.* Anal Chem, 2001. **73**(10): p. 2221-8.

60. Desai, A.S., et al., *Fluorescent nanosensors for intracellular measurements: synthesis, characterization, calibration, and measurement.* Front Physiol, 2013. **4**: p. 401.

61. Clark, H.A., et al., *Subcellular optochemical nanobiosensors: probes encapsulated by biologically localised embedding (PEBBLEs).* Sensors and Actuators B: Chemical, 1998. **51**(1-3): p. 12-16.

62. Buck, S.M., et al., *Optochemical nanosensor PEBBLEs: photonic explorers for bioanalysis with biologically localized embedding.* Curr Opin Chem Biol, 2004. **8**(5): p. 540-6.

63. Chauhan, V.M., Burnett, G.R., and Aylott, J.W., *Dual-fluorophore ratiometric pH nanosensor with tuneable pKa and extended dynamic range.* Analyst, 2011. **136**(9): p. 1799-801.

64. Sumner, J.P., et al., *A fluorescent PEBBLE nanosensor for intracellular free zinc.* Analyst, 2002. **127**(1): p. 11-6.

65. Nielsen, L.J., Olsen, L.F., and Ozalp, V.C., *Aptamers embedded in polyacrylamide nanoparticles: a tool for in vivo metabolite sensing.* ACS Nano, 2010. **4**(8): p. 4361-70.

66. Giuntini, F., et al., *Orthogonally bifunctionalised polyacrylamide nanoparticles: a support for the assembly of multifunctional nanodevices.* Nanoscale, 2012. **4**(6): p. 2034-45.

67. Resch-Genger, U., et al., *Quantum dots versus organic dyes as fluorescent labels.* Nat Methods, 2008. **5**(9): p. 763-75.

68. Michalet, X., et al., *Quantum dots for live cells, in vivo imaging, and diagnostics.* Science, 2005. **307**(5709): p. 538-44.

69. Li, J., and Zhu, J.J., *Quantum dots for fluorescent biosensing and bio-imaging applications.* Analyst, 2013. **138**(9): p. 2506-15.

70. Wang, Y., et al., *Functionalized quantum dots for biosensing and bioimaging and concerns on toxicity.* ACS Appl Mater Interfaces, 2013. **5**(8): p. 2786-99.

71. Algar, W.R., Tavares, A.J., and Krull, U.J., *Beyond labels: a review of the application of quantum dots as integrated components of assays, bioprobes, and biosensors utilizing optical transduction.* Anal Chim Acta, 2010. **673**(1): p. 1-25.

72. Liu, J., Lee, J.H., and Lu, Y., *Quantum dot encoding of aptamer-linked nanostructures for one-pot simultaneous detection of multiple analytes.* Anal Chem, 2007. **79**(11): p. 4120-5.

73. Bagalkot, V., et al., *Quantum dot-aptamer conjugates for synchronous cancer imaging, therapy, and sensing of drug delivery based on bi-fluorescence resonance energy transfer.* Nano Lett, 2007. **7**(10): p. 3065-70.

74. Wu, X., et al., *Immunofluorescent labeling of cancer marker Her2 and other cellular targets with semiconductor quantum dots.* Nat Biotechnol, 2003. **21**(1): p. 41-6.

75. Webste, T.J., *Safety of Nanoparticles: From Manufacturing to Medical Applications*. 2009, New York, USA: Springer. 95097.

76. Chou, L.Y. and Chan, W.C., *Nanotoxicology. No signs of illness.* Nat Nanotechnol, 2012. **7**(7): p. 416-7.

77. Bradburne, C.E., et al., *Cytotoxicity of quantum dots used for in vitro cellular labeling: role of QD surface ligand, delivery modality, cell type, and direct comparison to organic fluorophores.* Bioconjug Chem, 2013. **24**(9): p. 1570-83.

78. Mandala, A., and Tamaia, A.N., *Luminescence enhancement of water soluble CdTe quantum dots by proper surface modification with ethylene diamine.* Chem Phys Lett, 2011. **507**(4-6): p. 248-252.

79. Yu, W.W., et al., *Water-soluble quantum dots for biomedical applications.* Biochem Biophys Res Com, 2006. **348**(3): p. 781-6.

80. Wang, Q., et al., *Luminescent properties of water-soluble denatured bovine serum albumin-coated CdTe quantum dots.* J Phys Chem B, 2006. **110**(34): p. 16860-6.

81. Biju, V., et al., *FRET from quantum dots to photodecompose undesired acceptors and report the condensation and decondensation of plasmid DNA.* ACS Nano, 2012. **6**(5): p. 3776-88.

82. Fernandez-Arguelles, M.T., et al., *Synthesis and characterization of polymer-coated quantum dots with integrated acceptor dyes as FRET-based nanoprobes.* Nano Lett, 2007. **7**(9): p. 2613-7.

83. Liu, M., et al., *A FRET chemsensor based on graphene quantum dots for detecting and intracellular imaging of Hg(2)(+).* Talanta, 2015. **143**: p. 442-9.

84. Sonnichsen, C., et al., *A molecular ruler based on plasmon coupling of single gold and silver nanoparticles.* Nat Biotechnol, 2005. **23**(6): p. 741-5.

85. Jain, P.K., et al., *Review of some interesting surface plasmon resonance-enhanced properties of noble metal nanoparticles and their applications to biosystems.* Plasmonics, 2007. **2**(3): p. 107-118.

86. El-Sayed, I.H., Huang, X., and El-Sayed, M.A., *Surface plasmon resonance scattering and absorption of anti-EGFR antibody conjugated*

gold nanoparticles in cancer diagnostics: applications in oral cancer. Nano Lett, 2005. **5**(5): p. 829-34.

87. Mayer, K.M., and Hafner, J.H., *Localized surface plasmon resonance sensors.* Chem Rev, 2011. **111**(6): p. 3828-57.

88. Huang, X.H., et al., *Cancer cell imaging and photothermal therapy in the near-infrared region by using gold nanorods.* J Am Chem Soc, 2006. **128**(6): p. 2115-2120.

89. Eustis, S., and El-Sayed, M.A., *Why gold nanoparticles are more precious than pretty gold: noble metal surface plasmon resonance and its enhancement of the radiative and nonradiative properties of nanocrystals of different shapes.* Chem Soc Rev, 2006. **35**(3): p. 209-17.

90. Link, S., and El-Sayed, M.A., *Spectral Properties and Relaxation Dynamics of Surface Plasmon Electronic Oscillations in Gold and Silver Nanodots and Nanorods.* J. Phys. Chem. B, 1999. **103**: p. 8410-8426.

91. Wang, Y., et al., *Silicon nanowires for biosensing, energy storage, and conversion.* Adv Mater, 2013. **25**(37): p. 5177-95.

92. Luther, J.M., et al., *Localized surface plasmon resonances arising from free carriers in doped quantum dots.* Nat Mater, 2011. **10**(5): p. 361-6.

93. Huang, X., Neretina, S., and El-Sayed, M.A., *Gold nanorods: from synthesis and properties to biological and biomedical applications.* Adv Mater, 2009. **21**(48): p. 4880-910.

94. Willets, K.A. and Van Duyne, R.P., *Localized surface plasmon resonance spectroscopy and sensing.* Annu Rev Phys Chem, 2007. **58**: p. 267-97.

95. Szunerits, S. and Boukherroub, R., *Sensing using localised surface plasmon resonance sensors.* ChemComm, 2012. **48**(72): p. 8999-9010.

96. Park, J.H., et al., *High-sensitivity detection of ATP using a localized surface plasmon resonance (LSPR) sensor and split aptamers.* Biosens Bioelectron, 2015. **73**: p. 26-31.

97. Costas, C., et al., *Using Surface Enhanced Raman Scattering to Analyze the Interactions of Protein Receptors with Bacterial Quorum Sensing Modulators.* Acs Nano, 2015. **9**(5): p. 5567-5576.

98. Nie, S.M., and Emery, S.R., *Probing single molecules and single nanoparticles by surface-enhanced Raman scattering.* Science, 1997. **275**(5303): p. 1102-1106.

99. Yun, C.S., et al., *Nanometal surface energy transfer in optical rulers, breaking the FRET barrier.* J Am Chem Soc, 2005. **127**(9): p. 3115-3119.

100. Green, R.J., et al., *Surface plasmon resonance analysis of dynamic biological interactions with biomaterials.* Biomaterials, 2000. **21**(18): p. 1823-35.

101. Yu, C., Nakshatri, H., and Irudayaraj, J., *Identity profiling of cell surface markers by multiplex gold nanorod probes.* Nano Lett, 2007. **7**(8): p. 2300-6.

102. Hong, W., et al., *Nanoscale label-free bioprobes to detect intracellular proteins in single living cells.* Sci Rep, 2014. **4**: p. 6179.

103. Baptista, P., et al., *Gold nanoparticles for the development of clinical diagnosis methods.* Anal Bioanal Chem, 2008. **391**(3): p. 943-50.

104. Jain, S., Hirst, D.G., and O'Sullivan, J.M., *Gold nanoparticles as novel agents for cancer therapy.* Bri J Radiology, 2012. **85**(1010): p. 101-113.

105. Endo, T., et al., *Label-free cell-based assay using localized surface plasmon resonance biosensor.* Anal Chim Acta, 2008. **614**(2): p. 182-9.

106. Kang, B., Mackey, M.A., and El-Sayed, M.A., *Nuclear targeting of gold nanoparticles in cancer cells induces DNA damage, causing cytokinesis arrest and apoptosis.* J Am Chem Soc, 2010. **132**(5): p. 1517-9.

107. McNay, G., et al., *Surface-enhanced Raman scattering (SERS) and surface-enhanced resonance Raman scattering (SERRS): a review of applications.* Appl Spectrosc, 2011. **65**(8): p. 825-37.

108. Xie, W., et al., *Application of surface-enhanced Raman scattering in cell analysis.* J Ram Spec, 2011. **42**(6): p. 1248-1254.

109. Qian, X.M., et al., *In vivo tumor targeting and spectroscopic detection with surface-enhanced Raman nanoparticle tags.* Nat Biotechnol, 2008. **26**(1): p. 83-90.

110. Stuart, D.A., et al., *In vivo glucose measurement by surface-enhanced Raman spectroscopy.* Anal Chem, 2006. **78**(20): p. 7211-7215.

111. Sha, M.Y., et al., *Surface-enhanced Raman scattering tags for rapid and homogeneous detection of circulating tumor cells in the presence of human whole blood.* J Am Chem Soc, 2008. **130**(51): p. 17214-15.

112. Lee, S., et al., *Biological imaging of HEK293 cells expressing PLCgamma1 using surface-enhanced Raman microscopy.* Anal Chem, 2007. **79**(3): p. 916-22.

113. Chen, W., and Bai, C., *Single Molecule Chemistry and Physics: An Introduction*. 2006, Heidelberg, Germany: Spriner.

114. Ru, E.L., and Etchegoi, P., *Principles of Surface-Enhanced Raman Spectroscopy: and related plasmonic effects*. 2014, Oxford, UK: Elsevier.

115. Varadan, V.K., Chen L.F., and Xie, J., *Nanomedicine: Design and Applications of Magnetic Nanomaterials, Nanosensors*. 2008, West Sussex, UK: Wiley.

116. Kaittanis, C., et al., *The Assembly State between Magnetic Nanosensors and Their Targets Orchestrates Their Magnetic Relaxation Response.* J Am Chem Soc, 2011. **133**(10): p. 3668-3676.

117. Wang, Y.X., et al., *Recent advances in superparamagnetic iron oxide nanoparticles for cellular imaging and targeted therapy research.* Curr Pharm Des, 2013. **19**(37): p. 6575-93.

118. Bulte, J.W.M. and Modo, M., *Nanoparticles in Biomedical Imaging: Emerging Technologies and Applications*. 2008, New York, USA: Springer.

119. Laurent, S., et al., *Magnetic iron oxide nanoparticles: Synthesis, stabilization, vectorization, physicochemical characterizations, and biological applications.* Chem Rev, 2008. **108**(6): p. 2064-2110.

120. Lee, H., et al., *Chip-NMR biosensor for detection and molecular analysis of cells.* Nat Med, 2008. **14**(8): p. 869-74.

121. Lorkowski, S., and Cullen, P.M., *Analysing Gene Expression, A Handbook of Methods: Possibilities and Pitfalls*. 2003, Weinheim, Germany: Wiley.

122. Grimm, J., et al., *Novel nanosensors for rapid analysis of telomerase activity.* Cancer Res, 2004. **64**(2): p. 639-643.

123. Chang, B.S., et al., *Surface functionalization of magnetic mesoporous silica nanoparticles for controlled drug release.* J Mat Chem, 2010. **20**(44): p. 9941-9947.

124. Larson, T.A., et al., *Hybrid plasmonic magnetic nanoparticles as molecular specific agents for MRI/optical imaging and photothermal therapy of cancer cells.* Nanotechnology, 2007. **18**(32).

125. Shekhawat, G.S., and Dravid, V.P., *Nanomechanical Sensors: Bent on detecting cancer.* Nat Nanotechnol, 2013. **8**(2): p. 77-78.

126. Boisen, A., and Thundat, T., *Design & fabrication of cantilever array biosensors.* Materials Today, 2009. **12**(9): p. 32-38.

127. Burg, T.P., et al., *Weighing of biomolecules, single cells and single nanoparticles in fluid.* Nature, 2007. **446**(7139): p. 1066-9.

128. Cao, G., et al., *Nanostructres and nanomaterials: Synthesis, Properties and Applications*. Vol. 2. 2004, New Jersey, USA: World Scientific Publishing Co.

129. Alvarez, M., and Lechuga, L.M., *Microcantilever-based platforms as biosensing tools.* Analyst, 2010. **135**(5): p. 827-36.

130. Yang, Y.T., et al., *Zeptogram-scale nanomechanical mass sensing.* Nano Lett, 2006. **6**(4): p. 583-6.

131. Arlett, J.L., Myers, E.B., and Roukes, M.L., *Comparative advantages of mechanical biosensors.* Nat Nanotechnol, 2011. **6**(4): p. 203-15.

132. Hwang, K.S., et al., *Micro- and nanocantilever devices and systems for biomolecule detection.* Annu Rev Anal Chem, 2009. **2**: p. 77-98.

133. von Muhlen, M.G., et al., *Label-free biomarker sensing in undiluted serum with suspended microchannel resonators.* Anal Chem, 2010. **82**(5): p. 1905-10.

134. Loo, L., et al., *Highly sensitive detection of HER2 extracellular domain in the serum of breast cancer patients by piezoelectric microcantilevers.* Anal Chem, 2011. **83**(9): p. 3392-7.

135. Kerr, C.A. and de la Rica, R., *Photoluminescent nanosensors for intracellular detection.* Analytical Methods, 2015. **7**(17): p. 7067-7075.

136. Hoo, C.M., et al., *A comparison of atomic force microscopy (AFM) and dynamic light scattering (DLS) methods to characterize nanoparticle size distributions.* J Nanopart Res, 2008. **10**: p. 89-96.

137. Chauhan, V.M., et al., *Mapping the pharyngeal and intestinal pH of Caenorhabditis elegans and real-time luminal pH oscillations using extended dynamic range pH-sensitive nanosensors.* ACS Nano, 2013. **7**(6): p. 5577-87.

138. Honeychurch, K.C., *Nanosensors for Chemical and Biological Applications: Sensing with Nanotubes, Nanowires and Nanoparticles*. 2014, Oxford, UK: Elsevier.

139. McNeil, S.E., *Characterization of Nanoparticles Intended for Drug Delivery*. 2011, New York, USA: Humana Press.

140. Grobmyer, S. R., and Moudgil, B.M., *Cancer Nanotechnology: Methods and Protocols*. 2010, New York, USA: Humana Press.

141. Available from: http://www.malvern.com/en/pdf/secure/TN101104ZetaPotentialIntroduction.pdf

142. Desai, A., *Development of optical pH nanosensors for biological insights into the intracellular trafficking of nanomedicines*, in *School of Pharmacy*. 2014, University of Nottingham: Nottingham, UK.

143. Goodhew, P.J., Humpherys., J., and Beanland, R., *Electron Microscopy and Analysis*. 2001, London, UK: Taylor & Francis.

144. Echlin, P., *Handbook of Sample Preparation for Scanning Electron Microscopy and X-Ray Microanalysis*. 2009, New York, USA: Springer.

145. Reimer, L., *Transmission Electron Microscopy: Physics of Image Formation and Microanalysis*. Fourth ed. Springer Series in Optical Sciences. 1997, Heidelberg, Germany: Springer.

146. Lakowicz, J.R., *Principles of Fluorescence Spectroscopy*. Second ed. 1999, New York, USA: Springer. 11-25, 237-275.

147. Markus, S., Hofkens, J., and Enderlein, J., *Handbook of Fluorescence Spectroscopy and Imaging: From Ensemble to Single Molecules*. 2011, Weinheim, Germany: Wiley.

148. Valeur, B., and Brochon, J.C., *New Trends in Fluorescence Spectroscopy: Applications to Chemical and Life Sciences*. 2001, New York, USA: Springer.

149. Goldys, E.M., *Fluorescence Applications in Biotechnology and Life Sciences*. 2009, Massachusetts, USA: Wiley-Blackwell.

150. Lakowicz, J.R., *Topics in Fluorescence Spectroscopy: Principles*. Vol. 2. 2002, New York, USA: Kluwer Academic Publishers. 127-132.

151. Resch-Genger, U., *Standardization and Quality Assurance in Fluorescence Measurements II: Bioanalytical and Biomedical Applications*. Springer Series on Fluorescence. 2008, Heidelberg, Germany: Springer.

152. Fernandez-Suarez, M., and Ting, A.Y., *Fluorescent probes for super-resolution imaging in living cells.* Nat Rev Mol Cell Biol, 2008. **9**(12): p. 929-43.

153. Taki, M., et al., *Development of highly sensitive fluorescent probes for detection of intracellular copper(I) in living systems.* J Am Chem Soc, 2010. **132**(17): p. 5938-9.

154. Dean, K.M., and Palmer, A.E., *Advances in fluorescence labeling strategies for dynamic cellular imaging.* Nat Chem Biol, 2014. **10**(7): p. 512-23.

155. Khanna, V.K., *Nanosensors, Physical, Chemical, and Biological*. 2012, Florida, USA: CRC Press. 122-124.

156. Evans, S.M., Janson A.M., and Nyengaard J.R., *Quantitative Methods In Neuroscience: A neuroanatomical Approach*. 2004, Oxford, UK: Oxford University Press. 92-110.

157. Cusano, A., et al., *Optochemical Nanosensors*. 2013, Florida, USA: CRC Press. 147-148; 307-340.

158. Buck, S.M., et al., *Nanoscale probes encapsulated by biologically localized embedding (PEBBLEs) for ion sensing and imaging in live cells.* Talanta, 2004. **63**(1): p. 41-59.

159. Cao, Y., Koo, Y.E.L., and Kopelman, R., *Poly(decyl methacrylate)-based fluorescent PEBBLE swarm nanosensors for measuring dissolved oxygen in biosamples.* Analyst, 2004. **129**(8): p. 745-50.

160. Burns, A., Ow, H., and Wiesner, U., *Fluorescent core-shell silica nanoparticles: towards "Lab on a Particle" architectures for nanobiotechnology.* Chem Soc Rev, 2006. **35**(11): p. 1028-42.

161. Sondergaard, R.V., Henriksen, J.R., and Andresen, T.L., *Design, calibration and application of broad-range optical nanosensors for determining intracellular pH.* Nat Protoc, 2014. **9**(12): p. 2841-58.

162. Si, D., et al., *Nanoparticle PEBBLE sensors for quantitative nanomolar imaging of intracellular free calcium ions.* Anal Chem, 2012. **84**(2): p. 978-86.

163. Poulsen, A.K., Scharff-Poulsen, A.M., and Olsen, L.F., *Horseradish peroxidase embedded in polyacrylamide nanoparticles enables optical detection of reactive oxygen species.* Anal Biochem, 2007. **366**(1): p. 29-36.

164. Xu, H., Aylott, J.W., and Kopelman, R., *Fluorescent nano-PEBBLE sensors designed for intracellular glucose imaging.* Analyst, 2002. **127**(11): p. 1471-7.

165. Sun, H., et al., *Phosphate sensing by fluorescent reporter proteins embedded in polyacrylamide nanoparticles.* ACS Nano, 2008. **2**(1): p. 19-24.

166. Ray, A., et al., *Two-photon nano-PEBBLE sensors: subcellular pH measurements.* Analyst, 2011. **136**(18): p. 3616-22.

167. Kuruppuarachchi, M., et al., *Polyacrylamide Nanoparticles as a Delivery System in Photodynamic Therapy*. Mol. Pharm, 2011. **8**(3): p. 920-931.

168. Wang, S., et al., *Multifunctional biodegradable polyacrylamide nanocarriers for cancer theranostics--a "see and treat" strategy.* ACS Nano, 2012. **6**(8): p. 6843-51.

169. Sun, H., et al., *Synthesis and Characterization of Ratiometric, pH Sensing Nanoparticles with Covalently Attached Fluorescent Dyes.* Chem. Mater., 2006. **18**(15): p. 3381-33984.

170. Wang, F., et al., *Luminescent nanomaterials for biological labelling.* Nanotechnology, 2006. **17**(1): p. 1-13.

171. Wang, L., and Tan, W., *Multicolor FRET silica nanoparticles by single wavelength excitation.* Nano Lett, 2006. **6**(1): p. 84-8.

172. Burns, A., et al., *Core/Shell fluorescent silica nanoparticles for chemical sensing: towards single-particle laboratories.* Small, 2006. **2**(6): p. 723-6.

173. Bagwe, R.P., Hilliard, L.R., and Tan, W., *Surface modification of silica nanoparticles to reduce aggregation and nonspecific binding.* Langmuir, 2006. **22**(9): p. 4357-62.

174. Zhang, Y., et al., *Silica-based nanocapsules: synthesis, structure control and biomedical applications.* Chem Soc Rev, 2015. **44**(1): p. 315-35.

175. Tamba, B.I., et al., *Silica nanoparticles: preparation, characterization and in vitro/in vivo biodistribution studies.* Eur J Pharm Sci, 2015. **71**: p. 46-55.

176. Lin, Y.S., Abadeer, N., and Haynes, C.L., *Stability of small mesoporous silica nanoparticles in biological media.* ChemComm, 2011. **47**(1): p. 532-4.

177. Stöber, W., Arthur F., and Bohn, E., *Controlled Growth of Monodisperse Silica Spheres in the Micron Size Range.* J Col Interface Sci, 1968. **26**: p. 62-69.

178. Xu, J., et al., *Multicolor dye-doped silica nanoparticles independent of FRET.* Langmuir, 2010. **26**(20): p. 15722-5.

179. He, X., et al., *In vivo study of biodistribution and urinary excretion of surface-modified silica nanoparticles.* Anal Chem, 2008. **80**(24): p. 9597-603.

180. Cai, L., et al., *MUC-1 aptamer-conjugated dye-doped silica nanoparticles for MCF-7 cells detection.* Biomaterials, 2013. **34**(2): p. 371-81.

181. Wu, S.H., Mou, C.Y., and Lin, H.P., *Synthesis of mesoporous silica nanoparticles.* Chem Soc Rev, 2013. **42**(9): p. 3862-75.

182. Coble, P., et al., *Aquatic Organic Matter Fluorescence*. 2014, Cambridge, UK: Cambridge University Press.

183. Valeur, B., and Berberan-Santos, M.N., *Molecular Fluorescence: Principles and Applications*. 2012, Weinheim, Germany: Wiley, VCH.

184. Owen, C.S., *Comparison of spectrum-shifting intracellular pH probes 5'(and 6')-carboxy-10-dimethylamino-3-hydroxyspiro [7H-benzo[c] xanthene-7, 1'(3'H)-isobenzofuran]-3'-one and 2',7'-biscarboxyethyl-5(and 6)-carboxyfluorescein.* Anal Biochem, 1992. **204**(1): p. 65-71.

185. Griffiths, J.R., *Are cancer cells acidic?* Br J Cancer, 1991. **64**(3): p. 425-7.

186. Valli, M., et al., *Intracellular pH distribution in Saccharomyces cerevisiae cell populations, analyzed by flow cytometry.* Appl Environ Microbiol, 2005. **71**(3): p. 1515-21.

187. Benjaminsen, R.V., et al., *Evaluating nanoparticle sensor design for intracellular pH measurements.* ACS Nano, 2011. **5**(7): p. 5864-73.

188. Damaghi, M., Wojtkowiak, J.W., and Gillies, R.J., *pH sensing and regulation in cancer.* Front Physiol, 2013. **4**: p. 370.

189. Casey, J.R., Grinstein, S., and Orlowski, J., *Sensors and regulators of intracellular pH.* Nat Rev Mol Cell Biol, 2010. **11**(1): p. 50-61.

190. Orij, R., et al., *In vivo measurement of cytosolic and mitochondrial pH using a pH-sensitive GFP derivative in Saccharomyces cerevisiae reveals a relation between intracellular pH and growth.* Microbiology, 2009. **155**(Pt 1): p. 268-78.

191. Boron, F.W., and Boulpaep, E.L., *Medical Physiology: A Cellular And Molecular Approach*. 2009, Philadelphia, USA: Elsevier.

192. Shapiro, H.M., *Practical Flow Cytometry*. 2003, New Hesy, USA: John Wiley & Sons Ltd. 47-48.

193. Doussineau, T., Trupp, S., and Mohr, G.J., *Ratiometric pH-nanosensors based on rhodamine-doped silica nanoparticles functionalized with a naphthalimide derivative.* J Colloid Interface Sci, 2009. **339**(1): p. 266-70.

194. Park, E.J., et al., *Ratiometric optical PEBBLE nanosensors for real-time magnesium ion concentrations inside viable cells.* Anal Chem, 2003. **75**(15): p. 3784-91.

195. Gao, X., et al., *Carbon-dot-based ratiometric fluorescent probe for imaging and biosensing of superoxide anion in live cells.* Anal Chem, 2014. **86**(14): p. 7071-8.

196. Albers, A.E., Okreglak, V.S., and Chang, C.J., *A FRET-based approach to ratiometric fluorescence detection of hydrogen peroxide.* J Am Chem Soc, 2006. **128**(30): p. 9640-1.

197. Bozym, R.A., et al., *Measuring picomolar intracellular exchangeable zinc in PC-12 cells using a ratiometric fluorescence biosensor.* ACS Chem Biol, 2006. **1**(2): p. 103-11.

198. Chen, X., et al., *Using aptamer-conjugated fluorescence resonance energy transfer nanoparticles for multiplexed cancer cell monitoring.* Anal Chem, 2009. **81**(16): p. 7009-14.

199. Roy, S., et al., *Novel multiparametric approach to elucidate the surface amine-silanization reaction profile on fluorescent silica nanoparticles.* Langmuir, 2010. **26**(23): p. 18125-34.

200. McIlvaine, T.C., *A Buffer Solution for Colorimetric Comparsion.* J. Biol. Chem., 1921. **49**: p. 183-186.

201. Adsley, R., *Visualization of the cellular uptake of nanoparticles*, in *School of Pharmacy*. 2013, University of Nottingham: Nottingham, UK.

202. Sun, H., et al., *Polymeric nanosensors for measuring the full dynamic pH range of endosomes and lysosomes in mammalian cells.* J Biomed Nanotechnol, 2009. **5**(6): p. 676-82.

203. Rossi, L.M., et al., *Stober synthesis of monodispersed luminescent silica nanoparticles for bioanalytical assays.* Langmuir, 2005. **21**(10): p. 4277-80.

204. Rao, K.S., et al., *A novel method for synthesis of silica nanoparticles.* J Col Interface Sci, 2005. **289**(1): p. 125-31.

205. Canton, G., et al., *Modified Stöber synthesis of highly luminscent dye-doped silica nanoparticles.* J Nanopart Res, 2011. **13**: p. 4349-4356.

206. Lim, J., Ha, A.S., and Lee, J.K., *Precise Size-control of Silica Nanoparticles via Alkoxy Exchange Equilibrium of Tetraethyl Orthosilicate (TEOS) in the Mixed Alcohol Solution.* Bull. Korean Chem. Soc., 2012. **33**(3): p. 1067-1070.

207. Estévez, M.C., et al., *Highly Fluorescent Dye-Doped Silica Nanoparticles Increase Flow Cytometry Sensitivity for Cancer Cell Monitoring.* Nano Res, 2009. **2**: p. 448-461.

208. Ow, H., et al., *Bright and stable core-shell fluorescent silica nanoparticles.* Nano Lett, 2005. **5**(1): p. 113-7.

209. Kim, J.W., Kim, A.L.U., and Kim, C.K., *Size Control of Silica Nanoparticles and Their Surface Treatment for Fabrication of Dental Nanocomposites.* Biomacromol, 2007. **8**: p. 215-222.

210. Weimarn, P.P.V., *The Precipitation Laws.* Chem. Rev., 1925. **2**(2): p. 217-242.

211. Nozawa, K., et al., *Smart control of monodisperse Stober silica particles: effect of reactant addition rate on growth process.* Langmuir, 2005. **21**(4): p. 1516-23.

212. van Blaaderen, A., van Geest, A.J., and Vrij, A., *Monodisperse colloidal silica spheres from tetraalkoxysilanes: Particle formation and growth mechanism.* J Col Interface Sci, 1992. **154**(2): p. 481-450.

213. Yun, D.S., Kim, H.J., and Yoo, A.J.W., *Preparation of Silica Nanospheres: Effect of Silicon Alkoxide and Alcohol on Silica Nanospheres.* Bull. Korean Chem. Soc., 2005. **26**(12): p. 1927-1928.

214. Tephly, T.R., *The toxicity of methanol.* Life Sci, 1991. **48**(11): p. 1031-41.

215. Im, S.H., et al., *Synthesis and characterization of monodisperse silica colloids loaded with superparamagnetic iron oxide nanoparticles.* Chem Phy Let, 2005. **401**(1-3): p. 19-23.

216. Deng, Y.H., et al., *Investigation of formation of silica-coated magnetite nanoparticles via sol–gel approach.* Colloids and Surfaces A: Physicochemical and Engineering Aspects, 2005. **262**(1-3): p. 87-93.

217. He, C., et al., *Effects of particle size and surface charge on cellular uptake and biodistribution of polymeric nanoparticles.* Biomaterials, 2010. **31**(13): p. 3657-66.

218. Frohlich, E., *The role of surface charge in cellular uptake and cytotoxicity of medical nanoparticles.* Int J Nanomedicine, 2012. **7**: p. 5577-91.

219. Gupta, R., and Chaudhury, N.K., *Entrapment of biomolecules in sol-gel matrix for applications in biosensors: problems and future prospects.* Biosens Bioelectron, 2007. **22**(11): p. 2387-99.

220. Borisov, S.M., and Wolfbeis, O.S., *Optical biosensors.* Chem Rev, 2008. **108**(2): p. 423-61.

221. Walker, G.M., *Yeast Physiology and Biotechnology*. 1998, West Sussex, UK: John Wiley & Sons Ltd. 1-11; 101-108.

222. Schaechte, M., *Eukaryotic Microbes*. 2012, California, USA: Elsevier Inc. 3-17.

223. Walker, J.M., and Rapley, R., *Molecular Biology and Biotechnology*. 2009, Cambridge, UK: RSC Publishing. 159-170.

224. Li, S.C., and Kane, P.M., *The yeast lysosome-like vacuole: endpoint and crossroads.* Biochim Biophys Acta, 2009. **1793**(4): p. 650-63.

225. Wiederhold, E., et al., *The yeast vacuolar membrane proteome.* Mol Cell Proteomics, 2009. **8**(2): p. 380-92.

226. Day, D.A., Miller, H., and Whelan, J., *Plant Mitochondria: From Genome to Function*. Vol. 17. 2004: Springer Science. 25-27.

227. Toole, G., and Toole, S., *Essential A2 Biology for OCR*. 2004, Cheltenham, UK: Nelson Thornes.

228. Ruiz-Herrer, J., *Fungal Cell Wall: Structure, Synthesis, and Assembly*. Second Edition ed., Florida, USA: CRC Publisher.

229. Lipke, P.N., and Ovalle, R., *Cell wall architecture in yeast: new structure and new challenges.* J Bacteriol, 1998. **180**(15): p. 3735-40.

230. Aguilar-Uscanga, B., and Francois, J.M., *A study of the yeast cell wall composition and structure in response to growth conditions and mode of cultivation.* Lett Appl Microbiol, 2003. **37**(3): p. 268-74.

231. van der Rest, M.E., et al., *The plasma membrane of Saccharomyces cerevisiae: structure, function, and biogenesis.* Microbiol Rev, 1995. **59**(2): p. 304-22.

232. Griffin, D.A., *Fungal Physiology*. Second ed. 1993, New York, USA: Wiley-Liss, Inc. 110-118.

233. Werner-Washburne, M., et al., *Stationary phase in the yeast Saccharomyces cerevisiae.* Microbiol Rev, 1993. **57**(2): p. 383-401.

234. Hardwic, W., *Handbook of Brewing*. 1995, New York, USA: Marcel Dekker, Inc. 329-331.

235. Herman, P.K., *Stationary phase in yeast.* Curr Opin Microbiol, 2002. **5**(6): p. 602-7.

236. Satyanarayana, T., and Kunze, G., *Yeast Biotechnology: Diversity and Applications*. 2009: Springer. 348.

237. Groves, J.D., et al., *Functional cell surface expression of the anion transport domain of human red cell band 3 (AE1) in the yeast*

Saccharomyces cerevisiae. Proc Natl Acad Sci U S A, 1996. **93**(22): p. 12245-50.

238. Xiao, W., *Yeast Protocols*. Second ed. 2006, New Hersy, USA: Humana Press. 8-12.

239. Imai, T., and Ohno, T., *The relationship between viability and intracellular pH in the yeast Saccharomyces cerevisiae.* Appl Environ Microbiol, 1995. **61**(10): p. 3604-8.

240. Orij, R., Brul, S., and Smits, G.J., *Intracellular pH is a tightly controlled signal in yeast.* Biochim Biophys Acta, 2011. **1810**(10): p. 933-44.

241. Diakov, T.T., Tarsio, M., and Kane, P.M., *Measurement of vacuolar and cytosolic pH in vivo in yeast cell suspensions.* J Vis Exp, 2013(74).

242. Martinez-Munoz, G.A., and Kane, P., *Vacuolar and plasma membrane proton pumps collaborate to achieve cytosolic pH homeostasis in yeast.* J Biol Chem, 2008. **283**(29): p. 20309-19.

243. Hughes, A.L., and Gottschling, D.E., *An early age increase in vacuolar pH limits mitochondrial function and lifespan in yeast.* Nature, 2012. **492**(7428): p. 261.

244. Mason, A.B., Kardos, T.B., and Monk, B.C., *Regulation and pH-dependent expression of a bilaterally truncated yeast plasma membrane H+-ATPase*. Biochim Biophys Acta, 1998. **1372**(2): p. 261-71.

245. Valkonen, M., et al., *Noninvasive high-throughput single-cell analysis of the intracellular pH of Saccharomyces cerevisiae by ratiometric flow cytometry.* Appl Environ Microbiol, 2013. **79**(23): p. 7179-87.

246. Haworth, R.S., and Fliegel, L., *Intracellular pH in Schizosaccharomyces pombe--comparison with Saccharomyces cerevisiae.* Mol Cell Biochem, 1993. **124**(2): p. 131-40.

247. Breeuwer, P. and Abee, T., *Assessment of the intracellular pH of immobilized and continuously perfused yeast cells employing fluorescence ratio imaging analysis.* J Microbiol Methods, 2000. **39**(3): p. 253-64.

248. Imai, T., and Ohno, T., *Measurement of Yeast Intracellular Ph by Image-Processing and the Change It Undergoes during Growth-Phase.* J Biotechnol, 1995. **38**(2): p. 165-172.

249. Slavik, J., *Intracellular pH of yeast cells measured with fluorescent probes.* FEBS Lett, 1982. **140**(1): p. 22-6.

250. Navon, G., et al., *Phosphorus-31 nuclear magnetic resonance studies of wild-type and glycolytic pathway mutants of Saccharomyces cerevisiae.* Biochem, 1979. **18**(21): p. 4487-99.

251. Gillies, R.J., et al., *31P NMR studies of intracellular pH and phosphate metabolism during cell division cycle of Saccharomyces cerevisiae.* Proc Natl Acad Sci U S A, 1981. **78**(4): p. 2125-9.

252. Weigert, C., et al., *Application of a short intracellular pH method to flow cytometry for determining Saccharomyces cerevisiae vitality.* Appl Environ Microbiol, 2009. **75**(17): p. 5615-20.

253. Kunze, I.I., et al., *The green fluorescent protein targets secretory proteins to the yeast vacuole.* Biochim Biophys Acta, 1999. **1410**(3): p. 287-98.

254. Dang, T.D., et al., *Monitoring the intracellular pH of Zygosaccharomyces bailii by green fluorescent protein.* Int J Food Microbiol, 2012. **156**(3): p. 290-5.

255. Kresnowati, M.T., et al., *Measurement of fast dynamic intracellular pH in Saccharomyces cerevisiae using benzoic acid pulse.* Biotechnol Bioeng, 2007. **97**(1): p. 86-98.

256. Guldfeldt, L.U., and Arneborg, N., *Measurement of the effects of acetic acid and extracellular pH on intracellular pH of nonfermenting, individual Saccharomyces cerevisiae cells by fluorescence microscopy.* Appl Environ Microbiol, 1998. **64**(2): p. 530-4.

257. Aon, J.C., and Cortassa, S., *Fluorescent measurement of the intracellular pH during sporulation of Saccharomyces cerevisiae.* FEMS Microbiol Lett, 1997. **153**(1): p. 17-23.

258. Pena, A., et al., *Proton pumping and the internal pH of yeast cells, measured with pyranine introduced by electroporation.* J Bacteriol, 1995. **177**(4): p. 1017-22.

259. Poulsen, A.K., et al., *Probing glycolytic and membrane potential oscillations in Saccharomyces cerevisiae.* Biochem, 2008. **47**(28): p. 7477-84.

260. Chung, T.H., et al., *The effect of surface charge on the uptake and biological function of mesoporous silica nanoparticles in 3T3-L1 cells and human mesenchymal stem cells.* Biomater, 2007. **28**(19): p. 2959-66.

261. Costantini, L.M., Gilberti, R.M., and Knecht, D.A., *The phagocytosis and toxicity of amorphous silica.* PLoS One, 2011. **6**(2): p. e14647.

262. Hocherl, A., et al., *Competitive cellular uptake of nanoparticles made from polystyrene, poly(methyl methacrylate), and polylactide.* Macromol Biosci, 2012. **12**(4): p. 454-64.

263. Yue, Z.G., et al., *Surface charge affects cellular uptake and intracellular trafficking of chitosan-based nanoparticles.* Biomacromolecules, 2011. **12**(7): p. 2440-6.

264. Lankoff, A., et al., *Effect of surface modification of silica nanoparticles on toxicity and cellular uptake by human peripheral blood lymphocytes in vitro.* Nanotoxicology, 2013. **7**(3): p. 235-50.

265. Nomura, T., et al., *Exposure of the yeast Saccharomyces cerevisiae to functionalized polystyrene latex nanoparticles: influence of surface charge on toxicity.* Environ Sci Technol, 2013. **47**(7): p. 3417-23.

266. Arvizo, R.R., et al., *Effect of nanoparticle surface charge at the plasma membrane and beyond.* Nano Lett, 2010. **10**(7): p. 2543-8.

267. Jacobson, B.C., and Branton, D., *Plasma membrane: rapid isolation and exposure of the cytoplasmic surface by use of positively charged beads.* Science, 1977. **195**(4275): p. 302-330.

268. Kenausis, G.L., et al., *Poly(L-lysine)-g-Poly(ethylene glycol) Layers on Metal Oxide Surfaces: Attachment Mechanism and Effects of Polymer Architecture on Resistance to Protein Adsorption.* J. Phys. Chem. B, 2000. **104**: p. 3298-330.

269. Asenio, J.A., *Separation Prcess in Biotechnology*. 1990, New York, USA: Marcel Dekker Inc. 688-700.

270. Coogan, M.P., et al., *Probing intracellular oxygen by quenched phosphorescence lifetimes of nanoparticles containing polyacrylamide-embedded [Ru(dpp(SO3Na)2)3]Cl2.* Photochem Photobiol Sci, 2010. **9**(1): p. 103-9.

271. Kawai, S., Hashimoto, W., and Murata, K., *Transformation of Saccharomyces cerevisiae and other fungi: methods and possible underlying mechanism.* Bioeng Bugs, 2010. **1**(6): p. 395-403.

272. Piper, P.W., et al., *Hsp30, the integral plasma membrane heat shock protein of Saccharomyces cerevisiae, is a stress-inducible regulator of plasma membrane H(+)-ATPase.* Cell Stress Chaperones, 1997. **2**(1): p. 12-24.

273. Miyazaki, J., et al., *Adhesion and internalization of functionalized polystyrene latex nanoparticles toward the yeast Saccharomyces cerevisiae.* Advanced Powder Technology, 2014. **25**: p. 1394–1397.

274. Herman, P., et al., *Electroporative adjustment of pH in living yeast cells: ratiometric fluorescence pH imaging.* J Fluoresc, 2005. **15**(5): p. 763-8.

275. Goldman, E., and Green, L.H., *Practical Handbook of Microbiology*. Second ed. 2008, Florida, USA: CRC Press. 17-19.

276. Peng, J., et al., *Noninvasive monitoring of intracellular pH change induced by drug stimulation using silica nanoparticle sensors.* Anal Bioanal Chem, 2007. **388**(3): p. 645-54.

277. Wang, X.D., et al., *Ultra-small, highly stable, and sensitive dual nanosensors for imaging intracellular oxygen and pH in cytosol.* J Am Chem Soc, 2012. **134**(41): p. 17011-4.

278. Ruedas-Rama, M.J., et al., *Quantum dot photoluminescence lifetime-based pH nanosensor*. ChemComm, 2011. **47**(10): p. 2898-900.

279. Dechant, R., et al., *Cytosolic pH is a second messenger for glucose and regulates the PKA pathway through V-ATPase.* Embo Journal, 2010. **29**(15): p. 2515-2526.

280. Ozalp, V.C., et al., *Time-resolved measurements of intracellular ATP in the yeast Saccharomyces cerevisiae using a new type of nanobiosensor.* J Biol Chem, 2010. **285**(48): p. 37579-88.

281. Wolfbeis, O.S., *Fluorescence Spectroscopy: New Methods and Applications*. 1993, Berlin, Germany: Springer-Verlag. 79-81.

282. Tang, Y., and Stratton, C.W., *Advanced Techniques in Diagnostic Microbiology*. Second ed. 2013, New York, USA: Springer. 418-420.

283. Albani, J.R., *Principles and Applications of Fluorescence Spectroscopy*. 2007, Oxford, UK: Blackwell Science Ltd. 139-151.

284. Demchenko, A.P., *Introduction to Fluorescence Sensing*. 2009: Springer. 69-70.

285. Buxbaum, E., *Biophysical Chemistry of Proteins: An Introduction to Laboratory Methods*. 2011, New York, USA: Springer. 44-48.

286. T. Förster, *Zwischenmolekulare Energiewanderung und Fluoreszenz.* Annalen. Phys., 1948. **2**: p. 55-75 [Article in In German, English translation available from; Mielczarek EV, Greenbaum, E., and Knox, R.X., Biological physics. 1993, New York , USA: American Institute of Physics. 148–160].

287. Latt, S.A., Cheung, H.T., and Blout, E.R., *Energy Transfer. A System with Relatively Fixed Donor-Acceptor Separation.* J Am Chem Soc, 1965. **87**: p. 995-1003.

288. Gao, F., et al., *A DNA hybridization detection based on fluorescence resonance energy transfer between dye-doped core-shell silica nanoparticles and gold nanoparticles.* Analyst, 2011. **136**(19): p. 3973-80.

289. Qiang, W., et al., *Label-free detection of adenosine based on fluorescence resonance energy transfer between fluorescent silica nanoparticles and unmodified gold nanoparticles.* Anal Chim Acta, 2014. **828**: p. 92-98.

290. Nguyen, D.N., Ngo, T.T., and Nguyen, Q.L., *Highly sensitive fluorescence resonance energy transfer (FRET)-based nanosensor for rapid detection of clenbuterol.* Adv. Nat. Sci.: Nanosci. Nanotechnol, 2012. **3**: p. 035011.

291. Chen, G., et al., *Fluorescent Nanosensors Based on Fluorescence Resonance Energy Transfer (FRET).* Industrial & Engineering Chemistry Research, 2013. **52**(33): p. 11228-11245.

292. Jue, T., *Handbook of Modern Biophysics: Biomedical Applications of Biophysics*. 2010, New York: Humana Press. 121-133.

293. Stryer, L., *Fluorescence energy transfer as a spectroscopic ruler.* Annu Rev Biochem, 1978. **47**: p. 819-46.

294. Stryer, L., and Haugland, R.P., *Energy transfer: a spectroscopic ruler.* Proc Natl Acad Sci USA, 1967. **58**(2): p. 719-26.

295. Braslavsky, S.E., et al., *Pitfalls and limitations in the practical use of Förster's theory of resonance energy transfer.* Photochem. Photobiol. Sci., 2008. **7**: p. 1444-1448.

296. Pawley, J.B., *Handbook of Biological Confocal Microscopy*. Third ed. 2006, New York, USA: Springer. 792-793.

297. Wu, P., and Brand, L., *Resonance energy transfer: methods and applications.* Anal Biochem, 1994. **218**(1): p. 1-13.

298. Freeman, R., and Willner, I., *Optical molecular sensing with semiconductor quantum dots (QDs).* Chem Soc Rev, 2012. **41**(10): p. 4067-85.

299. van der Ploeg, R., Goudelis, S.T., and den Blaauwen, T., *Validation of FRET Assay for the Screening of Growth Inhibitors of Escherichia coli Reveals Elongasome Assembly Dynamics.* Int J Mol Sci, 2015. **16**(8): p. 17637-54.

300. Manoharan, G.B., et al., *FRET-based screening assay using small-molecule photoluminescent probes in lysate of cells overexpressing RFP-fused protein kinases.* Anal Biochem, 2015. **481**: p. 10-7.

301. He, X., et al., *A highly selective sandwich-type FRET assay for ATP detection based on silica coated photon upconverting nanoparticles and split aptamer.* Talanta, 2013. **111**: p. 105-10.

302. Zhou, W., et al., *Aptamer-based biosensors for biomedical diagnostics.* Analyst, 2014. **139**(11): p. 2627-40.

303. Carlson, H.J., and Campbell, R.E., *Genetically encoded FRET-based biosensors for multiparameter fluorescence imaging.* Curr Opin Biotechnol, 2009. **20**(1): p. 19-27.

304. Piston, D.W., and Kremers, G.J., *Fluorescent protein FRET: the good, the bad and the ugly.* Trends Biochem Sci, 2007. **32**(9): p. 407-14.

305. Gu, Y., et al., *Quantitative fluorescence resonance energy transfer (FRET) measurement with acceptor photobleaching and spectral unmixing.* J Microsc, 2004. **215**(Pt 2): p. 162-73.

306. Kim, G., et al., *The detection of platelet derived growth factor using decoupling of quencher-oligonucleotide from aptamer/quantum dot bioconjugates.* Nanotechnology. 2009. **20**(17): p. 175503.

307. Zhang, C.Y., and Hu, J., *Single quantum dot-based nanosensor for multiple DNA detection.* Anal Chem, 2010. **82**(5): p. 1921-7.

308. Medintz, I.L., et al., *Self-assembled nanoscale biosensors based on quantum dot FRET donors.* Nat Mater, 2003. **2**(9): p. 630-8.

309. Tyagi, S., Bratu, D.P., and Kramer, F.R., *Multicolor molecular beacons for allele discrimination.* Nat Biotechnol, 1998. **16**(1): p. 49-53.

310. Algar, W.R., et al., *Semiconductor quantum dots in bioanalysis: crossing the valley of death.* Anal Chem, 2011. **83**(23): p. 8826-37.

311. Wang, X., and Guo, X., *Ultrasensitive Pb2+ detection based on fluorescence resonance energy transfer (FRET) between quantum dots and gold nanoparticles.* Analyst, 2009. **134**(7): p. 1348-54.

312. Wolfbeis, O.S., *An overview of nanoparticles commonly used in fluorescent bioimaging.* Chem Soc Rev, 2015. **44**(14): p. 4743-68.

313. Shi, J., et al., *A fluorescence resonance energy transfer (FRET) biosensor based on graphene quantum dots (GQDs) and gold nanoparticles (AuNPs) for the detection of mecA gene sequence of Staphylococcus aureus.* Biosens Bioelectron, 2015. **67**: p. 595-600.

314. Aoki, T., et al., *Fluorescence resonance energy transfer-based assay for DNA-binding protein tagged by green fluorescent protein.* Biosci Biotechnol Biochem, 2006. **70**(8): p. 1921-7.

315. Heim, R., and Tsien, R.Y., *Engineering green fluorescent protein for improved brightness, longer wavelengths and fluorescence resonance energy transfer.* Curr Biol, 1996. **6**(2): p. 178-82.

316. Clegg, R.M., *The history of FRET: From conception to the labor of birth, in Reviews in Fluorescence*. 2006, New York: Springer. 1-45.

317. Dexter, D.L., *A Theory of Sensitized Luminescence in Solids.* J. Chem. Phys., 1953. **21**: p. 836.

318. Hagaman, E.W., et al., *13C NMR characterization of the organic constituents in ligand-modified hexagonal mesoporous silicas: media for the synthesis of small, uniform-size gold nanoparticles.* Langmuir, 2004. **20**(22): p. 9577-84.

319. Murphy, C.F., et al., *Probing Förster and Dexter Energy-Transfer Mechanisms in Fluorescent Conjugated Polymer Chemosensors.* J. Phys. Chem. B, 2994. **198**(5): p. 1537-1543.

320. Li, Z., Li, Z.R., and Men, H., *Organic Light-Emitting Materials and Devices*. 2007, Florida, USA: CRC Press. 415-417.

321. Chen, G., et al., *Fluorescent Nanosensors Based on Fluorescence Resonance Energy Transfer (FRET).* Ind. Eng. Chem. Res., 2013. **52**(33): p. 11228-11245.

322. Breshike, C.J., Riskowski, R.A., and Strouse, G.F., *Leaving Förster Resonance Energy Transfer Behind: Nanometal Surface Energy Transfer Predicts the Size-Enhanced Energy Coupling between a Metal Nanoparticle and an Emitting Dipole.* J Phys Chem C, 2013. **117**(45): p. 23942-23949.

323. Li, M., et al., *Detection of mercury(II) by quantum dot/DNA/gold nanoparticle ensemble based nanosensor via nanometal surface energy transfer.* Anal Chem, 2011. **83**(18): p. 7061-5.

324. Dubertret, B., Calame, M., and Libchaber, A.J., *Single-mismatch detection using gold-quenched fluorescent oligonucleotides.* Nat Biotechnol, 2001. **19**(4): p. 365-70.

325. Hevekerl, H., et al., *Forster resonance energy transfer beyond 10 nm: exploiting the triplet state kinetics of organic fluorophores.* J Phys Chem B, 2011. **115**(45): p. 13360-70.

326. Jennings, T.L., Singh, M.P., and Strouse, G.F., *Fluorescent lifetime quenching near d = 1.5 nm gold nanoparticles: probing NSET validity.* J Am Chem Soc, 2006. **128**(16): p. 5462-7.

327. Jennings, T.L., et al., *NSET molecular beacon analysis of hammerhead RNA substrate binding and catalysis.* Nano Lett, 2006. **6**(7): p. 1318-24.

328. Yun, C.S., et al., *Nanometal surface energy transfer in optical rulers, breaking the FRET barrier.* J Am Chem Soc, 2005. **127**(9): p. 3115-9.

329. Griffin, J., et al., *Size- and distance-dependent nanoparticle surface-energy transfer (NSET) method for selective sensing of hepatitis C virus RNA.* Chemistry, 2009. **15**(2): p. 342-51.

330. Swathi, R.S., and Sebastian, K.L., *Resonance energy transfer from a fluorescent dye molecule to plasmon and electron-hole excitations of a metal nanoparticle.* J Chem Phys, 2007. **126**(23): p. 234701.

331. Chatterjee, S., et al., *Investigating the distance limit of a metal nanoparticle based spectroscopic ruler.* Biomed Opt Express, 2011. **2**(6): p. 1727-33.

332. Kikkeri, R., et al., *Quantum dot nanometal surface energy transfer based biosensing of sialic acid compositions and linkages in biological samples.* Anal Chem, 2013. **85**(8): p. 3864-70.

333. Samanta, A., et al., *Fluorescence quenching of quantum dots by gold nanoparticles: a potential long range spectroscopic ruler.* Nano Lett, 2014. **14**(9): p. 5052-7.

334. Pons, T., et al., *On the quenching of semiconductor quantum dot photoluminescence by proximal gold nanoparticles.* Nano Lett, 2007. **7**(10): p. 3157-64.

335. Liu, Y., et al., *Fluorescence quenching between unbonded graphene quantum dots and gold nanoparticles upon simple mixing.* RSC Adv., 2014. **4**: p. 35673-35677.

336. Reineck, P., et al., *Distance and wavelength dependent quenching of molecular fluorescence by Au@SiO2 core-shell nanoparticles.* ACS Nano, 2013. **7**(8): p. 6636-48.

337. Gao, F., et al., *Efficient fluorescence energy transfer system between CdTe-doped silica nanoparticles and gold nanoparticles for turn-on fluorescence detection of melamine.* J Agric Food Chem, 2012. **60**(18): p. 4550-8.

338. Lee, E.A., *The Distance-Dependent Fluorescence Enhancement Phenomena in Uniform Size Ag@SiO2@SiO2(dye) Nanocomposites.* Bull. Korean Chem. Soc., 2013. **34**(2): p. 539-544.

339. Bertry, L., et al., *Experimental evidence of luminescence quenching at long coupling distances in europium (III) doped core-shell gold silica nanoparticles.* Gold Bulletin, 2013. **46**(4): p. 349-355.

340. Ray, P.C., et al., *A gold-nanoparticle-based fluorescence resonance energy transfer probe for multiplexed hybridization detection: accurate identification of bio-agents DNA.* Nanotechnology, 2007. **18**(37): p. 375504.

341. Lin, H.H., and Chen, I.C., *Study of the Interaction between Gold Nanoparticles and Rose Bengal Fluorophores with Silica Spacers by*

Time-Resolved Fluorescence Spectroscopy. J Phys Chem C, 2015. **119**(47): p. 26663-26671.

342. Abadeer, N.S., et al., *Distance and plasmon wavelength dependent fluorescence of molecules bound to silica-coated gold nanorods.* ACS Nano, 2014. **8**(8): p. 8392-406.

343. Zhang, C.Y., and Johnson, L.W., *Single quantum-dot-based aptameric nanosensor for cocaine.* Anal Chem, 2009. **81**(8): p. 3051-5.

344. Lukman, S., et al., *Hybrid assembly of DNA-coated gold nanoparticles with water soluble conjugated polymers for studying protein–DNA interaction and ligand inhibition.* RSC Adv., 2014. **4**: p. 8883-8893.

345. Oh, J.H., and Lee, J.S., *Designed hybridization properties of DNA-gold nanoparticle conjugates for the ultraselective detection of a single-base mutation in the breast cancer gene BRCA1.* Anal Chem, 2011. **83**(19): p. 7364-70.

346. Feng, Y., et al., *Efficient fluorescence energy transfer system between fluorescein isothiocyanate and CdTe quantum dots for the detection of silver ions.* Luminescence, 2015.

347. Liberman, A., et al., *Synthesis and surface functionalization of silica nanoparticles for nanomedicine.* Surf Sci Rep, 2014. **69**(2-3): p. 132-158.

348. Wu, X., Wu, M., and Zhao, J.X., *Recent development of silica nanoparticles as delivery vectors for cancer imaging and therapy.* Nanomedicine, 2014. **10**(2): p. 297-312.

349. Tang, L., and Cheng, J., *Nonporous Silica Nanoparticles for Nanomedicine Application.* Nano Today, 2013. **8**(3): p. 290-312.

350. Wang, Y., Wang, Y., and Liu, B., *Fluorescent detection of ATP based on signaling DNA aptamer attached silica nanoparticles.* Nanotechnology, 2008. **19**(41): p. 415605.

351. Herr, J.K., et al., *Aptamer-conjugated nanoparticles for selective collection and detection of cancer cells.* Anal Chem, 2006. **78**(9): p. 2918-24.

352. Mukherjee, A., et al., *Development and screening of a series of antibody-conjugated and silica-coated iron oxide nanoparticles for targeting the prostate-specific membrane antigen.* Chem Med Chem, 2014. **9**(7): p. 1356-60.

353. Wang, L., Yang, C., and Tan, W., *Dual-luminophore-doped silica nanoparticles for multiplexed signaling.* Nano Lett, 2005. **5**(1): p. 37-43.

354. García-Martíne, J., *Nanotechnology for the Energy Challenge*. 2013, Weinheim, Germany: John Wiley & Sons. 142-145.

355. Liu, B., et al., *Water-soluble polymer functionalized CdTe/ZnS quantum dots: a facile ratiometric fluorescent probe for sensitive and selective detection of nitroaromatic explosives.* Chemistry, 2014. **20**(8): p. 2132-7.

356. Zhao, X., et al., *A rapid bioassay for single bacterial cell quantitation using bioconjugated nanoparticles.* PNAS, 2004. **101**(42): p. 15027-15032.

357. Medley, C.D., et al., *Aptamer-conjugated nanoparticles for cancer cell detection.* Anal Chem, 2011. **83**(3): p. 727-34.

358. Rao, K.S., et al., *A novel route for immobilization of oligonucleotides onto modified silica nanoparticles.* Anal Chim Acta, 2006. **576**(2): p. 177-83.

359. Moore, C.J., et al., *Controlling colloidal stability of silica nanoparticles during bioconjugation reactions with proteins and improving their longer-term stability, handling and storage.* J. Mater. Chem. B, 2015. **3**(10): p. 2043-2055.

360. Tang, L., et al., *Aptamer-functionalized, ultra-small, monodisperse silica nanoconjugates for targeted dual-modal imaging of lymph nodes with metastatic tumors.* Angew Chem Int Ed Engl, 2012. **51**(51): p. 12721-6.

361. An, Y., et al., *Preparation and self-assembly of carboxylic acid-functionalized silica.* J Colloid Interface Sci, 2007. **311**(2): p. 507-13.

362. Han, L., et al., *Synthesis of carboxylic group functionalized mesoporous silicas (CFMSs) with various structures.* J. Mater. Chem, 2007. **17**: p. 1216-1221.

363. Hermanson, G.T., *Bioconjugate Techniques*. Second ed. 2008, Oxford, UK: Elsevier.

364. Fox, M.A., and Whitesel, J.K., *Organic Chemistry*. Third ed. 2004, Oxford, UK: Jones and Bartlett International Publishers. 606-610.

365. Wong, S.S., *Chemistry of Protein Conjugation and Cross-Linking*. 2000, Florida, USA: CRC Press. 37-42.

366. Genzer, J., *Soft Matter Gradient Surfaces: Methods and Applications*. 2011, New Jersy, USA: Wiley & Sons Ltd.

367. Xu, H., et al., *Room-temperature preparation and characterization of poly (ethylene glycol)-coated silica nanoparticles for biomedical applications.* J Biomed Mater Res A, 2003. **66**(4): p. 870-9.

368. Cai, X., et al., *Galactose decorated acid-labile nanoparticles encapsulating quantum dots for enhanced cellular uptake and subcellular localization.* Pharm Res, 2012. **29**(8): p. 2167-79.

369. Mallik, R., Wa, C.L., and Hage, D.S., *Development of sulfhydryl-reactive silica for protein immobilization in high-performance affinity chromatography.* Anal Chem, 2007. **79**(4): p. 1411-1424.

370. Chiu, S.J., et al., *Versatile Synthesis of Thiol- and Amine-Bifunctionalized Silica Nanoparticles Based on the Ouzo Effect.* Langmuir, 2014. **30**(26): p. 7676-7686.

371. Zhang, Q., et al., *Functionalized Mesoporous Silica Nanoparticles with Mucoadhesive and Sustained Drug Release Properties for Potential Bladder Cancer Therapy.* Langmuir, 2014. **30**(21): p. 6151-6161.

372. Labéguerie-Egéa, J., McEvoy, H.M., and McDonagh, C., *Synthesis, characterisation and functionalisation of luminescent silica nanoparticles.* J Nanopart Res, 2011. **13**(12): p. 6455-6465.

373. Montalti, M., et al., *Dye-doped silica nanoparticles as luminescent organized systems for nanomedicine.* Chem Soc Rev, 2014. **43**(12): p. 4243-4268.

374. Lahiri, J., et al., *A strategy for the generation of surfaces presenting ligands for studies of binding based on an active ester as a common reactive intermediate: a surface plasmon resonance study.* Anal Chem, 1999. **71**(4): p. 777-90.

375. Burns, A., et al., *Core/Shell Fluorescent Silica Nanoparticlesfor Chemical Sensing: Towards Single-Particle Laboratories.* Small, 2006. **2**(6): p. 723-726.

376. Ding, H.L., et al., *Fe3O4@SiO2Core/Shell Nanoparticles: The Silica Coating Regulations with a Single Core for Different Core Sizes and Shell Thicknesses.* Chem Mater, 2012. **24**(23): p. 4572-4580.

377. Wilson, K. and Walker, J., *Principles and Techniques of Biochemistry and Molecular Biology*. Seventh ed. 2010, Cambridge, UK: Cambridge University Press.

378. Johansson, M.K., et al., *Intramolecular dimers: a new strategy to fluorescence quenching in dual-labeled oligonucleotide probes.* J Am Chem Soc, 2002. **124**(24): p. 6950-6.

379. Gu, M.G., and Kim, H.S., *Advances in Biochemical Engineering/ Biotechnology: Biosensors Based on Aptamers and Enzymes*. 2014, Heidelberg: Springer.

380. Tuerk, C., and Gold, L., *Systematic Evolution of Ligands by Exponential Enrichment - RNA Ligands to Bacteriophage-T4 DNA-Polymerase.* Science, 1990. **249**(4968): p. 505-510.

381. Ellington, A.D., and Szostak, J.W., *Invitro Selection of RNA Molecules That Bind Specific Ligands.* Nature, 1990. **346**(6287): p. 818-822.

382. Mascini, M., *Aptamers in Bioanalysis*. 2009, New Jersey, USA: John Wiley & Sons, Inc.

383. Ma, H., et al., *Nucleic acid aptamers in cancer research, diagnosis and therapy.* Chem Soc Rev, 2015. **44**(5): p. 1240-56.

384. Sun, H.G., et al., *Oligonucleotide Aptamers: New Tools for Targeted Cancer Therapy.* Mol Therapy: Nucleic Acids, 2014. **3**.

385. Hermann, T. and Patel, D.J., *Adaptive recognition by nucleic acid aptamers.* Science, 2000. **287**(5454): p. 820-5.

386. Chen, A. and Yang, S., *Replacing antibodies with aptamers in lateral flow immunoassay.* Biosens Bioelectron, 2015. **71**: p. 230-42.

387. Toh, S.Y., et al., *Aptamers as a replacement for antibodies in enzyme-linked immunosorbent assay.* Biosens Bioelectron, 2015. **64**: p. 392-403.

388. Tombelli, S., Minunni, A., and Mascini, A., *Analytical applications of aptamers.* Biosens Bioelectron, 2005. **20**(12): p. 2424-2434.

389. Torres-Chavolla, E., and Alocilja, E.C., *Aptasensors for detection of microbial and viral pathogens.* Biosens Bioelectron, 2009. **24**(11): p. 3175-82.

390. O'Sullivan, C.K., *Aptasensors - the future of biosensing.* Analytical and Bioanal Chem, 2002. **372**(1): p. 44-48.

391. Bunka, D.H.J., and Stockley, P.G., *Aptamers come of age - at last.* Nat Rev Microbiol, 2006. **4**(8): p. 588-596.

392. Wang, Y., Xu, D.K., and Chen, H.Y., *Aptamer-based silver nanosensor for multiple protein detection.* Lab on a Chip, 2012. **12**(17): p. 3184-89.

393. Keefe, A.D., Pai, S., and Ellington, A., *Aptamers as therapeutics.* Nat Rev Drug Discov, 2010. **9**(7): p. 537-550.

394. Ni, X., et al., *Nucleic Acid Aptamers: Clinical Applications and Promising New Horizons.* Curr Med Chem, 2011. **18**(27): p. 4206-4214.

395. Jayasena, S.D., *Aptamers: an emerging class of molecules that rival antibodies in diagnostics.* Clin Chem, 1999. **45**(9): p. 1628-50.

396. Freeman, R., et al., *Self-assembly of supramolecular aptamer structures for optical or electrochemical sensing.* Analyst, 2009. **134**(4): p. 653-6.

397. Sefah, K., et al., *Nucleic acid aptamers for biosensors and bio-analytical applications.* Analyst, 2009. **134**(9): p. 1765-75.

398. Zuo, X., et al., *A target-responsive electrochemical aptamer switch (TREAS) for reagentless detection of nanomolar ATP.* J Am Chem Soc, 2007. **129**(5): p. 1042-3.

399. Feng, C., Dai, S., and Wang, L., *Optical aptasensors for quantitative detection of small biomolecules: a review.* Biosens Bioelectron, 2014. **59**: p. 64-74.

400. Cha, T.G., et al., *Optical nanosensor architecture for cell-signaling molecules using DNA aptamer-coated carbon nanotubes.* ACS Nano, 2011. **5**(5): p. 4236-44.

401. Artemyev, M., and Nabiev, I., *Molecular beacons involving highly luminescent colloidal quantum dots.* J Nanophot, 2012. **6**: p. 060304-1:060304-3.

402. Li, H.X., and Rothberg, L.J., *DNA sequence detection using selective fluorescence quenching of tagged oligonucleotide probes by gold nanoparticles.* Anal Chem, 2004. **76**(18): p. 5414-5417.

403. Ho, F.M., and Hall, E.A., *A strand exchange FRET assay for DNA.* Biosens Bioelectron, 2004. **20**(5): p. 1001-10.

404. Wu, L., et al., *Sensitive electrochemical aptasensor by coupling "signal-on" and "signal-off" strategies.* Anal Chem, 2013. **85**(17): p. 8397-402.

405. Sassolas, A., Blum, L.J., and Leca-Bouvier, B.D., *Electrochemical Aptasensors.* Electroanalysis, 2009. **21**(11): p. 1237-50.

406. Zhou, N., et al., *A label-free electrochemical aptasensor for the detection of kanamycin in milk.* Analytical Methods, 2015. **7**(5): p. 1991-1996.

407. Zhu, B., et al., *Label-free electrochemical aptasensor for femtomolar detection of 17beta-estradiol.* Biosens Bioelectron, 2015. **70**: p. 398-403.

408. Wang, G., et al., *Extracellular silica nanocoat confers thermotolerance on individual cells: a case study of material-based functionalization of living cells.* ChemBioChem, 2010. **11**(17): p. 2368-73.

409. Wang, L., Fang, L., and Liu, S., *Responsive hairpin DNA aptamer switch to program the strand displacement reaction for the enhanced electrochemical assay of ATP.* Analyst, 2015. **140**(17): p. 5877-80.

410. Deng, B., et al., *Aptamer binding assays for proteins: the thrombin example--a review.* Anal Chim Acta, 2014. **837**: p. 1-15.

411. Zhang, J., et al., *A novel electrochemical aptasensor for thrombin detection based on the hybridization chain reaction with hemin/G-quadruplex DNAzyme-signal amplification.* Analyst, 2013. **138**(16): p. 4558-64.

412. Xu, W., et al., *Porous platinum nanotubes modified with dendrimers as nanocarriers and electrocatalysts for sensitive electrochemical aptasensors based on enzymatic signal amplification.* ChemComm, 2014. **50**(12): p. 1451-3.

413. Labib, M., and Berezovski, M.V., *Electrochemical aptasensors for microbial and viral pathogens.* Adv Biochem Eng Biotechnol, 2014. **140**: p. 155-81.

414. Wang, L., et al., *Label-free, regenerative and sensitive surface plasmon resonance and electrochemical aptasensors based on graphene.* ChemComm, 2011. **47**(27): p. 7794-6.

415. He, J.L., et al., *Fluorescence aptameric sensor for strand displacement amplification detection of cocaine.* Anal Chem, 2010. **82**(4): p. 1358-64.

416. Qian, Z.S., et al., *A fluorescent nanosensor based on graphene quantum dots-aptamer probe and graphene oxide platform for detection of lead (II) ion.* Biosens Bioelectron, 2015. **68**: p. 225-31.

417. Li, W., et al., *A sensitive, label free electrochemical aptasensor for ATP detection.* Talanta, 2009. **78**(3): p. 954-8.

418. Hamaguchi, N., A. Ellington, and M. Stanton, *Aptamer beacons for the direct detection of proteins.* Anal Biochem, 2001. **294**(2): p. 126-31.

419. Dinarello, C.A., *Historical insights into cytokines.* Eur J Immunol, 2007. **37 Suppl 1**: p. S34-45.

420. Fitzgerald, K.A., *The Cytokine Facts Book*. 2001, London: Academic Press. 13-14.

421. Richard, F.M., Eisenberg, D.D., and Kim, P.S., *Advances in Protein Chemistry: Cytokines*. Vol. 52. 1999, California, USA: Academic Press.

422. Available from: https://www.us.elsevierhealth.com/media/us/samplechapters/9781416048428/Ch023.pdf

423. Caligiuri, M.A., and Lotze, M.T., *Cytokines in the Genesis and Treatment of Cancer*. 2007, New Jersey, USA: Humana Press.

424. Came, P.E., and Carter, W.A., *Interferons and Their Applications*. 1984, Heidelberg, Germany: Springer-Verlag.

425. Goldstein, D., and Laszlo, J., *The role of interferon in cancer therapy: a current perspective.* CA Cancer J Clin, 1988. **38**(5): p. 258-77.

426. Shen, P., and Fillatreau, S., *Antibody-independent functions of B cells: a focus on cytokines.* Nat Rev Immunol, 2015. **15**(7): p. 441-51.

427. Sweetman, S.C., *Martindale : the complete drug reference*. 2011, Pharmaceutical Press: London.

428. Cheng, M., et al., *NK cell-based immunotherapy for malignant diseases.* Cell Mol Immunol, 2013. **10**(3): p. 230-52.

429. Ehtesham, M., et al., *Treatment of intracranial glioma with in situ interferon-gamma and tumor necrosis factor-alpha gene transfer.* Cancer Gene Ther, 2002. **9**(11): p. 925-34.

430. Wei, X., et al., *Inhibition of hepatitis C virus infection by interferon-gamma through downregulating claudin-1*. J Interferon Cytokine Res, 2009. **29**(3): p. 171-8.

431. Kokordelis, P., et al., *An effective interferon-gamma-mediated inhibition of hepatitis C virus replication by natural killer cells is associated with spontaneous clearance of acute hepatitis C in human immunodeficiency virus-positive patients.* Hepatology, 2014. **59**(3): p. 814-27.

432. Brunton, L.L., et al., *Goodman & Gilman's The pharmacological basis of therapeutics*. 2011, New York: McGraw-Hill. 659, 830.

433. Woodroofe, M.N., et al., *Detection of interleukin-1 and interleukin-6 in adult rat brain, following mechanical injury, by in vivo microdialysis: evidence of a role for microglia in cytokine production.* J Neuroimmunol, 1991. **33**(3): p. 227-36.

434. Nuntaprasert, A., et al., *Establishment of swine interleukin-6 sandwich ELISA.* Comp Immunol Microbiol Infect Dis, 2005. **28**(2): p. 121-30.

435. Helms, T., et al., *Direct visualization of cytokine-producing recall antigen-specific CD4 memory T cells in healthy individuals and HIV patients.* J Immunol, 2000. **164**(7): p. 3723-32.

436. Smedman, C., et al., *ELISpot analysis of LPS-stimulated leukocytes: human granulocytes selectively secrete IL-8, MIP-1beta and TNF-alpha.* J Immunol Methods, 2009. **346**(1-2): p. 1-8.

437. Schafer, H., et al., *Monoclonal antibodies to guinea pig interferon-gamma: tools for cytokine detection and neutralization.* J Immunol Methods, 2007. **328**(1-2): p. 106-17.

438. Zhang, P., et al., *Detection of interleukin-33 in serum and carcinoma tissue from patients with hepatocellular carcinoma and its clinical implications.* J Int Med Res, 2012. **40**(5): p. 1654-61.

439. Bosnjakovic, A., et al., *A dendrimer-based immunosensor for improved capture and detection of tumor necrosis factor-alpha cytokine.* Anal Chim Acta, 2012. **720**: p. 118-25.

440. Castanheira, A.P., et al., *Multiplexed femtomolar quantitation of human cytokines in a fluoropolymer microcapillary film.* Analyst, 2015. **140**(16): p. 5609-18.

441. Proupin-Perez, M., et al., *Studies on the attachment of DNA to silica-coated nanoparticles through a Diels-Alder reaction.* Nucleosides Nucleotides Nucleic Acids, 2005. **24**(5-7): p. 1075-9.

442. Crowthe, J.R., *Methods in Molecular Biology; The ELISA Guidebook*. Vol. 149. 2001, New Jersey, USA: Humana Press.

443. Voller, A., Bartlett, A., and Bidwell, D., *Immunoassays for the 80s*. 1981, Lancester, UK: MTP Press Limited.

444. Wild, D., *The Immunoassay Handbook*. Third ed. 2005, Amsterdam, The Netherlands: Elsevier.

445. Macey, M.G., *Flow Cytometry: Principles and Applications*. 2007, New Jersy: Humana Press. 1-5.

446. Prussin, C., and Metcalfe, D.D., *Detection of intracytoplasmic cytokine using flow cytometry and directly conjugated anti-cytokine antibodies.* J Immunol Methods, 1995. **188**: p. 117-128.

447. Zelnickova, P., et al., *Intracellular cytokine detection by flow cytometry in pigs: fixation, permeabilization and cell surface staining.* J Immunol Methods, 2007. **327**(1-2): p. 18-29.

448. Hill, H.R., and Martins, T.B., *The flow cytometric analysis of cytokines using multi-analyte fluorescence microarray technology.* Methods, 2006. **38**(4): p. 312-6.

449. de Jager, W., et al., *Simultaneous detection of 15 human cytokines in a single sample of stimulated peripheral blood mononuclear cells.* Clin Diagn Lab Immunol, 2003. **10**(1): p. 133-9.

450. Sklar, L.A., *Flow cytometry for biotechnology*. 2005, Oxford: Oxford University Press. 16-21.

451. Davey, H.M., and Kell, D.B., *Flow cytometry and cell sorting of heterogeneous microbial populations: the importance of single-cell analyses.* Microbiol Rev, 1996. **60**(4): p. 641-96.

452. Zhang, H., et al., *Ultrasensitive assays for proteins.* Analyst, 2007. **132**(8): p. 724-37.

453. Qureshi, A., Gurbuz, Y., and Niazi, J.H., *Biosensors for cardiac biomarkers detection: A review.* Sensors and Actuators B: Chemical, 2012. **171-172**: p. 62-76.

454. Baraket, A., et. al., *Cytokine detection using diazonium modified gold microelectrodes onto polyimide substrates with integrated Ag/AgCl reference electrode.* Procedia Engineering, 2012. **47**: p. 1181-1184.

455. Baraket, A., et al., *Diazonium modified gold microelectrodes onto polyimide substrates for impedimetric cytokine detection with an integrated Ag/AgCl reference electrode,.* Sensors and Actuators B: Chemical, 2013. **189**: p. 165-172.

456. Liu, Y., et al., *Detecting multiple cell-secreted cytokines from the same aptamer-functionalized electrode.* Biosens Bioelectron, 2015. **64**: p. 43-50.

457. Liu, Y., Kwa, T., and Revzin, A., *Simultaneous detection of cell-secreted TNF-alpha and IFN-gamma using micropatterned aptamer-modified electrodes.* Biomater, 2012. **33**(30): p. 7347-55.

458. Liu, Y., Zhou, Q., and Revzin, A., *An aptasensor for electrochemical detection of tumor necrosis factor in human blood.* Analyst, 2013. **138**(15): p. 4321-6.

459. Matharu, Z., et al., *Detecting transforming growth factor-beta release from liver cells using an aptasensor integrated with microfluidics.* Anal Chem, 2014. **86**(17): p. 8865-72.

460. Liu, Y., et al., *Micropatterned aptasensors for continuous monitoring of cytokine release from human leukocytes.* Anal Chem, 2011. **83**(21): p. 8286-92.

461. Christodoulides, N., et al., *A microchip-based multianalyte assay system for the assessment of cardiac risk.* Anal Chem, 2002. **74**(13): p. 3030-6.

462. Zhang, B., et al., *Multiplexed cytokine detection on plasmonic gold substrates with enhanced near-infrared fluorescence.* Nano Research, 2013: p. 113-120.

463. Wang, C.W., et al., *Development of combination tapered fiber-optic biosensor dip probe for quantitative estimation of interleukin-6 in serum samples.* J Biomed Opt, 2010. **15**(6): p. 067005.

464. Wang, C.W., et al., *Quantitative Estimation of IL-6 in Serum/Plasma Samples Using a Rapid and Cost-Effective Fiber-Optic dip-probe.* Proc Soc Photo Opt Instrum Eng, 2010. **7559**(75590G).

465. Wang, C.W., and Kapoor, R., *Highly specific detection of IL-8 protein using combination tapered fiber-optic biosensor dip-probe.* Proc Soc Photo Opt Instrum Eng, 2010. **7559**: p. 75590V1-75590V6.

466. Kapoor, R., and Wang, C.W., *Highly specific detection of interleukin-6 (IL-6) protein using combination tapered fiber-optic biosensor dip-probe.* Biosens Bioelectron, 2009. **24**(8): p. 2696-701.

467. Ruslinda, A.R., et al., *Highly sensitive detection of platelet-derived growth factor on a functionalized diamond surface using aptamer sandwich design.* Analyst, 2012. **137**(7): p. 1692-7.

468. Pan, L., et al., *Label-free fluorescence probe based on structure-switching aptamer for the detection of interferon gamma.* Analyst, 2013. **138**(22): p. 6811-6.

469. Tuleuova, N., et al., *Development of an aptamer beacon for detection of interferon-gamma.* Anal Chem, 2010. **82**(5): p. 1851-7.

470. Cooper, M.A., *Optical biosensors in drug discovery.* Nat Rev Drug Discov, 2002. **1**(7): p. 515-28.

471. Gautschi, G., *Piezoelectric Sensorics: Force Strain pressure acceleration and acoustic emission sensors and amplification*. 2002, Berlin: Springer-Verlag. 5-15.

472. Pasche, S., et al., *Monitoring of cellular immune responses with an optical biosensor: a new tool to assess nanoparticle toxicity.* Procedia Chemistry, 2009. **1**: p. 738-741.

473. Pasche, S., et al., *Integrated optical biosensor for in-line monitoring of cell cultures.* Biosens Bioelectron, 2010. **26**(4): p. 1478-85.

474. Sipova, H., et al., *Surface plasmon resonance biosensor based on engineered proteins for direct detection of interferon-gamma in diluted blood plasma.* Sensors and Actuators B-Chemical, 2012. **174**: p. 306-311.

475. Yang, C.Y., et al., *Detection of picomolar levels of interleukin-8 in human saliva by SPR.* Lab Chip, 2005. **5**(10): p. 1017-23.

476. Chou, T.H., Chuang, C.Y., and Wu, C.M., *Quantification of Interleukin-6 in cell culture medium using surface plasmon resonance biosensors.* Cytokine, 2010. **51**(1): p. 107-11.

477. Chang, C.C., et al., *Amplified surface plasmon resonance immunosensor for interferon-gamma based on a streptavidin-incorporated aptamer.* Biosens Bioelectron, 2012. **37**(1): p. 68-74.

478. Luo, J., et al., *Quartz crystal microbalance biosensor for recombinant human interferon-beta detection based on antisense peptide approach.* Anal Chim Acta, 2007. **590**(1): p. 91-7.

479. Min, K., et al., *A simple and direct electrochemical detection of interferon-gamma using its RNA and DNA aptamers.* Biosens Bioelectron, 2008. **23**(12): p. 1819-24.

480. Peng, J., et al., *Synthesis of silver nanoparticle-hollow titanium phosphate sphere hybrid as a label for ultrasensitive electrochemical detection of human interleukin-6.* Small, 2011. **7**(20): p. 2921-8.

481. Yang, T.L., *Electrochemical sensor utilizing ferrocene loaded porous polyelectrolyte nanoparticles as label for the detection of protein biomarker IL-6.* Sensors and Actuators B: Chemical, 2011. **158**: p. 361-365.

482. Munge, B.S., et al., *Nanostructured immunosensor for attomolar detection of cancer biomarker interleukin-8 using massively labeled superparamagnetic particles.* Angew Chem Int Ed Engl, 2011. **50**(34): p. 7915-8.

483. Yang, T., et al., *An electrochemical impedance sensor for the label-free ultrasensitive detection of interleukin-6 antigen.* Sensors and Actuators B: Chemical, 2013. **178**: p. 310-315.

484. Yan, G., et al., *A highly sensitive label-free electrochemical aptasensor for interferon-gamma detection based on graphene controlled assembly and nuclease cleavage-assisted target recycling amplification.* Biosens Bioelectron, 2013. **44**: p. 57-63.

485. Hun, X., and Zhang, Z., *Functionalized fluorescent core-shell nanoparticles used as a fluorescent labels in fluoroimmunoassay for IL-6.* Biosens Bioelectron, 2007. **22**(11): p. 2743-8.

486. Wu, H., et al., *Dye-doped silica nanoparticle labels/protein microarray for detection of protein biomarkers.* Analyst, 2008. **133**(11): p. 1550-5.

487. Kim, G.I., et al., *The detection of platelet derived growth factor using decoupling of quencher-oligonucleotide from aptamer/quantum dot bioconjugates.* Nanotechnology, 2009. **20**(17): p. 175503.

488. Hoa, X.D., Kirk, A.G., and Tabrizian, M., *Enhanced SPR response from patterned immobilization of surface bioreceptors on nano-gratings.* Biosens Bioelectron, 2009. **24**(10): p. 3043-8.

489. McQueenie, R., et al., *Detection of inflammation in vivo by surface-enhanced Raman scattering provides higher sensitivity than conventional fluorescence imaging.* Anal Chem, 2012. **84**(14): p. 5968-75.

490. Chiang, C.Y., et al., *Fiber-optic particle plasmon resonance sensor for detection of interleukin-1beta in synovial fluids.* Biosens Bioelectron, 2010. **26**(3): p. 1036-42.

491. Hurk, R., and Evoy, S., *Deflection cantilever detection of interferon gamma.* Sensors and Actuators B: Chemical, 2013. **176**: p. 960-65.

492. Chaves, A.R., and Queiroz, M.E., *Immunoaffinity in-tube solid phase microextraction coupled with liquid chromatography with fluorescence detection for determination of interferon alpha in plasma samples.* J Chromatogr B Analyt Technol Biomed Life Sci, 2013. **928**: p. 37-43.

493. Cai, L., et al., *Silica nanoparticles based label-free aptamer hybridization for ATP detection using hoechst33258 as the signal reporter.* Biosens Bioelectron, 2011. **29**(1): p. 46-52.

494. Dietz, K.J., and Herth, S., *Plant nanotoxicology.* Trends Plant Sci, 2011. **16**(11): p. 582-9.

495. Fuller, D.N., et al., *A general method for manipulating DNA sequences from any organism with optical tweezers.* Nucleic Acids Res, 2006. **34**(2): p. e15.

496. Cao, Y.C., Jin, R., and Mirkin, C.A., *Nanoparticles with Raman spectroscopic fingerprints for DNA and RNA detection.* Science, 2002. **297**(5586): p. 1536-40.

497. McCauley, T.G., Hamaguchi, N., and Stanton, M., *Aptamer-based biosensor arrays for detection and quantification of biological macromolecules.* Anal Biochem, 2003. **319**(2): p. 244-50.

498. Association, A.P., *The United States Pharmacopeia 30-NF 25*. 2007: Washington DC, USA.

499. Gunawan, C.A., Ge, M., and Zhao, C., *Robust and versatile ionic liquid microarrays achieved by microcontact printing.* Nat Commun, 2014. **5**: p. 3744.

500. Armbruster, D.A., and Pry, T., *Limit of blank, limit of detection and limit of quantitation.* Clin Biochem Rev, 2008. **29 Suppl 1**: p. S49-52.

501. Peng, H., et al., *DNA hybridization detection with blue luminescent quantum dots and dye-labeled single-stranded DNA.* J Am Chem Soc, 2007. **129**(11): p. 3048-9.

502. Yang, Y., et al., *NIR photoresponsive crosslinked upconverting nanocarriers toward selective intracellular drug release.* Small, 2013. **9**(17): p. 2937-44.

503. Cai, H., et al., *Carbon nanotube-enhanced electrochemical DNA biosensor for DNA hybridization detection.* Anal Bioanal Chem, 2003. **375**(2): p. 287-93.

504. Wang, X., et al., *QDs-DNA nanosensor for the detection of hepatitis B virus DNA and the single-base mutants.* Biosens Bioelectron, 2010. **25**(8): p. 1934-40.

505. Wu, Z.S., et al., *Optical detection of DNA hybridization based on fluorescence quenching of tagged oligonucleotide probes by gold nanoparticles.* Anal Biochem, 2006. **353**(1): p. 22-9.

506. Delport, F., et al., *Real-time monitoring of DNA hybridization and melting processes using a fiber optic sensor.* Nanotechnology, 2012. **23**(6): p. 065503.

507. Liu, S.Q., *Bioregenerative Engineering: Principles and Applications*. 2007, New Jersey, USA: John Wiley & Sons. Inc.

508. Wang, D., et al., *Highly stable surface functionalization of microgas chromatography columns using layer-by-layer self-assembly of silica nanoparticles.* Anal Chem, 2013. **85**(17): p. 8135-41.

509. Siawaya, D., et al., *An evaluation of commercial fluorescent bead-based luminex cytokine assays.* PLoS One, 2008. **3**(7): p. e2535.

510. Houser, B., *Bio-Rad's Bio-Plex(R) suspension array system, xMAP technology overview.* Arch Physiol Biochem, 2012. **118**(4): p. 192-6.